

Chapter 1: Introduction and Background

A. Introduction

Phreatomagmatism occurs when rising magma encounters external ground water. When the proportion of water is very high, pillow lavas form and if water:magma is very low, pyroclastic cinder and pumice cones result. In the narrow range between these two end members, the volcanic morphologies of maars, tuff cones, and tuff rings are formed (Figure 1). All three of these volcano types are the products of highly energetic, dominantly fine-grained phreatomagmatic pyroclastic surges and falls.

Tepexitl tuff ring is a monogenetic rhyolitic center in the Serdán-Oriental Basin, a bimodal volcanic field active from late Pleistocene through Holocene time, located at the eastern end of the Trans-Mexican Volcanic Belt (TMVB) (Figure 2). Tepexitl was studied only once, in 1975, by a group of scientists investigating the possibility that it originated as a meteor impact crater (Maupomé et al., 1975). After they determined Tepexitl was volcanic in origin, no further studies were made at the maar. Tepexitl's well-preserved deposits and easily accessible crater deposits, not obscured by an inner crater dome, make it an excellent location to study the near-vent facies and ash shapes that result from the interaction of rhyolitic magma with external water. Evidence for water in the eruptive system includes abundant bomb sags, accretionary lapilli, scour channels, undulatory bedding, and iron-rich lithic clasts that have altered surrounding lapilli in-situ (a post-deposition process dependent on water and heat). The presumed source of water was from saturated sediments or shallow groundwater.

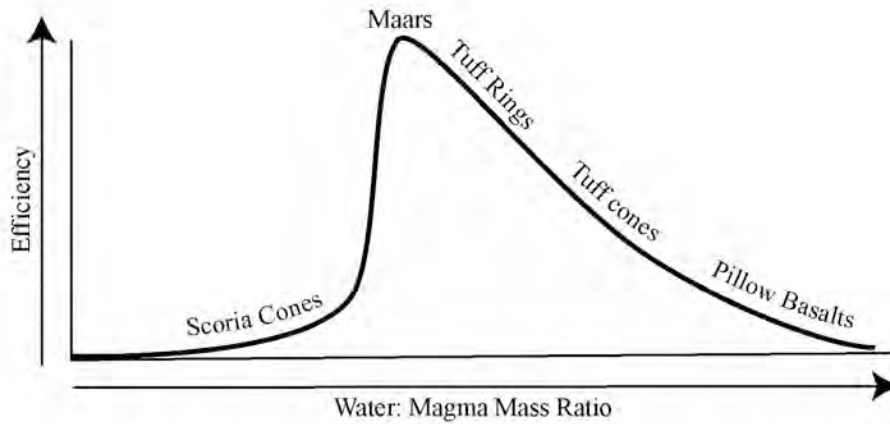


Figure 1: How changing amounts of water and basaltic magma available for thermal transfer affects eruption efficiency and the resulting deposits. Adapted from Wohletz and Sheridan, 1983.

B. Purpose and Objectives

The study of volcanic hazards is a rapidly growing field, but comprehensive evaluations of hazards associated with small phreatomagmatic eruptions are scarce. Only recently was an in-depth assessment of the hazards associated with basaltic maar eruptions compiled (Lorenz, 2007). Lorenz discussed common syn-eruption hazards such as ballistic blocks, surges, earthquakes, ash fallout, and the release of noxious gases and their effects on local communities, agriculture, animals, and infrastructure. He also discussed hazards more specific to diatreme development, such as problematic deepening of the groundwater table and possible contamination of drinking water. Post-eruption, other hazards from maar-forming eruptions must be considered. Landslides, slumping, and lahars can be hazards for some time after activity ends. The long repose periods

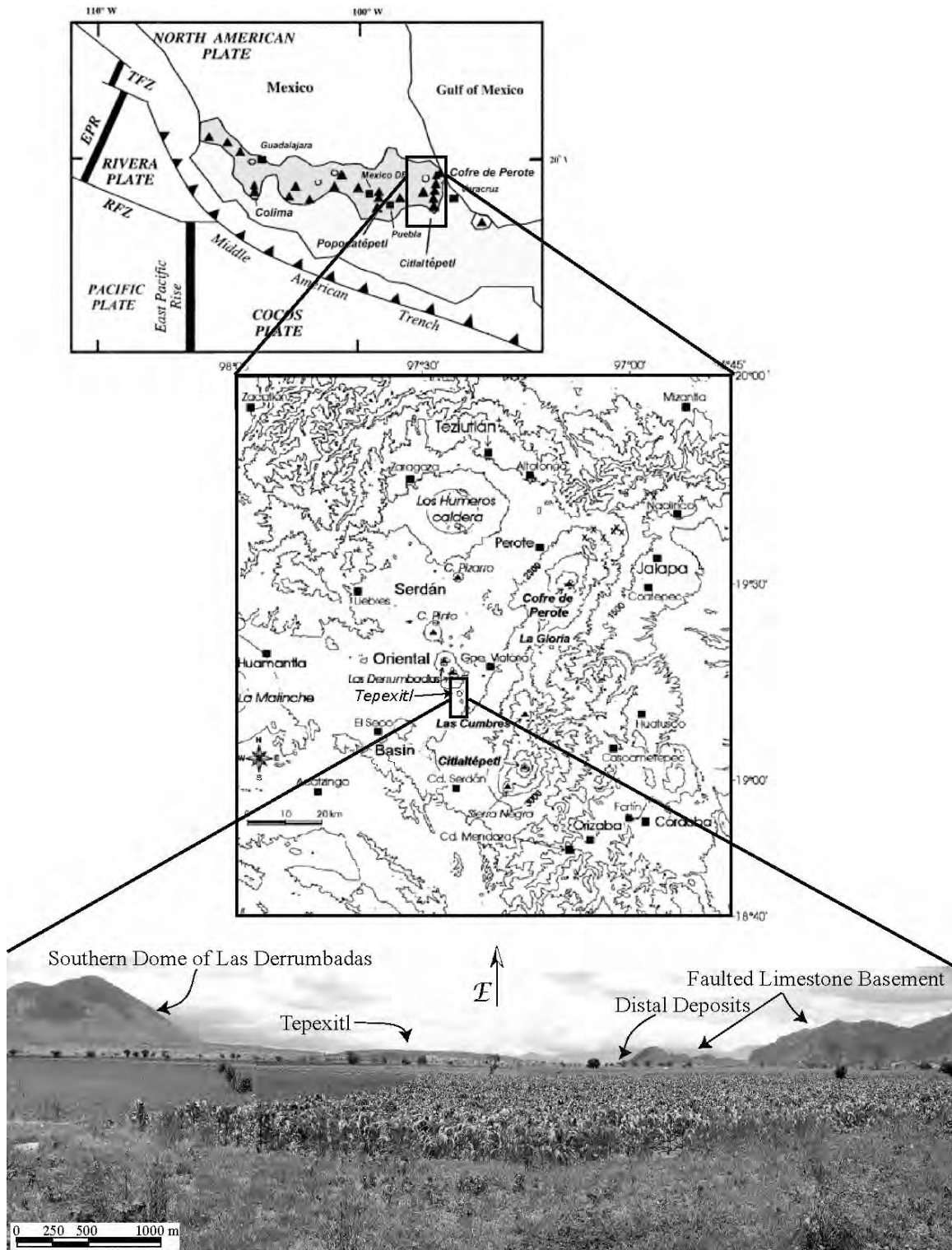


Figure 2: Location of Tepexitl tuff ring within the Serdan-Oriental Basin, a topographic low near the eastern edge of the Trans-Mexican Volcanic Belt (shown in the shaded region in the upper picture). Adapted from Siebe et al., (1993), and Siebert and Carrasco-Núñez, (2002).

common to maar-forming eruptions (days to weeks) can lure people into a false sense of security, causing injury or death if activity resumes again unexpectedly. Additionally, dangerous gases can persist in the crater for a long time after cessation of eruption.

The average basaltic maar-forming eruption lasts from several days to 15 years, and has an average destruction radius of 3-5 km from the vent center (Lorenz, 2007). However, at the 1977 eruption of Ukinrek, fine ash was reported over a 20,000-25,000 km² area, even though significant accumulation was limited to only a 3-km radius from the vent (Sheridan and Barberi, 1983). Wohletz and Zimanowski (2000) warn that one of the major hazards associated with shallow phreatomagmatism is the opening of a large vent, triggering a large-scale eruption from the resulting decompression. Rhyolitic pyroclastic eruptions need to be included in this discussion. Siebe et al. (1995) echoed this sentiment when they called for a need to understand the hazards of different kinds of rhyolitic eruptions in more detail because of population growth the Serdán-Oriental Basin.

Although depositional patterns suggest that external water was present during the eruption and formation of Tepexitl, it remained unclear to what extent this water was involved in the fragmentation process. Therefore, the first objective of this study was to determine what role phreatomagmatism played in the formation of Tepexitl. Field evidence suggests that rhyolitic phreatomagmatism routinely occurs, but creates deposits of different morphologies than phreatomagmatic eruptions at basaltic maars (e.g. Sheridan and Updike, 1975; Sieh and Bursik, 1986; Heiken and Wohletz, 1987; Sheridan et al., 1987; Heiken and Wohletz, 1987; Houghton et al., 1987; Heiken et al., 1988; Brooker et al., 1993; Roache et al., 2000). Previous research also suggests that effective

coarse mixing between a vesiculating rhyolite and external water is difficult to achieve, which should theoretically limit phreatomagmatic fragmentation (Zimanowski et al., 1991; Zimanowski, 1998).

In order to evaluate the mechanisms for and consequences of rhyolitic phreatomagmatism at Tepexitl, it was necessary to reconstruct an eruptive history based on depositional evidence. Based on these data, a second objective was identification of the variables and controls on the fragmentation process at Tepexitl. Additionally, because it could be determined that phreatomagmatism contributed to the fragmentation process, a mechanism for which a highly viscous magma may react explosively with water is proposed. The conclusions of this study were accomplished through a detailed examination of the deposits: small-scale changes of grain-size distributions, componentry, and ash morphology of the tuff as well as large-scale changes of bulk chemistry, petrology, and textural analyses of juvenile material with time.

Because the fragmentation process is directly related to the amount of energy released by the system, this study can be used in future research to determine the scale of eruption and the associated hazards specific to rhyolitic intrusions through saturated sediments, a realistic situation for future eruptions in active volcanic fields. Rhyolitic phreatomagmatism is sensitive to many variables and needs to be examined in greater detail than it has been in the past.

C. Geologic Setting:

The Serdán-Oriental Basin is a topographic low between the cities of Veracruz and Puebla at the eastern margin of the E-W-trending TMVB (Figure 2), with an average elevation of 2500 m (Rodríguez, 2005). The basin contains numerous volcanic features of

various types – cinder cones, basaltic maars, tuff cones, and rhyolitic domes – that record activity dating back to Miocene time (Riggs and Carrasco-Núñez, 2004). Its bimodal nature is thought to be related to shallow subduction of the Cocos and Rivera Plates under the North American Plate along the western edge of Mexico (e.g. Siebert and Carrasco- Núñez, 2002; Rodriquez, 2005) and/or to partial melting of the lower crust (Verma, 1999). A series of N-S aligned volcanic chains crosses the TMVB, with the youngest activity focused on the southernmost volcano in each chain (Siebert and Carrasco-Núñez, 2002). The Serdán-Oriental Basin lies inland of the easternmost such chain, the Altiplano Highlands, which has Citlalteptl (Pico de Orizaba) at its southern end (Figure 2). To the north is Los Humeros caldera and to the west lies the Cofre de Perote-Citlatepetl chain. Underlying the volcanic rocks of the Serdán-Oriental Basin are highly deformed Cretaceous limestone and minor shale, faulted and folded during the Laramide orogeny (Siebe and Verma, 1988). Large outcrops of this limestone occur throughout the Serdán-Oriental Basin, in ranges that are oriented NW-SE (Rodriquez, 2005).

The Serdán-Oriental Basin has served as a natural “catchment” for reworked Quaternary unconsolidated material from surrounding volcanoes. Locally called Toba Café, this mixture of fine-grained eolian and ephemeral fluvial deposits (Siebe and Verma, 1988) is still accumulating. Toba Café has not been studied in great detail, so its extent, depth, and age are largely unknown. However, it is inferred to be the aquifer that serves as a water source for many of the maars in the area (Ort and Carrasco-Núñez, 2004; Carrasco-Núñez et al., 2007). Localized Toba Café at the base of Tecuitlapa, a basaltic maar 15.5 kilometers southwest of Tepexitl, consists of massive tan-colored tuff with intermittent laterally discontinuous beds of larger clasts - dominantly rounded river

cobbles of basalt and andesite between 4 cm and 100 cm in diameter. Cold, wet periods of glaciation and subsequent melting are possible periods of fluvial deposition within the Toba Café sequence, whereas the eolian deposits may have been deposited during the hot, dry interglacial periods (Siebe, 1986).

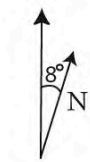
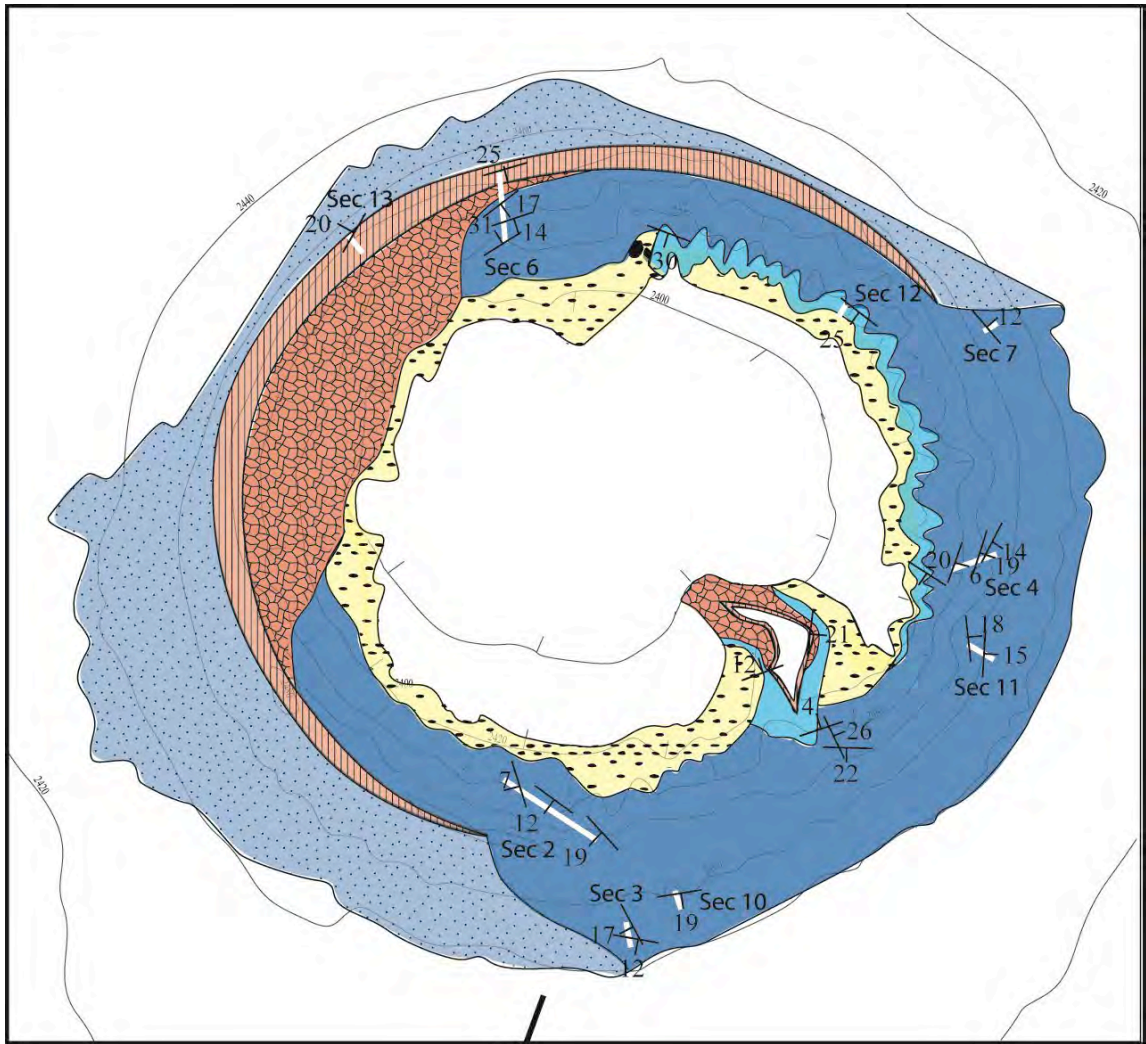
A dome complex called Las Derrumbadas, which lies between Tepexitl and Cerro Pinto rhyolitic complex, marks the middle of the Serdán-Oriental Basin (Figure 2). Cerro Pinto, Las Derrumbadas, and Tepexitl have remarkably similar petrology and form a series of rhyolitic tuff cones and domes along a NW-SE-trending thrust fault of basement limestone (Campos-Enriquez and Garduño-Monroy, 1987).. Their morphological differences have been attributed to the controls that govern the growth of monogenetic silicic centers (Siebe et al., 1995). Las Derrumbadas is a 10-40 ka polygenetic volcano with active fumaroles (Siebe and Verma, 1988). The lava of Las Derrumbadas, as at Tepexitl, is gray microcrystalline biotite-plagioclase rhyolite with accessory garnet (Siebe and Verma, 1988). The complex has a volume of 6-7 km³ and the domes were emplaced through older pyroclastic deposits (Siebe et al., 1995). Cerro Pinto is also a multi-stage peraluminous rhyolitic volcano with four individual domes and four tuff rings. The tuff ring eruptions are believed to have been initiated by phreatomagmatic interactions, grading into magmatic eruptions as time progressed (Zimmer, 2007).

Two other rhyolitic complexes in the area have been studied in detail, Cerro Pizarro directly north of Tepexitl, and Las Cumbres to the southeast (Figure 2), both of which also have similar chemistry to the Tepexitl-Las Derrumbadas-Cerro Pinto series. Cerro Pizarro is a mid-Pleistocene cone-shaped dome nestled inside a well-indurated vitrophyre ring with an eruptive volume of 1.1 km³ (Riggs and Carrasco-Núñez, 2004).

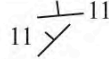
Las Cumbres is a polygenetic andesite to rhyolite complex located in the Altiplano volcanic chain, and was active from late Pliocene to Holocene time (Siebe et al., 2005). It has been linked to the voluminous Quetzalapa pumice deposit 23,000 years ago, an important regional stratigraphic marker within the Toba Café that is older than many maars and tuff rings in the Serdán-Oriental Basin (Rodríguez, 2005).

In addition to the well-studied rhyolitic centers in the Serdán-Oriental Basin, several mafic maars have been analyzed. Tecuitlapa is a basaltic maar described by Ort and Carrasco- Núñez (2004), whose maar surge deposits overlie a thick sequence of Toba Café, the assumed aquifer providing water to the eruption. Atexcac maar, northeast of Tepexitl, was formed by phreatomagmatic eruptions with water likely from deep fractures of Pliocene-Miocene andesitic lava (Carrasco-Núñez et al., 2007). Lastly, Cerro Xalapasco is a dacitic phreatomagmatic tuff ring on the slopes of La Malinche volcano, 25 km to the east of Tepexitl, also with phreatomagmatism fueled by saturated sediments (Abrams and Siebe, 1994). Almost twice the size of Tepexitl, Cerro Xalapasco had eruptive activity from 10 different vents. It is interesting to note that the mafic volcanic features within the Serdán-Oriental Basin are aligned in a roughly NE-SW lineament, parallel to the maximum regional horizontal stress (Carrasco-Núñez et al., 2005), whereas the silicic centers are aligned in a NW-SE direction, perpendicular to that stress.

Tepexitl crater, located in the center of the basin, is remarkably circular with a diameter of approximately 1 kilometer from rim to rim (Figure 3). The crater floor lies 20 m below the surrounding countryside and 75 m below the crater rim, but no contact was found with the pre-eruptive surface. Due to centuries-old agricultural cultivation both on the crater floor and the surrounding apron, exposure is largely limited to the crater walls.



Section 8 (1.5 km away)



0 50 100 200 300 400 500 600 Meters



LEGEND

 Exposed Tuff	 Late-Stage Tuff	 Final Breccias	 Debris Flow
 Covered Tuff	 Cultivated Fields	 Explosion Breccia	 Anomalous Ash

x \ Strike and Dip

Contour Interval = 20 meters

Measured sections are indicated with numbered white lines.

Figure 3: Surficial morphology map of Tepexitl tuff ring.

Only one distal deposit was found, a small outcrop of Tepexitl tuff lapping onto a limestone ridge 1 km to the southeast.

The inner crater is characterized by unusual features: poor to no exposure of western tuff deposits, a flat-topped “thumb” extending out from the SE crater wall, the presence of fragmented breccia only in drainages, and syn-eruptive slumping (Figure 3). Juvenile material is quartz-plagioclase-biotite-sanidine-phyric, peraluminous rhyolite with accessory almandine and occurs with variably stony, pumiceous, vitrophyric, perlitic and flow-banded textures. The dominant component in crater-wall surge and fall deposits is very poorly vesicular stony gray rhyolite. Tepexitl’s stratigraphy is characterized by poorly cemented laminae to medium beds that encompass six unique facies, which change every 10 to 100 cm vertically. Sharp contacts between beds suggest deposition by discrete blasts.

D. Molten Fuel-Coolant Interactions

a. Phreatomagmatic Fragmentation and Explosion

Phreatomagmatic explosions are a type of molten fuel-coolant interaction (MFCI) in which lava is the fuel and water the coolant. The highly explosive eruptive dynamics resulting from the direct contact between fuel and coolant have been explored in great detail for mafic melts, through a combination of field observations, lab experiments, and resultant grain size and shape analysis (e.g. Wohletz, 1983; Büttner et al., 1999; Zimanowski et al., 2003; Dellino et al., 2004). Wohletz and Heiken (1992) state that, because standing water is so abundant in and on the Earth’s crust, most volcanic fields have at least one feature that was produced by phreatomagmatic activity. However,

although volcanic MFCI is common, it is a very complex process that is not yet fully understood.

MFCI explosions develop and are perpetuated because of rapid transfer of heat from fuel to coolant resulting in a tremendous transfer of thermal energy into fragmentation, seismic, acoustic, expansion and transportation energy (Wohletz and Zimanowski, 2000). Because the transfer of thermal to mechanical energy is greater in phreatomagmatic eruptions than in magmatic eruptions, the resulting kinetic energy release is also greater (Zimanowski, 1998), which relates to a more powerful explosion than would be expected with the same magma but without water. The process of melt fragmentation and expulsion for more mafic (and thus more fluidal) melts has been described as a four-step process.

Stage 1: Coarse Mixing

Upon initial contact of magma and coolant, a mm-thick vapor film (Dellino, 2000) develops, which thermally separates the two immiscible fluids (called the Leidenfrost effect) and allows for coarse mixing (White, 1996; Zimanowski et al., 1997a, b; Wohletz and Zimanowski, 2000). In order for this vapor phase to form, contact must occur when the ambient pressure is below the hydrostatic pressure (Zimanowski et al., 1997a; Wohletz and Zimanowski, 2000). Mixing is accomplished because of instabilities that develop along this temporary interface due to the relative movement of fuel and coolant. Kelvin-Helmholtz instabilities are caused by shear stresses related to movement along the boundary and Rayleigh-Taylor instabilities form diapirs because of density differences between the two fluids (Morrissey et al., 2000) (Figure 4). This phase lasts from seconds to minutes and is a prerequisite for intensive MFCI (Zimanowski, 1998; Morrissey et al.,

2000). Due to the high heat capacity of water, domains of melt trapped within it will quickly solidify. Therefore, the most explosive interactions occur when domains of water of a critical surface area become trapped inside the melt during this first stage (Zimanowski et al., 1997a, b).

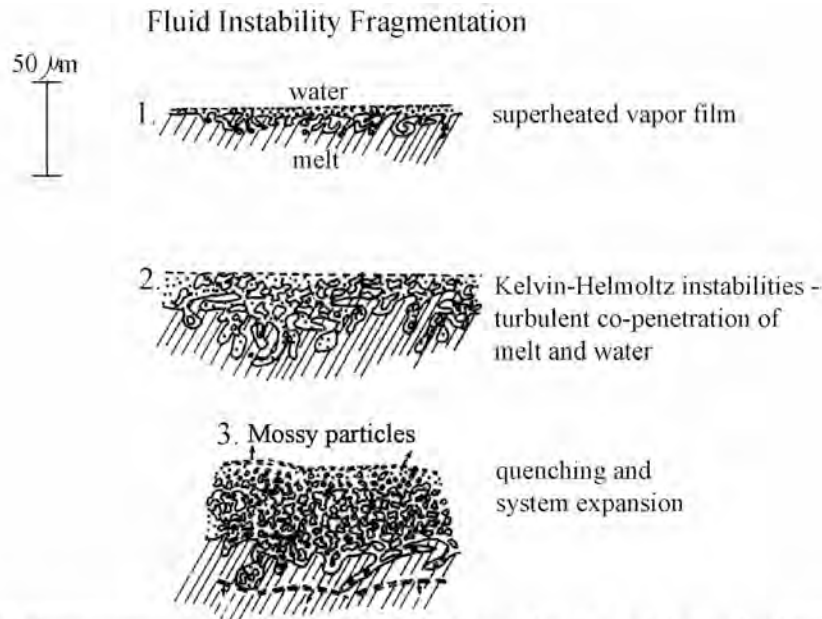


Figure 4: Stages of phreatomagmatic fragmentation, initiated by Rayleigh-Taylor instabilities, show the fluidal, coarse dynamic mixing typical of a basalt (adapted from Wohletz, 1983).

Stage 2: Vapor Film Collapse

The vapor film that develops between fuel and coolant eventually collapses quasi-coherently either because of its own instabilities (Wohletz, 1986), overcooling and rapid condensation (Morrissey et al., 2000), or because of an external trigger causing a seismic disturbance (i.e. thermal fracturing, rock falls, etc.; Zimanowski, 1998; Wohletz and Zimanowski, 2000). The fuel and coolant are then hydraulically coupled and their direct contact causes the transfer of heat to increase by 1-2 orders of magnitude (Zimanowski, 1998; Büttner et al., 2002). Although this stage lasts only microseconds (Zimanowski,

1998), it causes dynamic responses in the system as the melt is rapidly cooled and the water is rapidly heated (Büttner et al., 2002).

Stage 3: Brittle Response and Fine Fragmentation

Vapor film collapse causes very high fluid pressures to act on the melt, and simultaneous direct contact of fuel with coolant leads to thermal granulation as the cooling rate of the magma increases. The result is brittle deformation of the melt along the hydraulically coupled interface - a system called “fine fragmentation” (Zimanowski et al., 1997a, b; Zimanowski, 1988; Morrissey et al., 2000). The release of hydrostatic pressure through fragmentation sends out a series of intense shock waves at rates that exceed the bulk modulus of the melt, leading to a front of brittle failure that penetrates downward through the melt (Zimanowski et al., 1997a, b; Zimanowski, 1998; Lorenz, 2000; Morrissey et al., 2000; Wohletz and Zimanowski, 2000). This stage lasts only milliseconds (Wohletz and Zimanowski, 2000), but releases a large amount of kinetic energy (Büttner et al., 2002).

Stage 4: Expansion and Passive Fragmentation

During fine fragmentation, the coolant becomes superheated, quickly reaching a point at which it cannot absorb any more heat. The water then flashes to vapor, decouples from the liquid, and expands at a rate of 1 m/s (Zimanowski et al., 1997b; Morrissey et al., 2000). Provided the vapor pressure exceeds the overburden pressure (Cas and Wright, 1987), this expansion triggers a highly energetic explosion of seismic and kinetic energy and lasts from milliseconds to minutes (Zimanowski, 1988). During eruption, portions of the melt adjacent to the MFCI interface not affected by brittle fragmentation are ejected as fluidal particles (White, 1996; Büttner et al., 2002).

The MFCI process occurs repeatedly because of a positive feedback mechanism that happens as brittle failure of the melt caused by fine fragmentation allows water to penetrate farther into the melt, increasing fuel-coolant surface area (Zimanowski et al., 1997b; Zimanowski, 1998). Thus, the rate of transfer of thermal to mechanical energy is increased (Büttner et al., 2002). This process is linked to both the pulsatory nature of phreatomagmatic eruptions (Cas and Wright, 1987; Dellino, 2000) and to the increasing depth of explosive interaction between magma and coolant (Wohletz, 1983; Lorenz, 2000b).

b. Phreatomagmatic Ash

Fragmentation processes occurring during MFCI are complex. MFCI fine fragmentation occurs directly on the interface of magma and water whereas brittle fragmentation can occur throughout the melt, as stress waves travel faster than thermal contraction (Morrissey et al., 2000). Additionally, vesiculating melt can be fragmented by purely magmatic processes (Fisher and Schmincke, 1984; Cas and Wright, 1987). If melt is flooded with water, non-explosive thermal granulation occurs because heat transfer is ineffective (Cas and Wright, 1987; Büttner et al., 2002). Despite these variables, the morphology of ash grains produced during MFCI is unique.

Extensive research of mafic ash grains has allowed identification of ‘active’ particles (those produced from direct contact with the coolant during fine fragmentation, at the source of transfer from thermal to mechanical energy) versus ‘passive’ particles (those produced by brittle fragmentation of the surrounding melt and fluidal ejecta from ductile fragmentation during vapor expansion) (e.g. Heiken, 1972; Wohletz, 1983; Zimanowski et al., 1997b; Büttner et al., 1999; Büttner et al., 2002). In studied

pyroclastic deposits, 'active' particles have been found exclusively in the grain-size range between 20 and 180 microns (3-5 phi; e.g. Zimanowski et al., 1991; Dellino and La Volpe, 1996).

Active particles represent only a very small portion of the final deposits but their total surface area is directly proportional to the energy released and thus to the intensity of the explosion (Zimanowski et al., 1991; Zimanowski, 1998; Büttner et al., 2002). The majority of thermal energy is converted to mechanical energy during fragmentation processes (Zimanowski, 1998; Dellino, 2000; Morrissey et al., 2000). Therefore, a more intense and more efficient interaction results in an increase of the surface area of particles created (Morrissey et al., 2000). It is important to note that, although fine ash is where morphological evidence of MFCI processes exists, its abundance alone is not a good indicator of fragmentation processes because a large abundance of fine ash can be produced by strictly magmatic processes as well (Dellino, 2000; Dellino et al., 2001; Zimanowski et al., 2003). Ash morphologies and interpretations specific to MFCI are discussed in more detail in Chapter 5.

c. Morphology of Phreatomagmatic Deposits

The landforms resulting from efficient phreatomagmatic eruptions are maars, tuff rings, and tuff cones (Zimanowski, 1998). These different morphologies generally result from a continuum of decreasing efficiency and excess water, with maars being the products of the most energetic and efficient eruptions (Fisher and Schmincke, 1984: Figure 1). Maars by definition excavate a crater below the pre-eruptive surface. Tuff rings and tuff cones have shallower eruption foci than maars, with crater floors at or above ground level (Sheridan and Barberi, 1983). Tuff cones have steeper sides than tuff

rings, a result of the higher cohesion of wetter surges (Cas and Wright, 1987; Wohletz and Zimanowski, 2000). A common theory for these differences has to do with the volume of external water available at the eruption focus, with more water (shallow marine, lake, etc.) preventing deepening of the explosion locus and depositing progressively wetter and stickier ash beds (e.g. Sheridan and Barberi, 1983; Lorenz, 1986).

Because of the rapidly cyclic character of phreatomagmatic eruptions, base surges develop repeatedly instead of a sustained eruption column (Dellino, 2000), which results in deposition primarily by surges and ballistic blocks that have a strong horizontal deposition direction (Zimanowski, 1998). Ash and lapilli fallout also contribute to deposit structures. The deposits are commonly thinly bedded, which supports deposition through multiple eruptions with a small mass production per event (Lorenz, 1987). Pyroclastic grains range in size from ash to small lapilli (Zimanowski, 1998). Crater fill consists of reworked slope material and recycled grains (White, 1989; Houghton and Smith, 1993; Lorenz, 2000).

d. Basaltic Maars and Tuff Rings

Although any surface water has the potential to fuel phreatomagmatic eruptions, saturated unconsolidated sediments are commonly reported as the likely source of MFCI (e.g. White, 1991; Sohn, 1996; Leat and Thompson, 1988; Ort and Carrasco-Núñez, 2004). Basaltic phreatomagmatic vents are also commonly reported along faults, zones of weakness where magma and water both travel (Wohletz and Heiken, 1992; Gevrek and Kazancı, 2000; Németh and White, 2003). Juvenile material is mostly vesicle poor (Zimanowski, 1998; Lorenz, 2000), with higher vesicularities associated with shallow

eruption centers and thus lower confining pressure (Sohn and Chough, 1992; Aranda-Gómez and Luhr, 1996). Up to 80% of the deposit composition can be fragmented country rocks, which reflects the high eruption intensity (Zimanowski, 1998; Lorenz, 2000). Multiple vents were observed erupting simultaneously at Ukinrek (Ort et al., 2000) and several explosion craters have been inferred in the formation of other maars as well (e.g. Sheridan and Barberi, 1983; Abrams and Siebe, 1994; Houghton et al., 1999; Freda et al., 2006). It is also not uncommon to have deposits of both magmatic and phreatomagmatic origin being erupted contemporaneously from nearby craters (Leat and Thompson, 1988; Houghton et al., 1999; Ort et al., 2000; Dellino et al., 2004), suggesting that the controls operating during phreatomagmatic eruptions are quite variable. Higher explosivity is associated with phreatomagmatic eruptions than magmatic eruptions from the same volcano (Gourgaud et al., 2000). The eruption commonly dries out toward the end as the water table lowers, resulting in cinder cones or effusive lava lakes depending on the volatile content of the melt (Heiken and Wohletz, 1985; White, 1991; Houghton et al., 1999; Gevrek and Kazanci, 2000; Vazquez and Ort, 2006). Following eruption cessation, groundwater flux may increase into the unconsolidated crater fill, resulting in a crater lake (White, 1991; Ort and Carrasco-Núñez, 2004; Carrasco-Núñez et al., 2007).

e. Rhyolitic Pyroclastic Deposits

Early explosive phases are frequently associated with silicic magmas and are explored in this section to compare the features seen at Tepexitl with other known rhyolitic fine-grained pyroclastic centers. A number of pumice rings and cones also exist (e.g. Medicine Lake – Heiken and Wohletz, 1987), but are not included in this discussion because they are generally coarser grained with much higher juvenile vesicularities than

Tepexitl. Only one rhyolitic maar-sensu-stricto has been reported – Viti maar, which formed on the side of Askja caldera in Iceland in 1961 (Lorenz, 1987). However, no comprehensive study on the maar has been conducted. The majority of rhyolitic tuff rings/cones are found in connection with dome extrusion (e.g. Sugarloaf Mountain, Arizona – Sheridan and Updike, 1975; Panum Crater – Sieh and Bursik, 1986; Heiken and Wohletz, 1987; Lipari and Vulcano – Sheridan et al., 1987; Heiken and Wohletz, 1987; Opo Bay – Houghton et al., 1987; Inyo Domes – Heiken et al., 1988; Pukatera – Brooker et al., 1993; Meninne Dam - Roache et al., 2000). The only other documented rhyolitic tuff ring not associated with a dome (besides Tepexitl) is Fyriplaka tuff ring on Milos Island, Greece (Campos Venuti and Rossi, 1996). These various pyroclastic centers are interpreted by these authors as resulting from a combination of magmatic, phreatomagmatic and/or phreatic processes, but it remains unclear if evidence of water in the eruptive system can be directly correlated to phreatomagmatic-triggered explosions.

f. Variables and Questions

Phreatomagmatic-triggered eruption appears to be sensitive to a number of variables, which are not fully understood. Changes in confining pressure, flux rate of both water and magma, the nature of the coolants, water:magma mass ratio, viscosity of the melt, and degree of vesiculation all affect the degree of coarse mixing, the eruption intensity, and the resulting deposits. High confining pressure limited the efficiency of phreatomagmatic explosions in experiments with thermite (Wohletz and Heiken, 1992), but its effect is generally poorly understood (Morrissey et al., 2000). Lorenz (1987) gives a range of 20-30 bars of pressure for efficient explosive interaction of magma and water. Phreatomagmatic eruptions tend to dry out with time as the flux of groundwater into the

crater decreases. Zimanowski et al. (1997a) found that 3-5 m/s injection velocities of melt into coolant allow effective coarse mixing, a rate that strongly depends on magma flux. Additionally, because most laboratory experiments have been conducted with pure water, the role of “impure” water is not fully understood, but is important to consider as saturated sediments can be a source of water in phreatomagmatic activity. Cas and Wright (1987) first suggested that heating causes convection of the interstitial pore water within saturated sediments, fluidizing them and making them able to mix with magma. White (1996) states that, although impure coolants have a higher viscosity than pure water, allowing for increased coarse mixing, they also have a lower heat capacity than pure water, damping the effectiveness of explosions.

One of the most important variables in efficiency of phreatomagmatic eruptions, the water:magma mass ratio, is also the hardest to constrain (Wohletz and Zimanowski, 2000; White, 1996). The observation of differing styles of eruption from nearby vents suggests that very shallow changes control the degree of the interaction of water and magma (Houghton et al., 1999). Most workers agree that a critical magma:water mass ratio is necessary for explosive MFCI (Morrissey et al., 2000; Cas and Wright, 1987; Lorenz, 1987; Fisher and Schmincke, 1984), but the ideal ratio is not universally agreed upon. Sheridan and Wohletz (1983) suggested that the mass ratio of 0.2-0.3 represents the maximum efficiency of an MFCI system, but experiments conducted by Zimanowski et al. (1997b) resulted in a much lower maximum efficiency ratio of 0.03-0.04 by mass. However, tuff rings and tuff cones on Cheju Island do not appear to be as sensitive to the amount of water as they are to other controls, such as the nature of the aquifers and the degree of degassing of the magma (Sohn, 1996). Zimanowski et al. (1997a) emphasize

that it is the rate of transfer of thermal energy to mechanical energy that governs efficiency, which in turn depends on the interfacial surface area able to coarsely mix. However, even at the most ideal mass ratios, White (1996) points out that most MFCI's are not fully efficient in that they do not transfer all their excess heat to the coolant.

One very important question is how an increase in viscosity affects the efficiency of phreatomagmatism. Although Lorenz (1987) suggests that phreatomagmatism can occur with any composition of melt, Zimanowski (1998) found that the degree of coarse mixing is primarily controlled by melt viscosity. Because coarse mixing can best be achieved when fuel and coolant are of similar viscosities (Morrissey et al., 2000), an increase in viscosity likely results in a decrease in the degree of surface area of melt exposed to coolant, thus limiting explosivity and intensity (Zimanowski et al., 1991). Zimanowski (1998) carried out experiments on melts of varying compositions at varying temperatures, injected with varying amounts of water. It was found that ultramafic rocks always responded with strong phreatomagmatic explosions whereas basalts, andesites, and tholeiites exploded strongly only at higher temperatures (1480° C) and dacites, phonolites, and rhyolites never exploded phreatomagmatically. This experimental relation corresponds directly with viscosity, although scaling issues mean the results are not directly applicable to natural systems.

A final important variable in this discussion is how the degree of vesiculation of the magma at the time when it encounters external water affects the intensity of phreatomagmatic explosion. Cas and Wright (1987) suggest that phreatomagmatic eruptions with vesiculating magmas would not produce the blocky, dense shards normally associated with phreatomagmatic ash, making it difficult to identify them.

Lorenz (1987) indicates that all phreatomagmatic fragmentation occurs prior to significant vesiculation and experimental evidence suggests that only vesicle-poor magmas explode on contact with external water (Zimanowski et al., 1991; Zimanowski, 1998). The authors note that these experimental-scale results do not preclude the existence of phreatomagmatism with vesiculated magmas, just that their intensity would be much lower if they do occur. One mechanism proposed to explain this phenomenon is that the presence of non-condensable bubbles (e.g. CO₂) limits the formation and collapse of an effective vapor film needed to induce fine fragmentation.

E. Rhyolitic Textures and Rhyolite Dome Models

In this section, rhyolitic emplacement conditions will be explored (dome growth vs. conduit processes) in order to gain a better understanding of the various juvenile components observed at Tepexitl. This information is necessary when examining fragmentation mechanisms based on field and componentry data.

Shallow rhyolitic extrusions that result in both explosive and effusive emplacement contain a variety of juvenile textures, including obsidian, flow-banded lava, pumice, and dense, stony rhyolite. Several drill cores through subaerial rhyolitic domes have revealed a series of dome textures (Figure 5) that can be related to the degassing and cooling histories and the relative location in the flow (Manley and Fink, 1987). The uppermost finely-vesicular zone (FVP) consists of many tiny vesicles up to 0.5 mm long and is related to surficial vesiculation post-extrusion, as the dome cooled (Manley and Fink, 1987). Higher cooling rates at the surface of the flow prevent crystallization and

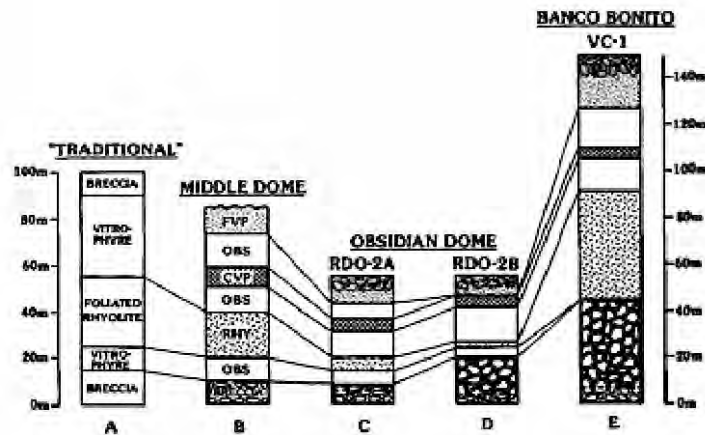


Figure 5: Vertical drilling results through rhyolitic domes, taken from Manley and Fink (1987).

bubble growth, resulting in a finely vesicular froth (Fink and Manley, 1987). The upper obsidian zone (OBS) lies beneath the FVP and is thought to have formed from vesicle collapse in the conduit, prior to extrusion (Manley and Fink, 1987). The underlying coarsely vesicular layer (CVP) is characterized by fewer but larger vesicles than the FVP and is enriched in volatiles when compared to other sections of the dome. CVP also has lower density than the overlying OBS and FVP, which can result in diapirs of CVP that reach the surface (Fink and Manley, 1987; Fink et al., 1992). The origin of the CVP is thought to relate to water vapor release during post-placement crystallization in the interior of the dome, which rises upward and collects underneath the overlying obsidian cap (Fink and Manley, 1987). The middle rhyolite consists of devitrified to crystalline material with lithophysae and spherulites (Manley and Fink, 1987). The basal and middle OBS zones both also contain spherulites and lithophysae, both of which are devitrification textures (Fink and Manley, 1987; Manley and Fink, 1987). Flow-banding is ubiquitous in the obsidian layers (Fink and Manley, 1987; Manley and Fink, 1987). It is also present in the CVP layer as alternation of cm-scale obsidian and cm- to m-scale

CVP (Manley and Fink, 1987). Lastly, flow banding occurs in the middle rhyolite layer (RHY), defined by higher abundances of crystals and vesicles (Fink and Manley, 1987).

Several different breccias are associated with dome growth. The outer layer of the dome commonly forms a carapace breccia, with vertical joints that extend through the upper layers (Fink and Manley, 1987). The carapace breccias of rhyolite flows in the Snake River plains have oxidized red ash matrices (Bonnichsen and Kauffman, 1987). The basal breccia seen in the dome profile is caused by extrusion of magma on top of carapace breccia, a process that can incorporate lithic material into the breccia (Manley and Fink, 1987; illustrated in chapter 3). The basal breccia of domes can also have blocky peperitic textures from mixing with fluidized wet sediments or crater fill (Kokelaar, 1982; McPhie et al., 1993; Dadd and Van Wagoner, 2002). However, as permeability of unconsolidated sediments increases (increased grain size and/or higher porosity), their ability to fluidize decreases. Fluidization is most efficient for wet fine-grained, well-sorted, and loosely packed sediment (Galerne et al., 2006). The margins and top of a rising cryptodome can also be peperitic, with both wispy and blocky juvenile clasts (Allen, 1992; Orth and McPhie, 2003). Internal dome breccias of monolithologic obsidian or stony rhyolite also occur due to shear stresses during flow that exceed tensile strength of the cooling dome (Manley and Fink, 1987). These breccias can have matrices of pulverized ash that can also be oxidized.

Pyroclasts with a combination of all these textures may reflect explosions from a growing dome, but they may also result from conduit processes. Pumiceous clasts may result from magmatic explosions; stony rhyolite may be from fragmentation of vesicle-poor areas of the rising plug, fragmented and ejected during explosive bursts; and

obsidian and flow-banded material may form along the conduit margins where shear is very high and the flux of volatile loss is higher. Flow-banded glassy pyroclasts are very common in rhyolitic tuff, and have been explained by some workers as originating from the conduit during ascent. The margins of the conduit experience higher shear than the center of the rising plug and open-system degassing is thought to occur through brecciated outer conduit obsidian, where the magma has a higher viscosity and lower ascent rates (Castro and Cashman, 1999; Tuffen et al., 2003; Rust et al., 2004). Brittle fracture is thought to occur from release of built-up shear stress from viscoelastic deformation (Tuffen et al., 2003). Rust et al. (2004) examined autobreccia textures of obsidian pyroclasts from the Mono craters eruption in 1340 CE and concluded that obsidian along conduit walls not only brecciates, but has time to re-anneal during ascent, and that this process may occur multiple times prior to eruption. Tuffen et al. (2003) and Gonnermann and Manga (2005) found that such re-annealing of fractured obsidian was connected to development of flow bands, as the healed fractures are distinct in color, vesicularity, and/or crystallinity. Subsequent relaxation and viscous deformation of the magma forced the fractures into sub-vertical flow foliations. The conclusion from these studies is that highly viscous magma exhibits both brittle and ductile behavior during ascent.

Tuffen et al. (2003) termed the fractures within the obsidian ‘tuffisite veins’ and describes them as densely welded juvenile clastic material that shows bedding structures, likely as the result from flow of gas-particle mixtures through the fractures during degassing. Both Tuffen et al. (2003) and Rust et al. (2004) found evidence of lithic material within these fractures, and suggest that neighboring particulate matter can be

incorporated into fractures prior to annealing and deformation. Experiments by Castro et al. (2005) concluded both that flow-banded obsidian forms in the conduit and the re-annealing and band formation occurs as a result of redistribution of oxide-rich domains. Band formation is increased by high volatile concentrations, shear stress, and viscous/frictional heating. The center of the conduit retains heat more effectively and has time for vesicle development during ascent (Castro and Cashman, 1999; Rust et al., 2004), resulting in pumice and flow-banded obsidian pyroclasts together in outcrop (e.g., Houghton et al., 1987; Campos Venuti and Rossi, 1996).

In summary, the combination of juvenile textures observed as pyroclastic material throughout the stratigraphic section may result from explosions of a dome or they may result from explosions within the conduit.

Chapter 2: Field Characteristics

A. Field Methods

Field maps were created by digitizing an INEGI (Instituto Nacional de Estadística Geografía e Informática) topographic map of UTM Zone 14N (San Salvador, El Seco, Puebla) in NAD 27 projection (contour interval is 20 meters and the base map scale was 1:50,000; Figure 3). A total of 13 stratigraphic sections were measured and described. Facies changes within each section were recorded, along with changes in average grain size (measured as the diameter of the grain size visually determined to be most representative of the deposit), sorting, continuity of the deposit (only possible within the visual extent of the outcrop), dominant composition, and textural variations (such as waveforms and scour channels). Blocks and bombs were recorded by average percent present (as an estimated volume percentage of the entire deposit), maximum and average size, dominant composition (by visual inspection), and vertical deformational extent of underlying fine-grained sediments (if any). Maximum clast sizes for lithic and juvenile clasts were determined by averaging the measurements of the largest 3-5 blocks seen in the outcrop.

Section 2, a composite section along a road in the southern inner crater, is considered the “type section” for Tepexitl (Figure 3), as it has excellent exposures and is easily accessible. Samples were collected along this section every meter, on average, to be analyzed for grain-size distribution and componentry. All sampling was conducted from bottom to top of each outcrop, with care taken to avoid contamination from upper and lower units.

B. Composition and Textures

a. Juvenile Clasts

Juvenile material is plagioclase-quartz-sanidine-biotite rhyolite. The following textures are found in varying percentages throughout crater deposits of bedded tuff:

Stony Rhyolite – light to dark gray and dense with sugary texture and little to no vesicularity.

Obsidian – black to medium gray and glassy, commonly with fractures between phenocrysts and rare breccia textures that include disseminated lithic clasts.

Perlite – medium gray and glassy with curved hydration fractures.

Slightly Pumiceous Rhyolite – light gray with fine vesicularity.

Flow-Banded – sub-mm to cm scale bands of alternating obsidian (various shades) and slightly pumiceous rhyolite.

In order to characterize crystallinity, vesicularity, and textures of juvenile material from Tepexitl, thin sections of rocks with the most common textures (stony rhyolite, obsidian, and flow-banded clasts) were examined (Figure 6; Table 1). Several samples from each texture category from various locations in Section 2 were described in order to identify any major changes in petrography as the eruption progressed (detailed stratigraphy and locations can be referenced by Plate 1). In general, the samples are homogenous with respect to crystal compositions and respective abundances (Table 2). All samples are poorly phyric (3-7 volume % phenocrysts), with crystals set into a matrix dominated by plagioclase microlites, as laths and/or granular even-sized crystals. Textures vary between trachytic and felty, depending on the sample.

Table 1: Petrologic differences between dominant juvenile textures

	Vesicle (vol. %)	Vesicle Size (mm)	Vesicle shape	Glass (%)	Flow Foliation	Flow Banding
Obsidian	0	N/A	N/A	40-50	Weak to none	None
Stony Rhyolite	20-25	0.005-0.05	Elongate, spherical, irregular	10-25	Weak to strong	Defined only microscopically
Flow-banded	0-10	0.005-0.05	Elongate, spherical, irregular	5-20	Strong	Yes

Table 2: Average phenocrysts characteristics for Tepexitl juvenile material

	Volume % (of total crystal %)	Size (mm)	Textures
Quartz	35-50	0.05-0.13	embayed to rounded
Plagioclase	30-40	0.05-0.4	Subhedral, twinned and/or zoned, commonly cumuloiphyric
Biotite	10-20	0.05-0.15	Thin laths with minor internal embayments
Sanidine	10-20	0.05-0.2	Cumuloiphyric, euhedral and rounded; often nucleated on older crystals

STONY RHYOLITE

Three stony rhyolite blocks were analyzed from different stratigraphic locations in Section 2: 2-12 (meter 9.5), 6,7D (meter 34.3), and D1 (crater-rim float). Sample D1 can be seen in Figure 6, a good representation of typical stony rhyolite hand-sample textures. The vesicles in all samples are aligned, either the result of flow or deformation. In samples 6,7D and D1, bubbles collected in ‘shadows’ behind large phenocrysts (Figure 7), a feature that resembles an eddy behind a boulder in a river and is most consistent with a flow origin for alignment rather than deformation. All samples are dominantly crystalline, but the presence of glass in the groundmass indicates that devitrification processes were not complete prior to fragmentation.

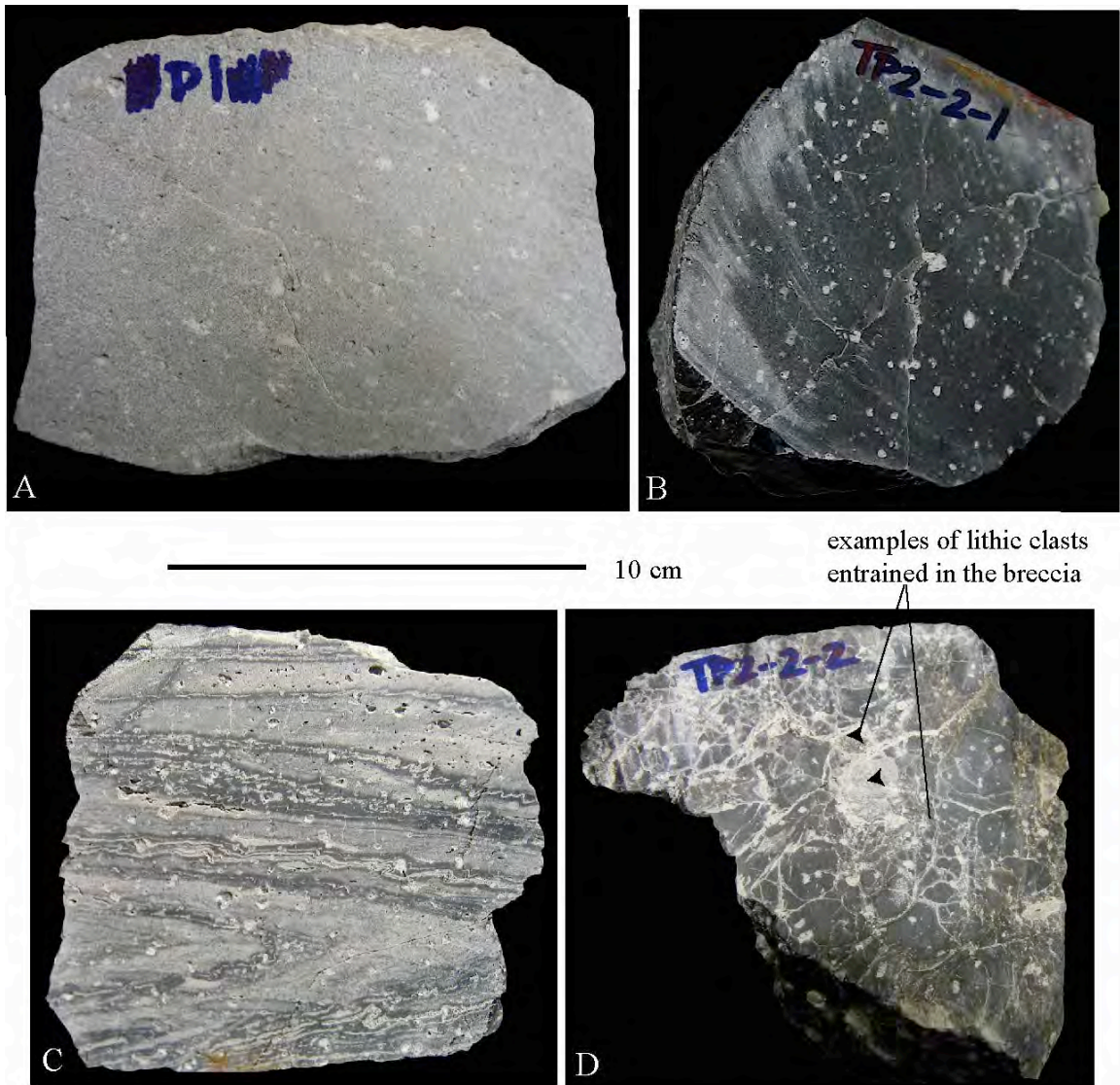


Figure 6: Examples of typical juvenile block textures found in the tuff-ring walls. (A) is sample D1, stony rhyolite and (B) is sample 2-1, obsidian. (C) is flow-banded stony rhyolite, obsidian, and pumice (sample F2). Obsidian can also be brecciated with disseminated lithic clasts (sample 2-2; D).

OBSIDIAN

Two obsidian samples were compared, 2-1 (meter 5.5) and OF (crater-rim float).

Sample 2-1 can be seen in Figure 6. These are both glassy, non-vesicular and have homogenous groundmasses.

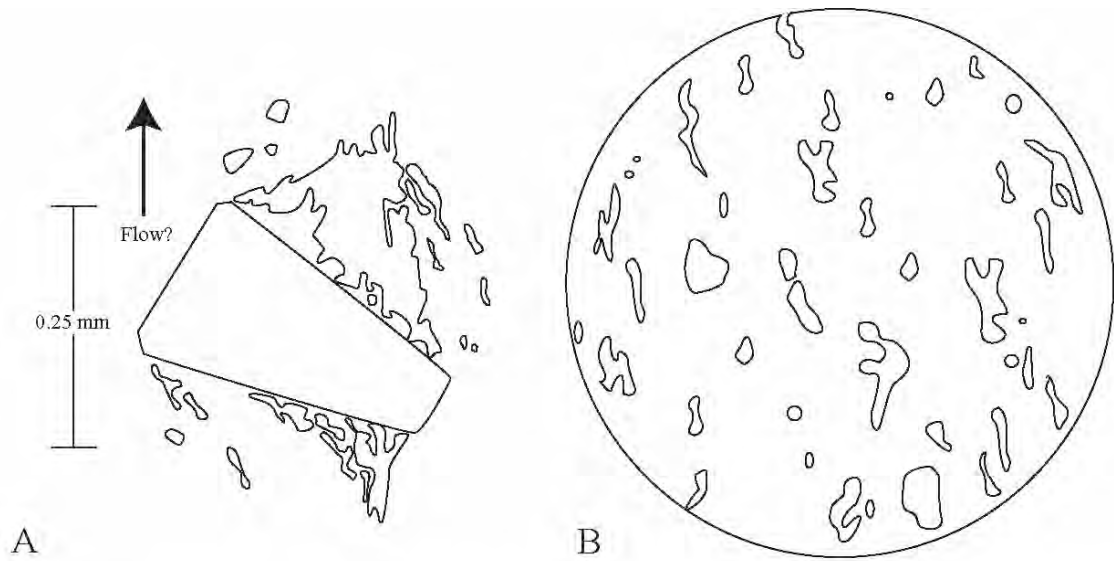


Figure 7: (A) Sketch of 'eddy-like' texture as bubbles adhere to a sanidine crystal in D1 (stony rhyolite), a texture seen in 6,7D (stony rhyolite) also. (B) is a drawing of average vesicle texture in stony rhyolite, taken from sample 6,7D. Note the elongate, asymmetrical features of the bubbles and the well-defined flow alignment. Diameter of view is 2 mm.

FLOW-BANDED RHYOLITE

Flow-banded texture is ubiquitous in juvenile material, but the nature of the flow-banding varies. Three samples were examined: sample 2-12 (meter 9.5), 4-6 (meter 17) and F2 (crater rim float; Figure 6), each with distinct flow-band characteristics (Table 3).

Sample 2-12 is banded on a mm scale, with the secondary bands (lower volume percent of sample) differentiated by the presence of 'cracks' that extend perpendicular to length (or flow; Figure 8). These cracks are parallel to each other, are about 0.01 mm in width on average, and are limited to the secondary bands (they do not extend into the primary bands). The groundmass of these bands is more equigranular and finer grained than the matrix of the primary bands. Such parallel cracking limited to one material is consistent with response of a more brittle material to tension caused during flow-related

Table 3: Petrologic differences between flow bands.

Sample	Band	Vesicularity	Distinguishing Features	Comments
2-12	Band 1	None	Coarser felty microlites	Cracks not visible macroscopically
	Band 2	Tensional cracking	More equigranular and finer-grained	
4-6	Band 1	10%	None	No microscopic difference between bands
	Band 2			
F2	Band 1	1-2%	Slightly glassier groundmass	Vuggy stony rhyolite
	Band 2	None	Slightly higher microlite concentrations	Obsidian
	Band 3	10%	Higher vesicularity and more complex folding patterns	Pumiceous band folded within band 2

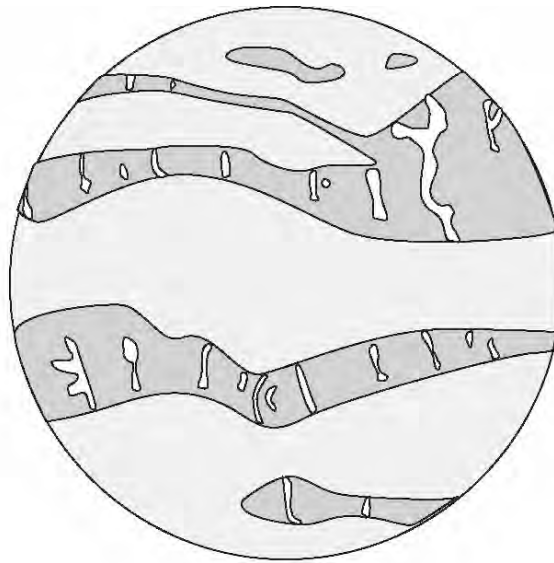


Figure 8: Flow-bands of sample 2-12F, distinguishable by the presence of cracks (white areas above), perpendicular to flow direction. Diameter of view is 8 mm.

extension. It also suggests that the sample 2-12 is the result of mingling and flow between two separate juvenile materials with different viscosities. The ‘cracked’ band perhaps experienced higher degrees of cooling or volatile loss prior to interacting with the primary material.

In contrast, the bands of sample 4-6 are distinct only on a macro-level (hand sample) as light and dark gray zones, and are truly indistinguishable on a micro-level. The groundmass is homogenous with no differences in crystallinity or vesicularity.

Sample F2 consists of cm-scale bands of light gray, vuggy, stony rhyolite banded with mm-scale dense black obsidian (Figure 6). Inside the black bands are sub-mm scale highly deformed white-colored bands, which are isoclinally folded in some places even though the host obsidian shows no additional deformation. The white bands are defined by 5-10 times higher vesicularity than that of the stony rhyolite and obsidian. This combination of textures indicates that multiple folding events took place in this sample (the white bands within the obsidian and the obsidian and stony rhyolite together). The bands are further defined by subtle differences in microlite concentration and vesicularity.

INTERPRETATION

In summary, the samples examined indicate that flow banding is evident between two juvenile components of different viscosities, color, vesicularities and groundmass textures. It is also apparent that multiple deformation events can occur, perhaps overprints of folding inside the conduit with later extrusion-related folding. The flow-banded samples examined contain no lithic clasts, evidence that banding occurred within

the conduit. Intermediate vesicularities are consistent with mingling of stony rhyolite with obsidian.

b. Stratigraphic Changes

Stony-rhyolite-rich samples from late in the eruption (6,7, D1 and F2) have characteristics that are distinct from all other samples (obsidian, stony rhyolite, and flow-banded clasts) from early in the eruption (Table 4). Changes in crystal characteristics and microscopic textures are most consistent with some change in the eruptive/supply system.

Table 4: Comparisons of petrologic characteristics of stony rhyolite from early and late in the eruption.

	Quartz textures	Plagioclase size (mm)	Glass (%)	Macroscopic Textures
Early	Embayed <i>(all juvenile material)¹</i>	0.05-0.08 <i>(all juvenile material)¹</i>	25	Vuggy with vapor film crystallization
Late	Rounded, non-embayed	0.2-0.4	10	Stony and dense

¹ ‘All juvenile material’ indicates that the phenocryst characteristics are the same for stony rhyolite, obsidian, and flow-banded clasts

INTERPRETATION

Highly embayed quartz results from resorption of the mineral back into the melt as a result of disequilibrium processes, such as from heating (magma mixing and/or convection in a magma chamber) or pressure decreases (decompression and/or magma residing at shallow levels for some time; Winter, 2001). Non-resorbed quartz grains in the final deposits of Tepexitl indicate that the disequilibrium resorption reaction did not occur. This suggests that the magma from the end of the eruption spent less time at shallow levels than magma from earlier in the eruption.

Larger plagioclase grains are also consistent with a change in eruptive regime that was likely related to a change in magma flux rate and residence time at shallow levels. Plagioclase crystals are in equilibrium with the melt at higher temperatures than quartz, which means they can continue to crystallize at depths where quartz grains are unstable. Large plagioclase grains in samples from the end of the eruption could result from relatively fast extrusion and explosion of deeper magmas that had resided lower in the conduit and/or chamber.

Higher degrees of crystallinity and vuggy textures with vapor film crystallization in stony rhyolite samples late in the eruption are absent in early stony rhyolite samples, and are consistent with shallow crystallization and/or cooling in a dome/plug (i.e. Manley and Fink, 1987). Rapid flux of hot magma onto the surface coupled with high cooling rates at shallow levels can account for the unique combination of textures seen in final stony rhyolite samples, characteristics consistent with dome/plug development at the end of the eruption. The textures seen in the obsidian float block (sample OF) are the same as deposits in lower stratigraphic levels (with embayed quartz and small plagioclase crystals), consistent with rafting of blocks that formed earlier in the eruption.

c. Sample 2-2 (Obsidian Breccia)

Sample 2-2 was collected from meter 5.8 and looked like a solid block of obsidian in outcrop. However, cut surfaces revealed a highly complex fracture network and brecciation pattern, with visible, disseminated lithic clasts between 2 mm and 15 mm in diameter (Figure 6). Thin-section examination exposed an unusual pattern, not observed in any other sample. The network of fractures seen in hand sample are filled with fine-grained lithic grains and crystals from sub-mm size to 3 mm in diameter (Figure 9). 75-

80% of the fracture volume is composed of mostly rounded, poorly sorted lithic grains, which include crystalline plagioclase-olivine basalt, plagioclase-rich palagonitic glass, altered limestone, crystalline rhyolite, crystalline plagioclase-hornblende andesite, and olivine, hornblende, and muscovite crystals. Individual grains are enclosed in a glassy fine-grained matrix (the remaining 20-25% of the fracture volume), which has a higher concentration of equigranular groundmass microlites than the matrix of the obsidian 'host', the same as was described for other obsidian clasts above. The fracture networks show no bedding structures or flow alignment. In plane light, the fractures are darker-colored than the host obsidian. Fracture thickness varies from sub-mm to mm-scale. Fractures and associated lithic grains account for approximately 50% of the slide by volume.

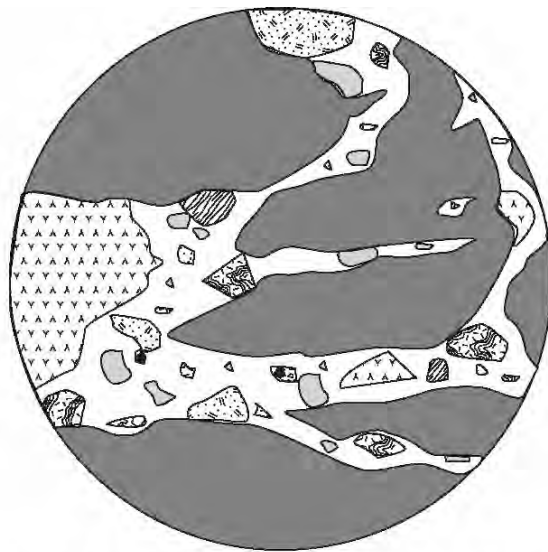


Figure 9: Obsidian breccia with dark gray area representing the obsidian host, cut by a network of fractures, in which poorly sorted lithic grains and crystals are concentrated. Diameter of view is 8 mm.

INTERPRETATION

The high concentration of lithic crystals in the fractures of this breccia indicates that Toba Café sediment and juvenile material were interacting in the early stages of eruption. The lack of peperitic textures suggests the obsidian behaved in a brittle way during this process. The matrix-supported nature of the fractures could result from fluidized sediment invading fractures of obsidian conduit wall material.

d. Lithic Clasts

Lithic blocks and bombs are dominantly rounded cobbles or smaller fragments of similar composition (dominantly black olivine basalt and red to dark gray hornblende-plagioclase andesite). Large limestone clasts are rare in outcrop, mostly found as scattered small float blocks in western inner-crater drainages. Lapilli compositions include cinders, white pumice, limestone, weathered rhyolite, and iron-altered mafic grains. Detailed descriptions of lithic samples are provided in Appendix 1.

INTERPRETATION

The majority of lithic clasts described are volcanic in origin, consistent with the wide variety of volcanic features in the Serdán-Oriental Basin, from which erosion caused extensive resedimentation within the basin as Toba Café. Rounded shapes are consistent with river cobbles, a common feature of Toba Café deposits. Rare limestone means that the eruption likely did not deepen into the underlying basement rocks. Limestone clasts could be resedimented basin fill and/or they could have been incorporated into the eruption from shear during upward pulses of Tepexitl magma, also ejected as blocks at the end of the eruptive interval.

C. Facies

a. Transportation and Depositional Processes

Because the transportation and depositional processes within an eruptive system have an effect on the final stratigraphy, grain-size distributions and ash textural features, they are important to examine. Transportation mechanisms of fragmented clasts in both magmatic and hydromagmatic pyroclast-forming eruptions include surges, ballistic trajectories, and fallout from buoyant plumes. Of these, surges are the most complex systems. Surges are primarily ground-hugging base surges but also form by column collapse, with transport direction controlled by wind and/or by topographic lows in the tuff rim (Self et al., 1980; Ort et al., 2000). Surges are dynamic density currents made up of a turbulent and dilute three-phase system (Fisher and Schmincke, 1984; Dellino, 2000). Their low grain concentrations – only between 0.1% and 1% solids by volume (Wilson and Houghton, 2000) – are dominated by coarse ash and lapilli (Wohletz, 2001). Surges travel at speeds of tens of meters per second (Wilson and Houghton, 2000) and can form from both magmatic and phreatomagmatic activity (Wohletz and Heiken, 1992; Fisher and Schmincke, 1984). Surge activity causes accumulation of material as thin beds in some places and erodes underlying deposits in other places (Sheridan and Barberi, 1983; Fisher and Schmincke, 1984; Wohletz, 2001).

Depositional mechanisms within a surge are complex. A single outcrop represents only one moment in time (Dellino et al., 2004) and its thickness is no indication of the thickness of the actual surge. Resulting deposits depend on concentration of particles, wetness of the system, energy/steadiness of the system, and distance from the vent (Valentine and Fisher, 2000; Wohletz, 2001). Additionally, as surges are capable of

carrying lapilli-sized clasts (Fisher and Schmincke, 1984), the grain size of the resulting deposits depends on the original fragmentation size of the material. Particles within a surge are sorted by settling velocity of individual grains, with coarser material concentrated at the base and finer material at the top (Dellino, 2000; Wilson and Houghton, 2000). Lapilli to coarse ash are deposited by grain-by-grain traction along a shear layer at the base of the flow, fine ash to coarse ash are deposited by saltation along the substrate, and the very fine ash is transported by turbulent suspension in the upper parts of the flow (Wilson and Houghton, 2000; Wohletz, 2001). A single surge passing over a single point leaves a three-phase deposit from the different depositional mechanisms of traction, saltation, and suspension (Valentine and Fisher, 2000; Dellino et al., 2004). This vertical succession is called a 'bedding set' (Wohletz, 2001) and can include a number of different facies. Tractional forces result in a coarse-grained, reverse-graded basal bed, the result of strong viscous forces along the substrate that force large grains upward out of the zone of maximum shear (also called kinetic sieving) (Fisher and Schmincke, 1984; Sohn and Chough, 1989; Sohn and Chough, 1992; Dellino et al., 2004). This coarse layer is commonly not very voluminous (again, depending on fragmentation mechanisms) and is mostly seen in the near-vent facies (Dellino, 2000). Sharp contacts exist between this tractional deposit and the overlying saltation-derived deposits (Dellino et al., 1990; Dellino, 2000), which are fine-grained, lapilli-poor tuff (Sohn and Chough, 1989; Dellino, 2000; Dellino et al., 2004). The final deposit from the suspended ash is a structureless very fine ash bed (Dellino et al., 2004), which is commonly eroded by subsequent surges (Dellino, 2000). It is noted that fall deposits can

be difficult to identify definitively post-eruption (Lorenz, 2000), as their characteristics can be very similar to those observed in traction carpet deposits.

b. Facies and Outcrop Textural Descriptions

PRIMARY FACIES

Facies are deposits that share a set of characteristics, such as grain size, sorting, and internal structures (Valentine and Fisher, 2000). The majority of deposits that built Tepexitl tuff cone can be grouped into six facies (Table 5; Figure 10; Figure 11), which are all interbedded on the scale of laminae to medium beds, with sharp upper and lower contacts. Each facies can be consistently identified laterally and vertically.

Table 5: Field characteristics and descriptions of each facies

	Description	Median grain size (phi)	Avg. deposit thickness	Comments
<i>Fine-Grained Facies</i>				
TI	Laminated ash tuff	2.5	5- 60	Poorly-defined laminae ('smeary')
AC	Accretionary lapilli	2.0	5-20	Massively bedded
Tlap	Alternating laminae of fine ash tuff, coarse ash tuff, and accretionary lapilli	1.6	50-300	Sharp internal contacts
<i>Coarse-Grained Facies</i>				
Bt	Tuff-lapilli breccia	-0.4	40-200	Fine ash coating on grains
Bl	Coarse ash to small lapilli breccia	-1.1	10-250	Commonly graded
B	Lapilli breccia	-2.6	5-50	Fines poor; angular clasts

INTERPRETATION

Each facies is the result of distinct eruptive, transportation, and/or depositional processes (Table 6). These processes occurred repeatedly throughout the formation of Tepexitl to create the textures associated with the deposition of each facies. Facies will be referred to by their abbreviation in all following discussions.

TEXTURAL FEATURES

In addition to the six primary facies, several other notable textural features occur throughout the vertical sequence at Tepexitl (Figure 12): 1) ‘bomb sags’ cause plastic deformation of underlying tuff; 2) ‘scour channels’ are small-scale, U-shaped channels cut into fine-grained beds by the current that emplaced an overlying coarser unit and are filled with coarse ash to small lapilli; 3) ‘Tu deposits’ are rare, discontinuous, thin lenses of undulatory, massive tuff that are plastically deformed by bomb sags, with up to 25 cm of vertical displacement; 4) iron-rich lithic lapilli that have “rusted” in-situ, staining surrounding bedded grains in an ellipse of red-orange alteration, are termed ‘Fe-clasts’; and 5) deformed tuff is rarely ‘sheared’ by an overlying coarser-grained deposit.

INTERPRETATION

These textures (scour features, undulatory ash, deformational features, and rusted lapilli) all reflect the presence of water in the eruptive system and are the result of deposition from water-rich surges. Additionally, they are commonly associated with deposits of certain facies, a useful diagnostic tool for depositional mechanism (Table 6). ‘Wet’ surges are those that have high amounts of condensed water in the transportation system, which becomes trapped by surface tension as thin films around the grains, causing strong grain cohesion and fluidization of the resulting deposit (Sheridan and

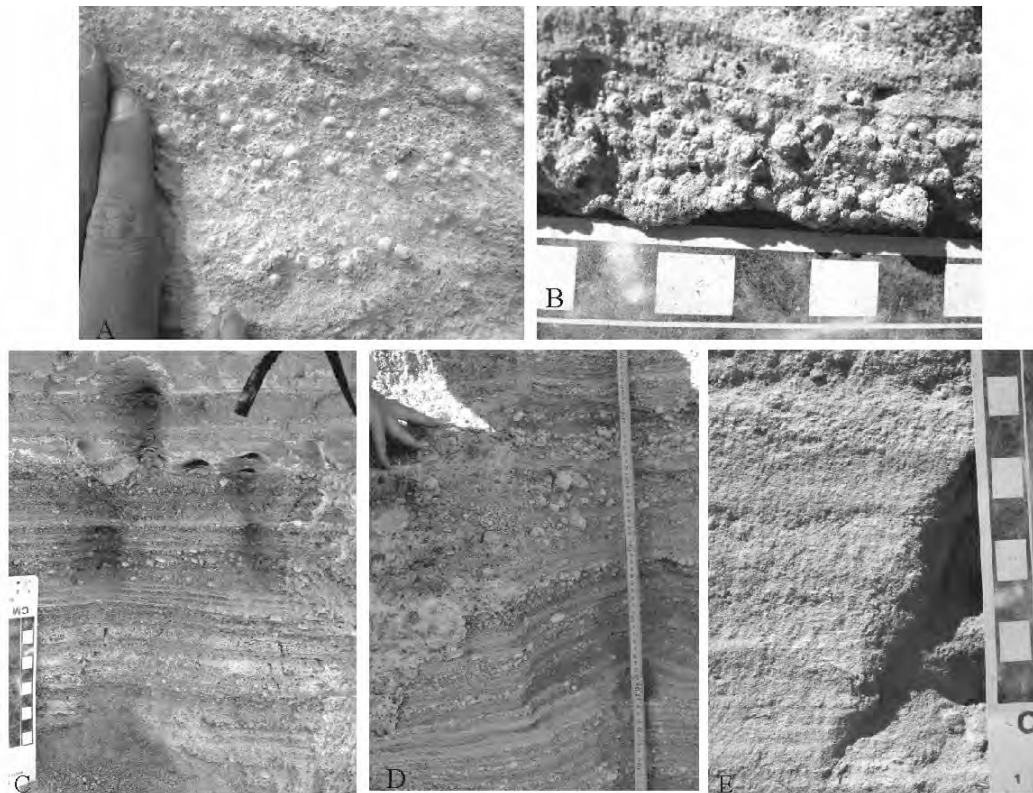


Figure 10: Fine-grained facies: (A) and (B) show AC, with a cm scale visible in (B). The AC in Pictures (C) and (D) are both of Tlap facies and (E) is of Tl.

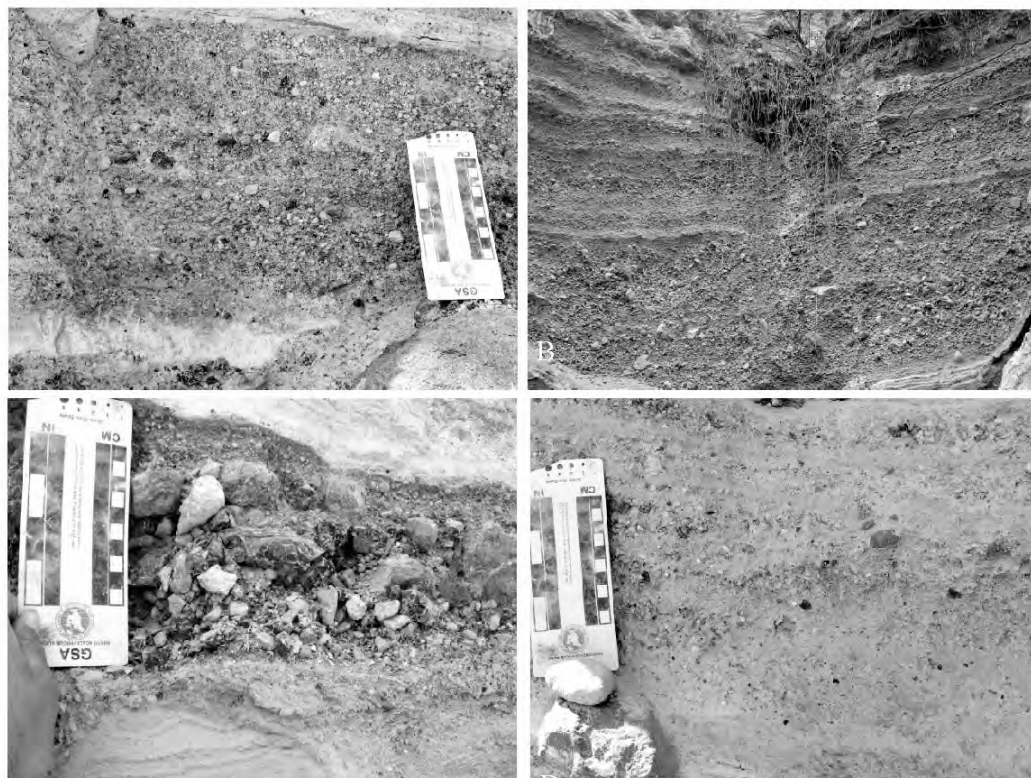


Figure 11: Coarse-grained facies: (A) and (B) are both of B1, (C) is of facies B, and (D) is a picture of Bt.

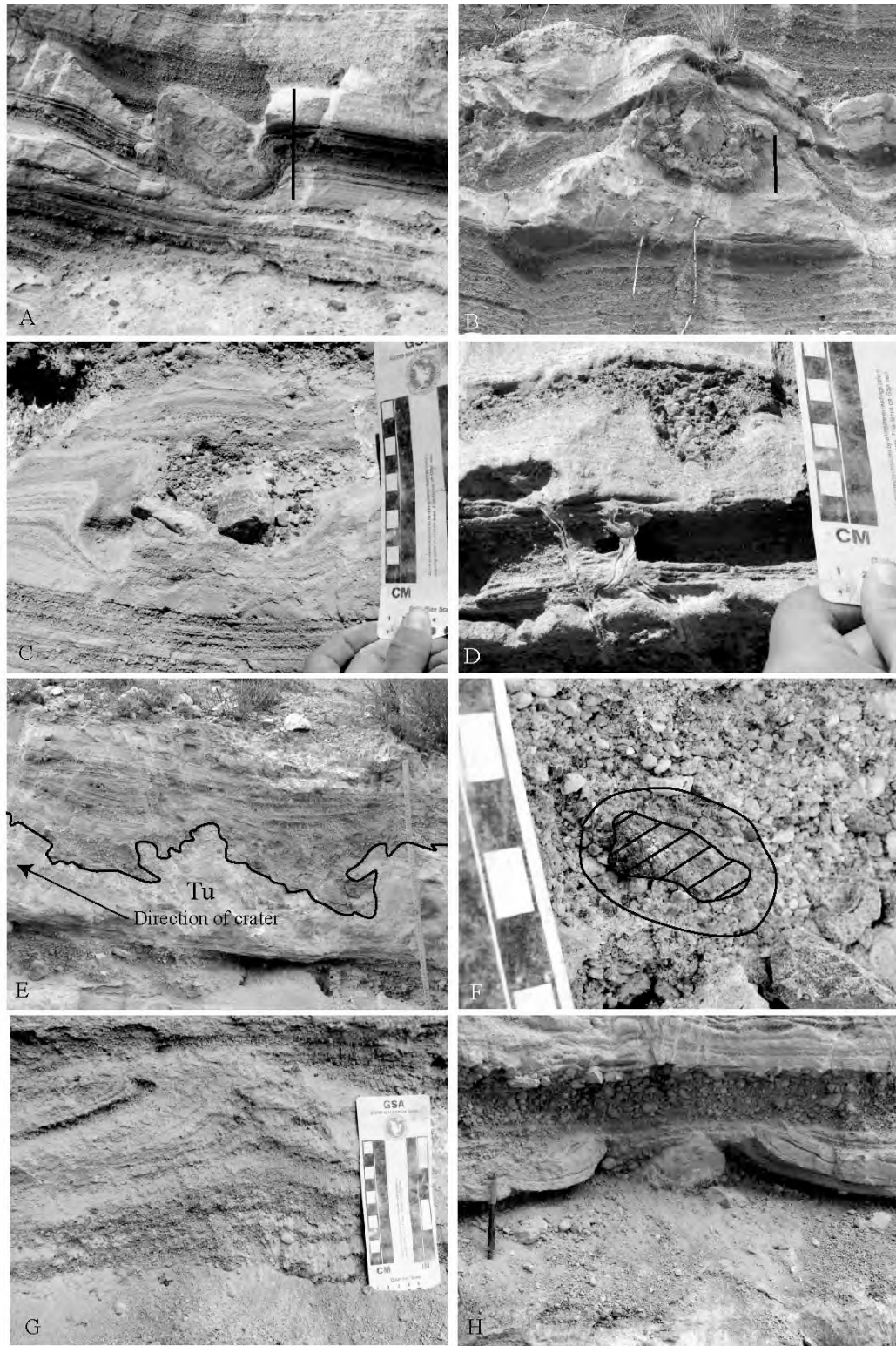


Figure 12: (A) and (B) are both bomb sags with black bars as a 15-cm scale. (C) and (D) are scour channels in surge deposits. The upper contact of a Tu deposit has been drawn in (E). The hachured area in (F) is a rusted lithic lapilli, an "Fe-clast", that has altered a ring of surrounding coarse ash in-situ (drawn-in boundary). (G) and (H) are both pictures of tuff, whose tops are sheared by deposition from an overlying coarser-grained bed.

Table 6: Facies descriptions and interpretations from field observations and patterns

Facies	Description	Interpretation
T1	Weakly laminated ash tuff with planar to mildly undulatory bedding and rare duneforms (1-3 cm in height). Scouring common along upper contacts with coarse-grained units (see Figure 15). Beds often deformed by bomb and lapilli sags. Sharp upper and lower contacts.	Scouring, bomb sags, and weak smeary laminae are indicative of saltation and suspension processes operating in a low-particle-density wet surge (Fisher and Schmincke, 1984; Chough and Sohn, 1990; Sohn and Chough, 1992). These deposits also likely have some contribution from co-surge ash fall.
AC	Mm-scale accretionary lapilli that fine outward and appear as: 1. discontinuous laminae to pods within fine-grained deposits. These accretionary lapilli are separated by a fine ash matrix. 2. Massive, thin- to medium-bedded deposits of accretionary lapilli-supported tuff.	1. Accumulation of ash into balls because of cohesive forces in the shear layer of wet, low-temperature surges (Fisher and Schmincke, 1984; Dellino et al., 1990; Wilson and Houghton, 2000). 2. Hydrostatic attraction and consequent clumping of fine ash in a moisture-rich eruption environment, resulting in fall deposits (Sheridan and Barberi, 1983; Fisher and Schmincke, 1984).
Tlap	Sub-cm-scale non-continuous laminae of alternating fine-ash tuff, coarse-ash tuff, and accretionary lapilli with occasional lapilli trains. Sharp internal, upper and lower contacts. Planar to undulatory bedding with rare dune forms (1-3 cm in height). Beds commonly deformed by bomb and lapilli sags.	Traction and saltation deposits from density-stratified, rapid wet surge pulses (Sohn and Chough, 1992; Sohn and Chough, 1993; Branney and Kokellar, 2002). Lapilli trains can be caused by traction-carpet deposition (Fisher and Schmincke, 1984; Dellino et al., 2004) or by fall deposits that get 'caught up' in surges (Wilson and Hildreth, 1998).
Bt	Massive, matrix-supported, very poorly sorted tuff-lapilli breccia. Intermittent, discontinuous weak laminae to pods of coarser ash and small lapilli. Most grains are coated in fine ash.	Column-collapse site with explosion maelstrom deposited close to the vent prior to any density stratification of clasts (Wohletz and Heiken, 1992) and/or a combination of early surge and fallout material causing unsteady flows and rapid deposition (Dellino et al., 2004). Ash coating suggests water-rich expulsion environment, which may have contributed to the unsteady surge pulses.
Bl	Poorly sorted, massive, coarse ash to small lapilli breccia, mostly clast-supported but with weak, intermittent laminae of fine-ash tuff. Grading, both normal and reverse, is common. Commonly scours underlying fine-grained deposits. Occasional coarse grains are coated in fine ash.	Traction-carpet deposition of high-particle density surges (Dellino et al., 2001; Vazquez and Ort, 2006) and/or fall deposits, which can result in both normal and reverse grading (Houghton et al., 2000; Wohletz, 2001) and/or a combination of both, as suggested by the intercalation of intermittent laminae in coarse-grained material (Wilson and Hildreth, 1998).
B	Massive, fines-poor, clast-supported lapilli breccia with moderately poor sorting. Mostly angular clasts. Graded in places, both normally and reverse.	Traction-carpet deposition of high-particle density surges (Dellino et al., 2001; Vazquez and Ort, 2006) and/or fall deposits from poorly energetic eruptive events (Sohn and Chough, 1992).

Barberi, 1983; Fisher and Schmincke, 1984). Wet-surge deposits are commonly thinly bedded and planar with associated accretionary lapilli (Sohn and Chough, 1992).

Wet-surge deposits commonly contain bomb or lapilli sags, in which fluidization of ash deposits results in deformation when impacted by ballistic clasts. 'Deformation' caused by the deposition of a block into wet ash can be measured from the vertical displacement of the top of the underlying ash bed. Scour channels are interpreted as originating from the erosive qualities of particle-rich, stratified wet surges traveling over cohesive, easily-deformed underlying deposits. Tu is interpreted as mud-rain deposits (Wohletz and Heiken, 1992; Dellino et al., 2001), rare deposits that proved to be excellent marker beds. The textures imparted by Fe-clasts onto the surrounding matrix indicate hot and wet deposition. As larger clasts, they retained their heat longer than the surrounding ash grains (Wilson and Houghton, 2000) . Some beds rich in Fe-clasts could be traced around the tuff ring and thus make good marker beds. However, other beds rich in Fe-clast distribution cannot be easily correlated with other sections, which means this distribution can also be very localized. The altered magnetite-rich oxyhornblende crystals of some andesite lithic clasts may be the source for the Fe-clasts. Because they are already 'rusted', heat and water could easily leach iron onto the surfaces of surrounding grains in-situ. Deformed and sheared tuff is evidence for strong lateral deposition of at least some coarse-grained deposits in a wet depositional system, possibly the result of coarse-grained surge pulses eroding underlying fine-grained, wet-surge deposits.

It should be noted that 'wet' and 'dry' are only descriptive terms used to describe the degree of deformation of the deposits based on outcrop observations, but are not directly related to the actual water content or fundamental character of the eruptive

system. A 'dry' surge may be the result of eruption through a completely dry system, efficient eruptions due to lower water:magma, and/or block- or lapilli-poor beds may mask the 'wet' nature of the deposits. Wet surges can be too hot for water to condense immediately after eruption and thus they are 'dry', but as the temperature drops with distance from the vent, they can become wet.

D. Stratigraphy

a. Crater Overview

An overview of Tepexitl crater dimensions (Table 7), measured sections, and general stratigraphic trends (Table 8) give the background information needed for an in-depth examination of the deposits. Inner-crater deposits in this discussion are those that crop out inside the crater wall and apron deposits are those that crop out on the distal side of the crater rim.

The crater floor lies approximately 20 m below the surrounding countryside. The slopes of the inner crater average 40° on the upper two-thirds and shallow to 20° toward the crater floor, a change that correlates with the transition from bedded tuff to syn-eruptive debris flow deposits near the crater floor. The volume estimate of bulk erupted juvenile tephra is based on these average angle measurements, crater dimensions, and average lithic content of 27% (Chapter 3). This minimum estimate does not account for distal deposits or any material remaining beneath the crater floor, but fits within the expected range of eruptive volume for tuff rings (Sheridan and Barberi, 1983; Fisher and Schmincke, 1984).

Table 7: Crater dimensions for Tepexitl tuff ring.

Dimension	Location	Value	
Volume	Tuff ring	36 x10 ⁶ m ³	
Diameter	Rim-to-rim	1015 m	
	Crater floor	745 m	
Height	Inner crater	75 m	
	Outer crater	55 m	
Slope	Avg. inner crater	30°	
	Avg. apron	13.9°	% of perimeter
	SW apron	10°	25
	SE apron	18°	32
	WNW-ENE apron	13°	43

The sections referred to in the following discussion are Section 2 (the type inner-crater section); Sections 4 and 6 (other complete inner-crater sections); Sections 3, 7, 10, and 11, (apron deposits); Section 8 (distal deposits; Figure 13); Section 12 (late-stage, inward-dipping crater deposits); and Section 13 (the near-rim deposits of the western inner crater). These section locations can be seen in Figure 14, with detailed descriptions of every measured section provided in Appendix 1.

Deposits within these sections can be broadly grouped into an upper and lower sequence, based on similar field characteristics (Table 8) and deposit distribution (Figure 14; Figure 15). The lower sequence comprises five units, while the upper sequence comprises three units. Figure 15 is a combination of geologic units (Figure 14) and crater morphology (Figure 3).

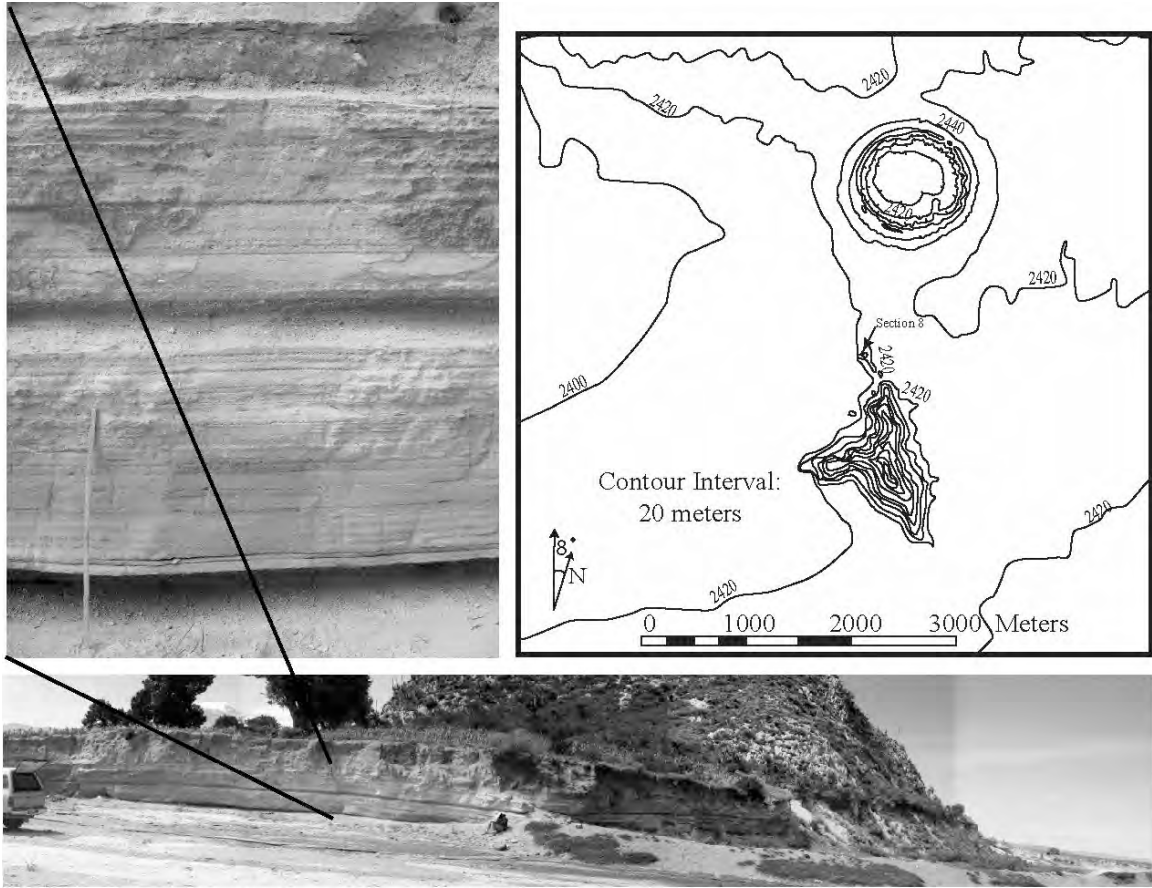


Figure 13: Section 8 (distal deposits) outcrop photos and topographic location, found 1.5 kilometers away from the crater, lapping onto limestone basement rock.

Table 8: Distinguishing field characteristics of lower and upper sequences.

Lower Sequence	Upper Sequence
Dominantly fine-grained	Dominantly coarse-grained
Abundance of deformed tuff	Less to no deformed tuff
Low abundance of blocks	High abundance of blocks
Blocks dominated by obsidian and lithic cobbles	Blocks dominated by stony rhyolite
Apron and distal deposits visible	No apron or distal deposits
Associated with three-stage deposits	No three-stage deposits

b. Unit Descriptions and Correlations

Relevant field data for each unit are summarized (Table 9; Figure 16), followed by deposit characterization and interpretation for each unit. Complete unit descriptions

and field measurements are located in Appendix 1. Unit descriptions are based on Section 2, the southernmost of the inner crater, and Section 13, the uppermost, bedded deposits stratigraphically.

Table 9: Summary of relevant field data for Section 2 deposits.

	Height ¹	Grain-size	Block % ²	Dom. Block(s)	PAD ⁴	Degree of Deformation ³
<i>LOWER SEQUENCE</i>						
<i>Unit 1</i>	5.8	fine	1-2	obsidian; lithic	SE	low; increases up-unit
<i>Unit 2</i>	5.5	fine	5-7	obsidian; lithic	SE	high
<i>Unit 3</i>	2.9	coarse/fine	<1	obsidian; lithic	SE	high
<i>Unit 4</i>	12.6	coarse	2-40	obsidian; lithic	SE	moderate
<i>Unit 5</i>	5.2	fine	1-2	obsidian; lithic	W	high
<i>UPPER SEQUENCE</i>						
<i>Unit 1</i>	8.2	coarse	20-30	stony rhyolite	W	moderate
<i>Unit 2</i>	9.2	coarse	20-30	stony rhyolite	W	none
<i>Unit 3</i>	5	v. coarse	n/a	stony rhyolite	W	none

¹ height refers to vertical stratigraphic height.

² block abundance is a volume percentage of the entire outcrop.

³ PAD stands for primary axis of deposition, a directional measurement based on stratigraphic correlation (data located in Plate 1 and Appendix 1).

⁴ degree of deformation is a qualitative assessment based on tuff deposits.

Single beds at Tepexitl cannot be easily traced around the perimeter of the tuff ring, a pattern observed by workers in the past at other pyroclastic cones (e.g. Brooker et al., 1993; Ort et al., 2000). In asymmetrically-distributed deposits, the most significant deposition occurs along a lateral axis of directed energy, a phenomenon referred to as the ‘primary axis of deformation’. In general, massive, coarse-grained Tepexitl deposits grade into laminated, planar, and finer-grained deposits both perpendicular to the primary axis of deposition and with increasing distance from the vent along the primary axis of deposition. This sequence is in agreement with deposition by surges that dilute with time, as proposed by Sohn and Chough (1989).

LOWER SEQUENCE:

Unit 1 (L1)

Description: Deposits consist predominantly of medium-bedded facies T1 with 20-40 cm interbedded deposits of facies B1 (Figure 17). Fine-grained deposits are planar to wispy and discontinuous, mostly nondeformed thin beds to laminae. Scour channels and bomb sags increase up-section. The coarse-grained beds are laterally continuous with coarse grading (both normal and reverse). Fe-clasts are present in Section 6, stratigraphically beneath the first outcrops in other inner-crater sections.

Interpretation: The fine-grained deposits are interpreted to result from increasingly wetter surges, while the small grain size that dominates unit-1 deposits suggests that highly efficient eruptions were occurring during deposition. Moreover, Fe-clasts deposited in the middle of the sequence indicate heat transfer was occurring between the magma and the saturated sediments, conditions consistent with phreatomagmatic explosions.

Unit 2 (L2)

Description: L2 deposits are thinly-bedded, alternating layers of facies T1 and B1/Bt, with sharp upper and lower contacts (Figure 18). The fine-grained layers are undulatory, discontinuous laminae with abundant bomb sags and scour channels. The coarse beds are continuous, fines-poor, and commonly crudely graded (both normal and reverse), with angular clasts that are commonly coated in fine adhering ash. The lowest coarse-grained breccia of L2 marks the beginning of a depositional pattern observed in L2, consisting of: 1) a basal, Fe-clast- and obsidian-rich breccia, sharply overlain by 2) a highly deformed, fine-grained ash deposit, sharply overlain by 3) a deposit with

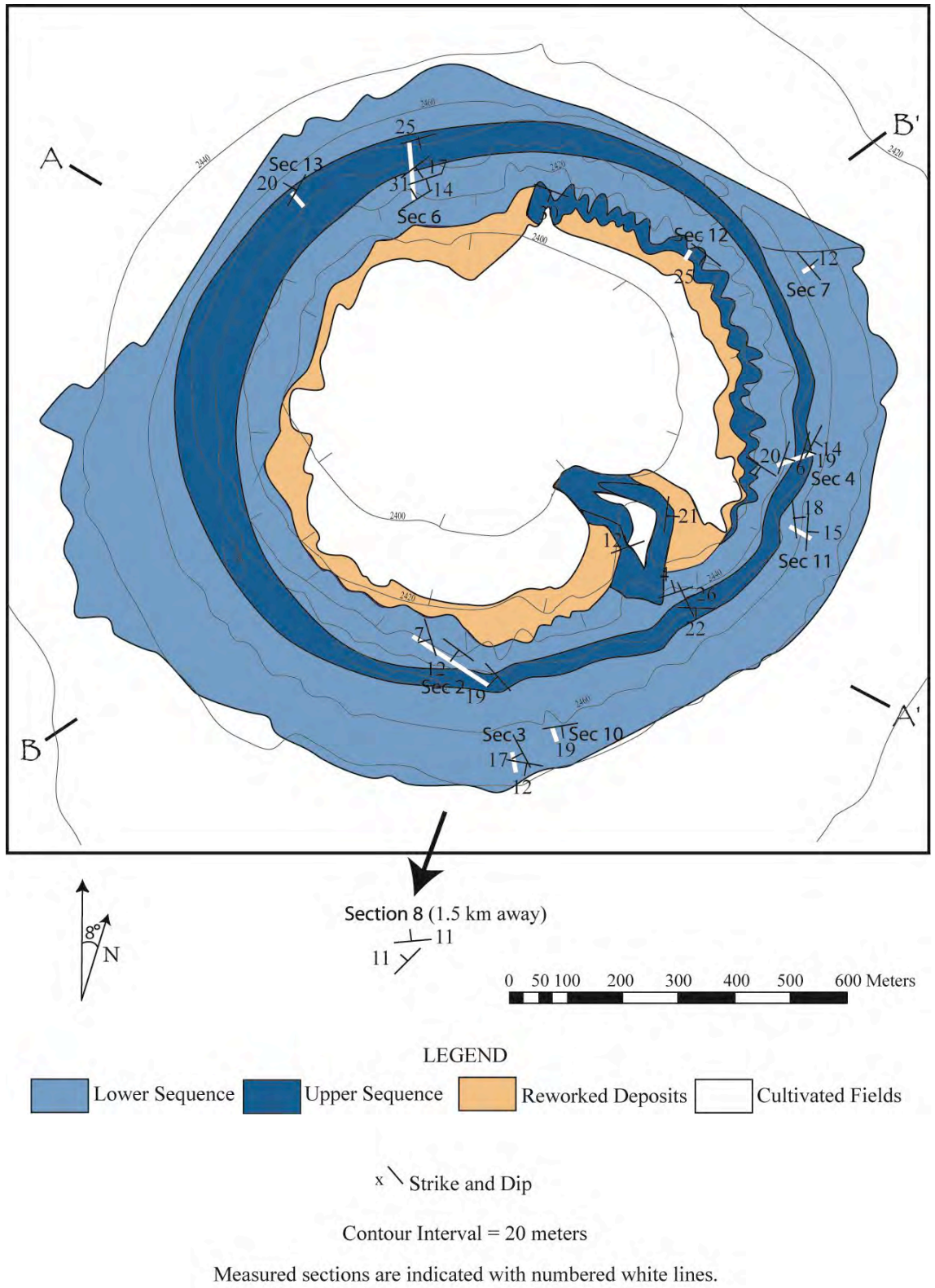


Figure 14: Geologic map of Tepexitl tuff ring, with cross-section end points marked (Figure 15).

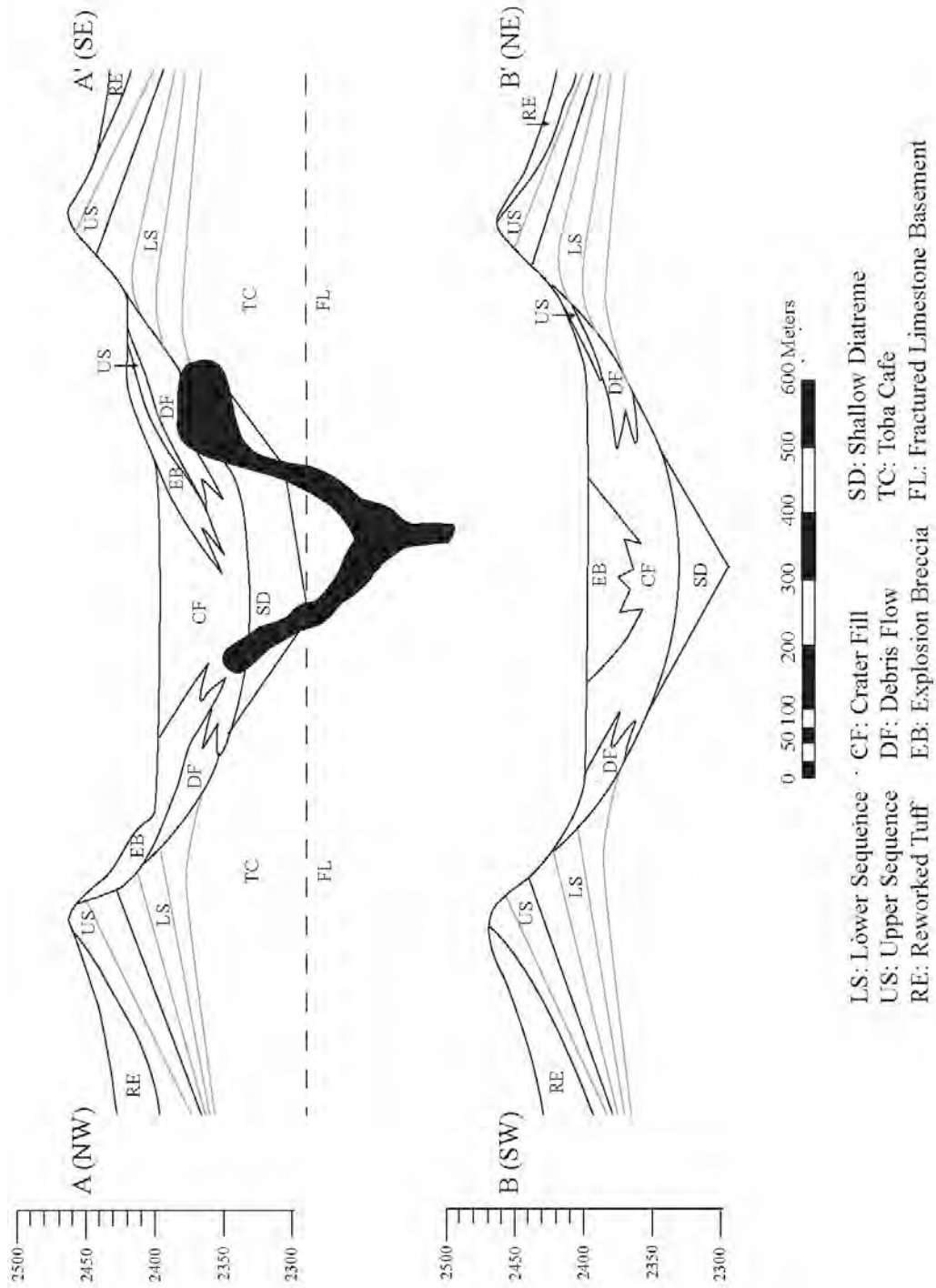


Figure 15: Cross-sections through Tepexitl Tuff Ring, as marked in Figure 14.

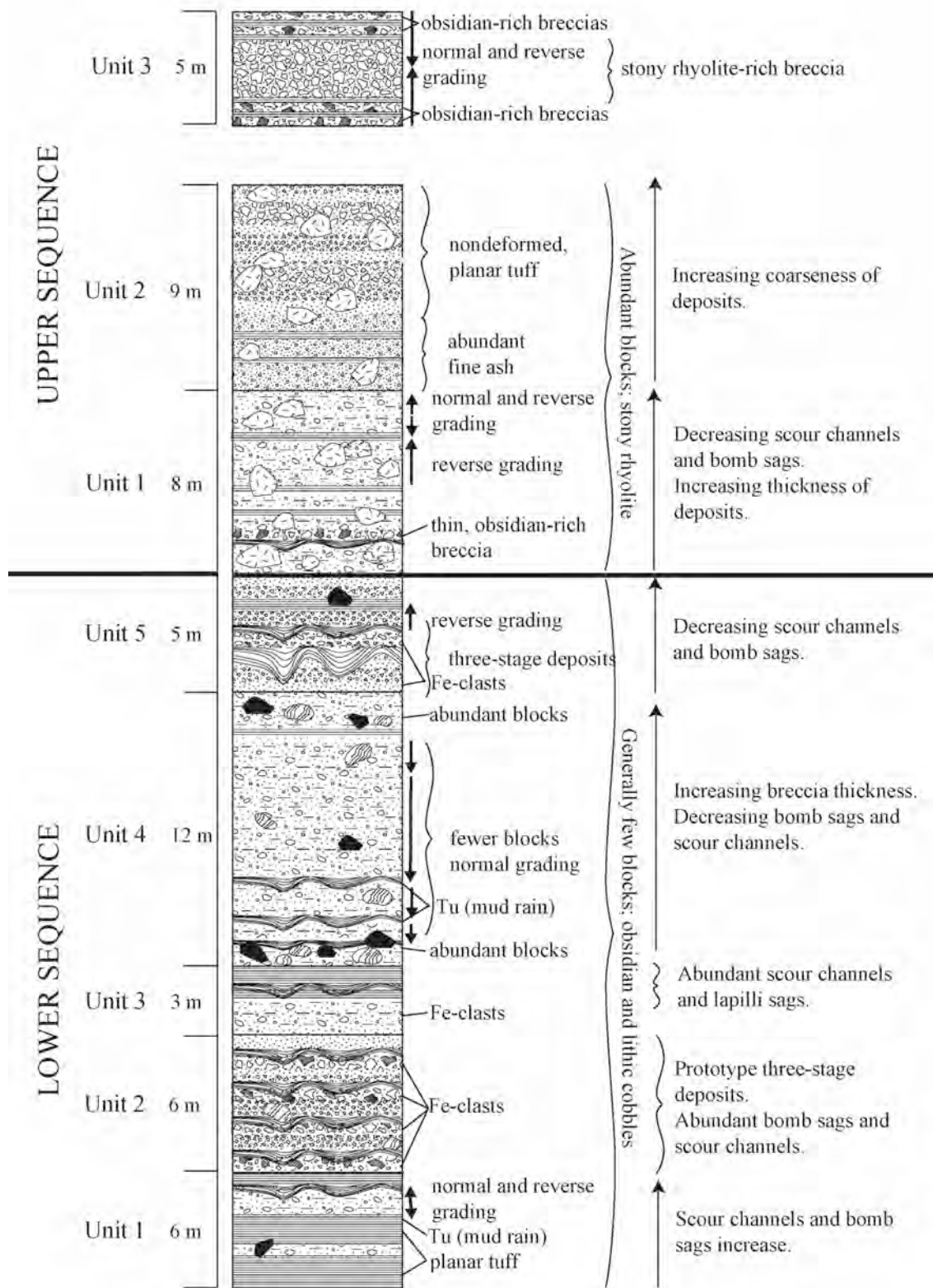


Figure 16: Generalized stratigraphic section for Tepexitl inner-crater deposits, as measured at Section 2 in the south. Unit 3 of the upper sequence was measured at Section 13 to the west.



A



B

Figure 17: (A) L1 deposits at the base of Section 4; (B) L1 deposits at Section 2.

grain size and deformational features intermediate between the two end members of deposit types 1 and 2. This characteristic sequence is herein termed the ‘three-stage deposit’.

Interpretation: The features seen in L2 (bomb sags, ash-coated clasts, and scouring) are consistent with an increase in water:magma from conditions during emplacement from the underlying deposits of L1. Fe-clasts in L2 indicate that heat transfer was occurring between fuel and coolant during deposition of L2. The three-stage deposit has been interpreted as an eruptive sequence resulting from distinct blasts, which deposited: 1) an obsidian-rich fall deposit, 2) wet surges, and 3) drier surges and falls. It is interpreted that L2 resulted from high energy, wet eruptive conditions, in which

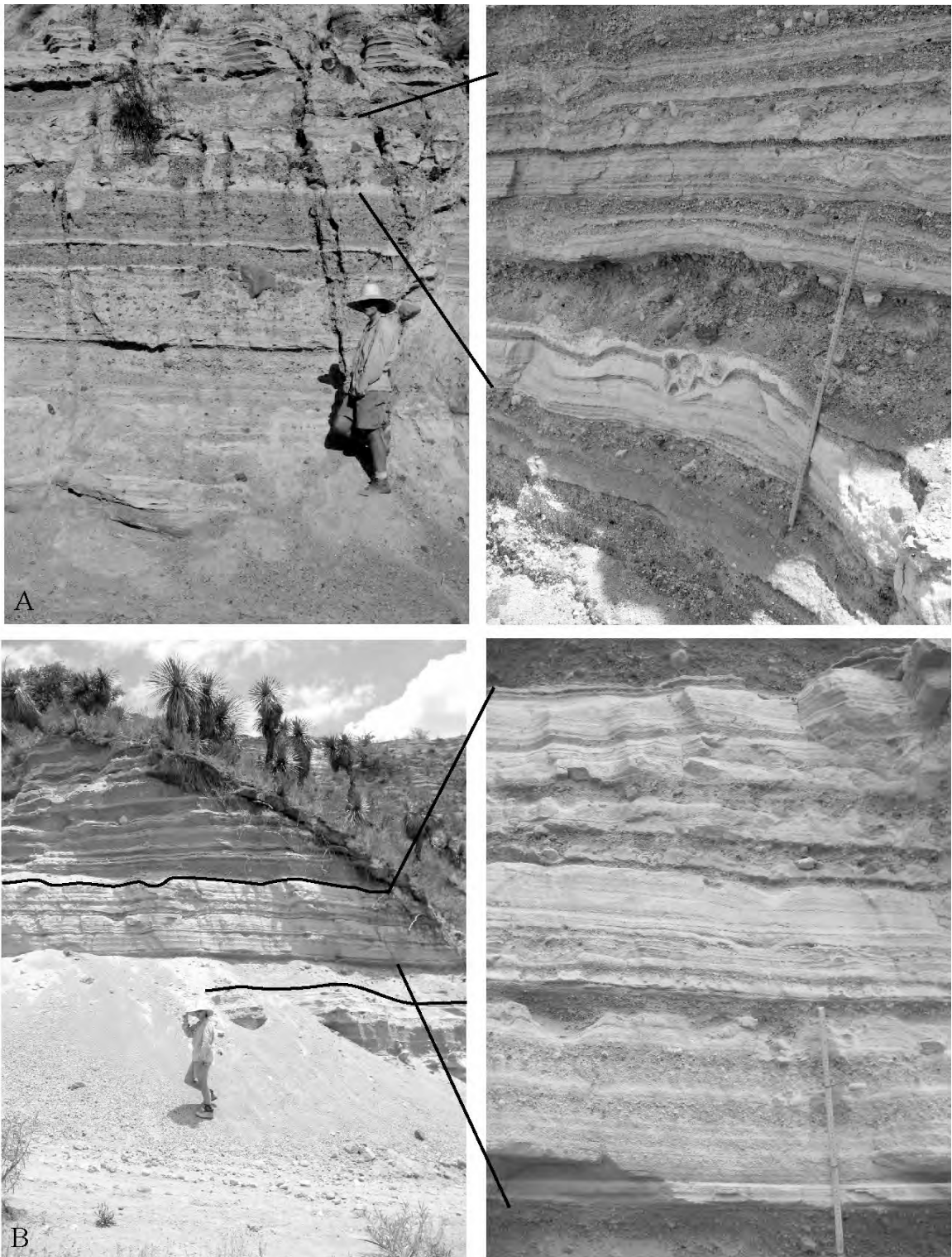


Figure 18: (A) L2 along the composite Section 2, with a close-up of the lapilli sags and undulatory bedding that characterize this unit (ruler is 0.75 m for scale); (B) L3 is outlined, with a close-up of the upper fine-grained deposits.

phreatomagmatic fragmentation may have occurred, and that the three-stage deposit is related to wet eruptive conditions.

Unit 3 (L3)

Description: L3 comprises a basal, thickly-bedded, Fe-clast- and obsidian-rich breccia (B1) followed by a thick sequence of dominantly fine-grained tuff of facies T1 (Figure 18). The breccia is laterally continuous. The tuff is undulatory with intermittent coarse-ash laminae and is characterized by abundant scour channels and lapilli sags.

Interpretation: Deformed ash and Fe-clasts indicate that wet surges and heat transfer from fuel to coolant were still occurring during deposition of L3, and the similarity of these deposits to the three-stage deposits seen in L2 indicate that similar eruptive conditions existed. L3 is interpreted to have been deposited by wet, high-energy blasts and surges that may have resulted from phreatomagmatic eruptions.

Unit 4 (L4)

Description: Deposits are dominated by thinly- to thickly-bedded B1 facies, with thinly interbedded, planar to undulatory tuff beds that contain sparse bomb sags and scour channels (Figure 19). Breccia layers contain rare Fe-clasts and are continuous, fines-poor, and commonly graded – both normal and reverse. L4 is the coarsest-grained and most voluminous sequence of the entire tuff ring, but it thins rapidly from the inner crater toward the apron.

Interpretation: The coarse-grained nature, large volume of erupted material, large percentage of blocks, and rapid lateral thinning are evidence that L4 resulted from lower efficiency eruptions than deposits lower stratigraphically (both fragmentation and depositional systems), with most deposition occurring near the vent. However, deformed

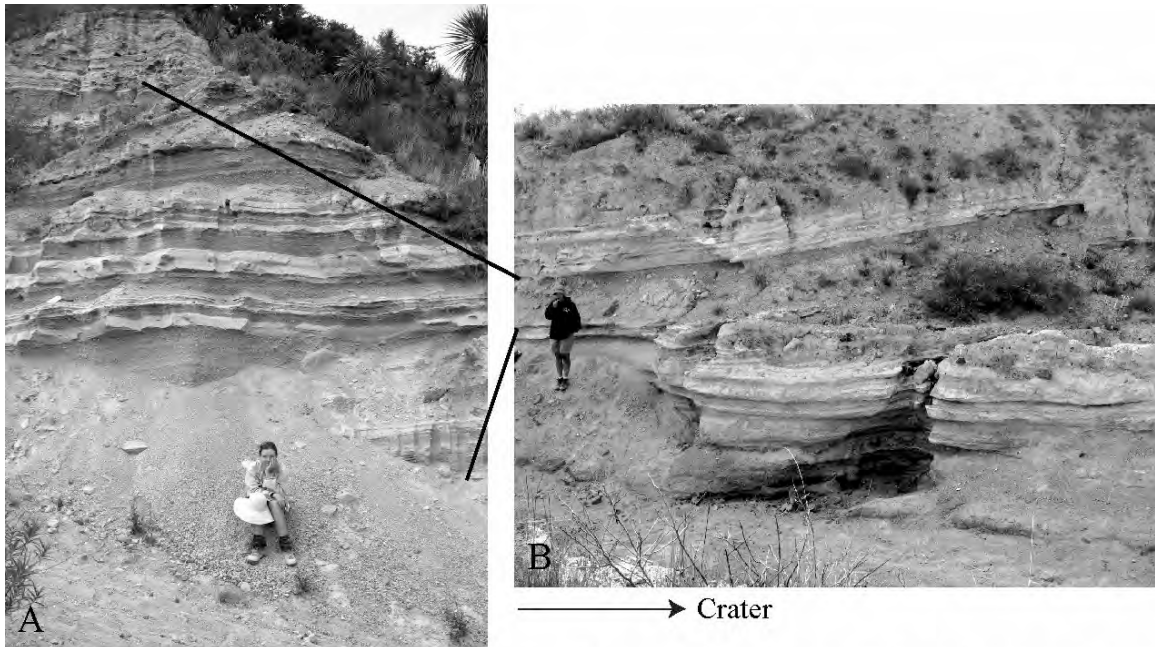


Figure 19: (A) the majority of L4 of inner-crater Section 2; (B) the entire L4 outcrop in the northern-apron Section 3, considerably thinner only 200 m laterally from the location of (A).

tuff indicates water was still present in the eruptive system and occasional Fe-clasts indicate some degree of heat transfer was occurring during deposition of L4. As seen in Figure 19, the tuff deposits underneath L4 have much steeper outward-dipping beds than those above L4, a result of cone building during near-vent deposition of a large volume of material. Figure 20 shows the only two instances of preserved primary inflection points throughout the tuff ring, both of L4 deposits. The migration of inflection points upward and outward during deposition of L4 indicates that the crater rim was becoming progressively enlarged, which demonstrates that L4 was also a time of crater widening.

Unit 5 (L5)

Description: These deposits are dominantly planar to slightly-undulatory T1 and T1ap facies, with interbedded deposits of facies AC. Minor, thinly-bedded, reversely-

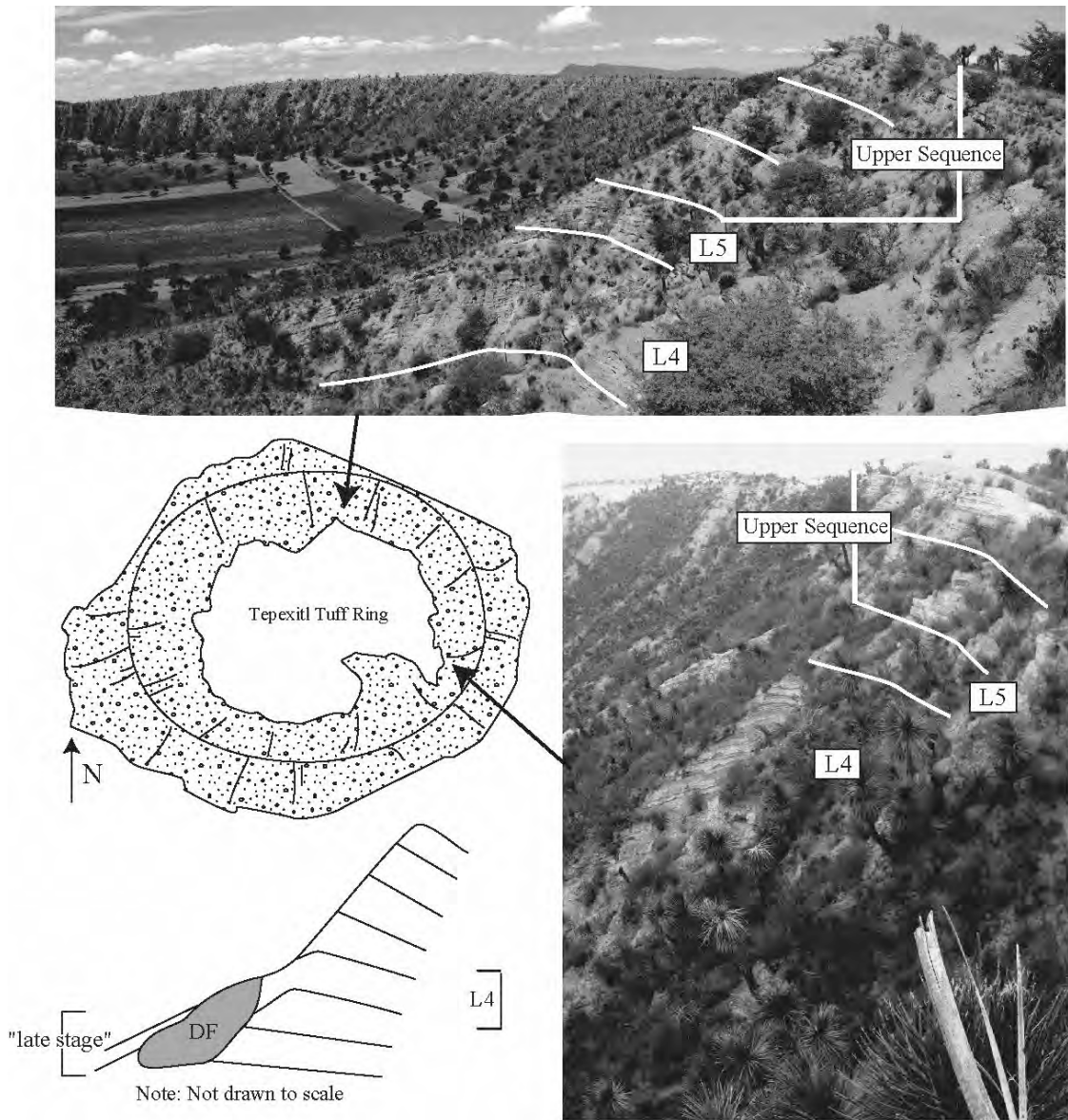


Figure 20: Two isolated drainages reveal inflection points of tuff beds in L4, a sequence that indicates a cone-building and crater-widening period. The schematic cross section shows the correlation between the crater-wall layered tuff beds, debris flows, and wet "late-stage" deposits.

graded, obsidian-rich, coarse-ash to small-lapilli deposits of B1 facies have fine-ash-coated grains and Fe-clasts (Figure 21). Fine-grained tuff contains abundant scour channels and bomb/lapilli sags.

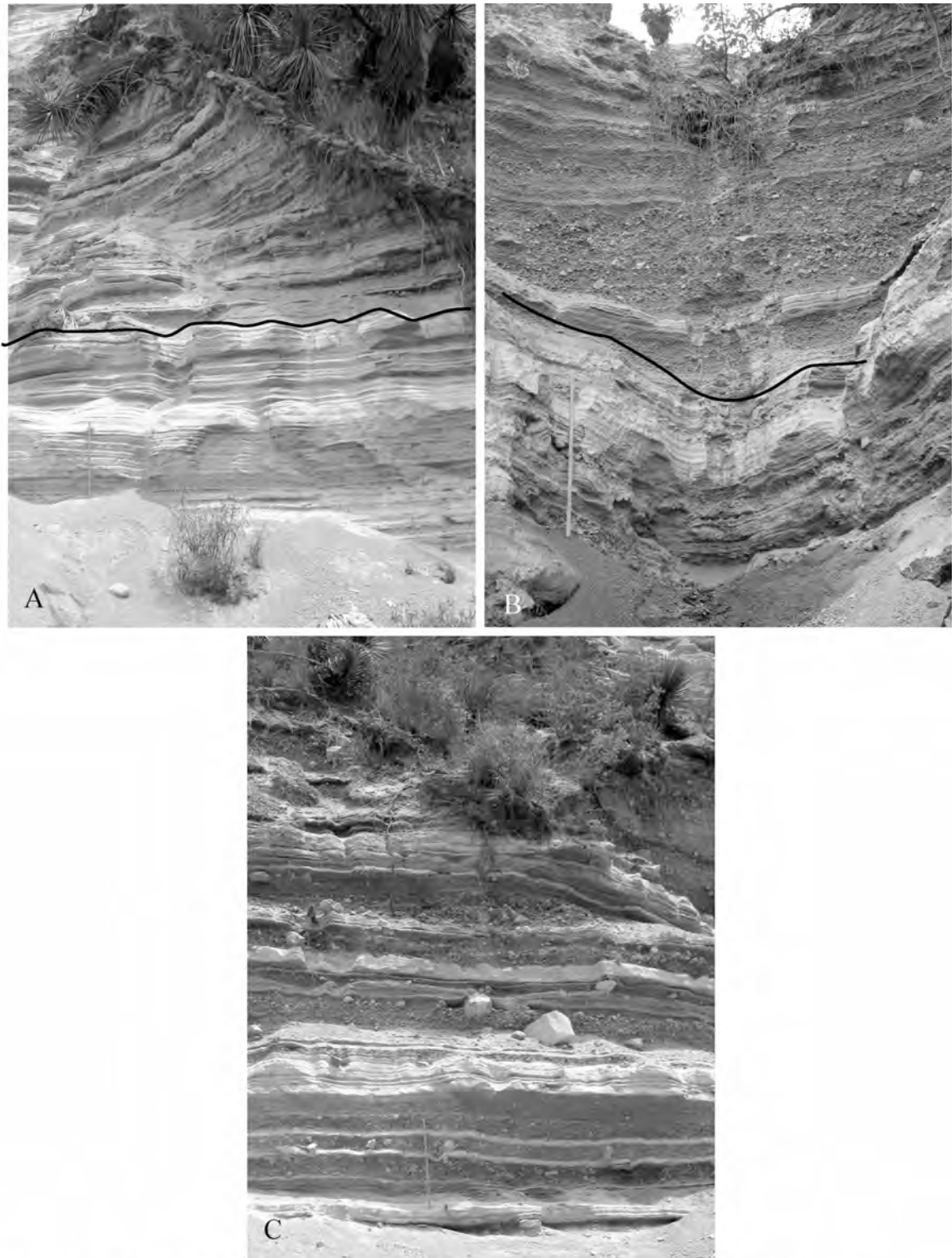


Figure 21: The dark line in (A) and (B) marks the contact between the lower and upper sequences. (A) is of laminated, fine-grained beds characteristic of L5 in Section 2 (B) is from Section 4; and (C) is a close up of U1 in Section 2. The ruler is 0.75 m for scale in all pictures.

Interpretation: Deformed ash, ash coatings on lapilli, and scour channels are indicative of water in the eruptive system. Deposits are similar in character to the three-stage deposits observed in L2, which suggests that L5 was also deposited by high-energy, wet surges and blasts that may have resulted from phreatomagmatic eruptions.

UPPER SEQUENCE

Unit 1 (U1)

Description: Thin- to medium-bedded, coarse-grained deposits of B1 facies dominate, with interbedded laminae to thin layers of tuff decreasing up-section (Figure 21). The coarse-grained breccias are laterally continuous with both normal and reverse crude grading. Intermittent fine-ash tuff is planar to undulatory with rare bomb sags and scour channels in the lowermost deposits.

Interpretation: Bomb sags and scour channels are consistent with water in the eruptive system, but a progressive decrease in water:magma occurs during deposition of upper-sequence U1. The coarse-grained deposits of upper-sequence U1 are interpreted to have formed from low-energy and low-efficiency eruptions.

Unit 2 (U2)

Description: At the base of U2, deposits of Bt facies dominate and are ash-rich, continuous, and planar with crude grading (both normal and reverse; Figure 22). Facies Tlap/Tl and B/B1 are interbedded toward the top of U2, with fine-grained, laminated deposits more abundant than in underlying U1. The fine-grained deposits are planar and non-deformed with no scour channels or bomb sags.

Interpretation: The decrease in ash deformation (no scour channels or bomb sags) suggests that U2 was the result of dry surges from a lower water:magma ratio in the vent

area. Similar to U1, U2 is interpreted to result from low-energy eruptions. The abundance of fine ash may relate to phreatic eruptions through crater fill or to primary fragmentation processes.

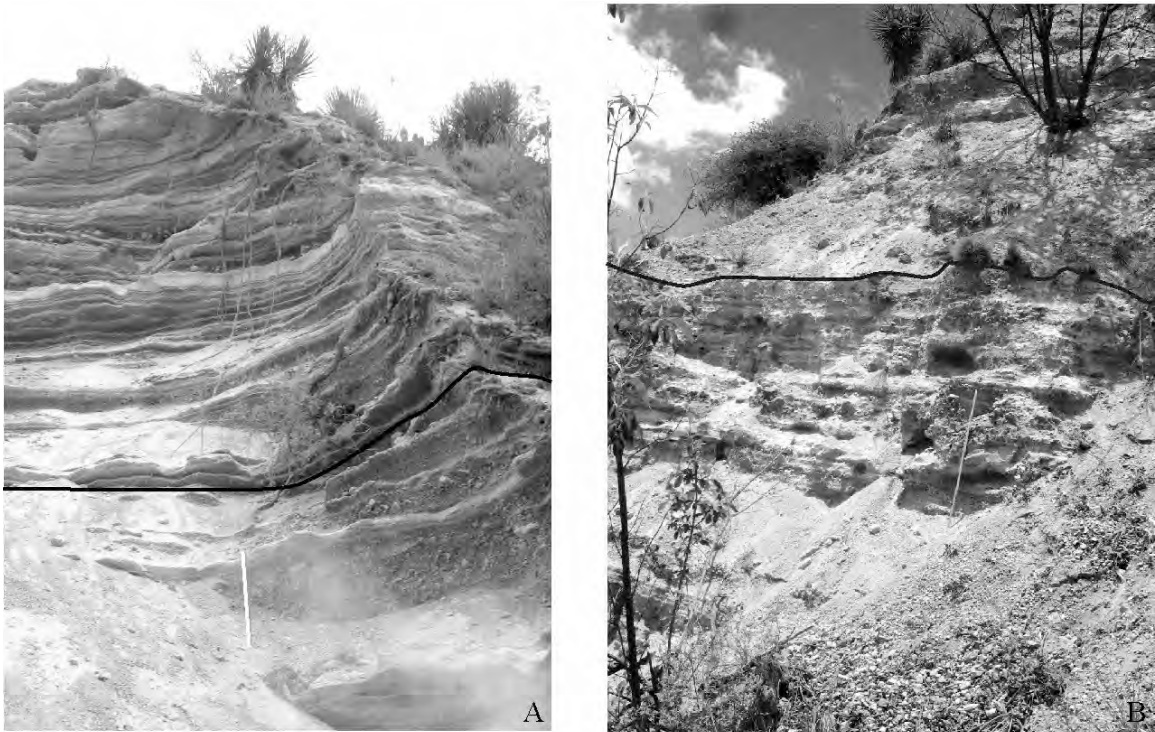
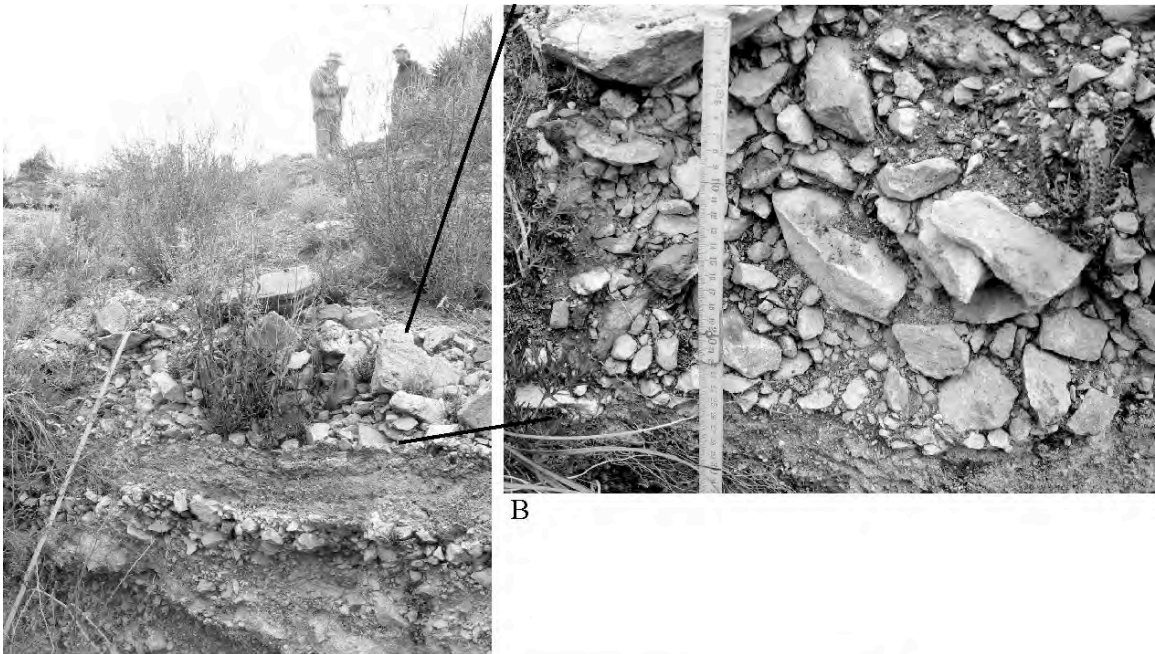


Figure 22: (A) the black line is the contact between U1 and U2 in Section 2; (B) the black line indicates the contact between U2 and U3 in Section 4. The ruler is 0.75 m for scale.

Unit 3 (U3)

Description: U3 was measured at the top of the western crater rim in Section 13 and is distinct from all previously described deposits (Figure 23). It is dominated by thickly-bedded, coarse-grained, clast-supported, fines-poor deposits of facies B, with angular, juvenile clasts and very-thinly-interbedded tuff deposits. The middle breccia is the thickest and coarsest-grained, dominated by stony rhyolite blocks that have occasional breadcrust textures. Breccias below and above the middle breccia are thinner and contain higher abundances of obsidian and flow-banded material. The uppermost

deposit is a thin bed of pumice- and obsidian-rich, yellow-coated lapilli and coarse-ash clasts. This deposit also contains coarse-ash-sized fragmented juvenile breccia clasts.



A

B



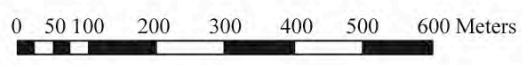
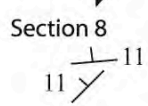
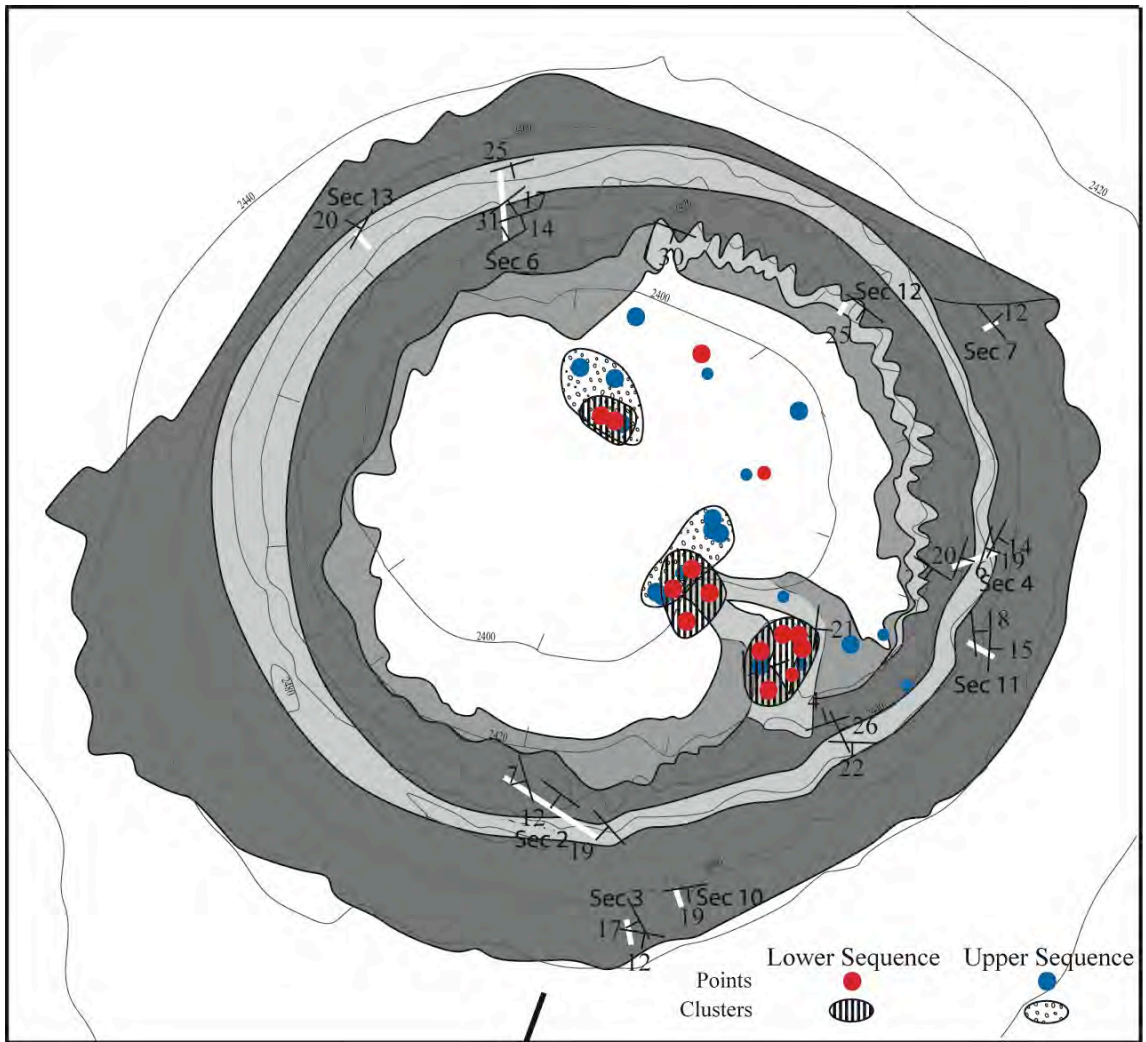
C

Figure 23: (A) the lower half of U3, with 1.3 meters of ruler for scale; (B) a zoom of the thick, middle breccia deposit; (C) the final deposit of U3, a thin veneer of yellow surficially-altered rhyolite clasts.

Interpretation: The coarse-grained, texturally-diverse, angular deposits of upper-sequence U3 contain a paucity of lithic clasts and are most consistent with dome/plug explosion at the end of the Tepexitl-forming eruption. The yellow coating on the final deposits may result from secondary alteration or vent-related alteration.

E. Vent Locations

A detailed analysis of strikes and dips was undertaken with the goal of gaining insight into vent location(s) and eruptive dynamics. Strike and dip locations were plotted by unit. For the attitudes of each unit, dip lines were extended into the crater. Because dip angles of inner crater tuff beds reflect the growth of the tuff ring, they should point back to the source of deposition – namely, the vent. Where lines intersected, a point was recorded. It became apparent from this exercise that points either clustered in high-concentration groups (shown in Figure 24) or stood alone as single points that could not be clustered with any precision (in Figure 24, these are shown by large circles that indicate line intersections and small circles that are the projected endings of single lines that do not intersect with any other lines from the same stratigraphic location, but do with lines from a different stratigraphic location). The clusters correlated to both lower and upper sequences and are located along a NW-SE oriented lineament. Some points from L5, U1 and U2 are concentrated in the eastern half of the crater and have a more random distribution. These differences in patterns mean that distinct periods of time can be analyzed based on depositional characteristics.



LEGEND

- Lower Sequence
- Upper Sequence
- Reworked Deposits
- Cultivated Fields

x \ Strike and Dip

Contour Interval = 20 meters

Measured sections are indicated with numbered white lines.

Figure 24: Map of potential vent locations at Tepexitl tuff ring.

INTERPRETATION:

Clusters are interpreted as possible vent locations, which suggest that eruptions occurred from several distinct areas of the crater. The conclusion from this analysis is that at least three vents were active during the formation of Tepexitl, likely with some degree of temporal overlapping activity. Additionally, the morphology of the growing tuff ring appears to have been affected by changes in vent location. It is interesting to note that all of the projected eruptive centers line up along a roughly NW – SE trending lineament, the same direction as the larger lineament of silicic centers in the area, which suggests that the vent activity was structurally controlled. At least two vents (those focused in the center of the crater) were active throughout the formation of Tepexitl, with a southern vent apparently active only during deposition of the lower sequence.

Deposition leading to the attitudes of the randomly distributed points correlates with a change in primary axis of deposition from the southeast to the west. These points may represent deposition from low-energy surges circulating within the crater opposite the primary axis of deposition. If surges were unable to make it out of the crater, they may have “ramped off” of crater walls prior to final deposition, leaving complicated strike and dip arrangements. Other possibilities for these random points include the introduction of inner crater obstacles that affected surge currents and apparent depositional direction and/or post-eruption deformation of tuff beds. Possible obstacles include syn-eruptive debris flow deposits or dome growth above the level of crater fill. The “thumb” is an unusual topographic high and may be explained by an underlying cryptodome that stagnated in the earlier vent either syn- or post-eruption. It is possible that such an intrusion could lift crater fill material and cause deformation of the crater

wall deposits along the “spine” of the thumb, which would also affect apparent dip direction.

F. Morphology

Despite the remarkably circular appearance of Tepexitl crater, the inner crater morphology is not straightforward (Figure 3). A distinct morphology difference exists from east to west. The inner crater walls along the eastern half of the crater are moderately well indurated with steep slopes that contain ‘typical’ tuff ring deposits - very well-exposed, thinly-bedded tuff deposits that are easily accessible through drainages and can be individually traced around the rim. The apron around the eastern half of the tuff ring has steep drainages that expose primary sections of bedded tuff, which can be correlated to the inner-crater units. However, inside the western crater, bedded tuff deposits are only visible for the top 10 meters toward the rim and cannot be followed to the beds in the eastern half of the crater. Western inner-crater walls and apron deposits are covered with debris that mostly obscures the bedded tuff underneath it. Yellow alteration affects surface deposits along the western crater rim.

Slumping has occurred on all slopes within the inner crater. This material is covered by steeply-dipping tuff deposits along the perimeter of the eastern inner crater. A small, localized deposit of massive ash, termed “anomalous ash”, also overlies slump deposits in the north. Unfortunately, characterization of crater fill was not possible because of extensive cultivation of the crater floor. Finally, a 200-m-long, 15-m-high flat-topped “thumb” sticks out into the crater from the southeastern inner wall and is covered in debris and cultivated along the top.

Western Crater Deposits

Exposed primary tuff deposits on the west side of the crater are rare, with only one good outcrop in a drainage half-way up the inner crater wall (Figure 25). This outcrop shows thinly-bedded, fine-ash to small-lapilli tuff (outward dipping), unconformably and sharply overlain by a massive, clast-supported, fines-poor, monolithologic, juvenile breccia that comprises the western inner-crater slopes (Figure 25). This breccia consists dominantly of stony-rhyolite blocks, some with breadcrust textures and jig-saw fracturing. In isolated outcrops within drainages of the western inner crater, this breccia deposit is pink in color, a feature that affects both large and small clasts alike (Figure 26). Detailed field descriptions of this outcrop are provided in Appendix 1.

The debris littering the western surfaces of the inner crater consists of a distinct mix of clasts, with an unusual percentage of very large blocks (Figure 26). The textures seen in these juvenile blocks are not observed anywhere else within the stratigraphy and include breadcrust pumice clasts, fractured blocks of cemented juvenile – lithic matrix-supported breccias (textures shown in Figure 27), and fragmented perlite blocks. The dominant float blocks are angular, dense, gray rhyolite up to 2 m across. Complete descriptions of the blocks seen in Figure 27 can be found in Appendix 1.

Pumice: A high concentration of friable pumice and breadcrust bombs occurs in the middle of the western inner-crater slopes (Figure 27). These cm- to dm-sized clasts include occasional obsidian textures. All clasts have slightly- to moderately-vesicular interiors with rare lithophysae.

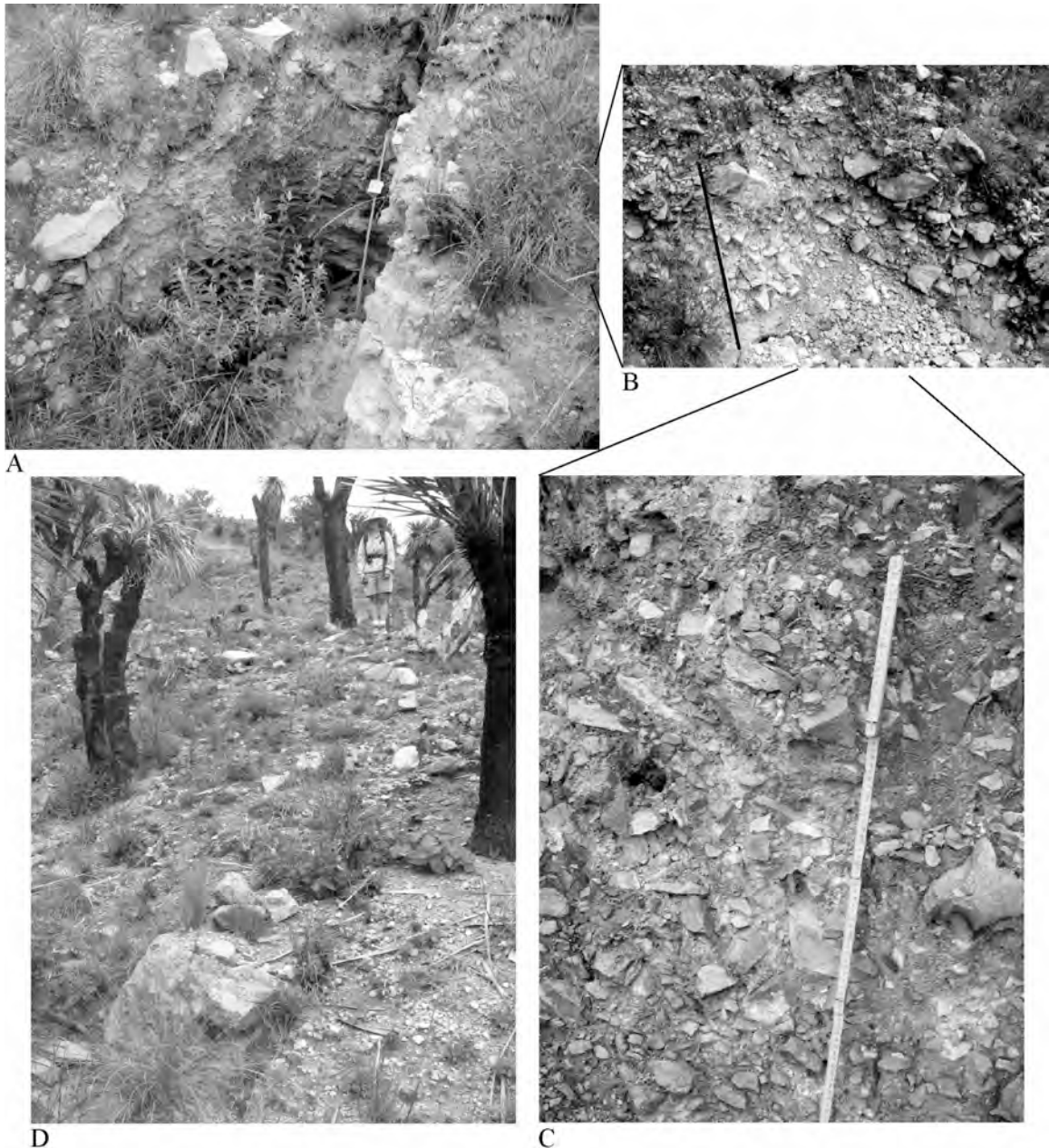


Figure 25: (A) layered tuff in the wester inner crater is unconformably overlain by a massive breccia deposit. Scale is 1 m; (B) a close-up view of the clast-supported breccia deposit. Note the clast angularity. Scale is 0.75 m; (C) further close-up view of the breccia. Note its monolithic nature. Scale is 0.75 m; (D) angular blocks litter the slopes and drainages of the western crater. Person for scale.

Breccias: The fragmented breccia blocks found as float blocks are larger versions of those found in the uppermost deposit of U3. They consist of angular, cemented chunks of matrix-supported, poly lithic breccias that contain clasts of dominantly angular to



Figure 26: Examples of some of the unique field textures observed in and around the explosion breccia on the western slopes of Tepexitl: pink-colored deposits (A), breadcrust bomb (B), fractured breccia cemented onto stony rhyolite (C and D), obsidian (E), and limestone (F).

rounded juvenile and minor lithic clasts (Figure 27). Some clasts appear to be imbricated within the matrix and some of the obsidian clasts have quenched margins. The ashy matrix ranges from yellow to pink to gray. These blocks are up to 80 cm in length, but average about 10 cm. One example was found of this breccia welded onto stony rhyolite

and then fractured and deposited (Figure 26). These textures indicate cementation occurred prior to fragmentation.

Perlite: D3 in Figure 27 is a block of medium gray, glassy obsidian cut by numerous intersecting, curved fractures that are consistent with hydration of volcanic glass (perlitic texture). F1 (Figure 27) has alternating bands of light-gray, poorly-vesicular stony rhyolite and dark-gray perlite. The perlite bands are between 1 and 3 cm in diameter and have sharp upper and lower contacts. As perlite is not seen as large blocks until the top of the eruptive sequence, it is assumed that the hydration of glass occurred prior to fragmentation.

The texture in F1 is consistent with flow-banding of perlitized obsidian, which became stretched by shear. This could happen in various locations where high shear and subsequent deformation would allow for viscous flow of hydrated glass prior to fragmentation: the vent, the conduit, and/or a dome/plug exterior. Flow-banded perlite argues for significant low-temperature hydration before cooling is complete. Perlite blocks present at the end of the eruption may have formed much earlier in the eruptive sequence (during deposition of the lower sequence, for example), only to be fragmented and ejected at the end of the eruption. Alternatively, perlite at the end of the eruption could represent water that came into contact with a rising plug but under ineffective conditions for phreatomagmatic explosion.

INTERPRETATION:

Primary layered western crater-wall tuff is obscured by a primary explosion breccia, as evidenced by: 1) the lack of lithic clasts (juvenile source), 2) the angular

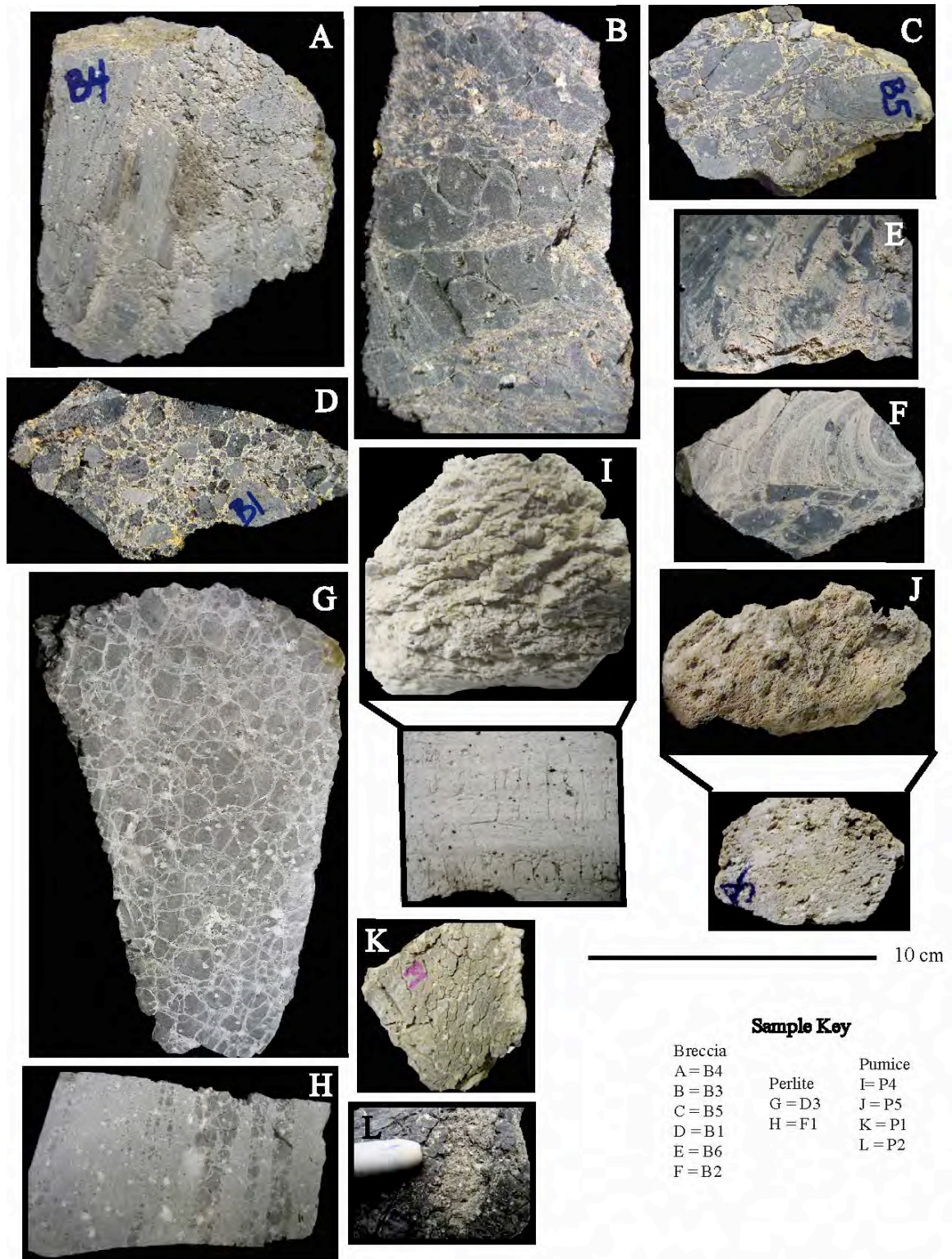


Figure 27: Unusual block textures found only as float blocks along the western inner crater.

blocks with jig-saw fractures and little matrix (little to no reworking), and 3) the pink color (deposition with heat). This explosion breccia is interpreted as the near-vent equivalent of the thick, middle breccia deposit of U3. The coarse-grained nature of the deposit and the textures of the pumice and breccias are consistent with a directed, shallow explosion of a dome or plug. The breccia blocks likely represent a combination of cemented crater fill, carapace breccia, and preserved peperitic interaction between magma and saturated crater fill. It is possible that cementation was caused by a shallow hydrothermal system associated with the rise of magma as a shallow intrusion. Perlite blocks indicate that water was present in the eruptive system at some point during the evolution of the tuff ring. This final stage may have appeared as a dome growing in 'tuff pond.'

Debris Flow and Late-Stage Deposits

Massive to very-crudely-bedded, poly lithic, very-poorly-sorted, matrix-supported deposits are found consistently around the inner crater. These are wedge-shaped beds with a maximum thickness of up to 20 m toward the crater wall, thinning in the direction of the crater and commonly obscuring the base of primary crater-wall deposits (Figure 28). To the east, these deposits are unconformably overlain by steep inward-dipping beds (20°-30°) of layered tuff and coarse ash-small lapilli breccia, which are plastically deformed by juvenile blocks and contain intermittent laminae of accretionary lapilli (Figure 29).

INTERPRETATION:

Syn-eruption, secondary debris flows caused reworking and redeposition of primary tuff within the crater. The bomb sags and the ability of the younger, overlying

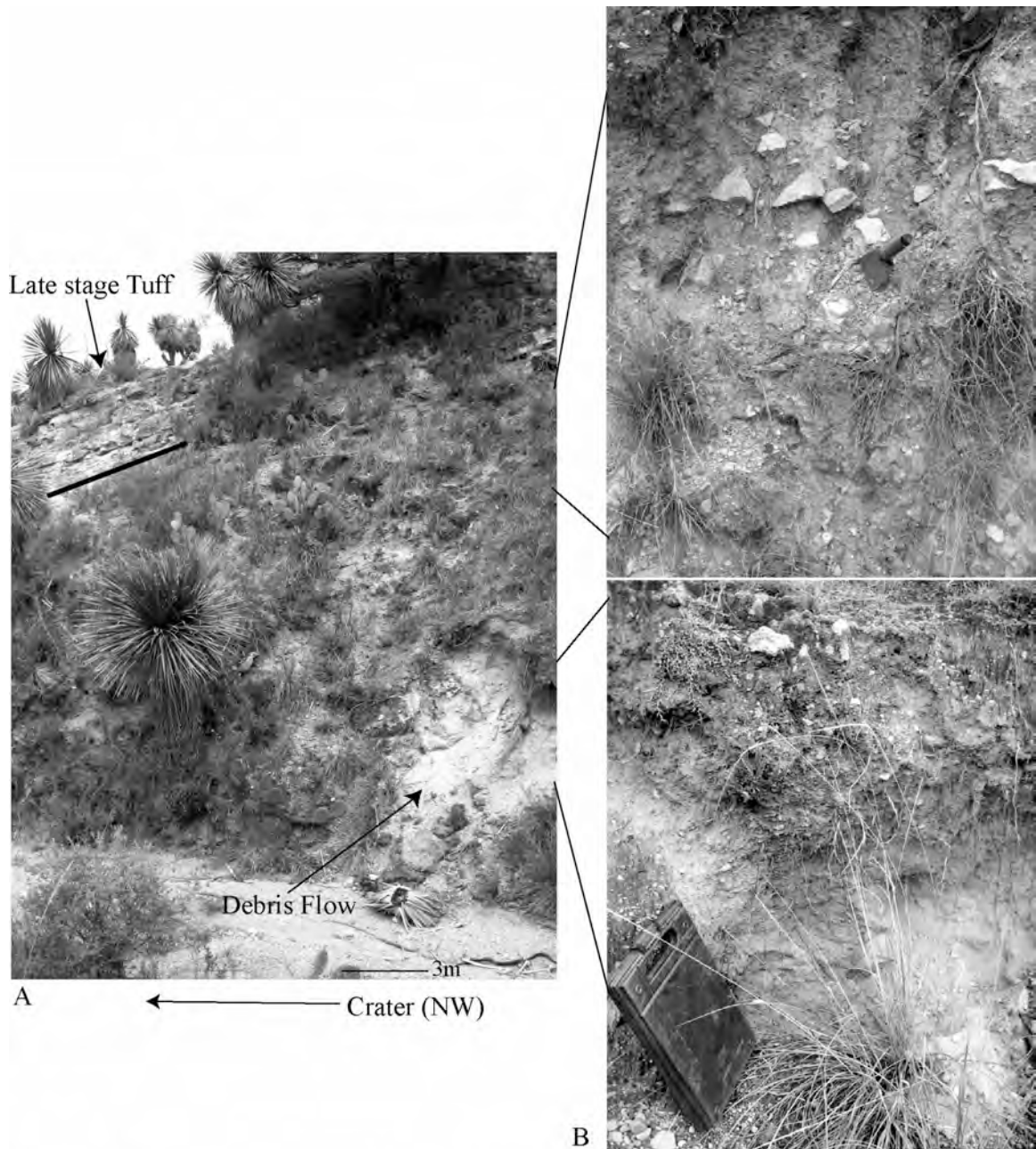


Figure 28: (A) a secondary, syn-eruption debris flow deposit with unconformably overlying, steeply-dipping, primary "late-stage" tuff; (B) close-ups of the debris-flow deposit. Shovel handle in the top picture of (B) is approximately 10 cm long.

primary tuff deposits to 'stick' to the crater walls is consistent with cohesive ash caused from wet eruptive conditions. These tuff deposits must have occurred late in the eruption

(or at least after deposition of the debris flows) and are termed “late-stage” deposits in following discussions.

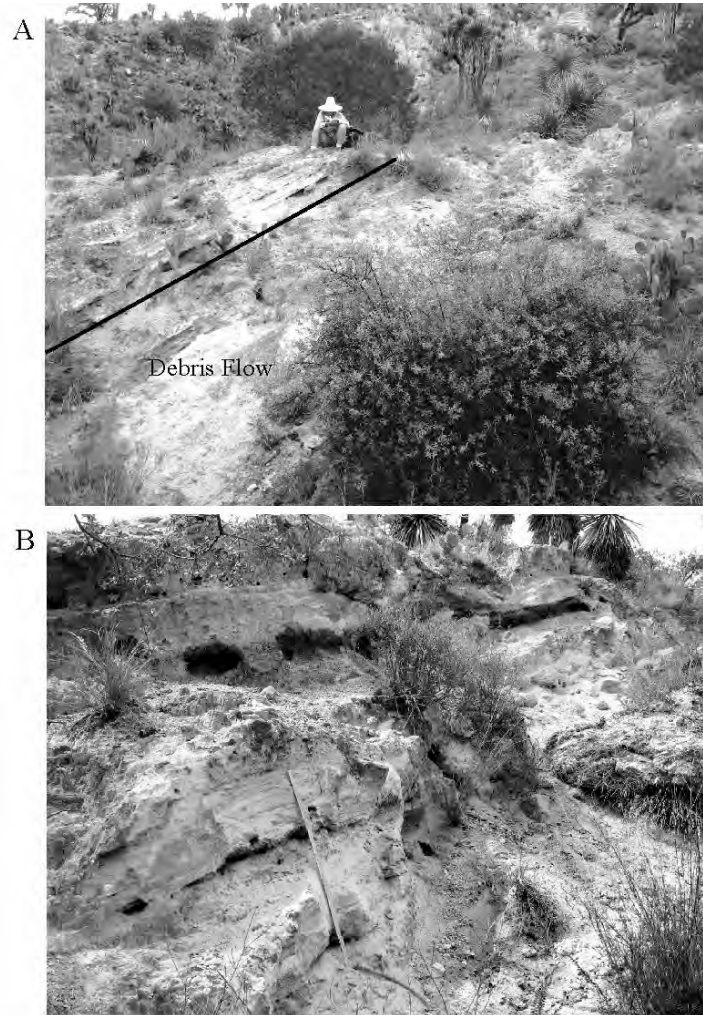


Figure 29: (A) "late-stage" deposits lapping unconformably onto debris-flow deposits along the base of the eastern inner-crater; (B) a close-up view of "late-stage" deposits in Section 12. Scale is 0.75 m.

Anomalous Ash

A small, very localized massive, fine-ash tuff on the eastern side of the northernmost slump has rare disseminated juvenile and lithic clasts up to 3 cm in diameter. It is well indurated, having resisted weathering more than the surrounding

deposits. The deposit is preserved on two high points on either side of a drainage, both of which have sharp, unconformable lower contacts with underlying slump deposits (Figure 30).

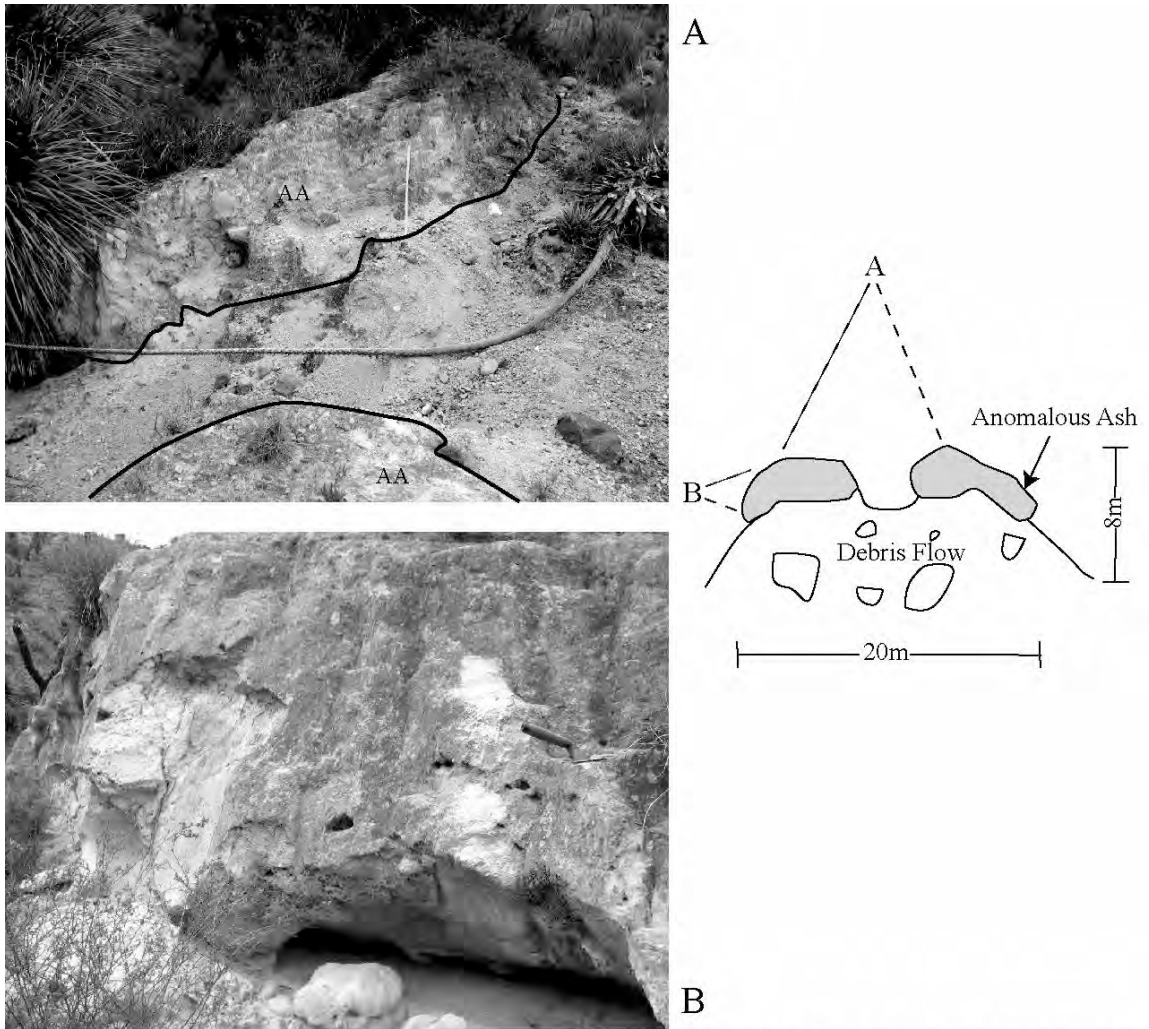


Figure 30: Anomalous ash outcrop photos, with a 0.75-m ruler for scale in (A) and a shovel for scale in (B), with the handle approximately 10 cm in length. A cross-sectional scale and morphology overview is drawn to the right., with approximate views for (A) and (B) indicated by dashed lines. Note the well-indurated, massive, fine-grained nature of the deposit.

INTERPRETATION:

This deposit may be the result of phreatic explosions through fine-grained crater and tuff ring material late in the eruption, but this mechanism should produce laminae or bedding structures from surges and/or fall. The anomalous ash may also be the result of secondary deposition, such as from eolian or lacustrine processes. However, such secondary processes would also be expected to produce some bedding structures. The lack of bedding may relate to bioturbation, which would be most consistent with an extended depositional period for the anomalous ash. The stratigraphic position, isolated nature, and unusual textural features of this deposit make it difficult to determine whether it is primary or secondary in nature.

The “Thumb”

A nearly complete cross-section of the thumb’s interior can be seen from its western drainage at the connection point with the inner crater (Figure 31). The basal >10 meters consist of a massive, matrix-supported, very-poorly-sorted, poly lithologic deposit with clasts ranging from 1 mm to 20 cm in size. This is overlain by 1.5 m of laminated to thinly-bedded tuff, with alternating fine-ash and coarse-ash deposits. Each bed is, on average, 20 cm thick and the fine-grained beds have sparse pods to discontinuous thin beds of accretionary lapilli. Sparse bombs cause vertical deformation of the deposits (5-15 cm). Overlying this tuff is approximately 1 m of massive, moderately-sorted, clast-supported, fines-poor, monolithologic breccia with angular juvenile clasts from 1 mm to 70 cm (dominated by stony rhyolite). This same deposit is also found around the tip of the thumb (Figure 31), with an average clast size of 7 cm and isolated patches of pink-red surfaces that extend uniformly through the matrix and clasts. Thinning toward the crater

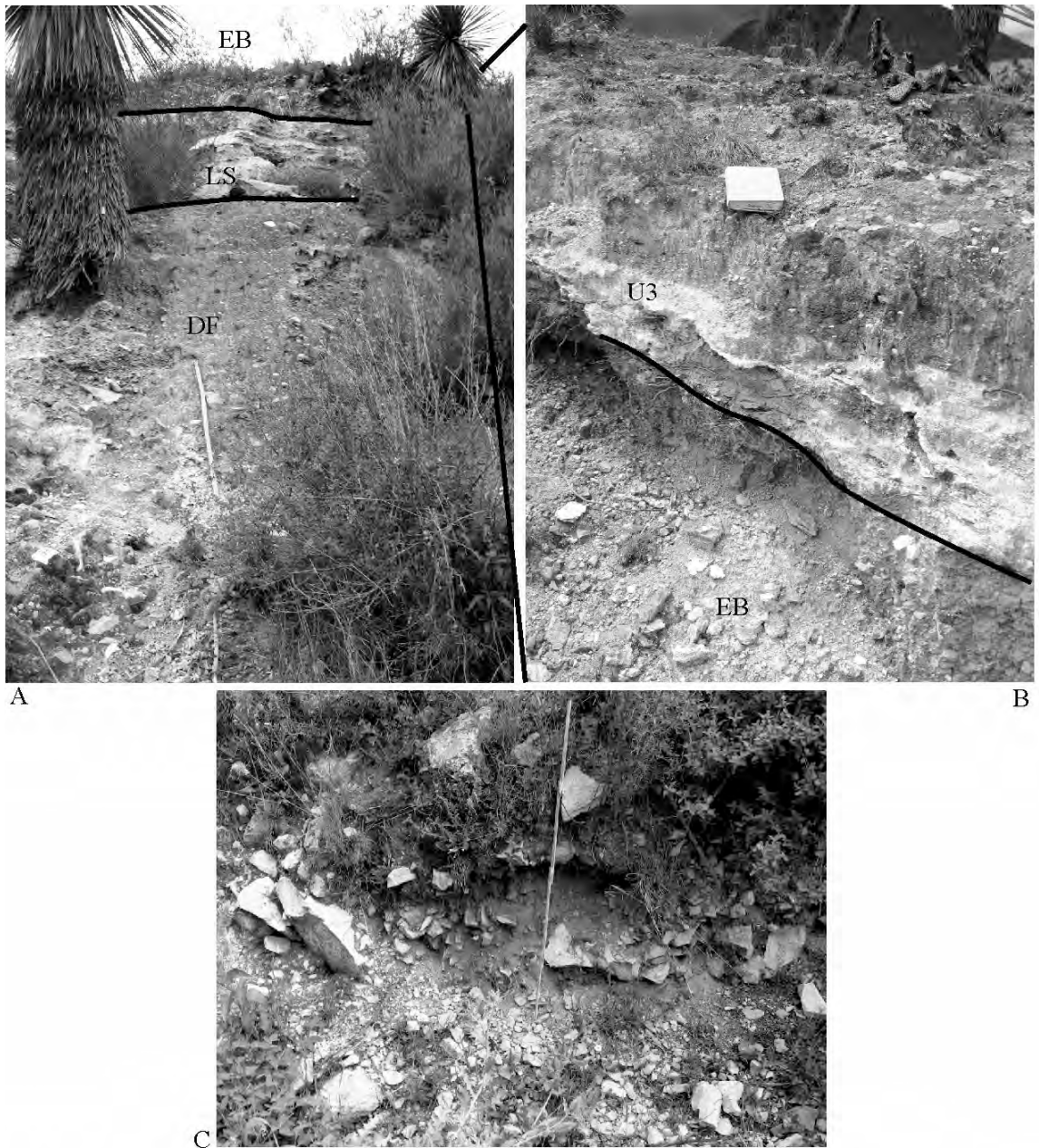


Figure 31: Deposits that make up the flat-topped "thumb": (A) a cross section of the "thumb", taken near the connection point with the crater wall up the western drainage. It shows a thick section of debris flow (DF), capped with a sequence of several meters of "late-stage" primary tuff (LS) and on top of that, primary clast-supported explosion breccia (EB), the same as that on the western slopes of the inner crater. 0.75-m ruler for scale; (B) a thin sequence of primary tuff from the upper sequence lies on top of the explosion breccia. Field book shown for scale; (C) explosion breccia at the tip of the "thumb", closest to the inner crater. 0.75-m ruler scale.

wall is the youngest deposit, a very thin (20 cm) layer of fine-grained, planar-laminated tuff, which is covered by up to 40 cm of soil. It is unclear if the feature's flat top is a primary feature or the result of centuries of farming. Another unusual feature of the "thumb" is the high concentration of fragmented breccia blocks on its top, slopes, and inside its drainages, very similar to those described from the western crater slopes. Disseminated juvenile and lithic clasts with surficial yellow alteration can also be found scattered around the thumb, with obsidian a dominant component.

INTERPRETATION:

Syn-eruptive, secondary debris-flow deposits are covered by deformed primary-tuff deposits. This sequence is overlain by primary explosion breccia and related primary tuff. The pink color of this deposit at the toe of the thumb indicates heat was present during deposition. This explosion breccia is interpreted to be the eastern lateral equivalent of the breccia found on the western crater. The thumb is interpreted to be either: 1) remnants of final, surface-level dome explosions (a sequence that may have ended with phreatic, wet-surge-producing eruptions through crater fill), or 2) the result of uplift from an underlying cryptodome. If uplift occurred syn-eruption, the tuff deposits may reflect primary deposition location. However, if uplift occurred post-eruption, the tuff units may represent uplifted crater fill.

G. Interpretation of Field Relations

Two phases of eruption at Tepexitl are identified through petrographic, stratigraphic, and field evidence. The phase that deposited the lower sequence ejected dominantly high-energy, fine-grained, wet surges, and may have resulted from

phreatomagmatic explosions. Stratigraphy during this time period is associated with the three-stage deposit and with cone building and crater widening (during deposition of L4). Deposition of the upper sequence was dominated by falls and/or blasts from a more magmatic phase, whose eruptions resulted from lower water:magma and had lower fragmentation and depositional energies (coarser-grained deposits limited to the inner crater). The eruption apparently shallowed during deposition of the upper sequence, experienced an increased flux rate of magma from a deeper storage area, and ended with dome/plug extrusion and subsequent, directed explosion. Eruptive activity occurred from at least three vents, with possible cryptodome uplift through the southernmost vent (either syn- or post-eruption), causing formation of the 'thumb'.

Chapter 3: Ash Analyses

A. Background

Grain-size-distribution data are a staple tool in analyzing pyroclastic deposits, as they reflect both transportation and fragmentation processes. However, these processes can be difficult to distinguish from each other (Fisher and Schmincke, 1984). Transportation by surge results in polymodal deposits, with distinct Gaussian subpopulations related to traction, saltation, and suspension mechanisms (Wohletz and Heiken, 1992; Dellino and La Volpe, 2000). Each volcano also has specific subpopulations of individual components that reflect fragmentation energy of explosions, with finer-grained distributions resulting from higher efficiency eruptions (i.e. Heiken and Wohletz, 1985; Wohletz and Heiken, 1992; Büttner et al., 2002; Kueppers et al., 2005). In order to quantify and compare grain-size distributions of samples, the K-ware SFT program was used in this study. The purpose of SFT is to discriminate transportation-related from fragmentation-related subpopulation ‘signatures’ (Wohletz et al., 1989). This program uses a “better-fit” model (lowest residuals) to identify an arrangement of Gaussian subpopulations that best account for the shape and volume of the grain-size-distribution curve (by phi). For each subpopulation, median phi, volume (weight percent) and maximum peak width (dispersion) can be measured and recorded, thus providing a quantitative means of comparing the grain-size distribution of samples. The program has further been used to determine magmatic from phreatomagmatic subpopulation signatures.

Field evidence and SEM studies suggest well-sorted (narrow-dispersion) peaks in the fine ash range (2 – 4 phi) are the result of phreatomagmatic explosions (e.g.. Heiken and Wohletz, 1987; Dellino et al., 1990; Dellino and La Volpe, 1995). Additionally, experimental studies (Zimanowski et al., 1991; 1997) found that ‘active’ particles were limited to the grain-size range between 3 phi and 5 phi. Wohletz and McQueen (1984) used experimental data from thermite explosions in order to quantify the ‘phreatomagmatic quality’ of a sample (R value). This calculation has been used to determine the water:magma mass ratio of a particular explosion (Wohletz et al., 1995; Ort et al., 2000). However, the conditions at Tepexitl present variables that cannot be resolved with SFT alone. First, the grain-size distribution of the lithic clasts is unknown, and may contribute to narrow fine-ash-sized peaks. Second, magmatic fragmentation and some degree of thermal granulation are both likely and viable processes operating during the formation of Tepexitl, mechanisms that also create very fine ash. Third, no study has been conducted that has quantified the grain-size distribution of phreatomagmatic rhyolite ash grains. Additionally, the effects of impure coolants such as saturated sediments on fragmentation processes make it unrealistic to back-calculate water:magma ratios (White, 1996). Therefore, grain-size data alone are not enough to discuss how or if phreatomagmatism occurred at Tepexitl. In this chapter, granulometry data are combined with componentry data from samples of Section 2 in order to better explore fragmentation mechanisms and eruption dynamics.

B. Methods

Samples were sieved from -5 to 4.5 phi in half-phi intervals. A Coulter LS was used for analysis of grain-size distributions from 4.5 phi to 11.5 phi. The total weight of

each fraction of each sample was normalized to 100 to calculate percentages. Based on these data, the SFT program was used to analyze subpopulations and calculate R values. For the purposes of this research, this method was used only as a qualitative representation of increasing percentage of peaks in the 2-4 phi range with narrow dispersions, as a way to identify potential sites of active particles. The -2-, 0-, and 2-phi sizes were selected for componentry analysis based on the presence of repeated peaks in the grain-size distribution around each of these modes. Using the optical microscope beyond the 2-phi size is not possible, as the grains are too small. Because of this limitation, and because fine ash grains are of high interest in this study (as potential indicators of phreatomagmatism), the componentry analyses done for this study were not meant to quantify changes across grain size (as has been done, for example, by Barberi et al., 1989). Instead, they were used as a stratigraphic overview of major changes in the componentry of coarse ash grains.

The goal of this procedure is to identify and examine any such changes in terms of changes in eruptive dynamics (thus, also potential variations in fragmentation mechanisms). An additional goal was to use R value and componentry together as a way to extrapolate to the componentry of fine ash (less than 2 phi) subpopulations. A final goal was identification of general patterns within facies and/or units as grains decrease from lapilli- to ash-sized particles, useful information in understanding fragmentation mechanisms. For componentry data, 200 grains were counted for every sample collected in Section 2 as well as those collected for U3 (Section 13), the final breccia sequence. All data were normalized to 100 percent. Each sample was washed and treated in ultrasonic

bath to remove the ubiquitous fine vitric ash that dusted most of the grains. Appendix 2 provides detailed descriptions of these methods.

C. Summary of Data

a. Granulometry by Facies

Granulometric data from Tepexitl show a strong correlation between grain-size distribution and facies (Figure 32), although there is no apparent vertical pattern or trend. All deposits are poorly to very poorly sorted, according to sorting parameters defined by the Folk and Ward method (1957). R value increases with weight percent fine ash (Table 10). Of the coarse-grained facies, B and B1 deposits are dominantly composed of broad-dispersion, lapilli-sized subpopulations, whereas Bt deposits have a higher degree of polymodality and a higher weight percent of fine ash (Figure 33).

In contrast, fine-grained facies (Tlap, AC, and T1) all have polymodal deposits with narrow-dispersion peaks in the range between 2 and 4 phi (Figure 33). AC facies show a wide range of narrow-dispersion, dominant subpopulation peaks between -2 phi and 1 phi, a pattern that reflects the varying sizes of the accretionary lapilli themselves. Smaller than 1 phi, the accretionary lapilli broke apart into their fine-ash components. The data for these subpopulations in deposits of T1 facies have the narrowest range of data points (0.9 phi to 1 phi) when compared to Tlap and AC deposits. Also apparent is that the finer-grained subpopulations in Tlap beds have as broader dispersions as those of AC and T1.

INTERPRETATION

Grain-size distribution is well correlated with facies, reflecting fragmentation and transport processes occurring during the eruption. The deposits of each facies type have

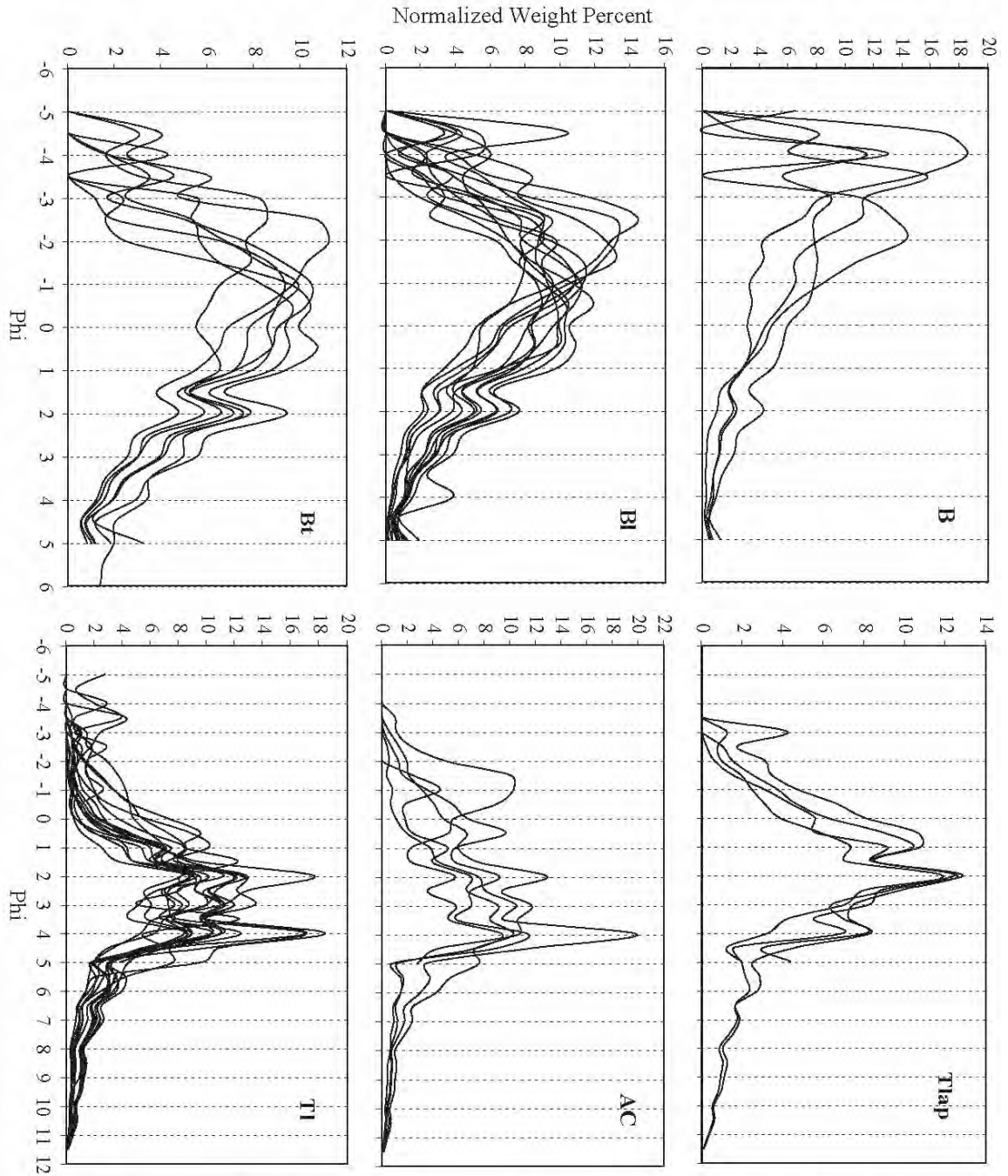


Figure 32: Grain-size distributions by facies of all samples taken from Section 2. The coarse-grained facies are above, with the 5-phi grain size representing the percentage of material left in the pan after sieving. This pan material was further analyzed for the fine-grained facies, shown at the bottom of the figure. Note that the normalized weight percentages on the y-axis are different for each facies even though the graphs are the same size.

peak around 2 phi in all sampled deposits, regardless of overall grain-size distribution or depositional mechanism, may represent an original fragmentation peak (Dellino and La Volpe, 1995). The narrow-distribution, lapilli-dominated subpopulation peaks of the coarse-grained facies are consistent with deposition by fall and represent primary fragmentation sizes for these deposits. The addition of broad subpopulation peaks in deposits of B1 and Bt facies is suggestive of some degree of disaggregation (longer tails) and is consistent with transport-related break-up, possibly from deposition from surge traction carpets. Facies Bt deposits are composed predominantly of coarse ash and lapilli, but have a larger abundance of fine ash than other coarse-grained deposits, as well as a dominant finer-grained subpopulation. The implication of these differences is that Bt deposits result from some combination of eruptive and/or transportation mechanism(s) that have a decreased degree of sorting between coarse and fine grains, possibly hybrid deposits or deposits close to the vent.

T1 and the matrix of AC deposits are consistently very fine-grained. The fine-grained subpopulations (between 1.8 and 3.9 phi) are all narrow dispersion peaks of high-precision data points (high degree of clustering) and indicate a higher degree of polymodality than the coarse-grained facies. Wohletz et al. (1989) concluded that magmatically-fragmented subpopulations have broader dispersions (between -0.4 and -0.6), whereas phreatomagmatically-fragmented populations have narrow dispersions (between -0.5 and 0.3). Deposits of T1ap facies contain more coarse ash than deposits of T1 or AC facies, evident by their broad subpopulation peaks between -0.5 and 1 phi, as well as the overall lower weight percentage of fine ash (13%). Based on their broader fine-grained subpopulation peaks, T1ap deposits appear to be more affected by

transportation-related break-up than Tl or AC facies, perhaps due to more particle collision in higher density surges.

Despite differences in facies and grain-size distribution of Tepexitl deposits, narrow dispersion peaks between 2 phi and 4 phi are seen repeatedly. The subpopulation characteristics at these grain sizes are of great interest because this is commonly the size range of active particles, which are records of high-fragmentation energy events (Zimanowski et al., 1991). Although saltation processes within a surge are associated with narrow subpopulations in the fine-ash size range (Figure 34; Wohletz et al., 1989), Dellino et al. (1990) found that the original fragmentation peaks are only slightly modified by transport. Dellino and La Volpe (1995) concluded that polymodality and overall grain-size distribution of a deposit is mostly related to fragmentation processes. Although magmatic and phreatomagmatic 'signature' peaks can be difficult to discriminate, the deposits of Tepexitl compare favorably with other rhyolitic tuff cones that have possible phreatomagmatic components (Figure 34). However, the well-sorted, polymodal, fine-grained deposits of Tepexitl may also be related in part to an overprint of Toba Café primary grain-size distribution. A Toba Café sample taken at Tecuitlapa maar (Figure 35) is shown here as one example of the grain-size distribution of the pervasive basin fill. However, it is important to note that this sample cannot be assumed to represent the nature of the deposits through which Tepexitl erupted. It is a useful comparison because it shows a strong fine-grained component and a strong polymodal distribution of subpopulations.

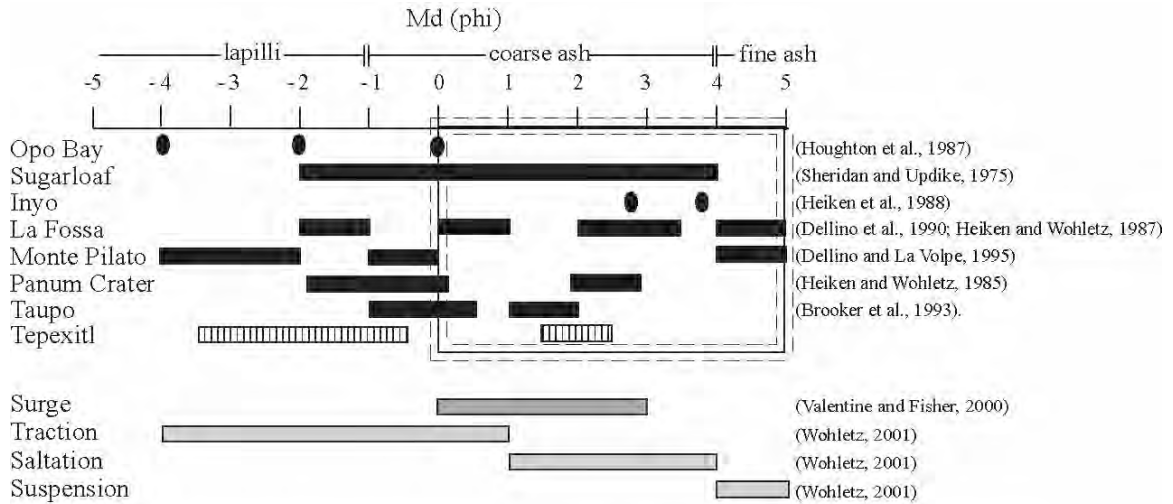


Figure 34: Average median grain size of Tepexitl deposits compared to other rhyolitic pyroclastic deposits. Dots correspond to single reported median grain sizes, whereas boxes represent a range of reported grain sizes. The boxed area incorporates all grain sizes that have potentially phreatomagmatic components. Dominant grain sizes carried and deposited by different mechanisms within a surge are also shown. Median grain sizes of average surge deposits are shown for reference.

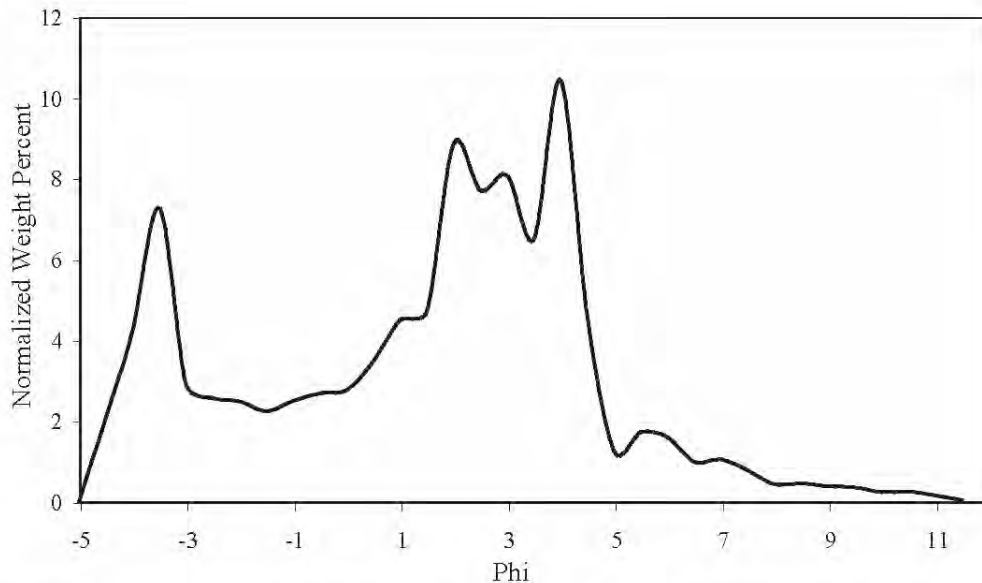


Figure 35: The grain-size distribution of Toba Cafe from Tecuitlapa maar, 15 km southwest of Tepexitl.

b. Componentry Categories

Grains in the Tepexitl deposits can be grouped into three main categories: juvenile, aggregate, and lithic clasts. The juvenile material consists of stony rhyolite, pumiceous rhyolite, obsidian, and juvenile. Aggregate grains are those that are larger in grain size than the components they comprise and include accretionary lapilli, armored lapilli (coated clasts), fragmented juvenile breccia, and cylindrical aggregates. Lithic material consists of stony lithic clasts, lithic crystals, iron-altered clasts, and lithic bubble shards.

It should be noted that recycling of clasts (e.g. Houghton and Smith, 1993; Dellino and La Volpe, 2000) is likely ubiquitous in tuff rings. A juvenile grain that is fragmented and ejected in explosion 1 but falls back in the vent and is re-erupted and physically deposited during explosion 2 is a recycled clast, but can look identical to a true juvenile grain from explosion 2 (either actively or passively fragmented). Because of these complications and for the purposes here, a juvenile grain is any counted, fragmented clast of Tepexitl magma, regardless of the length of time between fragmentation and deposition. This difficulty cannot be avoided but should be considered when looking at ash componentry, distribution, and morphology with the intent of understanding fragmentation.

A Toba Café sample taken from Tecuitlapa maar compares favorably to the lithic componentry categories and percentages of Tepexitl samples (Figure 36). The same grain types and similar percentages were observed at Tecuitlapa as were seen in Tepexitl deposits, strong evidence that the same saturated sediments pervasive in the Serdán-Oriental Basin directly underlie Tepexitl tuff deposits. Differences in component

percentages are likely related to the distance between Tecuitlapa and Tepexitl (15 km) and their relative position to source material and differences in local depositional environments.

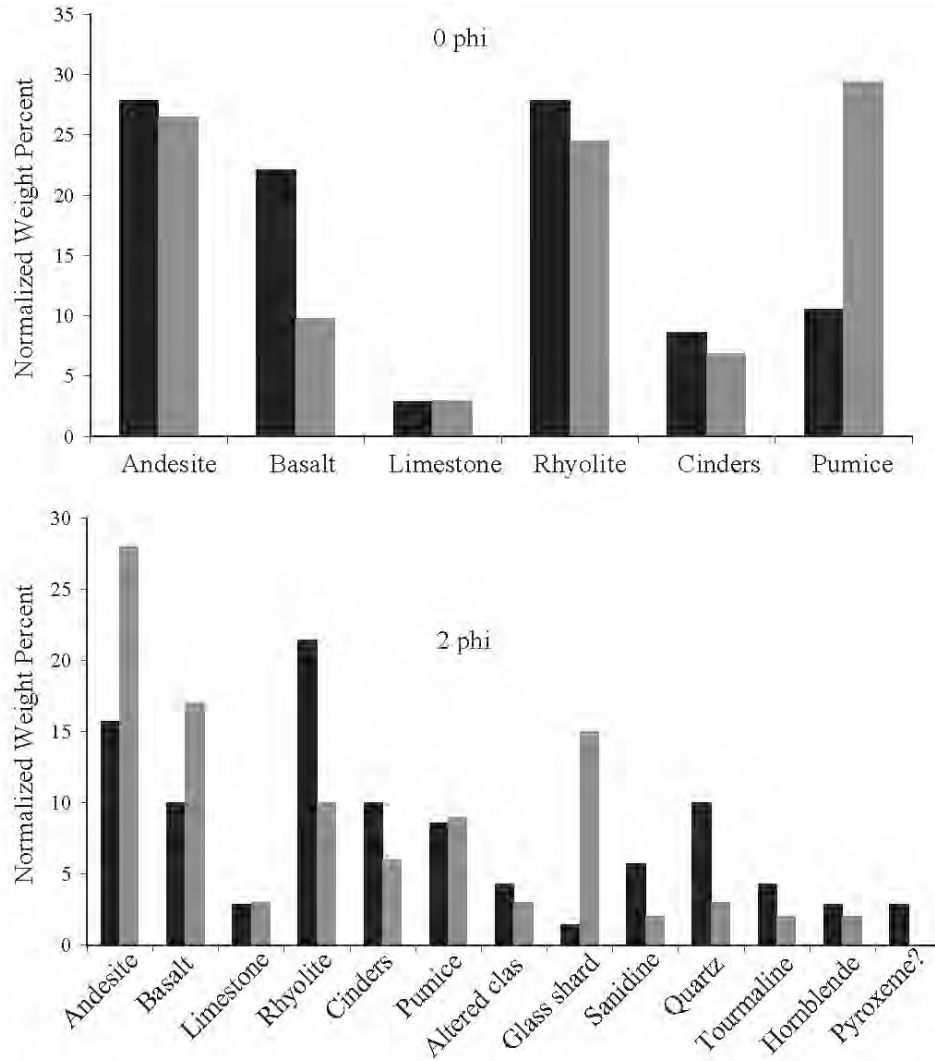


Figure 36: A comparison of 0-phi and 2-phi componentry of average lithic clasts abundances from Tepexitl Section 2 deposits (black bars) and Tecuitlapa Toba Cafe grains (gray bars).

Juvenile

Stony Rhyolite

Stony rhyolite grains are sub-rounded to angular, light to medium gray in color, and dense to poorly vesicular (<1 to 20% vesicles – finely vesicular) with dominantly blocky grains and minor wedge to flaky shapes. Luster varies from dull to sugary to vitreous, and grains commonly have surficial pitting and/or minor micro-vesicles. Lath-shaped biotite crystals and sanidine/quartz phenocrysts are apparent in all samples (3-7 volume%).

Pumiceous Rhyolite

In the 0- and -2-phi fractions, pumiceous clasts are light gray to off-white and mostly sub-rounded with > 30% vesicles (“coarsely” vesicular). They have a dull to sugary luster and, like the stony rhyolite, contain lath-shaped biotite crystals and sanidine/quartz phenocrysts (3-7 volume%). The vesicles are generally poorly developed (micron-scale) and do not appear to coalesce very commonly. In the 2-phi grain counts, it was not possible to distinguish stony rhyolite from pumiceous rhyolite, so all such clasts were grouped together in the stony rhyolite category (the dominant juvenile clast in the 0 and -2 phi grain sizes). The 2-phi grains are translucent with a lacy appearance, scalloped edges, and fine vesicles and/or surficial pitting.

Obsidian

Obsidian is composed of light gray to black, dense, flaky to blocky fragments with a vitric luster, smooth edges, and no vesicles. All clasts have macroscopic biotite laths and quartz/sanidine crystals (3-7 volume%). The matrix of some grains has clear conchoidal fracture. In the 0 and -2 phi sizes, an average of 51% of the total obsidian component is mottled clasts, with intermingled rounded spots of clear and black glass. The boundaries

between the two colors of obsidian are sharp. Sub-mm flow banding is apparent in 18% of the clasts. Typically, the bands are of light and dark obsidian, but it is not uncommon for pumiceous bands to occur also with either light or dark bands. In the 2-phi samples, all obsidian grains were grouped together although rare mottled and banding textures are visible.

Juvenile crystals

Because Toba Café sediment contains abundant free crystals, including sanidine and quartz grains (Figure 36), distinguishing juvenile crystals from lithic crystals was a challenge. Juvenile sanidine and quartz had no characteristics that distinguish them from lithic crystals of the same composition (i.e., same shape, roundness, and textures).

Therefore, an estimate of the percentage of juvenile crystals present in a given sample had to be made. This was done by comparing lithic-rich samples from the lower sequence with lithic-poor samples from the upper sequence. The lithic-rich samples have much higher overall crystal percentages than the lithic-poor samples. Sanidine and quartz compose approximately 2-3% of the total componentry in all lithic-poor samples, whereas these crystals in the lithic-rich samples compose 15-20% of the total componentry. Therefore, it is assumed that the free quartz and sanidine concentrations in the lithic-poor samples are representative of average juvenile crystals percentages in the 2-phi size range.

Aggregates

Accretionary Lapilli

Accretionary lapilli are round balls of poorly consolidated very fine ash that break apart easily when probed. The fine-grained ash that makes up the accretionary lapilli is

dominantly composed of clear to slightly yellow, vitric fragments in the micron-size range.

Armored Lapilli (also called Coated Clasts)

Coated clasts are opaque, tan-yellow, dense round balls defined by a surficial “cement” that obscures the grain underneath. The cement is composed of clear to yellow, very fine vitric ash with flecks of black and red, and causes difficulty in identifying the composition of the affected grain. The coating is rarely removed by cleaning in an ultrasonic bath (described in Appendix 2), and even then removal only partially exposes the underlying grain (in that not all of the cement is removed). Based on grains that could be identified, juvenile grains, lithic clasts, and crystals are all coated-clast cores.

Cemented Tuff

Cemented tuff clasts are composed of well-indurated, fine- to coarse-ash, off-white vitric tuff. These fragments have flat to irregular surfaces, not spherical and rounded like accretionary lapilli, and commonly have broken, jagged edges. They are limited to coarser grain sizes (greater than 1- 2 phi) because the individual grain sizes that make up the aggregates are ash-sized particles in this size range. They survived sieving, which provides a qualitative measure of their hardness.

Fragmented Juvenile Breccia

Clasts of fragmented juvenile-lithic breccia are held together in a yellow cement, and are miniature versions of the large blocks found on slopes of the western inner crater.

Cylindrical Aggregates

Cylindrical aggregates are hollow, tube-like structures made of a very fine-ash cement, which is white in color and contains small fragments of crystals, juveniles, lithic clasts,

and glass. Some hollows have remnant organic material inside (non-charred roots and brown grass-like material), which are coated in a layer of very fine, sugary ash. The aggregates fine radially inward. They occur in grain sizes from -5 phi down to 0 phi.

Lithic grains:

Stony clasts

Stony lithic clasts are composed almost exclusively of resedimented volcanic grains from fluvial and eolian processes. The most abundant clasts seen (in all deposits) are rounded and weathered andesite, rhyolite, and basalt fragments. The andesite clasts are coarsely crystalline and range from gray to pink to red in color, with mm-scale feldspar and rare pyroxene phenocrysts. The basalt is sugary dark gray, olivine-phyric, and has a matte luster. Toba Café rhyolite grains are easily distinguished from juvenile rhyolite as they are light green to opaque, “dirty” looking and rounded, with abundant black microlites. Brown to black cinders with high vesicularity also occur throughout the sequence. A small percentage of clasts are weathered, yellow to gray to brown, rounded limestone grains. Acid tests in all analyzed phi sizes confirmed this identification. A highly vesicular, white, microlite-free pumice with rare yellow surfaces first occurs in L2. Rare rounded sedimentary conglomerate clasts are also found.

Iron-altered clasts (also called ‘Fe-clasts’)

Alteration gives these clasts an orange to red color. They commonly have mafic minerals with a strong red reaction rim.

Glass shards

These shards are thick Y-shaped bubble-wall shards to platy glass shards, and commonly have chipped edges, pitting and hackly fractures.

Minerals

Single mineral grains are ubiquitous in the 2-phi grain size. Quartz and sanidine crystals are the most abundant, although they were commonly difficult to tell apart unless conchoidal fracture or cleavage was observed. Other common minerals include translucent peridot-green to honey-colored prismatic crystals with a roughly 60-120 degree habit, commonly with internal black flecks (opaques), which may be olivine clasts. A fourth unidentified crystal is stubby to rounded, translucent, root-beer colored, and also has 60-120 cleavage. These are interpreted to be hornblende, the most common amphibole in the lithic clasts seen from the area. Rare garnet crystals are also observed.

c. Explanation for Plates 2-9

Plates 2 through 9 refer to each individual unit in the Tepexitl stratigraphy, and the reader is asked to refer to them in the following discussion, in which units are compared with the intention of identifying potential phreatomagmatic events. A brief explanation is given here of the various components seen in these plates. The stratigraphy for each unit from Section 2 (Plate 1) is shown for reference, with sample locations marked. In the text, sample locations are referred to by both their unit and their number. Grain-size distributions for each sample are shown on the right-hand side of the plate, in graph (A), with lines marked according to both facies (defined in the key) and sample number. Graphs (B) and (C) are dispersion and weight percent of the corresponding subpopulations, as calculated from the SFT program. Dispersion is a measurement of the width of the curve, measured as gamma in the SFT program (the formula and complete definition of this parameter are provided in Appendix 2). The data points in (B) and (C) are marked both by sample (number) and facies (shape of the symbol), also defined in the

legend. In order to distinguish samples from one another, each sample has a different symbol, but the shape always corresponds with facies, whether it is filled or not filled. The circled area in (B) encloses all grain-size subpopulations that fall within the “potential active particle range” – between 2 phi and 4 phi, with dispersion of -0.6 or higher. The circle in (C) indicates which of the subpopulations from the enclosed area in (B) represent >15 weight percent of the overall sample. Thus, the enclosed circle in (C) indicates samples whose fine-grained material may warrant closer inspection to discriminate potential fragmentation modes.

For the purposes of this study, R value was calculated as a quantification of the weighted average normalized gamma (or dispersion), as described in Appendix 2. A high R value correlates with a higher relative abundance of particles concentrated in narrow dispersion peaks in the fine ash range. However, as discussed above, the small grain size of Toba Café material created a challenge in separation of fine-grained juvenile fragmentation peaks from surficial resedimentation-related, fine-grained subpopulation distribution peaks. To identify potential phreatomagmatic deposits (defined as those with a high R value and associated production of juvenile fine ash, potentially through MFCI), R value is stratigraphically compared with corresponding changes in componentry.

For the 2-phi grain-size fraction, lithic clasts and total non-obsidian rhyolite grains are plotted stratigraphically. As the 2-phi grain size was too small to separate pumiceous fragments from stony rhyolite clasts, they were grouped together. For the 0-phi fraction, the stony rhyolite is plotted both as a combination curve (as in the 2-phi graph), and as individual componentry curves of pumice and stony rhyolite. Lithic grains are also plotted for comparison. For some of the deposits of facies AC, the 0 phi size was

dominated by accretionary lapilli. The stratigraphic section was corrected for these deposits so as to not introduce points generated from insufficient data. When discussing general trends in the following discussion, changes in 'lithic grains' refers to changes in the 2-phi category (as this is where lithic clasts are more abundant), unless otherwise indicated. Similarly, 'pumice' refers to the changes in 0-phi componentry, as pumice was not present in 2-phi fractions. The -2-phi sizes had very limited data points and thus were only useful in comparing the coarse-grained facies. As understanding fine ash fragmentation was the goal of this study, these -2-phi componentry graphs were not included in these Plates, but the raw data are included in Appendix 4. It should be noted that some componentry changes may not represent 'real' changes, but instead may reflect deviations within error. In general, any stratigraphic change greater than 10 wt% of a given component category is considered significant.

Normalized componentry graphs for each sample are also shown for the -2, 0 and 2 phi sizes, with each component designated by a different fill. The width of the bars relates to the number of components present within a given sample. White bars are also armored lapilli components. The -2-phi and 0-phi components in the unit graphs were adjusted to represent a normalized total of the grains that were counted (with a 200-grain count as 100%), as some fine-grained samples did not have 200 grains within these categories. Therefore, if fewer than 200 grains were counted for a particular sample, the total percentage of grains in comparison to a full count are indicated by the sum of the componentry bars for each category. All raw granulometric data are presented in Appendix 3 and all raw componentry data are in Appendix 4.

d. Data by Unit

LOWER SEQUENCE

Unit 1 (L1)

L1 deposits in Section 2 begin with 40 cm of a normally graded facies B1 deposit (Plate 2). Sample 1 was taken from the overlying 80 cm of facies T1ap – a stony-rhyolite-rich deposit with a low R value, lithic content, and obsidian content. The grain-size distribution of this sample is dominated (40 wt%) by a moderately broad subpopulation peak at 0 phi. This deposit is sharply overlain by a meter-thick sequence of planar, ‘dry’ facies T1 (sample 2), which is associated with a combination peak in lithic content (36 wt%) and pumice (31 wt%). R value and obsidian content increase from sample 1. This sample 2 deposit of T1 facies is overlain by a 1.1-m thick series of fines-rich, alternating T1 and B1 facies. Sample 3, a 1-meter-thick, poorly-sorted Bt deposit, sharply overlies this sequence and is associated with a peak in fine-grained obsidian (24 wt% in 2 phi). The overall componentry decreases in lithic content but corresponds with increasing R value. A 15-cm-thick deposit of AC facies (sample 4) overlies this Bt deposit and correlates with a peak in R value. Sample 4 contains coated clasts and an increased percentage of fine-grained stony rhyolite and 0-phi obsidian clasts. Lithic clasts continue to decrease in the overall componentry. This AC deposit is overlain by thin beds of facies B1 and T1. Samples 2 and 4 contain broken clasts of well-indurated fine-grained tuff. The percentage of narrow-dispersion, fine-grained subpopulations increase up-unit.

INTERPRETATION:

Sample 1 is T1ap facies, a deposit consistent with rapid surges. Its broad peak at 0 phi correlates with a minor compositional peak in obsidian. This event was followed by

more surge pulses containing exceptionally fines-rich material, which deposited pumice- and lithic-rich beds of facies T1 (sample 2). This deposit is the thickest fine-grained tuff deposit in the entire Section 2 stratigraphy, an important distinction, as large percentages of fine-grained material may indicate high-energy fragmentation processes were occurring during this time. The change in componentry from sample 1 to sample 2 suggests that a different process was operating during fragmentation and/or deposition of these samples. Sample 3 is a deposit of Bt facies interpreted to be a hybrid bed that resulted from a proximal explosion breccia deposited prior to significant sorting due to transportation. The peak in fine-grained obsidian may be related to quench fracturing (if water was present) or to a highly energetic fragmentation event of chilled magma. This is immediately followed by a fine-grained deposit (sample 4) that may be related to the settling of elutriated very fine ash. This sample contains the only coated clasts observed in L1. Pumice concentration appears to mimic changes in lithic concentration throughout this phase, both dominant in fine-grained beds.

Unit 2 (L2)

L2 deposits are thinly bedded with sharp contacts (Plate 3). The sequence begins with a very-thinly-bedded deposit of coarse-grained facies B (sample 1), the first fines-poor, well-sorted breccia deposit seen in the sequence. This deposit is rich in lapilli-sized obsidian and coarse-ash-sized stony rhyolite. It is depleted in pumice, and has lower lithic clast content and R value. Sample 1 is sharply overlain by 20 cm of T1 facies (sample 2), which corresponds to a peak in R value, lithic clasts and pumice, and a sharp decrease in stony rhyolite. Coated clasts are also present. The sample 2 deposit is overlain by 60 cm of facies B1, which grades into 15 cm of facies Bt, overlain by 20 cm of facies

Tlap and 40 cm of facies T1 with minor facies AC (sample 3), a progressively finer-grained sequence. Sample 3 has a peak in stony rhyolite, although pumice concentration is a trough. The grain-size distribution decreases in R value from sample 2 and lithic, obsidian, and coated clasts decrease in relative abundance. Sample 3 is overlain by a thinly-bedded deposit of facies B1, which is overlain by a veneer of facies T1, a thinly bedded facies Bt deposit (sample 4), and another veneer of facies T1. Sample 4 is associated with peaks in lithic clasts, obsidian (fine-grained), and pumice content, but has a trough in stony rhyolite and R value. This deposit contains coated clasts as well as abundant white, microlite-free, frothy, lithic pumice very unlike Tepexitl juvenile material, a component not observed in underlying deposits. Sample 4 is sharply overlain by a very thin bed of fines-poor B1 (sample 5), which is dominated by lapilli-sized obsidian clasts and fine-grained stony rhyolite. This sample also contains Fe-clasts. It is poor in coated clasts, and has troughs in fine-grained obsidian, lithic clasts, and R value and is sharply overlain by a thin veneer of facies AC (sample 6), which has a peak in R value and in fine-grained (2 phi) obsidian, lithic, and pumice concentrations. Immediately overlying sample 6 are thinly-bedded deposits of B1 facies (sample 7), with a low R value. This deposit has less pumice, lithic clasts, and obsidian than sample 6, and more stony rhyolite. Overlying sample 7 is a thin bed of facies AC and a thin bed of obsidian lapilli-dominated, fines-poor breccia (sample 8). The 2-phi fraction of sample 8 is dominated by a peak in stony rhyolite. Lithic clasts, fine-grained obsidian, and R value all have troughs and no pumice was observed. Sharply overlying this breccia is a thin bed of facies AC (sample 9), which exhibits an increase in R value and lithic clasts, with moderate increases in relative pumice and fine-grained obsidian. It has abundant coated

clasts. This AC deposit is sharply overlain by 50 cm of facies B1, which is overlain by a 10-cm deposit of facies T1, followed by a very thin bed of facies B1 (sample 10), which has a decrease in R value. Lithic grains in sample 10 are more abundant than in sample 9. Sample 10 is also poor in pumice, and has lower stony rhyolite and coated clast content, although the lapilli are mostly stony rhyolite. The sample 10 B1 deposit is sharply overlain by a 40-cm-thick deposit of dark brown, fine-grained facies AC (sample 11), which is also associated with sharp peaks in R value and lithic content. Coated clasts, but no pumice, are associated with this deposit. Narrow-dispersion subpopulations are present in Stage 2 and Stage 3 deposits, although the fine-grained subpopulations of sample 11 (Toba Café accretionary lapilli) also have narrow dispersions.

INTERPRETATION

The fines- and lithic-poor breccia deposit at the base of L2 (sample 1) is consistent with a fall-deposit from explosion of quenched magma and marks a change in the eruptive sequence from dominantly 'dry' tuff deposits to 'wetter' tuff deposits with interbedded thin breccia beds. L2 was sampled in detail because of: 1) the abrupt sedimentologic variability associated with the three-stage deposits; and 2) highly deformed tuff is consistent with an increase in water:magma ratio from L1 – and potentially include grains fragmented as a result of phreatomagmatism. The three-stage deposits identified in the field have repeating patterns in componentry as well as grain size. Stage 1 deposits have high concentrations of lapilli-sized obsidian and ash-sized stony rhyolite, but are poor in lithic clasts. They are the coarsest-grained deposits of L2, and have low R values. They are also the only beds in L2 associated with Fe-clasts, which are interpreted to indicate that heat from the magma was transferred to the

saturated sediments. These beds are most consistent with fall deposits, but may also be the traction-carpet deposition of high particle density, stratified surges. Included in this category are samples 1, 4, 8, and 12. Stage 2 deposits immediately overlie Stage 1 deposits and consist of finer-grained deposits of T1 to AC facies, the result of surges +/- fall. They have peaks in lithic grains, pumice, and R value and are commonly associated with sharp peaks in coated clast abundance. Stage 2 deposits include samples 2, 6, and 9. Finally, Stage 3 deposits have an increase in stony rhyolite and a decrease in R value. They vary in grain size and depositional mechanism (likely from surges and falls), but always overlie Stage 2 deposits. Stage 3 deposits include samples 3, 7 and 10. Three complete three-stage process deposits were sampled: 1) samples 1-3; 2) samples 5-7; and 3) samples 8-10. This cycle of deposits represents a repetitive succession of discrete events, each with very different characteristics. The variations in componentry of these series may be the result of sorting due to transportation (fall versus surge) and/or may represent a distinct style of eruption.

Sample 4 componentry fits into Stage 2, and may represent a fifth such cyclic event that was poorly sampled (with the underlying B1 bed as a potential Stage 1 deposit). However, sample 4 is a more poorly sorted Bt deposit that is coarser grained and thus has no peak in R value, and may be a hybrid bed resulting from near-vent explosion breccia, deposited prior to sorting of coarse and fine grains. Sample 4 is also associated with the introduction of lithic pumice, which is consistent with the Quetzalapa pumice from Los Cumbres. Quetzalapa pumice is white, highly vesicular to fibrous with 1-10% microphenocrysts of plagioclase and light brown to gold biotite set in a glassy matrix (Rodriguez et al., 2002). The introduction of this pumice is most consistent with a

deepening eruption center that bored through Toba Café. If the Quetzalapa pumice was deposited at the same time as the Tepexitl eruption, it would be expected to accumulate as distinct beds or pods of material within Tepexitl deposits, a texture not observed. Sample 11 is interpreted to represent dominantly accretionary lapilli of Toba Café material (more fine-grained and darker brown than juvenile accretionary lapilli with a sharp peak in lithic content) and may be the result of a phreatic eruption through saturated lithic sediments. The narrow subpopulations of this sample may reflect a high abundance of Toba Café material in narrow-dispersion subpopulation peaks. Thus, although L2 contains deposits from repeated three-phase events, occasional variations in depositional mechanisms resulted in deposits such as samples 4 and 11.

Unit 3 (L3)

L3 begins with a thick deposit (1.3 m) of facies B1 (sample 1), associated with abundant Fe-clasts and obsidian lapilli (Plate 4). Sample 1 is associated with a trough in lithic clasts and R value and an increase in fine-grained stony rhyolite. Pumice also increases from immediately underlying deposits. Sharply overlying the facies B1 deposit is a 2.1-m-thick sequence of deformed, fine-grained facies T1 deposits with intermittent laminae of coarser ash. Samples at the base, middle, and top of the fine-grained package were collected. Sample 2 shows a peak in lithic and pumice grains and also contains coated clasts. Sample 3 was taken only 15 cm above sample 1 and includes a coarse-ash lamina. Despite its close stratigraphic proximity to sample 2, the composition shows a trough in pumice and 0-phi lithic grains, with an increase in 0-phi stony rhyolite fragments. Coated clasts and 2-phi lithic grains are present in the same percentages as in sample 2. The top of the L3 (sample 4) is the most lithic-rich sampled bed of the entire

stratigraphic column, at 53 wt% of the 2-phi grain size. This sharp peak in lithic clasts correlates with a peak in pumice and R value and a decrease in coated clast abundance. All fine-grained samples have narrow dispersion subpopulations between 2 and 4 phi, although sample 3 has the highest wt% narrow-dispersion subpopulation at 2 phi.

INTERPRETATION

The deposits of L3 are consistent with deposition by a fall/blast, followed by pulsatory surges. The composition of sample 1 (B1-facies deposit) is consistent with the Stage-1 deposits described for L2, and the T1 facies tuff deposits (samples 2-3) are consistent with Stage-2 deposits. However, no Stage-3 deposit is present and sample 4, although rich in lithic clasts, contains no coated clasts. Additionally, the B1-facies deposit is thicker than breccias of L2. The tuff deposits of L3 are also thicker and finer-grained than the tuff deposits of L2. Lithic content increases within the tuff, from sample 2 to sample 4, with the sample 4 containing the highest concentration of lithic grains of all samples throughout the stratigraphic section. The lack of coated clasts in sample 4 is significant, as this suggests that formation of coated clasts is not directly related to lithic concentrations. The increase in weight percentage of the 2-phi subpopulation in sample 4 is notable because it correlates with a 2-phi fraction that is rich in lithic grains and may reflect a dominant subpopulation of the local Toba Café.

The similarity in L3-deposit componentry to the three-stage deposits of L2 indicates similar eruptive processes occurred during deposition of L2 and L3. However, L3 deposits have unique characteristics that mean the eruptive conditions during deposition of L2 and L3 were not identical. The fine-grained nature and thickness of

these deposits may be connected to an increase in efficiency in fragmentation of juvenile material, although it is possible that phreatic eruptions also occurred.

Unit 4 (L4)

Sharply overlying the fine-grained deposits of L3 is a 50-cm-thick deposit of facies B1, which contains abundant large obsidian and lithic blocks (sample 1; Plate 5). Sample 1 has sharp decreases in lithic content and R value from the top of L1, but retains the same pumice concentrations as the deposits at the top of L1 and increases sharply in stony rhyolite. It is dominated by one subpopulation – a broad peak at -1.3 phi (61 wt %). The 4+ meters of deposits overlying this basal breccia are dominated by B1-facies deposits but have interbedded deposits of facies T1ap and T1. Sample 2 was taken from another B1-facies deposit 1 m above sample 1. In between the two B1 deposits is a sequence of facies T1ap. The componentry of sample 2 is not very different from sample 1, except for a slight increase in stony rhyolite and a slight decrease in pumice. However, it has a dramatic decrease in lithic grains (from 53 wt% at the top of L1 down to 16 wt% in sample 2). Sample 2 has polymodal, broad-distribution subpopulations. Sample 3 was taken from a third B1 deposit, another meter above sample 2. It also shows a slight increase in stony rhyolite whereas pumice is nearly absent. Like sample 1, this deposit is dominated by one moderately broad subpopulation peak at -1.4 phi (63 wt%).

Sample 4 was taken from a fine-grained, thin bed of T1 facies approximately 60 cm above sample 3, the first T1-facies deposit in L4. Sample 4 has a sharp increase in R value and pumice, but only a very slight increase in lithic concentration. Stony rhyolite decreases in abundance and coated clasts are observed. Overlying this T1-facies deposit is a sequence of thinly interbedded facies B1 and T1, of which the upper T1 deposit was

sampled (sample 5). R value, coated clasts, pumice, and stony rhyolite decrease from sample 4 and lithic concentration peaks at 24 wt%. Stratigraphically above this T1 deposit is a lamina of facies AC, which is overlain by a normally-graded B1 deposit that becomes more ash-rich toward the top (grading into facies Bt). On top of the Bt deposit is a very thin deposit of facies T1 (sample 6). Sample 6 has peaks in R value, stony rhyolite, and coated clasts with a trough in lithic content. There is an increase in pumice from sample 5. These three fine-grained samples (4-6) all have a high concentration of material in narrow-dispersion subpopulations between 2 and 4 phi.

Sharply overlying sample 6 is a 4.3-m breccia sequence. The base of this sequence is facies B1 (sample 7), which has peaks in pumice and lithic clasts and troughs in stony rhyolite and R value. Coated clasts are absent in this deposit. It is dominated by one moderately broad peak at -0.7 phi (55 wt%). The top of this breccia sequence (sample 8) decreases in pumice content but is otherwise compositionally the same as sample 7. Its dominant subpopulation is a moderately broad peak at -2.3 phi (34 wt%). The 80 cm above the thick breccia sequence is interbedded facies B1 and AC. The final AC-facies deposit (sample 9) has more abundant lithic clasts and a higher R value. Accretionary lapilli dominate the grain-size distribution coarser than 1 phi, below which they are broken into their ash components. Thus, the two largest subpopulations reflect the size of the accretionary lapilli and the dominant grain size of the formerly agglomerated ash grains, respectively: a moderately broad peak at -1.6 phi (21 wt%) and a narrow peak at 3.8 phi (21 wt %). The final B1-facies deposit, which sharply overlies sample 9, has a peak in lithic grains (26 wt%), but a decrease in pumice and R value. This deposit also has a high concentration of lapilli-sized obsidian clasts.

INTERPRETATION

Samples 1 – 3 are B1 deposits and show a progressive decrease in pumice and lithic concentrations, with deposits becoming progressively more concentrated in stony rhyolite. This sequence is consistent with a magmatic eruptive pulse that was stratified with respect to volatiles (i.e. – bubbles were concentrated at the top of the magma plug, driving fragmentation and ejection of underlying denser, less degassed magma). The relatively well-sorted deposits of 1 and 3 (a single Gaussian distribution accounts for >60% of the grain size variations) are consistent with fall deposits. The decrease in lithic grains is the result of little to no lithic material being incorporated into the eruptive system as new juvenile ash is being created. This situation could result from 1) a rapid shallowing of the eruptive focus (less overlying fill to erupt through) and/or 2) a higher percentage of juvenile material being created than in underlying units and/or 3) rapid explosions that initially clear the overlying crater fill and subsequently limit the amount of fallback that becomes recycled in subsequent blasts.

Samples 4-6 are representative of the fine-grained deposits seen at the base of L4, likely the result of rapid pulsatory surges, and contrast sharply with the underlying B1-facies deposits. They are similar to the Group-2 deposits in L2, but they lack the strong associated peaks in lithic concentrations. All three samples contain coated clasts. However, the highest lithic concentration (in sample 5) correlates to troughs in pumice and R value. It is possible that these fine-ash deposits represent a similar eruptive mechanism as was operating during deposition of L2, but under different crater conditions - if fewer lithic clasts are in the vent area, fewer lithic clasts will be present in the deposits. The non-sampled breccia deposits in this sequence may well be Group-1-

and Group-3 deposits, but this cannot be assumed. The fine-grained deposits may also be the result of temporal overlap of different eruptive mechanisms operating from different vents at the same time.

Samples 7, 8, and 10 represent the coarse-grained deposits of the second half of L4, the result of an especially voluminous fragmentation event that deposited large percentages of coarse-grained juvenile material. Such a deposit may represent a column collapse site. Similar to the series at the base of L4 (samples 1-3), this series decreases steadily in pumice concentration, consistent with magmatic explosions of a body stratified with respect to degassing and vesicle content. However, in contrast to the underlying coarse-grained series, this set of samples shows a steady increase in the lithic clast content, implying that more lithic material is being introduced to the system. Although sample 9 is of facies AC and shows an increase in R value, it follows the trend in compositional changes that are observed in the coarser-grained samples 7, 8 and 10.

Unlike in L1-L3, increases in pumice concentrations in L4 do not mimic increases with lithic concentration. This becomes apparent in sample 1, in which the lithic component decreases but the pumice concentration stays the same. Samples 2-7 show offset peaks of pumice and lithic clasts, rather than peaks that mimic each other: pumice content peaks in samples 4 and 7 whereas lithic concentration peaks in sample 5. In L1-L3, pumice and lithic clasts were concentrated only in the fine-grained beds (suggestive of one mechanism controlling the two abundances), but high pumice concentrations occur in both coarse- and fine-grained L4 beds, regardless of changes in lithic concentrations. This difference implies that pumice concentrations in L4 are influenced by a separate mechanism than that which controls the lithic concentrations. Additionally, the strong

decrease in lithic concentrations from the top of L3 to the bottom of L4 suggests that a change in eruptive activity occurred between the deposition of L3 and the deposition of L4.

Unit 5 (L5)

Sharply overlying the block-rich, coarse-grained deposits that characterize L4 is a series of Tlap-facies deposits with thin laminae of interbedded coarse-grained material (Plate 6). Sample 1 was taken from one of the basal coarse-grained laminae and shows a lapilli-obsidian- and fine-ash-stony-rhyolite-rich deposit. Sample 1 is depleted in pumice and has a trough in lithic concentration. Sample 2 was taken from the top of the basal Tlap deposit, only 60 cm above sample 1. Sample 2 shows an increase in pumice, a peak in lithic concentration, and a trough in fine-grained stony rhyolite. Coated clasts are 10 wt% of the sample. Sharply overlying sample 2 is a 20-cm thick, coarser-grained Tlap-facies deposit that grades into fine-grained facies Tl (sample 3). Sample 3 has the same concentration of pumice as in sample 2, but has a trough in lithic concentration and a peak in R value. Stony rhyolite increases in abundance over sample 2. Sample 3 is the only deposit of L5 to have abundant material in fine-grained narrow-dispersion subpopulation peaks. Sharply overlying sample 3 is a poorly-sorted breccia sequence, with reversely graded Bt-facies deposits grading into coarser-grained Bl-facies deposits (sample 4). In sample 4, pumice content has decreased, lithic clasts peak in concentration, stony rhyolite continues to increase in concentration, and R value has decreased. Stratigraphically above sample 4 is a 1-m series of interbedded facies Bl and Tl. The unit ends with a 1.3-m sequence of Tlap facies (sample 5). Sample 5 shows an increase in pumice, stony rhyolite, and R value but a decrease in lithic concentrations.

INTERPRETATION

All deposits of L5 are consistent with deposition from multiple, density-stratified, pulsatory surges and minor fallout. Sample 1 fits the description of Group-1 deposits, described in L2. Similarly, sample 2 is a perfect fit to a Group-2 deposit from L2, with a peak in pumice mimicking a peak in lithic grains. Sample 3 shows increasing stony rhyolite, typical of Group-3 events, but also has higher pumice concentrations even though lithic concentration has decreased. In contrast to the patterns of L2, this pattern is much like the pumice trend of L4, in which pumice concentration is reflective of an independent, volatile-related stratification of the magma plug and did not correspond to changes in lithic grains. However, the subpopulations of sample 3 appear to reflect the highest fragmentation energy of L5, which could be due to either magmatic or phreatomagmatic processes. Sample 4 of L5 is also consistent with two mechanisms for peaks in pumice and lithic concentrations, as lithic clasts again increase, but pumice decreases. The opposite trend occurs with sample 5. Overall, the composition of L5 becomes gradually richer in stony rhyolite upward, which corresponds to a gradual decline in the overall abundance of lithic grains (down to 15% in sample 5). The data for this unit are consistent with a change in eruptive style from the underlying L4, with samples 1-3 similar to the three-stage deposits of L2. Overlying these deposits, the eruptive style is consistent with magmatically-triggered surges.

UPPER SEQUENCE

Unit 1 (U1)

The coarse-grained, block-rich breccias at the base of U1 sharply overlie the finer-grained deposits of L5 (Plate 7). The basal 1 m of U1 is interbedded medium-

bedded deposits of facies B1 and laminae of facies T1, becoming progressively finer-grained upward. Sample 1 was taken from the finest-grained T1 at the top of this sequence. Pumice content peaks at this location (30 wt%), whereas lithic clasts are lower in abundance than at the top of the lower sequence (down to 12%), and stony rhyolite increase. R value also has a peak in sample 1 from the top of the lower sequence. Overlying this T1 deposit is another 80 cm of facies B1, which is in turn overlain by 20 cm of facies T1 (sample 2). In sample 2, R value, pumice, and lithic concentrations are lower, but stony rhyolite concentration is higher than in sample 1. Immediately and sharply overlying sample 2 is a fines-poor, distinctive facies-B deposit (sample 3), which grade into more poorly sorted deposit of facies Bt (sample 4) and is capped with another distinct coarse-grained B deposit.

Sample 3 shows sharp changes in componentry from the underlying U1 deposits, with a notable increase in lithic concentration (from 13% to 33%) and strong decreases in stony rhyolite and pumice concentrations. Coated clasts are also prominent in this sample, as are lapilli-sized obsidian clasts. Sample 4, in contrast, is much like the componentry of samples 1 and 2. Lithic clasts have again decreased to 20%, pumice concentration peaks, and no coated clasts are observed in the deposit. On top of this breccia sequence is a thin facies-AC deposit, which is overlain by another breccia sequence (1.3 m), in which a deposit of facies B1 (sample 5) grades into facies Tlap, which is capped with a facies T1 bed (sample 6). Sample 5 has less lithic clasts and pumice, and more stony rhyolite than sample 4. Sample 6 has even more abundant stony rhyolite than sample 5, and is lower in pumice and lithic concentrations. It also peaks in R value. Unique to this sample is the presence of cylindrical aggregates, not observed in

any deposit beneath it. Overlying sample 6 is a 3.4-m series of B1-facies deposits, both inversely and normally graded, with intermittent fine-grained laminae. Sample 7 was taken toward the top of this series. The 2-phi grain size is composed entirely of stony rhyolite, with no lithic clasts. Pumice is slightly more abundant than in sample 6 and R value is lower. Only sample 1 has a high percentage of narrow dispersion fine-grained subpopulations. The coarse-grained deposits have dominantly narrow dispersion subpopulations in the lapilli size fraction.

INTERPRETATION

The breccia units of U1 have strong coarse-grain-dominant Gaussian curves consistent with some degree of sorting, the likely result of a fall-dominated depositional mechanism. These falls were punctuated by fine-grained surges that deposited the fine-grained beds. The componentry of U1 deposits shows a gradual decrease in lithic concentration (from 15 wt% to 0 wt%), irrespective of facies. The final breccia (sample 7) is completely devoid of lithic grains, consistent with an eruptive center above crater fill (no lithic clasts being incorporated into the pyroclasts) and implies that the fragmentation center shallowed over the course of eruption of U1. Pumice concentration peaks in sample 1, and becomes progressively less abundant up-section (with the exception of sample 3), a pattern consistent with a magmatically-driven eruption of a volatile-stratified plug, similar to that described in L4 and L5. The anomalous peak seen in composition of coarse-grained breccia sample 3 contains characteristics of both Stage-1 and Stage-2 deposits: it contains both coarse-grained obsidian like Stage 1, as well as the fine-grained lithic and coated clasts like Stage 2. Another difference between this deposit and those described earlier is the decrease in pumice concentration, which is a

contrast to the pumice peak observed in Group 2 deposits. These differences are significant, and suggest that sample 7 does not represent a three-stage deposit.

Unit 2 (U2)

The lowest 3.2 m of U2 are poorly-sorted facies-Bt deposits separated by laminae of facies AC (Plate 8). Sample 1 was taken at the base of this sequence and sample 2 at the top. Sample 1 shows an increase in pumice from the top of U1 and a slight increase in lithic clasts and R value. Sample 2 shows a very small decline in stony rhyolite and pumice and a slight increase in lithic concentrations. Sharply overlying these Bt-facies deposits is 1 m of facies Tlap (sample 3), which has slightly higher lithic concentrations and R value than sample 2. Pumice and stony rhyolite concentrations are slightly lower. Sample 3 grades into a thin bed of facies Tl, which is sharply overlain by a breccia sequence that ends with a 40-cm-thick, fines-poor, coarse-grained facies-B deposit. On top of this breccia is 20 cm of fine-grained facies Tl – the thickest laminated tuff deposit of U2 (sample 4). Sample 4 is devoid of pumice, but has more lithic clasts (17 wt%) than other samples in this unit, as well as a higher R value.

Overlying sample 4 is a thin bed of facies Bt, which underlies a 1-m deposit of facies Tlap/ AC (sample 5). The coarser-grained components (-2 and 0 phi) are dominated by accretionary lapilli, but the 2-phi componentry shows a trough in stony rhyolite grains. Lithic concentrations remain about the same as in sample 4, but R value decreases. This deposit contains cylindrical aggregates – similar to those found at the top of U1. Sharply overlying the sample 5 deposit is a coarsening-upward breccia sequence that ends with a 60-cm-thick fines-poor, coarse-grained B deposit (sample 6), similar to the one in the middle of U2. Sample 6 has a high concentration of stony rhyolite clasts (88 wt% in 2

phi) and an increase in the percentage of pumice from sample 5. Lithic concentration and R value are lower than in sample 5. Immediately overlying sample 6 is a facies AC/Tl bed (sample 7), which shows an increase in R value, pumice and lithic concentrations and a decrease in stony rhyolite compared with the underlying breccia,. This final deposit also contains cylindrical aggregates. Above sample 7 is a 15-cm Bt deposit that grades into a thin soil layer and marks the end of Section 2. Only the facies-Tl deposits (samples 4 and 7) have significant material concentrated in narrow-dispersion, fine-grained subpopulations peaks.

INTERPRETATION

The beds of U2 are consistent with deposits of both falls and surge (thinly laminated deposits from pulsatory surges and thick, fines-poor breccias from falls). Samples 1 and 2 are both of facies Bt, poorly-sorted deposits punctuated by facies AC, that have strong Gaussian coarse-grained distributions and fine-grained tails. This type of deposit is consistent with a hybrid deposit of fall and surge components, which suggests that two depositional mechanisms were operating simultaneously. The two main differences between samples 1 and 2 are that sample 2 has less abundant stony rhyolite and is coarser overall than sample 1. Stony rhyolite and pumice continue to decrease through surge deposit samples 3, 4, and 5, accompanied by a gradual increase in lithic grains. The changes in pumice show a trend from more volatile-rich to less-volatile-rich with increasing stratigraphic level, regardless of average grain size of the deposit. This is consistent with magmatic eruption of a volatile-stratified plug. However, the increase in lithic grains means a second mechanism is operating that is introducing more lithic clasts

into the eruptive system. Sample 6 has a strong coarse-grained, stony-rhyolite-dominant Gaussian distribution, consistent with a fall deposit from magmatic eruption.

Unlike the lithic-free final deposit of U1, the deposits of U2 have varying amounts of lithic grains. The R value correlates well with lithic clasts, which become gradually more abundant during deposition of U2, peaking at samples 4 (17 wt%) and 7 (15 wt%). This is still a low percentage, especially when compared to 53 wt% lithic content at the top of L3, but means that lithic grains are again being incorporated into the eruptive system, likely as recycled crater fill from a lower eruption center. The similar patterns observed in both R value and lithic concentration implies that a peak in lithic grains in the 2-phi fraction corresponds to an increased percentage of fine-ash-sized lithic grains smaller than 2 phi, reflected in the narrow-dispersion subpopulation peaks. Both samples 4 and 7 are fine-grained beds that sharply overlie thick, fines-poor, coarse-grained breccias rich in stony rhyolite clasts. Perhaps the segregation of lithic grains into the fine fraction is a result of a sorting by transportation method, with fine-grained material carried by ground-hugging surges.

Unit 3 (U3)

U3 is seen only on the crater rim to the west (Figure 3; Plate 9). Sample 1 is of the surface-expression explosion breccia from mid-inner crater at the location seen in Figure 25. Sample 1 is of a clast-supported lapilli-block-sized stony rhyolite breccia, and the componentry of the matrix is also dominantly stony rhyolite. Lithic clasts and pumice are negligible in percentage, and obsidian is between 6 and 15 wt%. The rest of the samples were taken from Section 13, near the western crater rim. Sample 2 is the lowermost bedded facies-B deposit associated with U3 (40-cm thick) and is the most pumice-rich

sample of U3 (between 33-42 wt% in the -2- and 0-phi fractions, respectively). This sample is also obsidian-rich, especially in the lapilli-size range. The 2-phi ash matrix is dominated by stony rhyolite. Overlying sample 2 is the second bedded B-facies deposit (sample 3), which has lower pumice and obsidian contents than sample 2. Pumice is 14-22 wt% (in the -2- and 0-phi sizes) and obsidian is a minor component in sample 3, which is dominated by stony rhyolite, both as lapilli-sized clasts and within the matrix.

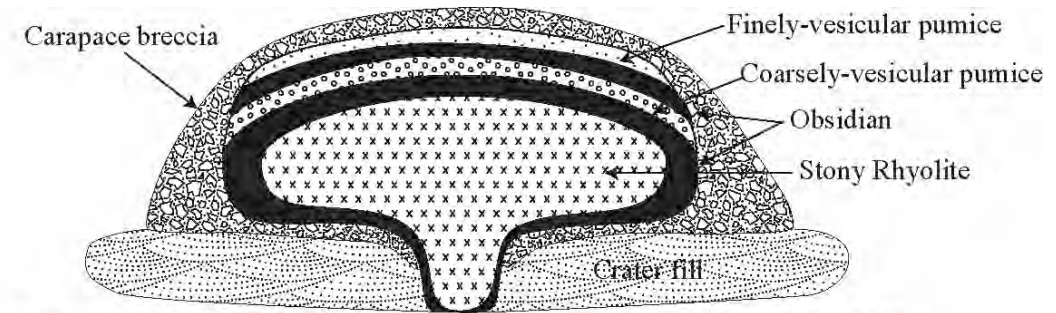
Overlying sample 3 is a 20-cm-thick facies-AC deposit (sample 4), with unusually large accretionary lapilli that are well-indurated. The grain-size distribution data for these accretionary lapilli include the lapilli themselves in grain sizes larger than 1 phi, with smaller grain sizes composed of disaggregated fine ash. The matrix is dominantly stony rhyolite, but also contains a high proportion of obsidian (29%) and minor coated clasts.

Sharply overlying sample 4 is a 3-m-thick B-facies deposit, the coarsest-grained breccia of the entire stratigraphic sequence (sample 5), which is dominated by angular stony rhyolite lapilli clasts. The matrix of this deposit is also dominated by stony rhyolite, but does contain pumice grains, which increase in abundance from the -2 phi to the 0-phi size range (9 to 22 wt%). Obsidian is a minor component, but also increases in abundance with decreasing size. Overlying sample 5 is a series of three thinly-bedded B-facies deposits (each separated by thin tuff deposits). The lowest of these breccias is represented by sample 6 and the uppermost breccia is represented by sample 7. Sample 6 contains the most obsidian of all samples through U3, with 31-34 wt% in the -2-phi and 0-phi sizes, respectively. Pumice is a minor component, present at only 11-12 wt%. The matrix is mostly stony rhyolite, but also contains 19% obsidian. The uppermost deposit seen at Tepexitl, sample 7, is a fine-grained breccia with abundant yellow-coated clasts. Coated

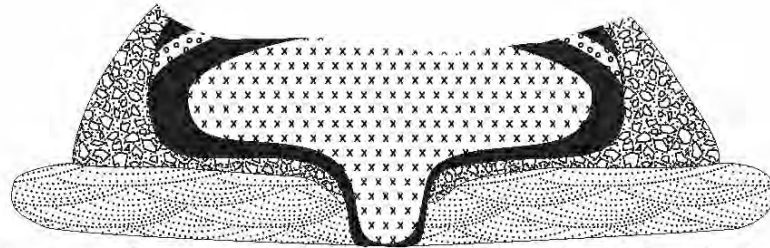
clasts dominate the -2-phi and 0-phi size populations, at 64 wt% and 47 wt%, respectively. Obsidian is slightly less abundant than in sample 6, although is still a significant component. Pumice and stony rhyolite are present in very small percentages. The matrix, however, has less coated clasts (26 wt%) and more stony rhyolite (37 wt%). Obsidian is also a major component (25 wt%). Perhaps the most interesting aspect of this sample is the very small percentage of fragmented breccia clasts in the -2 phi size range, which are smaller versions of the large breccias blocks found as western inner-crater float blocks.

INTERPRETATION

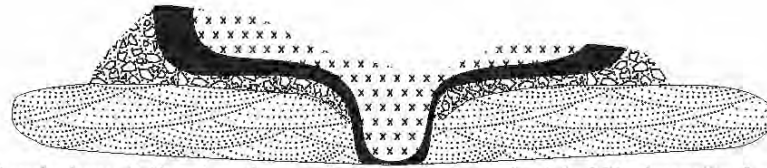
The sequence observed in the U3 deposits is consistent with explosion of a small dome with internal textures as described in Manley and Fink (1987). The deposits from top to bottom represent an “upside-down” dome, with the stratigraphically lowest samples representing the uppermost part of the dome (Figure 37). Samples 2 and 3 are the lowest samples and show a progressive decrease in pumice and obsidian, typical textures found when moving from the surface of a dome toward its interior. Sample 5 is the thickest deposit and the most stony-rhyolite-rich, two characteristics consistent with eruption of a dome interior. Samples 5 and 1 are the most similar in composition of all the breccia deposits, although sample 5 has slightly more pumice clasts than sample 1. These observations are consistent with a poorly energetic explosion of a voluminous dome interior. As the lateral equivalent of the slope-side explosion breccia (sample 1), it is reasonable to expect a relative enrichment of pumice in sample 5, due to the decreased density of pumice when compared to stony rhyolite. Sample 6 is obsidian-rich, consistent with the basal obsidian observed in dome cross-sections. Sample 7 is slightly unusual, in



A. Cross-section through the textures of a small dome prior to deposition of U3.



B. Morphology following the explosions that resulted in U3, deposits 2 and 3.



C. Morphology following the explosions that resulted in U3, deposits 5 and 1 (the explosion breccia covering western inner crater slopes).



D. Morphology following the explosions that resulted in U3, deposit 6.



E. Morphology following the explosions that resulted in U3, deposit 7.

Figure 37: Idealized model of step-by-step retrogressive dome explosions (A-E), based on componentry analyses, which are assumed to have resulted in the deposition of U3 and complete dome removal. Dome facies are based on Manley and Fink (1987). Please note that an off-center explosion center would result in a similar, but asymmetrical, final morphology.

that it contains fragmented breccias and hardened surficial yellow coatings on many of the clasts. One possible interpretation of these textures and components is that this small deposit represents a final explosion through the lowermost breccia of the dome and underlying hydrothermally altered and cemented material.

The paucity of lithic clasts throughout the deposits indicates that both dome growth and subsequent dome explosion occurred from above the crater floor. However, the accretionary lapilli of sample 4 indicate water was present in the eruptive system. The source of this water could be either weather or groundwater related. The tuff layers between each breccia deposit in U3 indicate that explosion occurred by distinct blasts, which correspond to componentry changes. The rapid changes in juvenile componentry suggest that the explosion center migrated progressively through the textural sequence from the dome top to the dome base. The presence of basal obsidian and breccia fragments are strong indicators that the dome was completely destroyed, with any evidence of it covered by crater fill. Peperitic textures within these breccia clasts (Chapter 2) indicate that groundwater may also have been present in the crater area during final eruptions, and may possibly have played a role in the dome removal process.

Anomalous Ash

The componentry of the anomalous-ash deposit in the north of the crater (Figure 38) is notable because it shows a high amount of cylindrical aggregates (20 wt%). It is low in lithic clasts, with the 2-phi grain size dominated by stony rhyolite. This deposit is also well sorted and very fine grained, with a dominant subpopulation at 3.9 phi (44 wt%).

INTERPRETATION

The 4-phi subpopulation of the anomalous-ash deposit is particularly abundant, especially when compared to 4-phi subpopulations of most deposits in Section 2. This

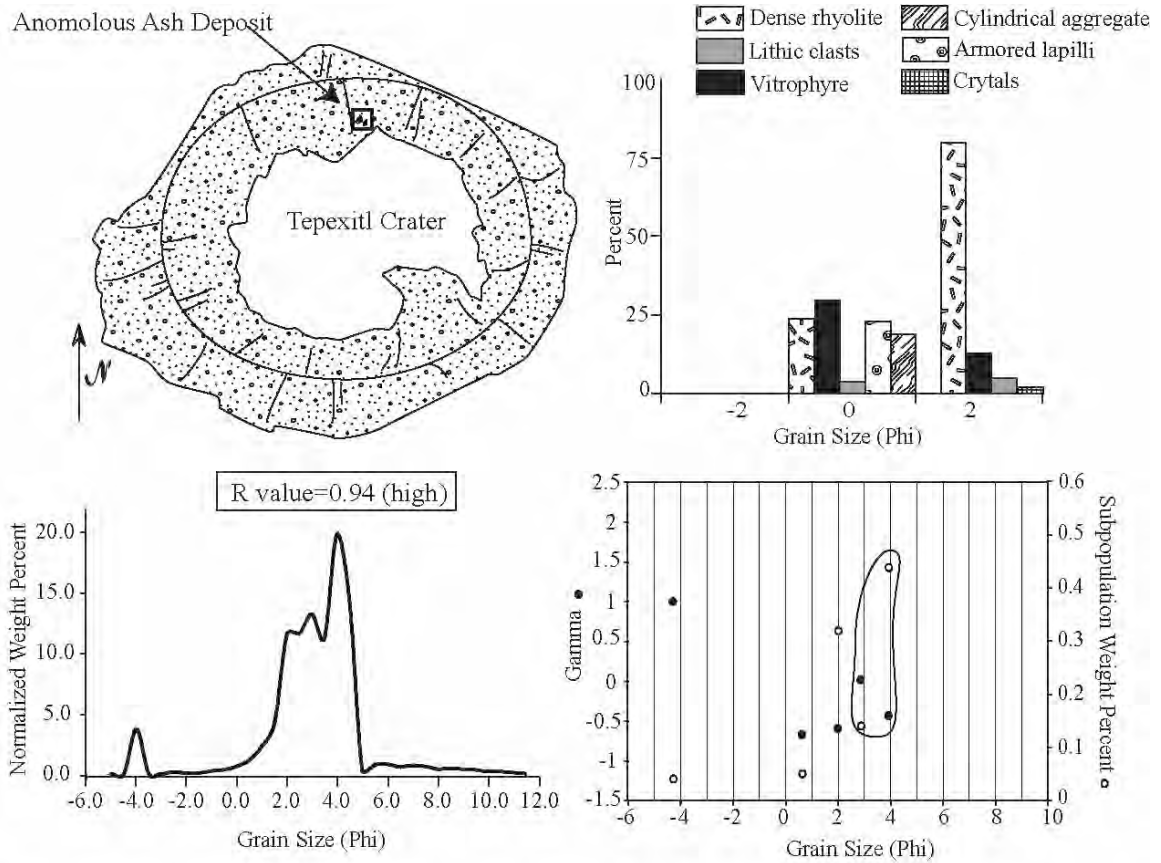


Figure 38: Granulometry and componentry of the anomalous-ash deposit. Dispersion (closed circles) and weight percent (open circles) of the subpopulations are shown in the same graph.

difference suggests that some distinct mechanism contributed to the formation of the anomalous-ash deposit, possibly eolian processes or settling of material through water, either which would have allowed for a larger degree of sorting of fine ash. The large percentage of Tepexitl juvenile material argues for a local origin of this deposit, but still does not discriminate between primary or secondary processes. The anomalous ash

deposit may be phreatic, but that does not explain why it has such a large abundance of fine-grained juvenile material with rare interspersed larger clasts. Additionally, a phreatic deposit would be expected to have a large abundance of lithic material. The lack of sedimentary structures and isolated nature of this deposit are additional factors that make the origin of the anomalous ash unclear. In conclusion, the depositional mechanisms that resulted in the formation of the anomalous ash remain a mystery.

The cylindrical aggregates found in this deposit are similar to the cylindrical aggregates found at the top of the upper sequence, where they are present in smaller percentages (8-14 wt%). If cylindrical aggregates are primary features, they suggest that anomalous ash and the top of the upper sequence may exist at the same stratigraphic level.

D. Overview of Patterns

a. Broad-Dispersion Subpopulations

Broad-dispersion subpopulation peaks are present in most samples (Table 11) and represent the more coarse-grained subpopulations, which can be eliminated as representative of phreatomagmatic fragmentation.

Table 11: Grain size (Md phi) of repeating, dominant, broad-dispersion subpopulation peaks (> -0.6 dispersion) by unit.

Lower	Unit 1						-1.9			-1				0			1	1.5	
	Unit 2	-4.7	-3.8		-2.5			-1.6		-1.1		-0.4		0	0.3		1		
	Unit 3						-1.9			-0.9							0.9		
	Unit 4				-2.5					-1.3		-0.8				0.5	0.7		
	Unit 5									-1.3		-0.8	-0.5	-0.2		0.4	0.7	1	
Upper	Unit 1			-3		-2.2		-1.6	-1.3	-1		-0.5			0.3	0.8			
	Unit 2		-3.8	-3	-2.6					-1.1		-0.6			0.4		0.9		
	Unit 3	-4.7	-3.6	-3			-1.9	-1.6											

b. Obsidian

Obsidian clasts are ubiquitous in all samples, concentrated in the coarse-ash and fine-lapilli grain sizes and decreasing in abundance with decreasing size (from 20-25 wt% in the 0-phi size to less than 10 wt% of the componentry in the 2-phi size; Figure 39). The obsidian percentage does not change significantly with stratigraphic height. The large average size of the obsidian clasts when compared to stony rhyolite and the low weight percentage in all deposits regardless of eruptive changes with time indicate that obsidian is both not subjected to high fragmentation energies and is not affected by changes in fragmentation regimes (i.e. phreatomagmatic to magmatic). These observations indicate that obsidian is likely found farther from the area in the conduit where most fragmentation energy is concentrated. Obsidian results from either rapid cooling or higher amounts of degassing ('drier' magma). Both of these situations are consistent with obsidian formation along the conduit margin and/or on the top of the rising plug – both areas where heat and volatile flux have the potential to be higher than the interior of the magma.

The mottled clasts are consistent with perlitic texture and were fractured and ejected post-hydration. This implies that at least some of the glass formed in an area with abundant water, also consistent with quenching along the sides or top of the rising magma plug. The formation of perlite is thought to be accelerated by hot aqueous solutions (Fisher and Schmincke, 1984). The presence of both perlite and non-hydrated obsidian implies that water abundance was not homogenous in the vent area. Some areas in which obsidian was formed must have been in contact with abundant water while other areas may have had little to no contact with external water.

Flow-banding is the result of shear flow along the margins and/or repeated annealing of fractures formed during upward movement. Both of these processes would also likely occur along the edges of the plug or within an extruding dome.

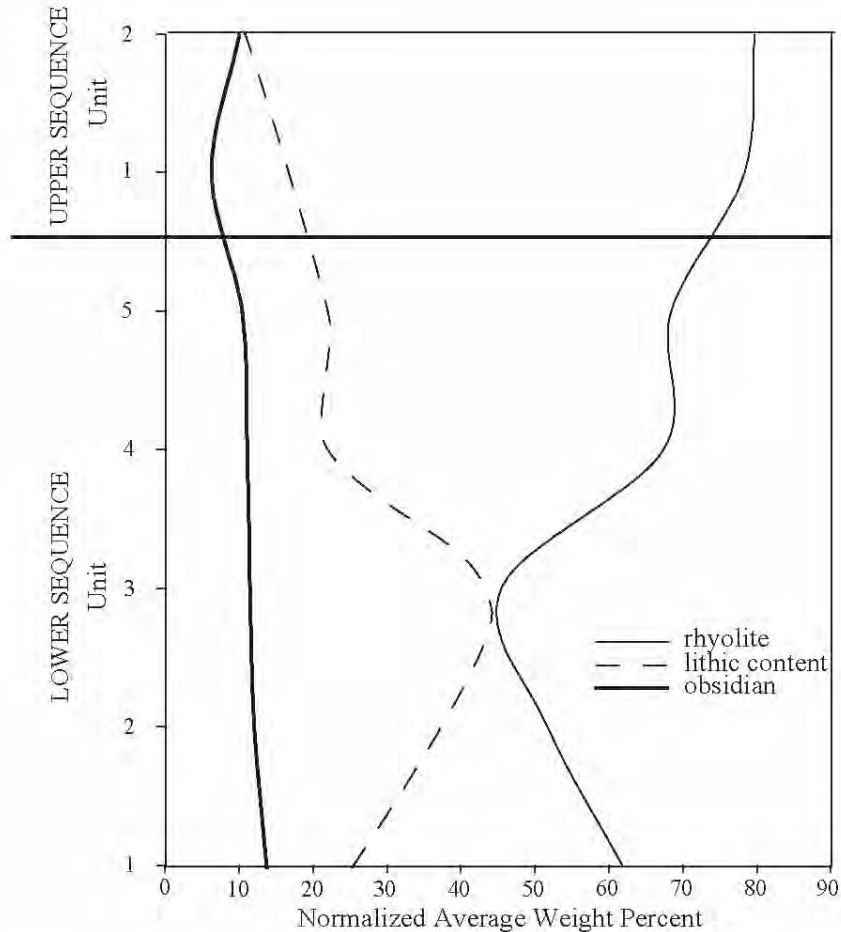


Figure 39: Normalized average values of rhyolite (stony rhyolite plus pumice), lithic clasts, and obsidian in the 2-phi grain size for each unit.

c. Stony Rhyolite

Dense to finely vesicular stony rhyolite clasts are the most abundant of all components within the Tepexitl deposits. They are interpreted to result from fragmentation of a rising magma plug prior to significant vesiculation and/or of a dome

(the exterior finely vesicular zone and/or the inner dense rhyolite zone). Stony rhyolite abundances vary considerably stratigraphically (Figure 39) and are the juvenile component most affected by changes in lithic content. Considering the argument above, that obsidian forms in a location of the magma plug not affected by high fragmentation energies, it follows that stony rhyolite would represent the areas of the rising plug most affected by fragmentation energies (by potentially both phreatomagmatic and magmatic processes).

d. Cylindrical Aggregates

The morphology of cylindrical aggregates is identical to descriptions of aggregates found in distal deposits (between 3.2 and 8.5 km from the crater) of El Chichón volcano (Scolamacchia et al., 2005), the first description of such clasts in the literature. Scolamacchia et al. (2005) suggest that these particles are formed during pre-deposition, medial-distal saltation in turbulent surge clouds along a vegetation-rich substrate where organic fragments can be swept up and rolled in the sticky, wet ash. However, the Tepexitl deposits with these particles are only found late in the eruptive sequence (anomalous ash and the upper sequence) and within near-vent facies (crater-wall deposits), so there may not have been a vegetation-rich substrate over which they could pass. Due to their small size, they were discovered only upon componentry analysis, so unfortunately it is not possible to determine whether these clasts were present in other sections around the crater of the same stratigraphic level. Thus, the cylindrical aggregates at Tepexitl may be genetically similar to those found at El Chichon, but the evidence for this is not conclusive. These rare clasts may also be the result of organic

leaching processes that caused aggradation of fine ash around roots of post-depositional vegetation.

e. Well-Indurated Tuff

The occurrence of well-indurated tuff is restricted to L1 and L4 of the lower sequence, both locations where deposition occurred during periods of time when fine ash was not as highly deformed, most likely due to a lower water:magma ratio. If there was less water present in the crater/vent area, it is possible that crater fill could 'dry out', causing some degree of cementation. Alternatively, heat from magma intrusion could cause 'baking' of crater-fill host material. Eruptions during these periods may have fragmented and ejected this hardened overlying/adjacent crater fill, incorporating them into deposits.

Either way, this textural feature is not interpreted to be very useful in looking at eruptive mechanisms, but it corroborates field evidence that suggests there was a lower water:magma ratio during deposition of L1 and L4. Well-indurated tuff is not seen in the upper sequence, which suggests that it is distinctive to conditions during early eruptions when water was less abundant.

f. Lithic Data

Tepexitl componentry and granulometry data are consistent with both the presence of Toba Café sediment underneath Tepexitl deposits and with a fine-grained saturated aquifer as the source of water. Componentry comparisons indicate that lithic grains in Tepexitl deposits are a good match to a typical Toba Café sediment componentry spread (Figure 36), which is strong evidence that Toba Café was present near/at the surface at the time of eruption. No lithic grains were found within Tepexitl

samples that were anomalous (in that all componentry categories of lithic grains correlate well with the Toba Café sample from Tecuitlapa), which suggests that Toba Café made up the majority of near-surface sediment (no evidence that eruptions penetrated any other overlying material) and that the eruptions did not deepen into underlying bedrock (limestone, for example).

The grain-size distribution of Toba Café sediments from Tecuitlapa (Figure 35) illustrate the polymodality and narrow dispersion of fine-grained subpopulation peaks of a typical Toba Café sample. SFT data for Tepexitl deposits further support this finding, as R value changes with stratigraphic height can be correlated with fine-grained lithic abundance, especially in the upper sequence. In upper sequence samples, a small increase in 2-phi lithic grains is associated with a much larger increase in R value, which is consistent with a high abundance of lithic grains in the fine-ash grain size. The SFT data show the fine ash subpopulations to be of narrow dispersion, which means that the material within these grain sizes is well sorted. Lithic material is also concentrated in the fine-grained deposits of Tepexitl's crater walls rather than the coarse-grained deposits, a process that may simply be a result of the small grain size of Toba Café sediment or that may reflect transportation- and/or fragmentation-related sorting. It is clear that external water was present in the vent area of Tepexitl (e.g. evidence includes deformed tuff, bomb sags, and accretionary lapilli). Fine-grained, well-sorted sediments were the likely components of the aquifer that provided water flux into the eruptive center. It is possible that an underlying fault could have been a 'zone of weakness' through which water easily percolated, saturating the overlying fine-grained sediment. Regardless, there is no evidence for a source of water other than Toba Café sediment.

Lithic concentration is the primary componentry variable because it can record changes in eruption depth. Sharp increases in lithic grains have been directly associated with an increase in the potential amount of external water available to the eruptive system (Houghton and Smith, 1993). Lithic material could increase in a deposit in a variety of ways: 1) low-energy phreatic eruptions through overlying material from varying depths below the surface can cause variability in lithic concentration; 2) the rate of explosive events may affect the final lithic concentration – rapid pulses may not leave time for fallback and accumulation in the crater, resulting in deposits with fewer lithic grains than those from less rapid explosions, which would have to erupt through overlying crater fill; and 3) finally, an increase in lithic grains may relate to a downward-migrating explosion locus that penetrates into underlying lithic material. L1-L3 show a systematic increase of lithic concentration within the fine-grained beds, most consistent with an eruptive center progressively deepening into underlying Toba Café (Figure 39). The gradual decrease in lithic concentration from L4 through the upper sequence is consistent with explosions that penetrated through less and less overlying material, a condition met by dome growth during this phase and shallower eruptions.

g. Three-stage Deposits

Three-stage deposits and potential three-stage deposits (defined as those deposits that have characteristics consistent with the three-stage cycle (Figure 40)., but due to a lack of data the association cannot be confirmed) are present in the lower sequence. This succession of compositional patterns begins with a coarse-grained fall bed rich in obsidian-sized lapilli (Stage-1 deposit). In Stage-1 deposits of L2 - L5, obsidian makes up at least 30 wt% of the 0-phi size and at least 45 wt% of the -2-phi size. The exception to

this 'general' rule is L1, in which obsidian is much more finely fragmented and is concentrated in the 2-phi grain size (L1, sample 3). Fe-clasts throughout the stratigraphy are limited solely to Stage-1 or potential Stage-1 deposits (although they are not found in every such deposit). Sharply overlying this breccia is a Stage-2 deposit - a fine-grained surge deposit rich in coated clasts (between 5 and 30 wt% in the 0-phi grain size and between 10 and 35 wt% in the 2-phi grain size), lithic grains, and pumice. Both lithic grains and pumice show increases relative to the underlying Stage-1 deposit and overlying Stage-3 deposit of at least 10 wt%. Again, L1 is an exception in this regard, as the increase in the 'Stage-2' deposit (sample 4) is not pumice but stony rhyolite. Stage-3 deposits can be coarse or fine grained, but in every case show a 10-20 wt% increase in stony rhyolite material when compared to the underlying Stage-2 deposits. Some Stage-3 deposits contain coated clasts, but these make up less than 20 wt% of the sample. Coated clasts are found exclusively in Stage-2 and Stage-3 fine-grained deposits (or potential Stage-2 and Stage-3 deposits). The coating affects all clast sizes of a given deposit, but not all clasts, which indicates that it was a localized process. Houghton and Smith (1993) interpret a similar texture as hot mud baked onto the surface of grains within the eruptive plume. The authors emphasize that this process does not occur when fine-grained mud is cold.

The entire three-stage sequence is composed of thinly bedded deposits (Figure 41) and characterized by rapid changes in componentry, which, although subtle, occur repeatedly and appear to represent an important eruptive process during the deposition of the lower sequence. Additionally, the three-stage deposits are associated with: 1) deformed tuff layers, which indicate higher water:magma ratios; 2) Fe-clasts and hot

mud, both of which indicate heat transfer was occurring from magma to saturated sediments; and 3) a progressive increase of lithic concentrations in L1 – L3, an indication of a deepening eruptive center into underlying sediment (Figure 39). This evidence is

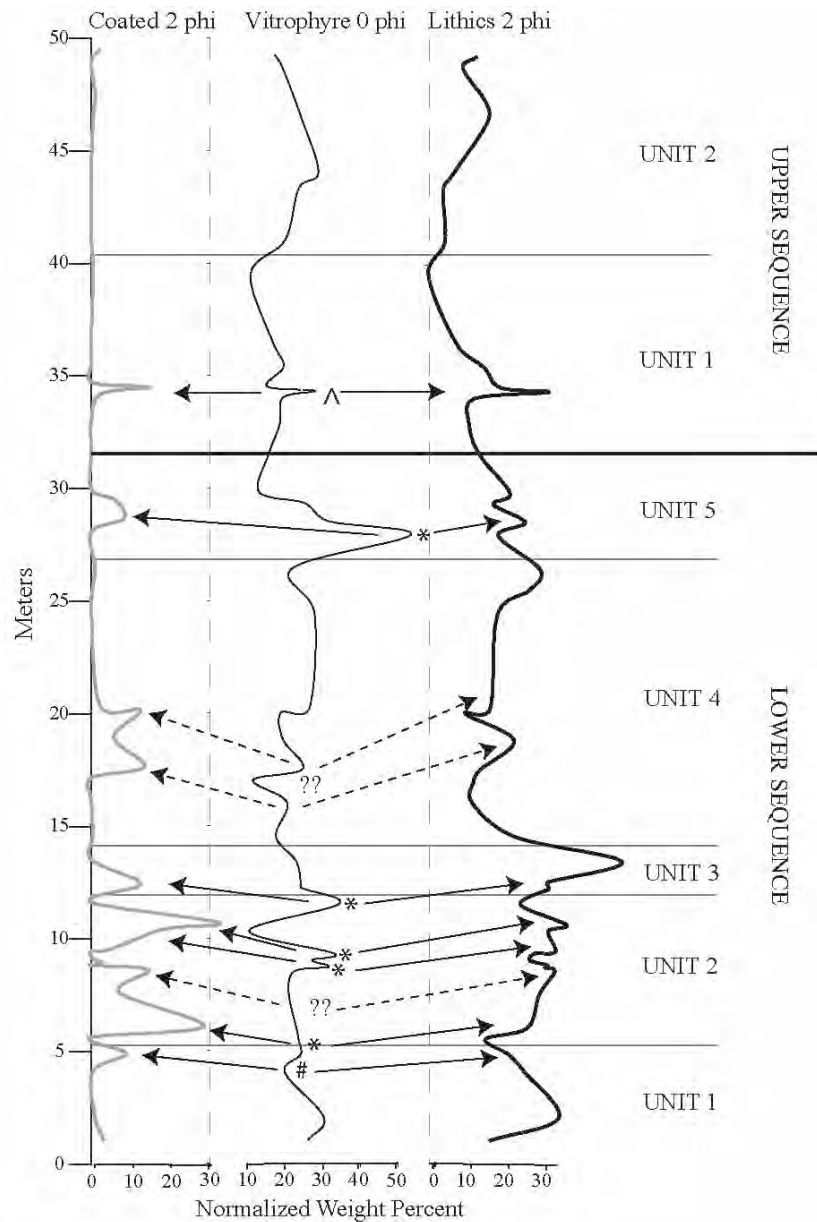


Figure 40: Correlations between Stage-1- and Stage-2 deposits: * = completely sampled 3-stage deposit; ?? = potential 3-stage deposits, but all relevant beds were not sampled; # = potential Stage-1 deposit associated with coarse ash obsidian rather than lapilli (hence the lack of an obsidian peak in 0 phi); ^ = Stage-1 and Stage-2 characteristics present in the same bed.

consistent with an interpretation that the three-stage process is the result of a unique fragmentation and eruption process of rhyolitic magma rising through shallow, water-rich, fluvial/eolian sediment. These deposits contain aspects consistent with phreatomagmatic explosion and may represent potential ‘fingerprints’ of interactions between highly viscous magma and fine-grained saturated sediment.

L4, sample 3 (Figure 40) is different from the others described above because characteristics of both Stage-1 and Stage-2 deposits appear in the same thin bed, but it is

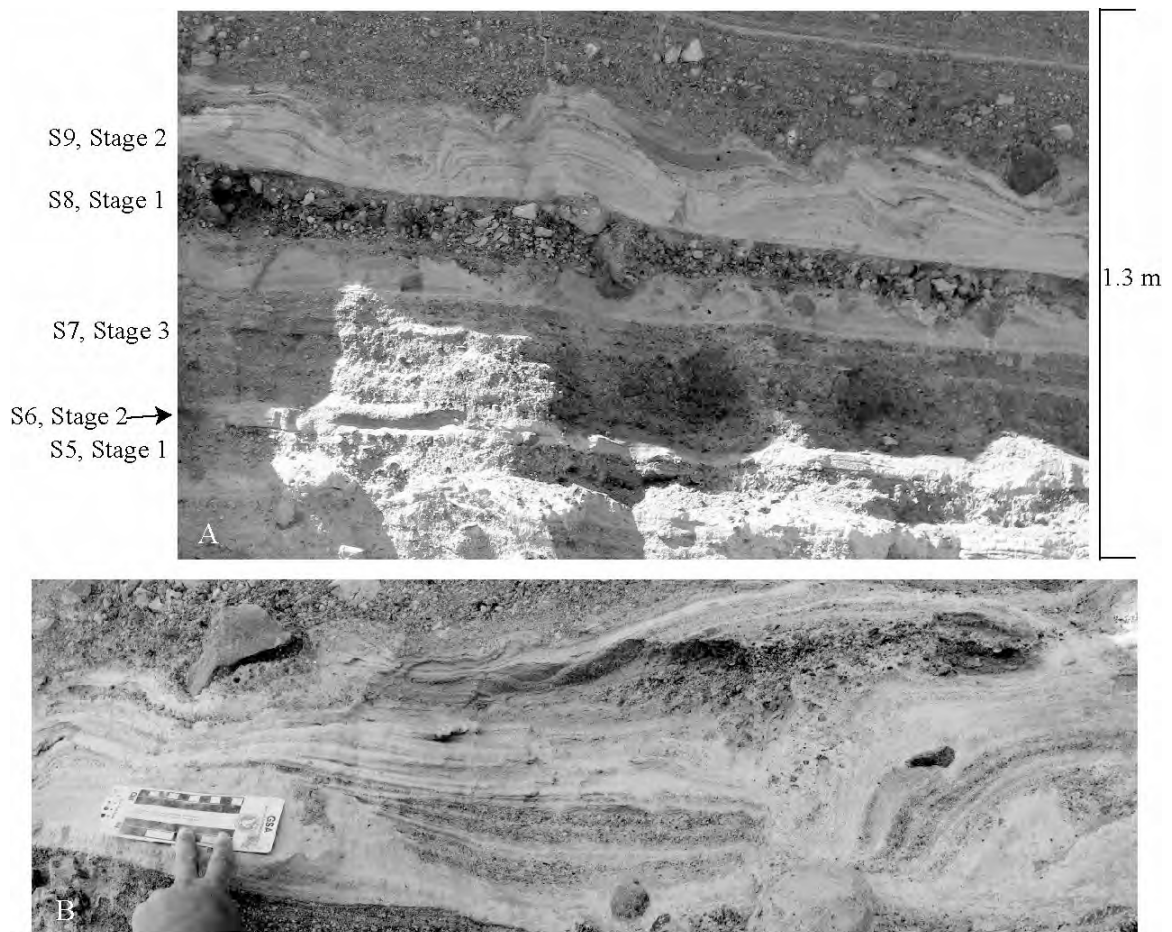


Figure 41: (A) deposits of the three-stage process in Section 2, L2, meters 8.5 to 9.8. Sample number (S) and stage are indicated. Note the very thinly bedded nature of each individual deposit; (B) a closeup of S9 from (A) shows the cohesive deformation typical of Stage-2 deposits.

also lacking in key characteristics that would tie it to the three-stage process (Figure 42). This deposit is a coarse-grained breccia and has a high abundance of fine-lapilli size

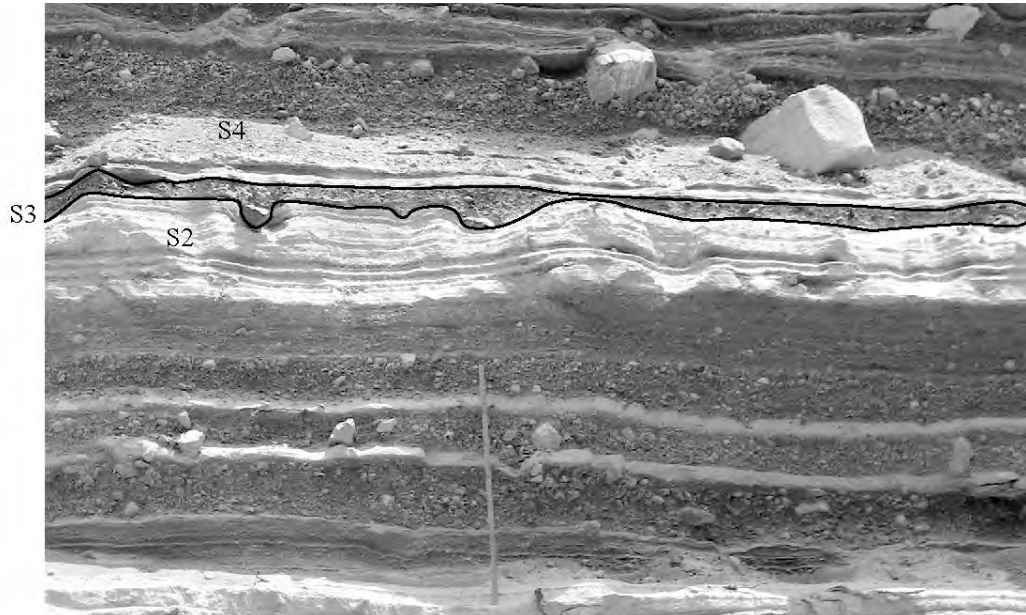


Figure 42: The breccia in Section 2, U1 is outlined. Scale is 1 m. Samples 2-4 are indicated.

obsidian clasts (32 wt% in the -2-phi grain size), coated clasts (15 wt% in the 2-phi size), and high abundance of lithic clasts (33 wt% in the 2-phi grain size compared to 13 wt% in underlying deposit and 20 wt% in the overlying deposit). This deposit is the only one in in the upper sequence to contain coated clasts. Pumice and stony rhyolite decrease in percentage from the underlying deposit. Stony rhyolite decreases from 78 wt% in the 2-phi fraction of sample 2 to 41 wt% in sample 3 and back to 74 wt% in the overlying deposit (sample 4). Pumice in the 0-phi fraction decreases from 19 wt% in sample 2 to 7 wt% in sample 3 and then increases to 20 wt% in sample 4. This compositional pattern is not consistent with the three-stage deposit and may represent a different process, perhaps vent clearing, as described in Lorenz and Kurszlauskis (2007). Material accumulated in

the vent area from fall-back of earlier eruptions would likely include coarse-grained obsidian, lithic clasts, and coated clasts. If no juvenile material was being fragmented and ejected during the explosion that deposited L4, sample 3, the total juvenile weight percent of the sample would decrease, with the only juvenile clasts deposited being those that were in the vent or overlying crater fill.

h. Pumice and Lithic Patterns

Although pumice is concentrated in fine-grained deposits and mimics changes in lithic grains during the three-stage processes in units, this trend is not observed in L4 or in the upper sequence. These eruptive sequences are characterized by coarser-grained, thicker deposits rich in stony rhyolite grains. Pumice concentrations within them do not have any apparent relation to other components (as seen by the shaded areas in Figure 43) and are interpreted to represent periods of time in which fragmentation processes different from those of the three-stage processes were dominating the depositional system. This situation is most consistent with magmatic fragmentation, as volatiles from the rising magma cause sufficient pressure at shallow levels to trigger eruptions. Resulting pyroclasts may then reflect volatile stratification within the rising plug and/or eruptions of dome material.

i. Fine Ash Subpopulation Components

R value mimics changes in lithic concentration and implies the Toba Café sediments were likely fine-grained and well-sorted, as well as the most likely source of external water during the eruption. However, Figure 43 shows that peaks in R value are not always directly related to peaks in lithic concentrations. This means that there must be other categories of grains contributing to narrow-dispersion, fine-grained

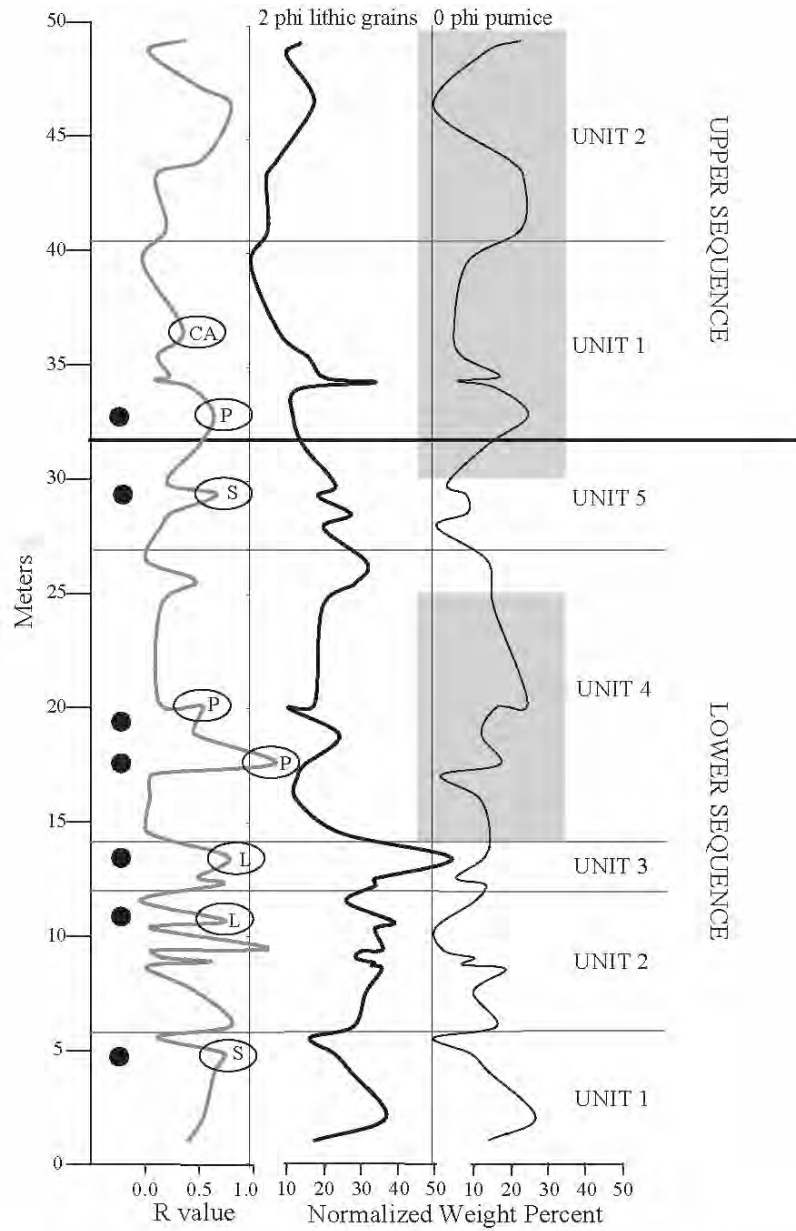


Figure 43: This graph shows two features- the different patterns observed between pumice and lithic concentrations and the peaks of R value that are associated with different components. The shaded regions are where pumice concentrations do not correlate with lithic changes. Circled peaks are labeled with the dominant fine-grained component. S = stony rhyolite; L = lithic grains; P = pumice; and CA = cylindrical aggregates. All unlabelled R-value peaks correspond with both lithic and pumice concentrations. The subpopulation percentages for samples marked with dots are graphed in Figure 45.

subpopulations. It is notable that every R-value peak in the lower sequence corresponds with a Stage-2 or Stage-3 deposit. Stage-2 deposits are associated with a peak in pumice whereas Stage-3 deposits are characterized by a fine-grained peak in stony rhyolite. L1 (sample 4) and L5 (sample 3) each have a single R-value peak that corresponds with stony rhyolite peaks in a Stage-3 deposit. Every R-value peak in L1 - L3 is a Stage-2 deposit that has both pumice and lithic concentrations contributing to the fine-grained material, with the exception of L2, sample 10. This bed is composed predominantly of dark brown accretionary lapilli with lithic-rich matrices that are not associated with a peak in pumice. L4, samples 4 and 6 (R value peaks in the middle of the unit) are potentially Stage-2 deposits, but do not have the normal lithic grain increase. Instead, the increased R value appears related only to the pumice concentration. L4, sample 9 (the R-value peak at the top of L4) is predominantly facies AC and may be a Stage-2 or Stage-3 deposit, but corresponding beds were not sampled. However, the upper-sequence deposits do not have the same pattern. Instead, all R-value peaks mimic peaks in lithic material. This suggests that little or no fine-grained juvenile material was being erupted and/or deposited during eruption of the upper sequence.

When the subpopulations marked in Figure 43 with a black dot were graphed by weight percent, they could be visually grouped according to componentry (Figure 44). These samples were chosen because their peak in R value corresponds closely to only one dominant componentry group, which provides a good array of points to examine the componentry of the ubiquitous narrow-dispersion subpopulations between 2 and 4 phi. From this graph, it becomes clear that each componentry group has a distinct pattern. The pumice-rich deposits are dominated in mass percent by a subpopulation centered around

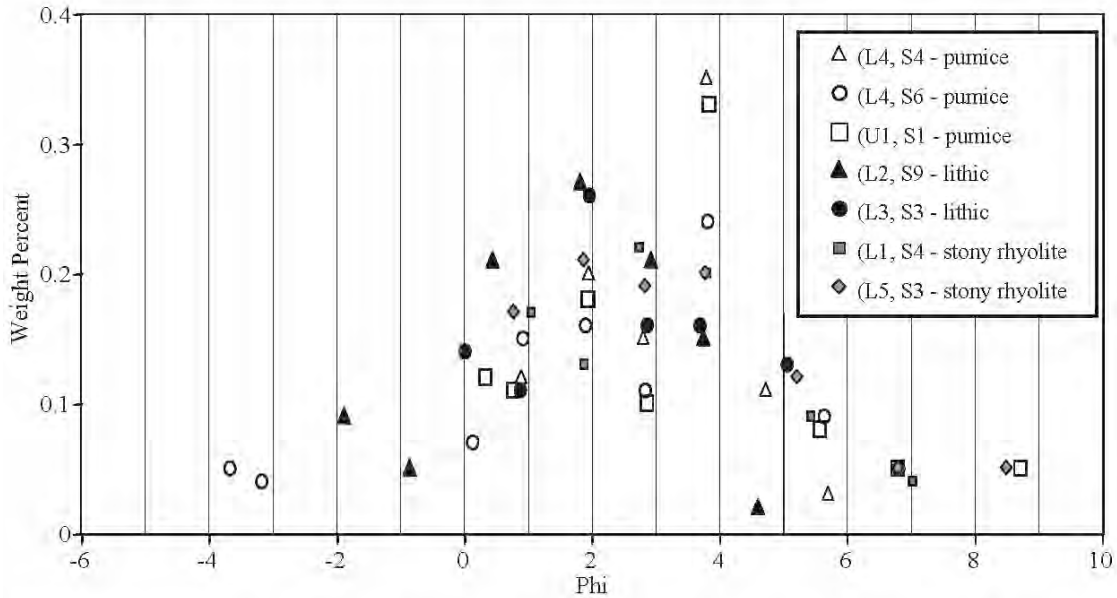


Figure 44: This graph couples dominant fine-grained componentry data with SFT data to analyze deposits with high R values. Between 2 and 4 phi, different components have different patterns of dominant subpopulation peak. In the key, samples are identified by sequence, unit, and sample number.

3.8 phi, although they have a secondary dominant peak at 1.9 phi. The lithic-rich samples are: Toba Café accretionary lapilli from L2 (sample 9) and the deposit with the highest amount of lithic grains in the entire stratigraphy (L3, sample 3). Both of these deposits are dominated in mass percent by a peak around 1.9 phi. Lastly, the stony-rhyolite-rich deposits have three dominant subpopulation peaks – at 1.9 phi, 2.8 phi, and 3.8 phi - all of about the same weight percentage.

In summary, Toba Café lithic sediment at Tepexitl is dominated by a subpopulation centered at 1.8 phi. However, there appears to be a juvenile component to the 1.8-phi subpopulation as well, with peaks in both the pumice and stony rhyolite beds. Additionally, every sample taken at Tepexitl has a peak around 2 phi, including the breccias of U3 that are not associated with any lithic material (Plate 9). Therefore, the 2-

phi 'signature' is a combination of lithic sediment and fine-ash fragmentation (likely magmatic). However, dominant peaks around 3.8 phi appear limited to pumice-rich deposits (all potentially Stage-2), with a narrow concentration of grains in the subpopulation typically associated with phreatomagmatic deposits. This implies that a large percentage of unimodal juvenile fine ash was created during these eruptive events, which corresponds with high fragmentation energies. Stage-3 stony-rhyolite deposits are characterized by equal subpopulation peaks (although smaller peaks than Stage-2 deposits) between 2 and 4 phi and suggest that juvenile fine ash was also created during these eruptive periods (although not in as high abundance). The lower percentage of material around 4 phi and the more polymodal nature of these deposits is consistent with a different fragmentation mechanism than that associated with the pumice-rich Stage-2 deposits. Based on these results, the 4-phi grain size was selected to examine in more detail during SEM analyses (Chapter 5) because: 1) the 4-phi peak appears to be a characteristic grain size resulting from fragmentation of juvenile material; 2) the fragmentation of juvenile material in the 4-phi size range may be related to phreatomagmatic processes; and 3) other mechanisms may also be causing fine fragmentation of juvenile material around this grain size mode, and SEM analyses may be able to distinguish these processes.

Chapter 4: Bulk Rhyolite Analyses

A. Introduction

Viscosity plays an important role both in the ability of a magma to interact with water and in the fragmentation mechanisms acting on a melt and resulting eruptive dynamics. Viscosity (η) is the measure of a material's resistance to flow under the application of stress and is measured in kg/m s. Composition and volatile content can affect the viscosity of a magma (Spera, 2000) and are explored in this chapter. Other parameters that affect viscosity include temperature, shear rate, and interaction with conduit walls during ascent (Spera, 2000) but these parameters cannot be accurately measured or assumed so are not addressed in this discussion.

B. XRF Data

Major-element data (Table 12) indicate that all Tepexitl samples are peraluminous rhyolite and have the same chemistry (within analytical error). Likewise, all trace-element data are within analytical error (Table 13). Compositional measurements were done with X-Ray Fluorescence (XRF) at UNAM (Universidad Nacional Autónoma de México). Samples were chosen to represent both different stages of the eruptive sequence and different textures of juvenile clasts. Obsidian and stony rhyolite were sampled from the base, the middle, and the top of the deposits (L2, U1, and float clasts on top of the crater rim). Additionally, a distinctly banded pumice float clast from the western inner-crater wall was analyzed by color (to see if the dark band had different chemistry from

Table 12: Tepexitil major element data (normalized)

Sample Location	Sample Texture	SiO ₂ %	TiO ₂ %	Al ₂ O ₃ %	F ₂ O ₃ %	MnO %	MgO %	CaO %	Na ₂ O %	K ₂ O %	P ₂ O ₅ %	LOI %	Total %
L2	Stony Rhyolite	72.468	0.028	13.508	1.195	0.04	0.254	0.739	4.255	4.203	0.059	2.73	99.479
L2	Obsidian	74.108	0.021	13.763	1.276	0.04	0.174	0.717	4.373	4.208	0.058	1.17	99.908
L4	Stony Rhyolite	73.257	0.025	13.674	1.179	0.044	0.167	0.692	4.228	4.218	0.053	2.14	99.677
L4	Obsidian	74.855	0.026	13.78	1.229	0.043	0.213	0.733	4.319	4.177	0.061	1.2	100.64
U3	Stony Rhyolite	73.882	0.032	13.829	1.229	0.042	0.184	0.734	4.389	4.182	0.057	1.99	100.55
U3	Obsidian	73.726	0.028	13.585	1.281	0.038	0.171	0.72	4.373	4.218	0.06	1.55	99.75
U3	Pumice, dark band	74.053	0.027	13.888	1.329	0.038	0.15	0.742	4.41	4.215	0.056	1	99.908
U3	Pumice, light band	74.077	0.027	13.867	1.14	0.039	0.185	0.735	4.466	4.191	0.057	1.06	99.844

Table 13: Tepexitil trace element data

Sample Location	Sample Texture	Rb ppm	Sr ppm	Ba ppm	Y ppm	Zr ppm	Nb ppm	V ppm	Cr ppm	Co ppm	Ni ppm	Cu ppm	Zn ppm	Th Ppm	Pb Ppm
L2	Stony Rhyolite	148	104	942	21	62	13	<5	8	14	6	8	74	5	16
L2	Obsidian	157	106	1050	24	62	17	<5	7	19	7	15	89	4	20
L4	Stony Rhyolite	147	99	939	21	64	13	<5	19	11	6	9	75	4	18
L4	Obsidian	158	94	968	24	60	12	<5	53	19	8	9	88	5	20
U3	Stony Rhyolite	152	110	1010	23	63	18	<5	33	17	7	36	77	4	21
U3	Obsidian	140	130	1102	24	79	18	<5	8	38	<0.5	16	64	<3	23
U3	Pumice, dark band	144	108	939	21	62	13	<5	7	11	6	6	77	4	19
U3	Pumice, light band	147	106	937	22	64	13	<5	3	14	6	7	77	4	19

the light band). These banded pumice samples are particularly enriched in Ba, and also have high concentrations of Sr and Rb, all LILEs (large ion lithophile elements).

INTERPRETATION

The similarity in chemical compositions of all samples is consistent with all juvenile material originating from the same magma chamber. Eruption was completed prior to any evolution of the magma at shallow levels during the course of the eruption, and there is no evidence for magma mixing during this time period. The high silica content relates directly to a high viscosity, as expected for a rhyolite. Cr, Co, and Cu have some anomalous values (although still low concentrations), which likely relate to contamination from the tungsten-carbide shatterbox and puck used in grinding the samples.

C. LOI Data

a. Methods

LOI (Loss-On-Ignition) is a measurement of the amount of water a sample loses at low and high temperatures. Although LOI was calculated during XRF calculations at UNAM (Table 12), additional measurements were made to better characterize changes in magmatic water content throughout the total stratigraphy (Figure 45). These data have consistently higher values than those calculated with the XRF measurements, which likely relates to the amount of time the samples were heated (a longer time at high temperature means more volatile loss).

At least one deposit from each unit was selected to collect LOI data. Deposits with a significant weight percentage of small lapilli in both the obsidian and stony

rhyolite categories within the -2-phi grain size, already counted and separated during componentry analyses (chapter 3), were chosen for this analysis. For each deposit, one sample of obsidian and one sample of stony rhyolite were analyzed. Thus, systematic changes could be analyzed both stratigraphically and between juvenile textures at a given level (obsidian vs stony rhyolite). Additionally, one breadcrust pumice float block from the western crater was also selected for LOI measurements. A total of 19 samples were analyzed: 9 deposits for both obsidian and stony rhyolite, and 1 lone pumice from the crater rim. At least 15 grams of material for each sample was crushed into a fine powder. From this powder, approximately 2.5 g was used in the heating experiment. Porcelain crucibles were weighed with and without powder and heated at 200 °C for 4 hours in order to drive off the low-temperature, meteoric water. After cooling, the crucibles (plus sample) were weighed again, placed back in the oven, and heated to 1000 °C for 4 hours in order to drive off the high-temperature, magmatic water. After cooling, the crucibles (plus sample) were weighed a final time.

To calculate weight percent water loss, the formula is:

$$\text{LOI} = ((S1-S2)/(S1-C))*100, \text{ where}$$

S1 is the weight of the crucible and sample prior to heating,

S2 is the weight of the crucible and sample after heating,

and C is the weight of the crucible.

This formula was adapted to calculate high temperature LOI by substituting S2 of LOI at 200 °C for S1 of LOI at 1000 °C.

As the goal of the analyses was to represent the juvenile volatile content at the time of the eruption, recycled grains from earlier in the eruption are potential

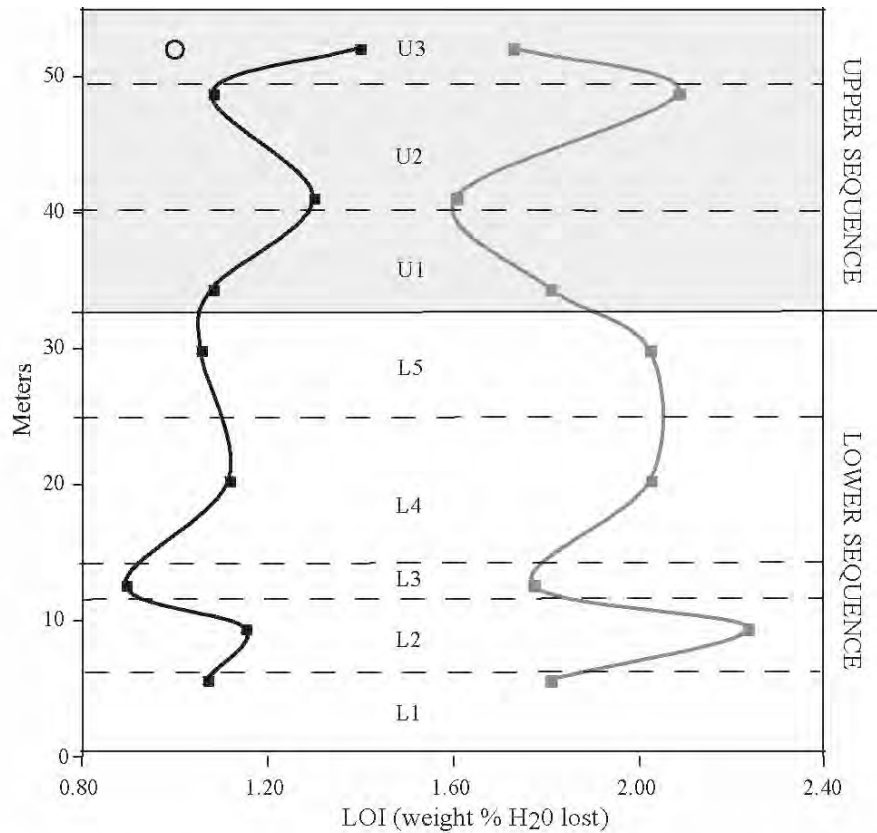


Figure 45: High-temperature LOI values for obsidian (black line on the left) and stony rhyolite (gray line on the right), plotted against stratigraphic height. The open circle in U3 is pumice. The shaded and unshaded regions correspond to both the upper and lower sequences and to changes in the LOI patterns between obsidian and stony rhyolite.

contaminants because they do not accurately represent the water content of the eruption of a particular stratigraphic level. Because recycled grains look identical to freshly fragmented grains, this problem could not be solved. As the counted grains of the 0-phi size category did not weigh enough to produce a statistically significant sample, the -2-phi grain size was used. However, it can be argued that these grains are still small enough that a significant proportion of the erupted material would make it out of the vent with each explosion and should thus be a relatively accurate representation of juvenile water content at the time of deposition.

b. Background

In order to place the data in Figure 45 within the context of past research, a brief overview of LOI and eruptive dynamics is summarized here. The low diffusivity of water in obsidian means that the high-temperature LOI values represent magmatic water contents at the time of quenching (Taylor et al., 1983). High-temperature LOI data from samples of obsidian domes are generally very low, between 0.1 to 0.4 wt% water, as quenching is thought to occur at the surface after significant degassing (Fink and Manley, 1987; Dunbar and Kyle, 1992; Fink et al., 1992; Rust et al., 2004). In contrast, obsidian pyroclasts have much higher LOI values (up to 3 wt% water), which indicates that the magma was only partially degassed at the time of quenching (Taylor et al., 1983; Fink and Manley, 1987; Dunbar and Kyle, 1992; Rust et al., 2004). This contrast in LOI values between dome material and obsidian pyroclasts is a common trend but the mechanism for the decrease in volatile content during this transition is unclear. It could be the result of a volatile-stratified magma body, with most volatiles concentrated at the top. This would cause the initial eruption to be explosive and grade into passive extrusion with time (e.g. Taylor et al., 1983; Fink and Manley, 1987). However, volatiles can also be lost during open system degassing at shallow levels (e.g. Manley and Fink, 1987; Fink et al., 1992). It is thought that most of a magma's internal water is lost within 1 km from the surface, through the conduit and/or brecciated debris in a funnel-shaped vent (Manley and Fink, 1987). Fink et al. (1992) speculate that small eruptions with small conduits and small amounts of juvenile magma especially can lose a significant amount of gas through the conduit at depth, which may also relate to the decrease in explosive activity with time. Gonnermann and Manga (2003) suggest that the brecciation and re-annealing that

characterize viscous flow of conduit-wall obsidian are viable mechanisms for significant volatile loss along the margins of a rising plug. However, it is likely that increasing driving pressure and increasing conduit diameter would decrease the efficiency of losing heat at depth, causing more degassing to occur at surface levels (Fink et al., 1992).

c. Interpretation of Data

Obsidian vs. Stony Rhyolite

LOI values for obsidian are consistently lower than those for the corresponding stony rhyolite in the same bed (Figure 45), which means that obsidian had consistently lost a greater percentage of its volatiles at the time of quenching than stony rhyolite lost upon fragmentation. This pattern is consistent, with obsidian having formed in an area where volatile loss was enhanced, but quenching occurred prior to complete degassing. These trends can be explained by obsidian formation along the conduit margin or the upper portions of a rising plug, and suggests open-system degassing played a role in the Tepexitl eruption. The data also suggest that the degree of degassing of the vesiculating conduit interior is preserved upon fragmentation.

Lower Sequence

The lower sequence is characterized by a mimicking LOI pattern between obsidian and stony rhyolite (Figure 45). There is a constant ratio of more degassed obsidian to less degassed stony rhyolite (stony rhyolite has consistently between 1.7 to 1.9 times the amount of magmatic water as the obsidian). If LOI values change, they change in both component groups in a way that maintains this ratio. This pattern can be best explained by open-system degassing, in which the gas content is proportionally higher in the middle of the conduit and lower along the edges, where the most significant

degassing occurs. In other words, the amount of degassing at the margins is directly related to the volatile concentration at the center of the plug at the time of fragmentation. The implication of the data is that the depth of fragmentation of both stony rhyolite and obsidian during deposition of individual deposits of the lower sequence is the same.

L2 has a notable increase in LOI in both obsidian and stony rhyolite, which means relatively less degassed magma was being fragmented and ejected. L3 data, however, indicate that the degree of degassing has sharply increased, with the lowest LOI values for obsidian of any sample. L4 and L5 fall uniformly between these two end-member extremes. These observations are consistent with a deepening of fragmentation level during emplacement of L2. The rapid degassing from L2 to L3 may be explained by an increased rate of shallow degassing and/or the equilibration of magma volatile release at a lower fragmentation level (rapid vesiculation post-pressure release). L4 and L5 are consistent with eruption from a stable level of fragmentation.

Upper sequence

The upper sequence is characterized by obsidian and stony rhyolite values mirroring each other rather than mimicking each other (Figure 45), which suggests that there was some change in eruptive dynamics from the lower sequence. This change in pattern implies that different degrees of degassing are recorded in obsidian and stony rhyolite clasts, which indicates that the level where obsidian is quenched and the level of subsequent fragmentation are different. The base of U1 to the base of U2 is associated with simultaneous eruption of both relatively more degassed stony rhyolite and obsidian that was less degassed at the time of quenching. This pattern can be seen again from the top of U2 to the float blocks associated with U3. The values seen for both U1 and U3 are

the same within error. Data for a finely-vesicular breadcrust pumice clast associated with U3 has the lowest LOI values of all measured samples. From the base to the top of U2, the reverse pattern is apparent – obsidian that has quenched at shallower levels (more degassing occurred) is erupted simultaneously with stony rhyolite clasts that are less degassed. These values are the same as seen in L4 - L5.

The combination of more-degassed stony rhyolite with less-degassed obsidian could be related to the rise of vesiculating magma, enveloped in an obsidian rind that quenched at lower levels within the vent or conduit than the level of fragmentation. Alternatively, magma could rise through the brecciated material at the base of the crater and incorporate older obsidian into the upward flow (as in Lorenz et al., 2002). Obsidian quenched in the conduit and incorporated into later, shallower eruptions would have higher LOI content (Dunbar and Kyle, 1992). In either case, this combination implies that the eruptive level shallowed during deposition of the upper sequence. The combination of patterns observed could be due to two different shallow-level processes: dome growth with surficial extrusion or a magma plug that rose within crater level but stalled out prior to reaching the surface (a cryptodome). It is also notable that the LOI values for the juvenile material of the upper sequence are much higher than those documented for established domes (as discussed above), which implies that shallowing of eruptive center occurred prior to complete degassing, or that degassing was unrelated to this process.

In the case of dome growth, most degassing would occur at surficial levels through the outer margins of the dome (the finely-vesicular zone). Crystallization within the dome would further drive water outward, leaving the interior devitrified and low in magmatic water (Manley and Fink, 1987). Because the stony rhyolite samples from all

deposits at Tepexitl are higher in LOI than the obsidian samples, this implies that degassing and devitrification processes of the dome were not complete upon extrusion and explosion. The pumice sample fits nicely with this theory, as it has the lowest LOI values of all samples, which is consistent with surficial degassing from the outer carapace of the dome (the finely-vesicular zone). The trend from the base of U1 to the base of U2 and from the top of U2 to U3 may result from two separate periods of dome growth and subsequent explosion or one period of dome growth with intermittent explosions. The opposing trend seen at the top of U2 (with values similar to those of the lower sequence), may then relate to either a deepening of explosion level between cycles of dome growth and/or it may be because of phreatic eruptions through crater fill, which deposited recycled clasts from earlier in the eruption.

The alternative to dome growth is a plug that resided at shallow levels within the conduit/crater but never extruded onto the surface. In this case, dominant shallow-level degassing mechanisms would not be surface-level degassing. Other mechanisms for degassing include: 1) increased fracture networks that develop at shallow levels and lower temperatures provide an escape pathway for the associated larger amounts of exsolved volatiles associated with these conditions; 2) open-system degassing through the brecciated vent and conduit allows volatile escape; and/or 3) a permeable foam that develops at low pressures, allowing gas to escape, which then collapses upon extrusion. In these situations, the deposits sampled at the top of U3 could still represent either of the two situations presented above: recycling through crater fill and/or a deepening of fragmentation level. The pumice sample may have been magmatic 'foam' that formed at shallow levels along conduit walls.

Chapter 5: SEM Back-Scatter Imagery of Ash samples

A. Background

A major advance in the understanding of basaltic phreatomagmatic fragmentation was the identification of major particle associations found in deposits from many volcanoes (Wohletz, 1983). These groups of ash shapes have proven to be very important in the study of pyroclastic deposits, as their quantification allows partial reconstruction of eruptive dynamics (Wohletz and Zimanowski, 2000). The five main pyroclast shapes identified in phreatomagmatic deposits of basaltic melts include: 1) blocky/equant, 2) mossy/convoluted, 3) drop-like to elongate, and 4) platy, and 5) vesicular (Figure 46). Blocky particles result from both fine fragmentation during rapid quenching and brittle failure of the melt following vapor-film collapse (Zimanowski et al., 1997b). Moss-like fragments are botryoidal aggregates produced from shear-induced Kelvin-Helmholtz instabilities along the interface (Wohletz and Zimanowski, 2000). Drop-like morphologies are related to Rayleigh-Taylor instabilities caused by high melt surface tension during mixing (Büttner et al., 2002). Elongate particles are formed during

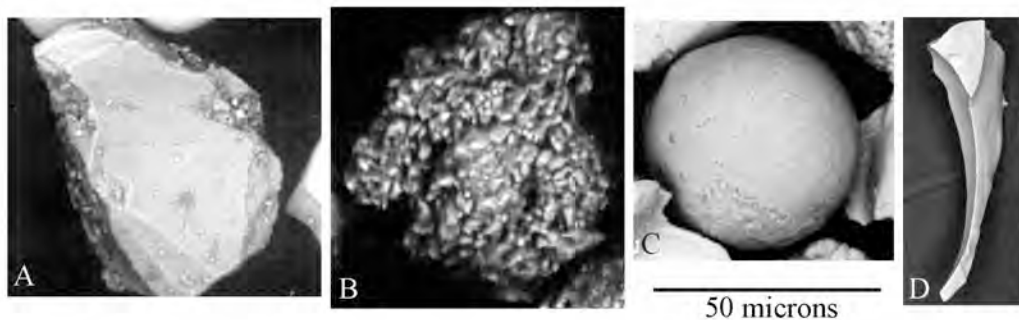


Figure 46: Common basaltic, phreatomagmatic ash morphologies - blocky (A; Büttner et al., 2002), mossy (B; Büttner et al., 2002), drop-like (C; Dellino and Kyriakopoulos, 2003), and platy (D; personal unpublished data, 2007).

passive, fluidal fragmentation of melt adjacent to the fuel-coolant boundary (Büttner et al., 2002). Platy particles are thought to relate primarily to thermal granulation, when hydraulic coupling of excess water and melt causes both very high shear stresses and very high cooling rates along the interface, which leads to quench-induced brittle reaction of the melt (Zimanowski et al., 1997b). One suggested model for the formation of these different ash morphologies is shown in Figure 47 as three separate diagrams, although these likely work together in a complex manner in natural systems. Vesicular pyroclasts are mostly limited to large, gas-rich explosions and are not necessarily connected with external water.

Detailed and unique experiments have been conducted to further our understanding of phreatomagmatic fragmentation processes with low viscosity melts and their connection to resulting grain morphologies. Results show that ‘active’ particles, those that formed from direct contact with water and thus that experienced the highest fragmentation energies, are limited to brittle-type fragmentation and resultant blocky particles. By calculating the total surface area of active particles, the energy released during a single eruption (one deposit) can be determined (e.g. Büttner et al., 2002). However, these active particles constitute less than 1% of experimentally produced phreatomagmatic basaltic pyroclasts (Zimanowski et al., 1997b). The rest of the particles are dominantly ‘passive’ particles formed from ductile deformational processes (both elongate and spherical particles). This distinction makes quantitative shape analysis an excellent method for calculating the percentage and surface area of active particles in basaltic deposits.

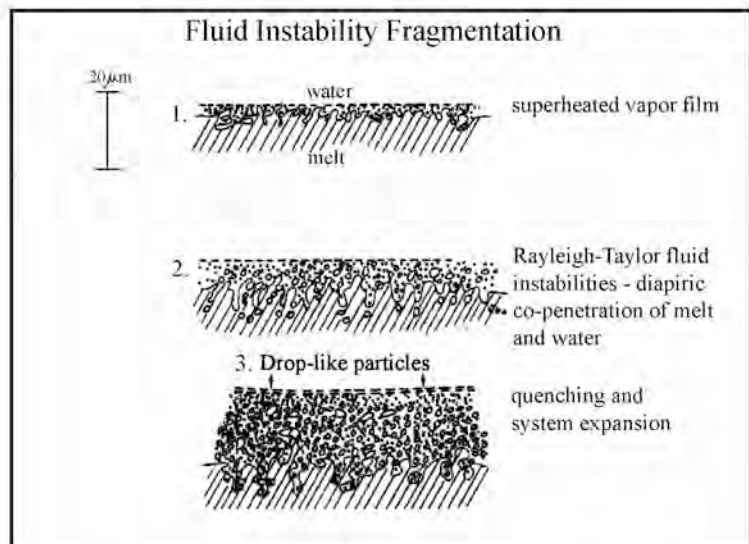
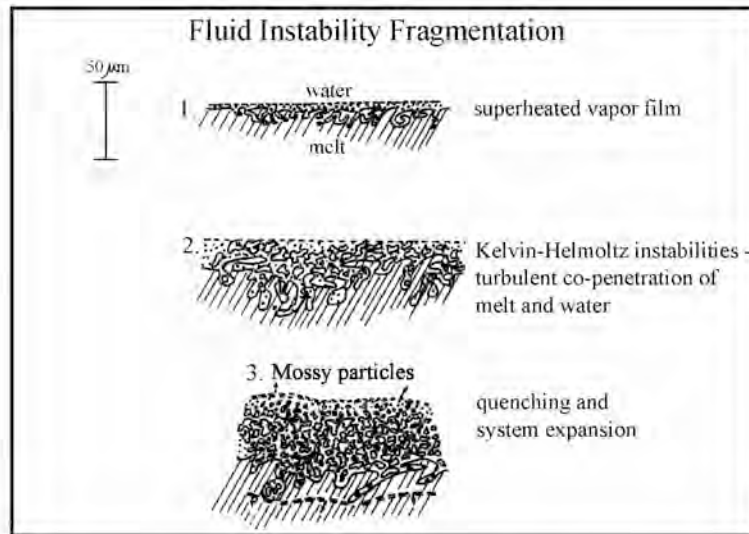
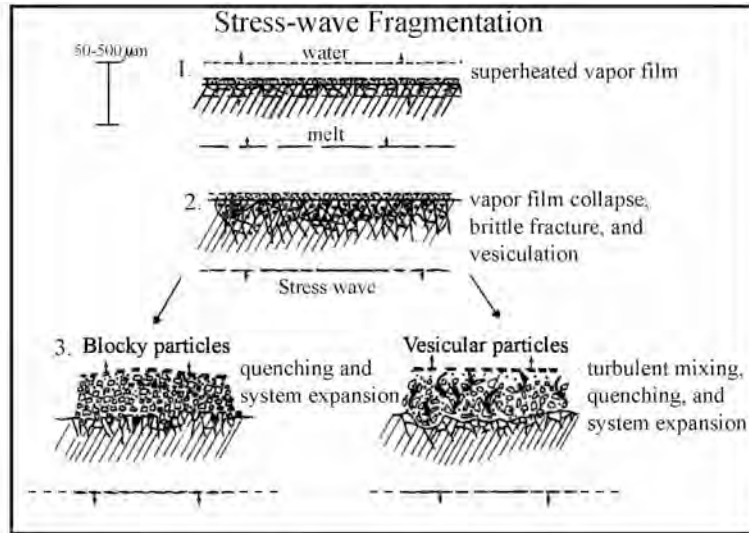


Figure 47: Mechanisms associated with basaltic phreatomagmatism are shown for different ash morphologies (adapted from Wohletz, 1983).

However, the problem with applying these theories to rhyolitic pyroclasts is that fragmentation of high-viscosity melts becomes dominated by brittle processes at very low driving pressures, with little to no ductile deformation (Zimanowski et al., 1997b). This is because much lower strain rates will exceed the bulk modulus of a rhyolite than of a basalt (Wohletz, 1983). Therefore, blocky grains in rhyolites cannot be assumed to result from phreatomagmatic behavior and distinguishing ‘active’ from ‘passive’ from ‘magmatic’ fragmentation modes presents a challenge. Zimanowski et al. (2003) present experimental results in which phreatomagmatically triggered brittle fragmentation of fine ash can only account for a small percentage of the resulting blocky particles. Additionally, the authors found that brittle fracture appears to be unaffected by low vesicle contents (15%). Dellino et al. (1996) addressed these issues at Monte Pilato pumice cone and found shape associations unique to rhyolitic pyroclastic deposits, with primary variations in form and vesicularity. These particle types are listed from most phreatomagmatic quality (1) to most magmatic quality (5), with examples of each category shown in Figure 48:

1. Blocky and equant with linear outline and low vesicularity
2. Angular with slightly irregular outline and low vesicularity
3. Elongate with very irregular outline and low/medium vesicularity
4. Angular with curved-elongate outline that has some re-entrants and high vesicle abundance (tubular to ovoid vesicle shape)
5. Irregular shapes with concave-convex outline and a very high abundance of tubular to contorted vesicles.

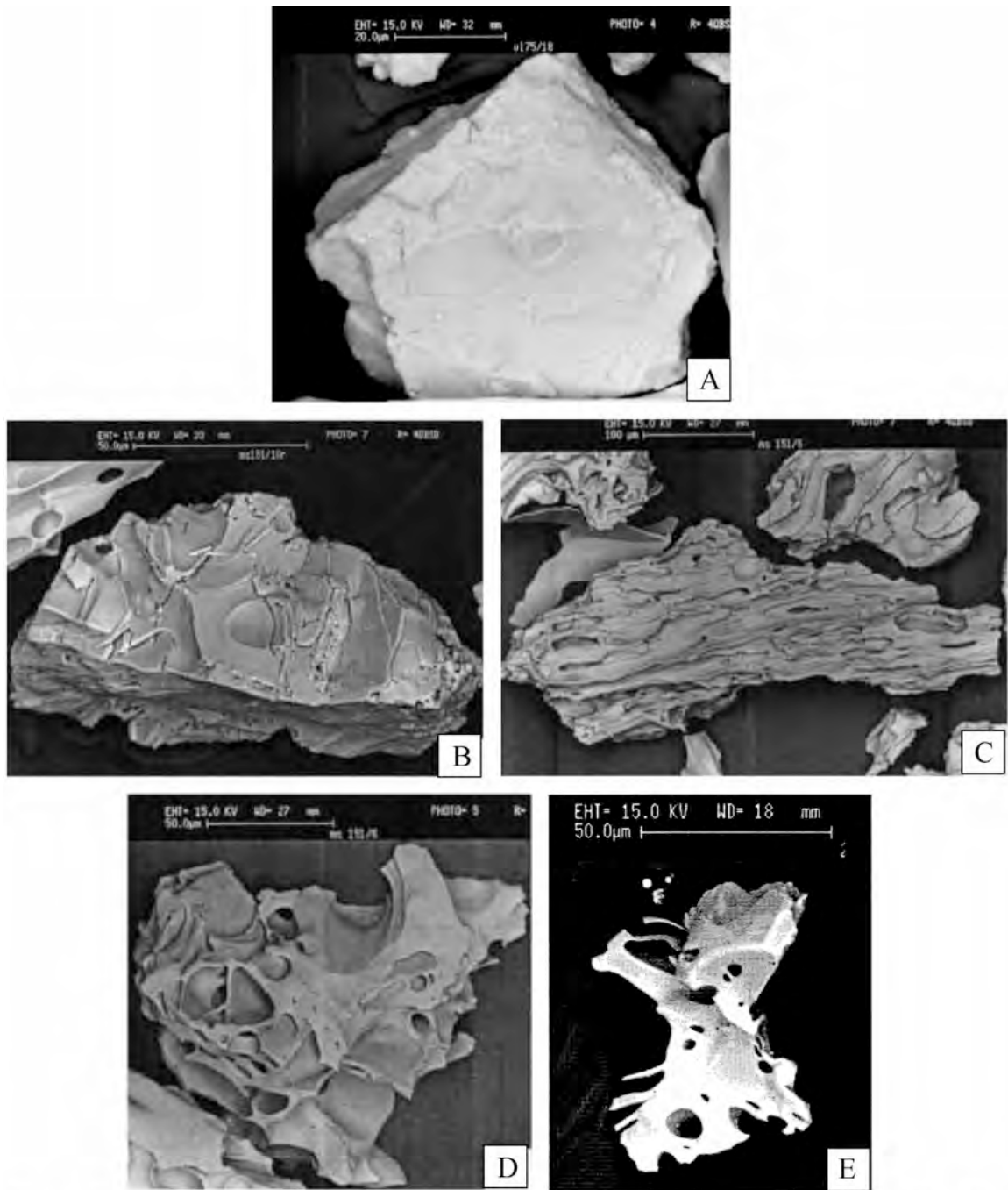


Figure 48: (A) a type-1 grain, with blocky form and planar surface (Buettner et al., 1999); (B) a type-2 grain with angular form and slightly irregular outline (Dellino et al., 2001); (C) a type-3 grain, with elongate form, high vesicularity and irregular outline (Dellino et al., 2001); (D) a blocky type-4 with blocky form and re-entrants defined by vesicle walls (Dellino et al., 2001); (E) a type-5 grain, with highly irregular shape (Dellino and Liotino, 2002).

Dellino et al. (2001) used these 5 categories with a multivariate statistical analysis technique to examine fragmentation processes of pyroclasts within a given deposit from Agnano-Monte Spina tephra. The authors found ash beds that contained both phreatomagmatic and magmatic pyroclasts, a process attributed to inhomogeneous gas exsolution during magma ascent and localized phreatomagmatic processes. The authors also found fine ash beds produced solely by magmatic processes, which emphasizes that fine ash alone cannot be used to determine fragmentation processes.

Furthermore, Dellino et al. (1996) found that only grain types 1-3 are associated with distinct surface features directly related to water-magma interactions, and these grains appear to be the most important characteristics in identifying phreatomagmatic eruptive processes. These features include dendritic quench cracks, stepped fractures, chemical pitting, and adhering ash particles (Figure 49). Branching quench cracks result from rapid acceleration of a newly fragmented particle through excess water. The difference between quench cracks and breadcrust texture is the interior – quenched grains have dense interiors whereas breadcrust bombs result from a vesiculating interior (Fisher and Schmincke, 1984). Quench cracks are also different from linear cracks on grains that result from bubble expansion, hydration, or transport abrasion (impact cracks). Stepped fractures are aptly named, as they resemble stairsteps, and are caused by a very high pressure of fragmentation that results in particles with a high surface area to mass ratio (Zimanowski et al., 2003) and indicate effective heat transfer (Büttner et al., 1999). Chemical pitting is caused by corrosive hot fluids on a fresh glass surface, a texture most easily acquired by particles directly involved in the fragmentation process (Heiken and Wohletz, 1985). The result is scattered spherical holes on the surface of a grain that are

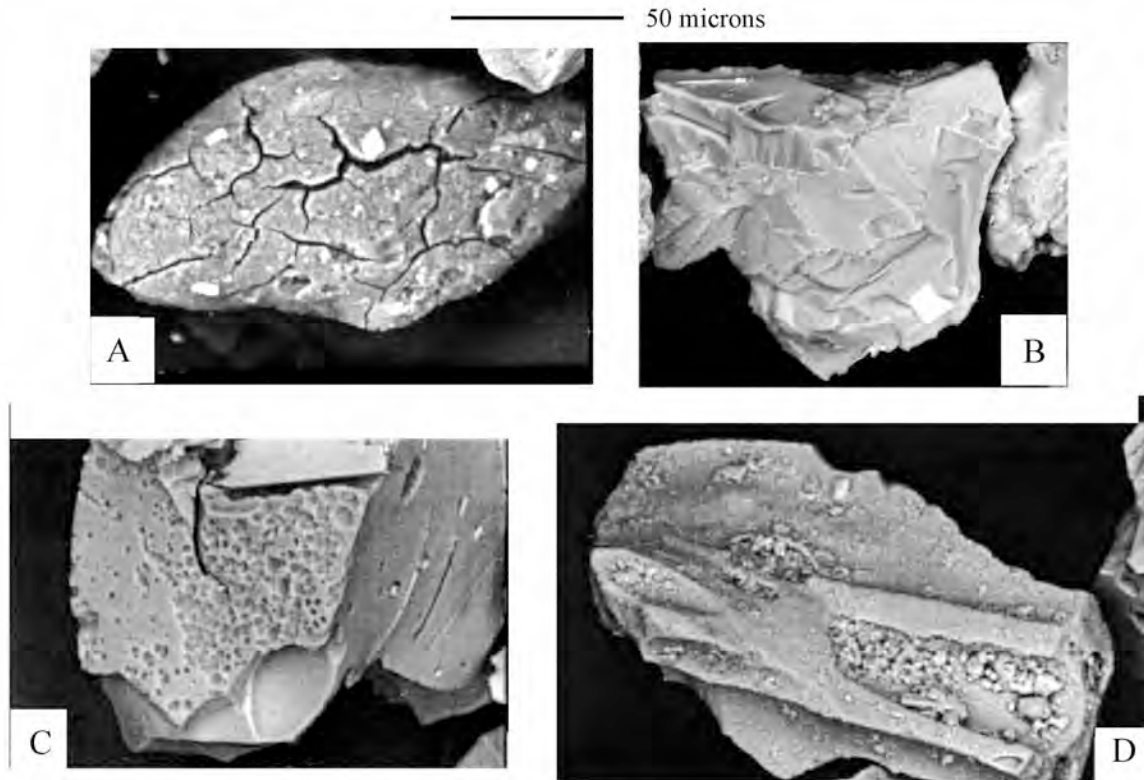


Figure 49: Surface textural features associated with phreatomagmatic fragmentation. (A) dendritic quench cracks (Büttner et al., 1999); (B) a type-1 grain with the characteristic, high surface area stepped fractures of active particles (Dellino and Kyriakopoulos, 2003); (C) micron-scale chemical pitting on the surface of a blocky clast (Dellino et al., 2001); (D) interstitial fine ash adhering to the vesicles of a type-3 grain (Dellino et al., 2001).

enriched in Mg and Fe (Dellino et al., 2001). Adhering fine ash is due to water in the eruptive system, which causes small vitric particles to ‘stick’ to larger grains. These same surface features were identified on experimental phreatomagmatic basaltic particles, which suggests that brittle response during phreatomagmatic fragmentation is similar for basalts and rhyolites, with similar textures and grain sizes being produced (Zimanowski et al., 1997b; Büttner et al., 1999).

E. SEM Analyses

a. Methods

Particle characterization was done for the 4-phi fraction of representative samples from each unit, using Back-Scatter Imagery (BSE) with a Scanning Electron Microscope (SEM). In addition to being an easy means of comparison with existing literature, the 4-phi grain size was characterized as an important subpopulation peak in Tepexitl stage-2 deposits, a trend that appears to reflect a primary fragmentation signature of the magma. The grain morphology categories from Dellino et al. (1996) were adopted for this study as a preliminary classification of Tepexitl deposits. For the purposes of this study, particle shape is analyzed in a qualitative way, with each deposit characterized by the dominant particle associations. Because the rhyolitic particle categories have not been subject to the same experimental evaluation as basaltic particles, the mechanisms for fragmentation remain poorly understood. Following experimental identification of the genetic origin of each association, quantitative analysis can be done (using detailed shape analysis to determine the surface area produced by phreatomagmatic fragmentation, which can then be used to estimate eruption energy of a given explosion).

Unfortunately, an energy dispersive spectrometer (EDS) was not available during imaging for surficial chemical composition. Therefore, particles were classified in a conservative manner so as to limit misidentification of juvenile grains. Crystals were recognized either by distinct cleavage or by rounded grains with conchoidal fracture (potential quartz or olivine). Lithic grains were identified by abraded surfaces, rounded edges, extensive chipping due to transport, and the lack of fresh glass. This category includes both Toba Café grains and recycled juvenile grains. Toba Café particles from Tecuítlapa were also examined to compare with Tepexitl images. This comparison, coupled with knowledge of the componentry, led to the identification of anomalous

highly vesicular clasts as cinders. Juvenile particles were defined as any grain with very fresh surfaces coupled with clear evidence of vesicles, branching quench cracks, chemical pitting, and/or fracture planes that could not be attributed to cleavage. All SEM pictures taken as part of this study are included in Appendix 5.

b. Particle Associations

The following are detailed descriptions of each particle association, as seen in Tepexitl deposits:

1. Blocky and equant grains with poor to no vesicularity have mostly planar surfaces that meet at sharp angles and cut across vesicles (Figure 50). Some of these grains have numerous intersecting fracture planes that cause irregular surfaces and have been interpreted as ‘stepped fractures’. Vesicles are 10-30 μm in diameter, spherical to ovoid in shape, and constitute 0-20% of the surface area. Curvilinear fracture surfaces are less common and are associated with rare larger vesicles ($>40 \mu\text{m}$). Fine ash commonly adheres to the surface and/or vesicles of these grains. Chemical pitting and/or branching fractures are seen in rare grains from this association (Figure 51).
2. Angular grains with irregular to wedge shapes have identical vesicularities and surface features as described for association 1, also seen in Figures 50 and 51.
3. Elongate grains with irregular to highly irregular outlines, as described by Dellino et al. (1996), were not observed in Tepexitl deposits.
4. Blocky to angular grains with irregular outlines defined by a combination of planar/curvilinear fracture and concave re-entrants give grains a convolute surface texture (Figure 52). These grains have a higher vesicle abundance, with at least 40% of the visible surface area defined by vesicle walls (rather than planar fracture).

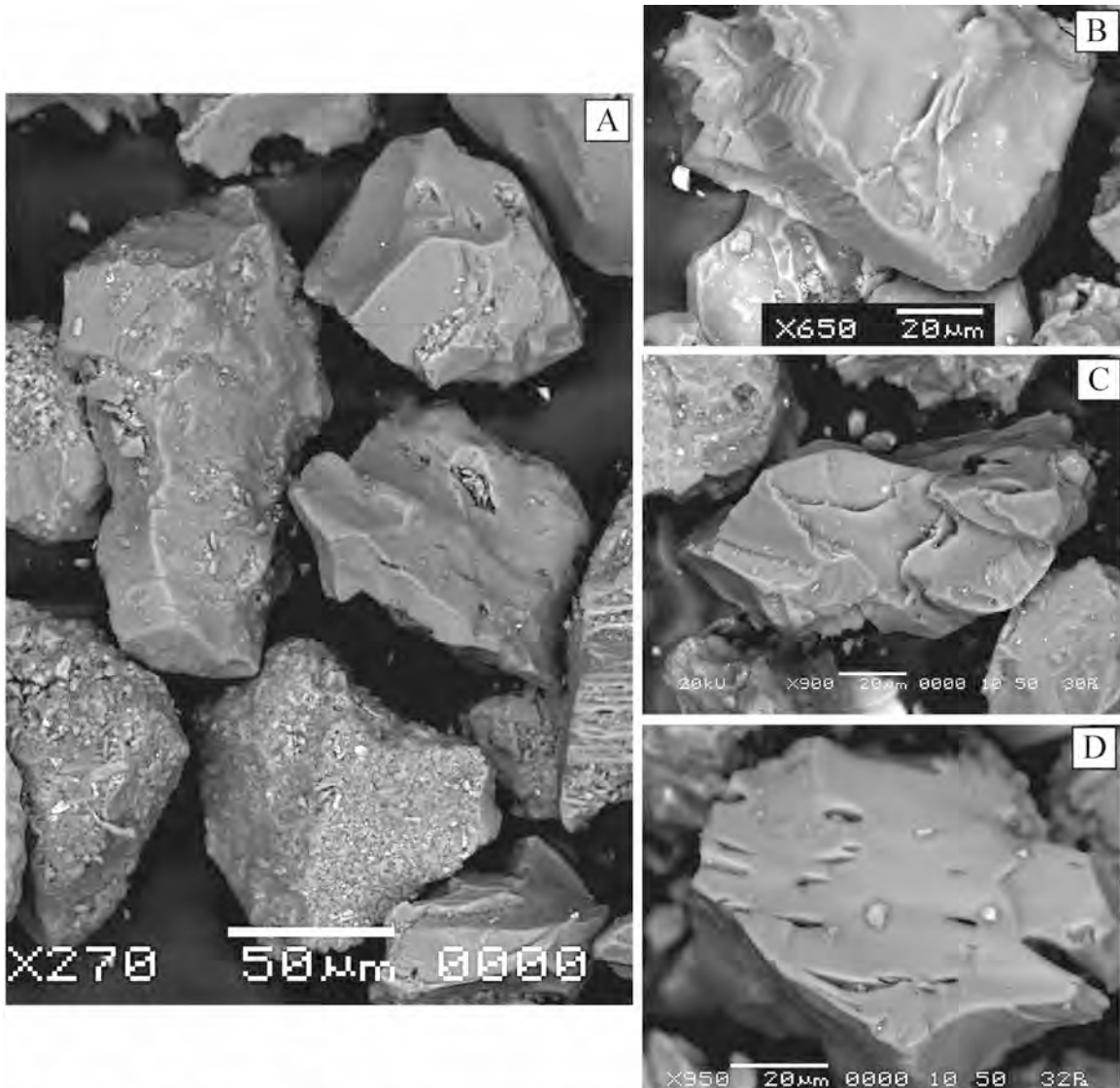


Figure 50: SEM images of brittle fragmentation textures seen in morphology associations 1 and 2: (A; L1 sample 2) poorly- to non- vesicular fresh juvenile glass and clasts coated in fine ash. The elongate grain on the left and the wedge-shaped grain on the lower right exemplify morphology association 2. The blocky clast seen in the upper right is a typical shape of morphology association 1 and shows both curvilinear and planar fracture planes; (B; L4 sample 5) and (C; L1 sample 2) are morphology associations 1 and 2, respectively, and are non-vesicular. Both grains have stepped fractures, but are of different scales, illustrating the spectrum of appearances this diagnostic feature displays; (D; L3 sample 3) a morphology association 1, blocky grain with a planar fracture that has cut across micron-scale elongate vesicles.

Vesicles themselves account for greater than 20% of total surface area. Remaining septa are μm -scale in thickness and have jagged, sharp edges. Vesicles are

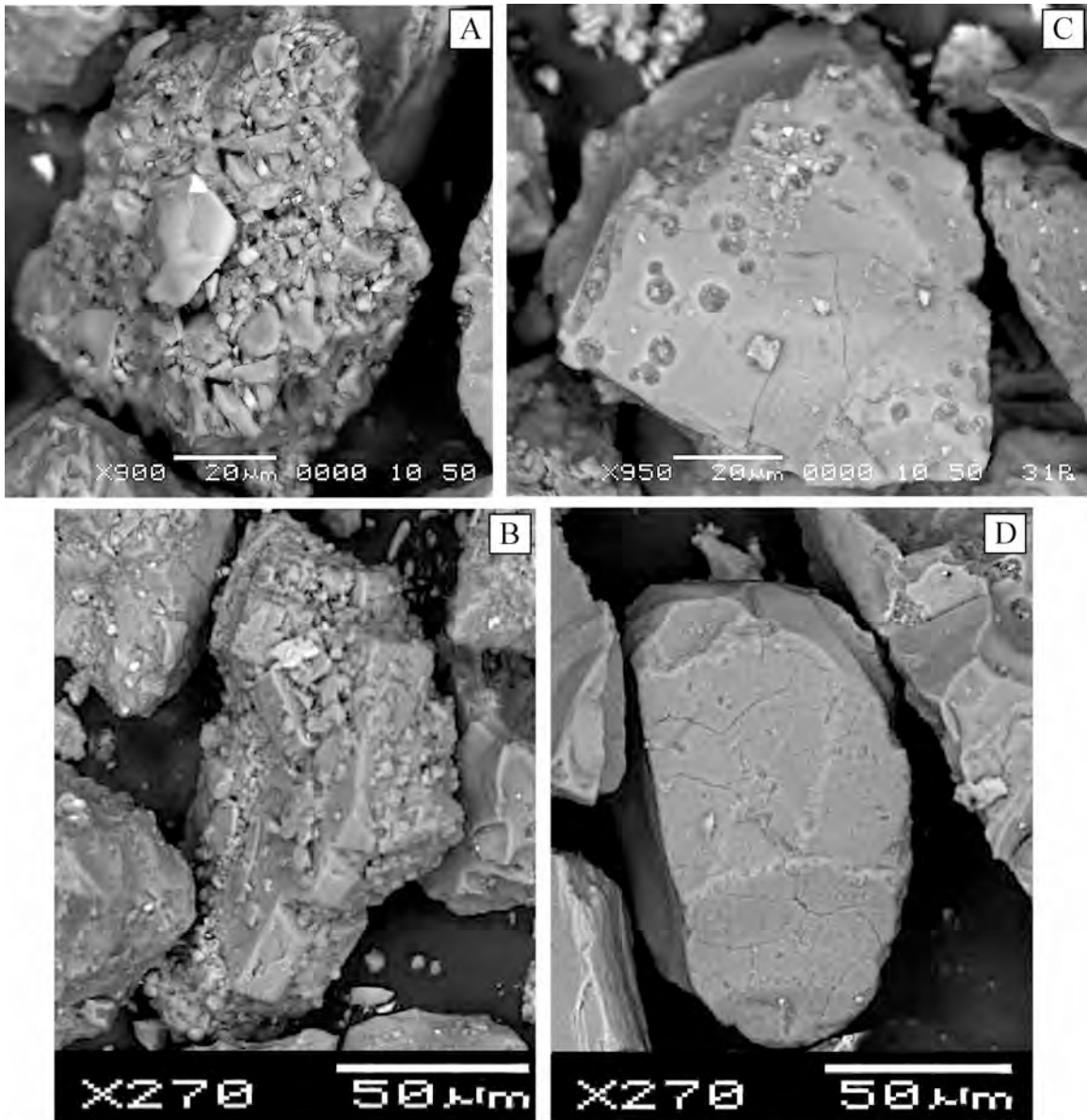


Figure 51: SEM images that illustrate micro-scale textures of surface features associated with grain morphology associations 1 and 2. (A; L1 sample 2) fine ash aggregation that defines the cement of coated clasts, obscuring the underlying clast; (B; L2 sample 1) the fine ash coating of a coated clast has chipped off in places, exposing the underlying larger, nucleus clast. Note that the coating is nearly 50 microns thick in the upper left; (C; L3 sample 3) micron-scale chemical pitting on the surface of a non-vesicular, association-1 juvenile clast, which also has minor quench cracks; (D; L2 sample 10) exemplifies dendritic quench cracks, on a non-vesicular association-2 juvenile clast.

dominantly tubular to ovoid, and are from a few μm to greater than $100 \mu\text{m}$ in length, with dominant sizes between $30\text{-}60 \mu\text{m}$. No branching cracks or chemical

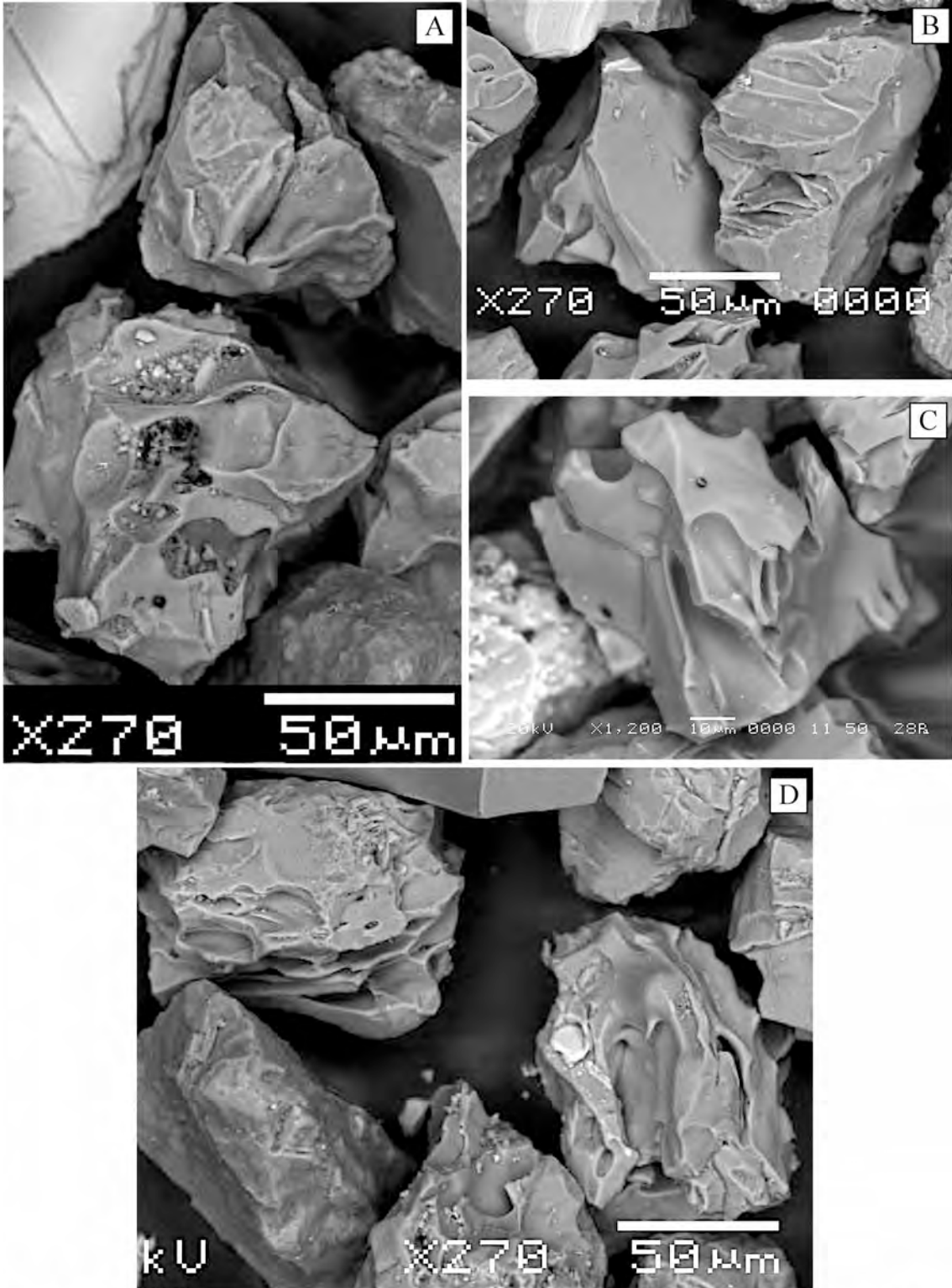


Figure 52: SEM images of particles with magmatic characteristics. (A; L4, sample 10) particle-association-4 grains. The top grain shows the 'viscous deformation' that characterizes many of these clasts; (B; U2, sample 3) the grain on the right illustrates the combination form of blocky, planar fracture and concave-convex outline, defined by vesicles, that characterizes particle-association-4 grains. (C; L4, sample 3) a grain of particle-association 5; (D; U2, sample 3) highly vesicular grains typical of upper sequence deposits.

pitting are visible, although rare interstitial fine ash and stepped fractures are observed. Many grains have a fluidal appearance that gives the impression of viscous deformation prior to (or because of) fragmentation.

5. Irregular shapes with concave-convex outlines and no planar fracture planes (Figure 52). At least 70% of the surface area is defined by vesicle walls, mostly ovoid to contorted, with remaining septa, vesicle characteristics, and surface features the same as those defined for association 4.

Finally, coated clasts (or armored lapilli) are rounded, blocky to elongate, fine-ash aggregates whose surface is characterized by a cemented accretion of dense, angular fine ash dominantly of 5-15 μm -scale, with a range of sizes from sub- μm to 20 μm (Figure 51). This coating is rarely chipped away to expose a larger underlying 'seed' grain (of greater than 50 μm in diameter). There does not appear to be any size grading of the accretionary material.

c. Sample Descriptions and Interpretation

Lower sequence deposits are dominated by dense, blocky particles of grain associations 1 and 2, commonly with surface textures that are consistent with both phreatomagmatic fragmentation and excess water in the crater area during eruption (stepped fractures, branching quench cracks, and chemical pitting; Table 14). The lack of surface textures on particles in L5 deposits is consistent with a decrease of water:magma, marking the transition from phreatomagmatic to magmatic fragmentation regimes. Bl-facies deposits in L4 with additional, dominant association-4 grains indicate that both magmatic and phreatomagmatic fragmentation mechanisms were occurring simultaneously late during deposition of the lower sequence.

Table 14: SEM observations and characterizations. ‘Branch’ is short for the dendritic quench cracks, ‘pitting’ for chemical pitting, ‘stepped’ for stepped fractures, and ‘fine ash’ for interstitial adhering fine ash.

Unit, Sample	Facies	Fresh Glass %	Coated Clasts %	Dominant Grain Association				Observed Surface Features			
				1	2	4	5	Branch	Pitting	Stepped	Fine Ash
L1, 2	Tl	25	20	X	X			x	x	x	x
L2, 1	Tl	15	40	X	X			x	x	x	x
L2, 3	Bt	10	40	X	X			x	x	x	x
L3, 4	Tl	10	20	X	X			x	x	x	x
L4, 3	Bl	60	0	X	X	X		x		x	x
L4, 5	Tl	30	25	X	X			x		x	x
L4, 10	Bl	60	<5	X	X	X		x		x	x
L5, 5	Tlap	75	<5	X	X					x	x
U1, 7	Bl	80	<5			X					x
U2, 3	Tlap	85	<5			X	X				x
U2, 7	Tl	40	<5			X					x

Table 15: SEM sample descriptions

Unit, Sample	Comments
L1, 2	Stage 2?; thickest tuff unit of Section 2
L2, 1	Stage 2
L2, 3	Stage 2
L3, 4	Stage 2?; deposit with most lithic clasts of Section 2
L4, 3	Stage 3?; breccia at base of L4
L4, 5	Stage 2?
L4, 10	Stage 1; leads into L5
L5, 5	Stage 3; leads into upper sequence
U1, 7	Eruptive center above the level of crater fill
U2, 3	Located at the base of U2
U2, 7	Contains rounded grains; upper-most deposit of U7

SEM observations of three-stage deposits in the lower sequence confirm componentry descriptions of this sequence (Table 15). Stage-2 deposits have 20-40% coated clasts, very low abundances of fresh glass (between 10-30%), and an average of 50% lithic clasts. Coated clasts are largely limited to stage-2 deposits, which supports the observation that a distinct mechanism during stage-2 eruptions caused an increased production of armored lapilli.

Upper sequence deposits are dominated by fresh glass: high-vesicularity particles of grain associations 4 and 5 that have no surface textures, consistent with eruptions of principally magmatic origin (Table 14). A dominance of grain-association-5 particles in U2 deposits (Sample 3; Table 14) is consistent with an increase of magmatic-dominant processes and a shallower eruption center (higher degrees of gas exsolution) at the end of the Tepexitl formation. The low percentage of fresh glass (40 wt%) and rounded grains in sample U2, 7 (Table 14; 15), the uppermost tuff deposit seen in Sequence 2, may be explained by deposition of recycled grains (perhaps from low-energy phreatic eruptions through crater fill).

The identification of dominant fragmentation textures is an important step toward understanding the mechanisms of fragmentation operating in a shallow, water-rich environment as a highly viscous rhyolite magma moves to the surface. Some significant generalities can be drawn from the SEM data presented here that may apply to such fragmentation at other rhyolitic volcanic centers as well. From these data, it appears that interstitial fine ash is not a good indicator of eruptive process, as it adheres to all grains regardless of fragmentation mechanism. An increase in lithic clasts (from both pre-eruptive sediment and recycled juvenile grains) corresponds to an increase in the phreatomagmatic quality of fresh juvenile grains, which may directly relate to the water:magma mass ratio, an important point that corresponds well with the data presented in chapter 3. Brittle fragmentation can result from both magmatic and phreatomagmatic processes, with planar fracture surfaces on most grains, even in the magmatic end range (grain association 4). Fragmentation does not appear to be related to deposition mechanisms at Tepexitl. Fine-grained deposits are present in magmatic upper-sequence

deposits and coarse-grained deposits with dominantly phreatomagmatic fine ash are present in lower sequence deposits. This means that fine-grained deposits cannot be assumed to be the result of phreatomagmatic processes and coarse-grained deposits cannot be assumed to be the result of purely magmatic processes, an important distinction.

Chapter 6: Discussion

A. Overview

a. Review of Purpose

The primary goal of this study is to examine the pyroclastic deposits of Tepexitl deposits with the intention of exploring fragmentation mechanisms that played a role in the formation of the tuff ring, as well as what the primary variables were that controlled changes in eruptive dynamics. Because it could be established that phreatomagmatic fragmentation did occur, the objective was then to determine both changing eruptive conditions and distinguishing characteristics of the resulting deposits. As this analysis resulted in data that were not consistent with the theories regarding phreatomagmatic fragmentation of the better studied basaltic melts, the ultimate goal was to use these data to propose a mechanism by which phreatomagmatic fragmentation may occur with rhyolitic magma.

b. Geologic Setting

Tepexitl is one of several rhyolitic centers located along a SE-NW trending lineament (with Las Derrumbadas, Cerro Pinto, and Cerro Pizarro to the north), all of which are peraluminous rhyolites, but with different ages and strikingly different morphologies. Fault-controlled activity and magma supply/amount of external water likely controlled the size and final appearance of these centers. Tepexitl appears to be the result of a small supply of magma (no final dome) that erupted without any significant pauses in time (no soil horizons or significant erosion within the stratigraphy). Strike and dip measurements indicate that at least three vents were active during the formation of

Tepexitl, and these vents project along the same SE-NW regional rhyolite-dome trend. Identification of the Quetzalapa pumice in Tepexitl deposits indicates eruption occurred less than 23 ky. A combination of field observations (poly lithic river cobbles in outcrop), componentry of lithic grains in comparison to known Toba Café grains from Tecuitlapa, grain-size distribution analyses of deposits, and identification of lithic sediment in thin section (sample 2-2) are strong evidence that saturated fine-grained Toba Café sediment was the pre-eruptive surface deposit and water source, even though it does not crop out within the crater itself.

c. Theories about Rhyolitic Fragmentation and Eruptive Dynamics

Many eruptive centers with silicic tuff rings/cones consist of a dome that has extruded onto its own earlier pyroclastic deposits (Sieh and Bursik, 1986; Sheridan et al., 1987; Houghton et al., 1987; Heiken et al., 1988; Wohletz and Heiken, 1992; Brooker et al., 1993; Roache et al., 2000). Most commonly, the mechanism is thought to be initially explosive phreatomagmatic activity that grades into dominantly magmatic eruptions and passive effusion at the end. The deposits of the phreatomagmatic tuff rings/cones described in the references above bear remarkable similarities to those found at Tepexitl: the tuff deposits are generally alternating thinly bedded coarse and fine beds from a combination of surges and falls, commonly with associated bomb sags and accretionary lapilli. The deposits are lithic poor with blocky, angular juvenile clasts that have overall low vesicularity and the craters contain reworked clasts and, in some cases, explosion breccia. More pumiceous clasts are consistently related to magmatic processes whereas vesicle-poor clasts are connected to phreatomagmatic activity, yet both types of clasts are commonly found in the same deposit

Similar morphologies and patterns can also be seen in the other rhyolitic centers in the Serdán-Oriental Basin. Cerro Pizarro is interpreted as an effusive dome intruding through earlier phreatic deposits, with magmatic pyroclastic material being ejected from the growing dome (and a possible phreatomagmatic component?) (Riggs and Carrasco-Núñez, 2004). The resulting deposits are weakly vesicular and poor in lithic fragments. Similarly, Las Derrumbadas dome complex began with phreatomagmatic pyroclastic eruptions that became drier and more magmatic with time, ending with dome extrusion (Siebe et al., 1995). Also, Cerro Pinto has both tuff rings and domes, with at least some phreatomagmatic component contributing to the formation of pyroclastic material (Zimmer, 2007).

The co-existence of cohesive tuff and coarse-grained juvenile breccia, coupled with both blocky and pumiceous clasts, in such rhyolitic centers have elicited extensive speculation about the fragmentation processes that govern the resulting morphology. Several theories are presented here and will be returned to following an examination of trends seen in Tepexitl data:

1. Pure phreatic (or phreatomagmatic) behavior during early pyroclastic deposition that gradually grades into passive effusion at the end of deposition, possibly as the result of decreases in water availability and/or degree of degassing (e.g.. Sheridan and Updike, 1975; Riggs and Carrasco-Núñez, 2004).
2. Phreatomagmatic and magmatic fragmentation occur simultaneously from different vents within the same crater (e.g.. Leat and Thompson, 1988; Houghton et al., 1999; Ort et al., 2000; Dellino et al., 2004). Shallow differences in magma

supply, conduit geometry, magma flux rate, and local magma:water mass ratios at different vent locations would have a large influence on the fragmentation style.

3. Phreatomagmatic/phreatic eruptions through wet crater fill occur simultaneously as magmatic fragmentation during dome growth (e.g., Houghton et al., 1987). Dellino et al. (1990) also found that phreatomagmatic eruption at La Fossa di Vulcano occurred when the conduit was entirely open, with the resulting deposits containing rare lithic clasts (3%).
4. Phreatomagmatic and magmatic fragmentation occur simultaneously from different areas of the same vent, a condition that does not necessarily require dome growth (Dellino and La Volpe, 1995; Dellino et al., 2001). Dellino and La Volpe (1995) propose that vesiculating magma in the conduit can be ejected at the same time as phreatomagmatic eruption of the dense, chilled magma along the conduit walls, which implies that the fragmentation mechanism may depend largely on conduit geometry and can be a very localized process.
5. Phreatomagmatic and magmatic fragmentation may occur from the same vent, alternating with each other on a short time scale, as repetitive magmatic response to release of pressure following decompression from phreatomagmatic eruption. Dellino et al. (2001) suggest that even a small phreatomagmatic explosion may be enough to trigger elastic expansion of the system and much larger magmatic response. Experimental evidence indicates that explosive fragmentation caused by rapid decompression is a viable mechanism for eruption of viscous magma (Alidibirov and Dingwell, 1996; Ichihara et al., 2002).

Additional variables have been suggested as controlling factors in rhyolitic phreatomagmatism. Some rhyolitic phreatomagmatic tuff rings formed when magma encountered saturated, unconsolidated sediments (Heiken and Wohletz, 1987; Brooker et al., 1993; Roache et al., 2000; Lorenz and Haneke, 2004), in some cases when traveling upward along a fault plane (Brooker et al., 1993; Lorenz and Haneke, 2004). Small rhyolitic diatremes only occur along faults in the Saar-Nahe Basin, not in the surrounding countryside (Lorenz and Haneke, 2004). Shallow eruption foci are commonly reported for the source of explosive activity (Houghton et al., 1987; Brooker et al., 1993) and may be connected to the lower percentage of lithic clasts found in rhyolitic phreatomagmatic tuff when compared to basaltic phreatomagmatic deposits.

Previous research on peperites demonstrates that viscosity is a large control on the style of mixing, which is limited to blocky, brittle fragmentation (Busby-Spera and White, 1987; Dadd and Wagner, 2002), rather than the globular mixing associated with Rayleigh-Taylor and Kelvin-Helmholtz instabilities that occur during MFCI. Given that coarse mixing has been determined to be a prerequisite for explosive phreatomagmatic eruption, increased viscosity has very important consequences for phreatomagmatism. An additional control that has a large effect on shallow eruptions of a gas-rich magma is the degree of vesiculation at the time of contact with external water. Dellino and La Volpe (1995) concluded that rhyolitic phreatomagmatic eruptions can only take place with poorly vesicular magma. Busby-Spera and White (1987) concluded that, in high-viscosity systems with low mass ratios of magma to water, insufficient heat transfer results and thus no dynamic mixing occurs. However, identification of active particles in rhyolitic pyroclastic deposits (e.g. Dellino et al., 1996) implies that even with limited coarse

mixing, phreatomagmatism can occur, which implies that there must be a different mechanism governing the eruptive dynamics between a high viscosity magma and shallow external water.

Phreatomagmatic eruptions do not commonly form a sustained eruption column but rather produce pulsatory, directed surges (Wilson and Houghton, 2000; Dellino et al., 2004; Vazquez and Ort, 2006). These discrete pulses can vary both in intensity on a short time scale (Wilson and Houghton, 2000) and in fragmentation of the pyroclast deposits (Valentine and Giannetti, 1995; Dellino et al., 2004). In the case of contemporaneous but differing fragmentation mechanisms, Dellino et al. (2004) found at Campi Flegrei that the more pumiceous, magmatically fragmented clasts were partitioned into the plume and subsequent fallout, whereas the dense and wet phreatomagmatic fragments were concentrated in surges. Similar patterns were observed at Ukinrek maars (Ort et al., 2000), Roccamonfina caldera (Valentine and Giannetti, 1995), and at Monte Pilato pumice cone (Dellino and La Volpe, 1995). From these examples, it is clear that style of fragmentation can play a dominant role in the subsequent energy of the system and the transportation and depositional systems that result, and should be considered when examining the eruptive sequence at Tepexitl

The researchers whose work is described above interpreted that fine-grained beds result from high-energy, high-efficiency eruptions - the consequence of phreatomagmatism and fine fragmentation of juvenile magma. However, there are other ways to generate fine-grained beds that do not involve phreatomagmatism and should also be taken into consideration. Magmatic fragmentation can cause fine fragmentation of ash grains (Zimanowski et al., 2003), including elutriated ash from the umbrella of a

sustained column. Phreatic eruptions through crater fill could also result in fine-grained deposits. Asymmetrical deposition of these fine-grained deposits may occur from directed blasts caused by vent geometry, wind, and/or topography and may not be associated exclusively with phreatomagmatic fragmentation.

B. Interpretation of the Lower Sequence

a. Overview

Lower sequence deposits are associated with 1. deformed, fine-grained tuff beds, 2. low percentages of blocks and bombs, which are dominated by lithic cobbles and obsidian, and 3. mimicking LOI values for stony rhyolite and obsidian, suggesting that fragmentation of stony rhyolite and quenching of the obsidian occurred at the same location. Additionally, three-stage deposits are limited to the lower sequence. Stage-2 and -3 deposits are connected with peaks in R value, which correspond to peaks in both lithic clasts and juvenile clasts. The peak at 4 phi in stage-2 deposits is a dominant fragmentation peak, with juvenile material likely being created in the fine ash size range. Grain morphology associations 1 and 2, which show surface features consistent with phreatomagmatic fragmentation, dominate the juvenile material in this size range. Thus, the lower sequence is interpreted to have been deposited by high-energy, wet surges ejected as a result of repeated phreatomagmatic explosion. The three-stage deposits and other important depositional changes can be used to further constrain the conditions required for effective phreatomagmatic eruption of a rhyolitic magma.

b. Proposed Mechanism for Phreatomagmatism

Patterns observed in Tepexitl deposits are evidence that coarse mixing of a high viscosity melt and external water can occur, but the manner and mechanism for such mixing needs to be explored. Any theory based on Tepexitl deposits must explain the observed componentry of the three-stage deposits, the sharp contacts and thinly bedded nature of this sequence, and the perceived deepening of the eruptive center during this process. Zimanowski et al. (1997a) emphasize that it is the rate of transfer of thermal energy to mechanical energy that governs phreatomagmatic efficiency, which in turn depends on the interfacial surface area able to coarsely mix. An increase in viscosity is thought to relate to a decrease in the degree of surface area exposed to coolant in the traditional sense, which would limit explosivity and intensity of eruption (Zimanowski et al., 1991). Preliminary melting experiments (not included in this study; Austin et al., in preparation) have demonstrated the very high viscosity of Tepexitl magma. The magma melted at much higher temperatures than expected, only becoming fully plastic after several hours at 1300-1350 °C. As a melt, it behaved much like play-doh and was quite sticky. Whereas a basalt at this temperature flows easily, Tepexitl rhyolite must be forcibly manipulated. This difference is mentioned just to provide a mental picture of the likely consistency of the magma when it encountered external water, and to imagine the implications for fragmentation. With such high viscosity magma, interfacial melt instabilities (Rayleigh-Taylor and Kelvin-Helmholtz) probably exist to such limited extents so as to be incapable of initiating phreatomagmatism.

It is proposed here that the requisite surface area needed for efficient heat exchange can be accomplished by hydraulically driven intrusions of fluidized sediment

into fractures that develop along the conduit walls/rising plug during emplacement. For this mechanism to work, the sediment must be able to become fluidized, there must be fractures along the conduit walls and/or tip of rising plug to provide a pathway for sediment, and there must be a way for large volumes of sediment to intrude these fractures. Porosity, permeability, grain size, sorting of the sediments, and degree of saturation are all variables affecting the ability of sediments to become fluidized. Galerne et al. (2006) suggest that fluidization is most efficient when lava interacts with wet, fine-grained, well-sorted, and loosely packed sediment – which could well describe the nature of the Toba Café at the time of eruption. The presence of fractures along conduit walls is also a reasonable assumption to make, as repeated fracturing and reannealing events are thought to occur during upward movement of the magma (as discussed in chapter 3).

Componentry data and LOI data support that obsidian formed along the chilled outer margins of rising Tepexitl magma, and thin-section analysis of sample 2-2 suggests that fluidized sediment was able to intrude fractures in this obsidian. Perlitic pyroclasts and flow-banded perlite are evidence for pre-fragmentation hydration, a localized process associated with hot conduit/vent fluids that come into contact with quenched obsidian. Several workers have proposed that, if fragmented lava is more permeable than the surroundings, high pore pressures will drive fluidized sediment into rapidly forming fractures (Wohletz and Heiken, 1992; Dadd and Van Wagoner, 2002; Gutmann, 2002). Work by Galerne et al. (2006) indicates that diapirs of sediment are able to intrude upward into a melt while protected by a vapor film. Such an interaction would potentially allow a significant amount of fluidized sediment to travel along fractures into the hotter interior of the melt, beyond the quenched exterior.

Vapor-film collapse along these fractures would allow for direct contact of coolant and melt, initiating heat transfer in a confined environment – an experimentally determined requirement for MFCI. If energy released during this process was greater than the overlying lithostatic pressure, a phreatomagmatic explosion would ensue. It is likely that fine fragmentation would occur during initial contact of this process, despite the limited coarse mixing, generating active particles that reflect the high fragmentation energy generated during thermohydraulic coupling. However, the preservation of sediment intrusions into fractures (sample 2-2) indicates that such explosive behavior does not happen along the interface of every fracture, and that the degree of cooling of the melt likely plays a large role in the ability of heat transfer to be effective. The link between water intrusion into fractures and subsequent eruption has already been documented for dome explosions following heavy rainfall events (e.g., Mastin, 1994; Elsworth et al., 2004), observations that supports the viability of this theory.

c. Interpretation of Three-Stage Deposits

The emplacement of the three-stage deposits begins with deposition of a fines-poor, lapilli-sized, obsidian-rich breccia that is associated with Fe-clasts (stage 1), which is followed by a wet, fine-grained bed that is rich in coated clasts, lithic clasts, and coarse ash pumice (stage 2), and finally a stony-rhyolite rich deposit of varying grain size (stage 3). Initial ejection of large obsidian clasts implies that the explosive center was located below or next to quenched obsidian. Fe-clasts found in these deposits indicate that heat transfer was occurring above/adjacent to the obsidian as well, with eruption incorporating nearby hot, wet iron-rich lithic clasts. Both stage-1 and stage-2 deposits contain active particles that indicate excess water interacted with newly fragmented grains at the time of

ejection. Two explanations exist for this process. The first, shown in Figure 53, is that the magma rose vertically through fractured limestone and overlying Toba Café until the energy required for continued upward movement was greater than the energy needed for viscous relaxation and lateral flow, thus causing intrusion into Toba Café (or unconsolidated crater fill) as a sill. Shallower pressures and potential vertical changes in the bedded sediments would likely affect this transition (i.e. from dense, well-packed sediment to looser-packed sediment at shallower levels). Several preserved rhyolitic sills that intruded into high-level unconsolidated wet sediments have been documented (e.g., Lorenz and Haneke, 2002, Dadd and Van Wagoner, 2002; Orth and McPhie, 2003).

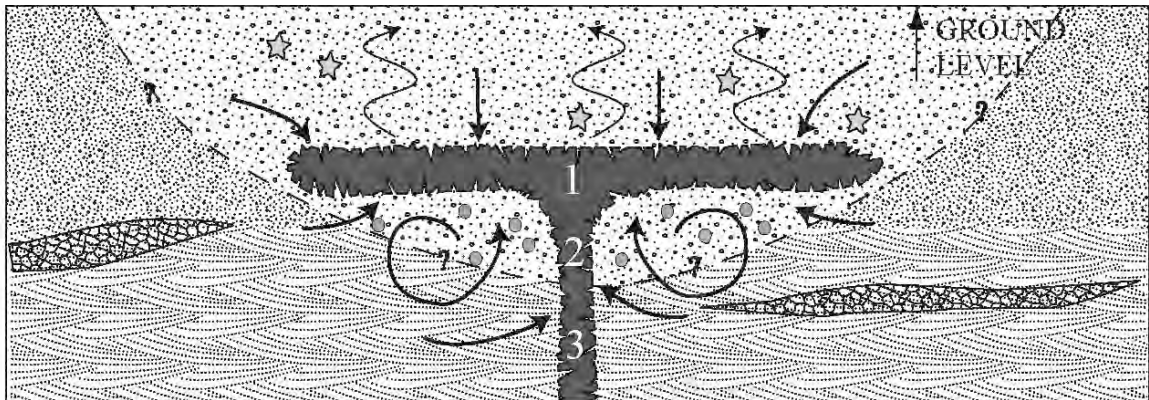


Figure 53: Phreatomagmatic eruption of a sill intrusion, resulting in a three-stage deposit. Numbers indicate hypothesized depth of explosion for each of the three stages. The parabola defined by the dashed line represents the assumed crater and associated fill, with the dark-colored 'T' representing the magma intrusion. Surrounding the crater are lithic sediments of varying properties, as changes in sediment character may affect intrusion level.  represents concentrations of river cobbles. The heavy dark lines indicate potential paths and intrusion sites of fluidized sediment/crater fill. The light black lines represent heat rising from the top of the cooling sill, which in turn may cause formation of Fe-clasts ☆. Potential location of coated clast ● formation is indicated, associated with circulating hot water underneath the pressure cap.

In this hypothesis, the sill would create a pressure cap, which could lead to generation of a localized hydrothermal system, causing convection and heating of underlying sediment (Heiken and Wohletz, 1985). Coated clasts may represent early cementation conditions: movement of hot fluids causes circulation and turbulence of the unconsolidated sediments, which encourages accretion of fine ash to individual, larger ash grains while limiting cementation of the entire sediment package. Circulation rate, age of the hydrothermal system (well-established systems may lead to complete cementation of sediments), and degree of saturation would all be likely controls on the type of deposit produced. Heat would also rise upward and outward from the cooling sill, affecting saturated sediment located above and around the intrusion. Fluidized sediment then has the potential to penetrate fractures along the base of the sill, the top of the sill, or along the conduit walls and cause phreatomagmatic interaction from inside the sill and/or conduit. The thin beds with sharp contacts suggest that each stage of this explosive process was the result of a distinct blast.

Stage 1: The first explosion would be initiated in the hot interior of the sill, initially causing brittle failure and ejection of the overlying quenched material. This would result in both large blocks of obsidian and any surrounding sediment and/or crater fill being deposited in a blast/fall deposit (Figure 53). Fe-clasts present in the lapilli-sized fraction of deposits from this stage indicate heat transfer was occurring to saturated lithic material near the quenched sill margin, which was then incorporated into the eruption. Active particles in the fine ash indicate a phreatomagmatic trigger.

Stage 2: The second blast would eject material from underneath the sill (including coated clasts from the hydrothermal system and lithic clasts from Toba Café; Figure 53)

in a turbulent wet surge. It is proposed that the pumice in stage-2 deposits result from shock-wave triggered fine vesiculation of melt adjacent to the water-magma interface and ejected along with the finer-grained active particles. The viability of fine vesiculation from decompression has been suggested already (Dellino et al., 2001; Lorenz and Haneke, 2004). Additionally, experiments by Ichihara et al. (2002) show that small bubbles are produced in a melt during decompression.

Stage 3: Rapid decompression of the system may also explain stage-3 deposits – shock waves cause brittle failure and fine vesiculation of the underlying magma plug, triggering magmatic response and further eruption (with transportation by both surges and falls) that results in possible deepening of the crater (Figure 53). Magmatic particles observed in the fine ash of L4 stage-3 deposits support this theory. An increase of gas pressure at shallow levels may also play a role in the magmatic fragmentation connected to this process.

The three-stage process is repeated multiple times and results in a deepening of the eruptive center, as each distinct blast taps a progressively lower portion of the rising magma. Deepening may occur into lower levels of pre-eruptive sediment or into lower levels of the crater itself, depending on the depth of the original interaction. The ability of this process to occur at very shallow crater levels may explain the paucity of lithic grains in some rhyolitic phreatomagmatic deposits (3 wt% lithic clasts) when compared to typical basaltic phreatomagmatic deposits (80 wt% lithic clasts; Lorenz, 1987, Dellino et al., 1990). The sharp contacts between beds suggests that some interval of time existed between each blast, possibly enough time for fallback into the crater so that each eruption penetrated overlying crater fill, thus accounting for the more minor variabilities in

componentry. The lack of stony rhyolite blocks in lower sequence deposits suggests that the vesiculating interior of the plug was either very narrow (thus not able to fragment into large blocks) or was very effectively fragmented into ash-sized particles.

Theoretically, the three-stage process could also occur from intrusion of a small obsidian-enveloped, brecciated plug into shallow, saturated sediments. In this case, fluidized sediment would penetrate cracks along the top or side of the plug, initiating phreatomagmatic eruption. The primary difference between a plug versus a sill would be the lack of a hydrothermal system associated with plug intrusion, which means coated clasts must form in the eruptive column from hot mud baking onto the surface of ash grains. However, this process does not explain the lack of coated clasts in stage-1 deposits, which also erupted with hot sediment (as evidenced by the presence of Fe-clasts). Additionally, the lack of coated clasts in sample 3 of L3 despite the high concentration of lithic and pumice clasts could result from the eruptive center deepening below the level of which coated clasts were being formed – more consistent with a hydrothermal genesis for coated clasts rather than from baked mud in the eruptive plume. Thus, intrusion of a sill into shallow, unconsolidated sediments seems more consistent with the data seen at Tepexitl. Deepening of the eruption locus would likely cause diatreme development, with the amount of blocks present in outcrop related to both the degree of diatreme development and the amount of time between explosions for fall-back to occur.

d. Interpretation of L-Units

Unit 1 (L1)

The presence of phreatomagmatic ash, the thick deposits of fine-ash tuff, and the

lack of deformational features in L1 deposits are characteristics consistent with highly efficient, phreatomagmatic eruption. Lithic material increases steadily during deposition of L1, indicative of a progressive deepening of the eruptive center. The lack of large blocks in L1 deposits may also be related to high-efficiency eruptions during the early stages of phreatomagmatism, prior to significant diatreme development (and associated fall-back into the crater).

Componentry data from L1 samples reveal a highly energetic three-stage eruption process was operating during deposition: Sample 2 is a stage-2 deposit without the coated clasts, sample 3 is a stage-1 deposit with an ash-size peak in obsidian (rather than the lapilli-size range), and sample 4 is a 'typical' stage-2 fine-grained deposit with coated clasts. The lack of coated clasts in sample 2 indicates that either excess water was not present in the crater or that hydrothermal circulation was not occurring. Coated clasts were first observed in sample 4, as crater conditions became wetter. Finally, fine-grained obsidian clasts are consistent with high-energy fragmentation of a chilled margin. These deposits are interpreted as resulting from early, highly efficient and energetic phreatomagmatic explosions and resulting surges during low water:magma conditions, in which diatreme development and hydrothermal circulation processes were first initiated.

Unit 2 (L2)

Outcrop features in L2 deposits (bomb sags, scouring, and abundance of dune forms) are consistent with an increase in the water:magma from L1, and LOI and componentry data support a progressive deepening of eruptive hub. The cyclic pattern of three-stage deposits observed in L2 deposits is consistent with multiple, distinct, phreatomagmatic eruptive blasts of similar mechanism, energy, and efficiency through

constant excess water in the vent area, traveling as high-energy wet surges and associated fall-out. L2 deposits contain a higher abundance of large blocks than L1 deposits, which correlates with likely recycling of coarsely fragmented obsidian that falls back into a deepening diatreme (ejected in subsequent blasts). The increase in water seen during deposition of L2 could be related to: 1) a deeper eruptive hub (putting the vent deeper within the water table), and/or 2) pressure release from initial blasts causes an influx of water from surrounding areas to percolate through unconsolidated sediments into the vent area.

Unit 3 (L3)

L3 is composed of deposits from a single three-stage process, each with progressively increasing lithic content. This pattern indicates that the eruptive center was deepening into Toba Café with each blast. Unusually thick stage-1 and stage-2 deposits are not followed by a ‘typical’ stage-3 deposit, but instead by a thick, fine-grained bed of the most lithic-rich ash sampled at Tepexitl (in the sub- 0-phi grain sizes). This sequence is interpreted as resulting from very energetic phreatomagmatic explosions and subsequent wet surges, too rapid and forceful for a magmatic response to occur. A moderate amount of deformational features indicate excess water was still present in crater/vent area and the lack of blocks is consistent with rapid, high-energy explosions that did not allow time for fallback of material into the crater.

Unit 4 (L4)

L4 is the most voluminous unit of the entire tuff ring, with coarse-grained deposits that have high degrees of lateral thinning, marking a change in eruptive style toward lower energy explosions. Additionally, preserved inflection points inside the

crater indicate that this eruptive period was a time of cone building and crater widening. LOI data, coupled with a sharp decrease in 2-phi lithic grains from the end of L3 to the beginning of L4, indicate a steady and/or shallowing of eruptive center (no longer deepening into Toba Cafe). However, the anomalously high abundance of blocks in the basal deposit of L4 supports a shallowing eruptive hub, as rafted chunks from the diatreme were likely incorporated into a rising plug and subsequent eruption. A steady (but slight) increase in lithic clasts during the second part of L4 could be related to localized deepening with crater fill during three-stage process eruptions.

Identification of three-stage deposits and active particles means that phreatomagmatism still played an active role in the fragmentation during L4. However, phreatomagmatic and magmatic activity must have occurred simultaneously, as magmatic ash was also identified in these samples. In addition, pumice concentrations appear to be more affected by magmatic than decompression-related processes. Analysis of pumice concentrations suggests that multiple, volatile-stratified magmatic pulses may have erupted during deposition of L4. It is also possible that L4 was a large-scale magmatic response to the powerful explosions that deposited L3.

The syn-eruption debris flows have also been largely interpreted as resulting from deposition of L4, likely due to slope instabilities common in the deposition of unconsolidated, wet tephra (Sohn and Chough, 1992). The larger clasts and large volume of material that dominate L4 beds were probably less cohesive and more permeable than the largely fine-grained beds below (L1-L3) and thus more susceptible to reworking along the moderate to high angle, water-lubricated contact between depositional units.

In summary, L4 was deposited by lower energy eruptions than those that deposited L1-L3. Both magmatic and phreatomagmatic processes contributed to explosions, which likely occurred from shallow levels within crater fill. The depositional mechanism was dominantly fall and/or directed explosion maelstroms that caused rapid cone building and simultaneous degradation events.

Unit 5 (L5)

The fine-grained, planar, surge-related deposits of L5 represent the end of the lower sequence. L5 begins with the last phreatomagmatic-triggered three-stage-deposit series seen in Tepexitl stratigraphy, which grades into stony-rhyolite-rich deposits whose pumice concentrations are primarily affected by magmatic processes. Ash grains from late L5 have few surface features that indicate excess water was present at the time of fragmentation (branching quench cracks and chemical pitting), but are still mostly composed of grain morphology associations 1 and 2. Deposits dominated by such 'passive' blocky particles may result from magmatic-triggered brittle fragmentation and/or recycling of crater fill. The low percentage of blocks in L5 could also be caused by low-energy phreatic eruptions through crater fill, but may additionally relate to higher efficiency eruptions than those that deposited L4 and/or shallower eruptive levels. Regardless, L5 is interpreted to mark the transition from high-energy phreatomagmatic explosions typical of the lower sequence (early L5) to lower energy magmatic explosions typical of the upper sequence (late L5). It is possible this transition was accompanied by (or caused by) a growing dome and decreasing water:magma.

C. Interpretation of the Upper Sequence

a. Overview

The coarse-grained deposits of the upper sequence lack deformed tuff and three-stage deposits, and are dominated by smooth-textured, grain-morphology-association-4 particles— all strong evidence for deposition from magmatic eruptions. Additionally, pumice concentrations in the upper sequence are consistent with magmatic degassing processes rather than shock-wave triggered vesiculation. Upper sequence deposits are not preserved over the crater rim and block abundance increases significantly from the lower sequence, both characteristics consistent with deposition from lower-energy eruptions. A decrease in fragmentation energy during eruption of the upper sequence is also indicated, as R-value peaks indicate that little to no juvenile material was created in the fine-ash subpopulations.

The eruptive center shallowed during the upper sequence, as evidenced by a significant, progressive decrease in the concentration of lithic grains. Periods of the eruption incorporated no lithic grains at all into the deposits, consistent with an explosion locus above the level of crater fill. LOI values that mirror each other during this eruptive sequence are interpreted to result from different quenching and fragmentation levels, also consistent with a shallowing of eruptive center. This shallowing is likely related the change of dominant juvenile block composition from obsidian to stony rhyolite.

b. Interpretation of U-Units

Unit 1 (U1)

The lower two meters of U1 contain deformed tuff units, indicating that at least some water was still present in the eruptive system when deposition of the upper

sequence began. Above these tuff deposits is a breccia that has a unique combination of clasts: it is rich in coated clasts, obsidian lapilli, and lithic clasts, but depleted in pumice. This breccia is interpreted to result from a vent-clearing event, as such a combination of denser clasts would concentrate in the crater area from recycling during explosive fallback (creating the crater fill, through which an explosive blast must penetrate).

Following this breccia, tuff deposits are non-deformed and 'drier', becoming increasingly poor in lithic clasts. The uppermost deposit is completely devoid of lithic clasts, consistent with an eruptive center above the level of crater fill. This progression is consistent with a shallowing during this phase (dome/plug growth), accompanied by weak, dry pyroclastic eruptions.

Unit 2 (U2)

U2 deposits again contain lithic grains, indicative of a slight deepening of eruptive center, to a level within crater fill. Pumice concentrations suggest that a volatile-stratified magmatic pulse erupted during the second half of U1 deposition, which may have again lowered the fragmentation level to within crater fill during eruption of U2. Fresh, vesicular, magmatic ash particles dominate lower deposits, but the uppermost deposit of U2 is lithic-rich, composed of dense, rounded grains. Such a deposit is consistent with low-energy, phreatic eruptions through crater fill.

Unit 3 (U3)

The thick, lithic-poor breccia deposits and distinct block compositions found along the western inner crater indicate U3 eruptions were unique when compared to the overall stratigraphy for the rest of the tuff ring. U3 is interpreted to be the lateral equivalent of the explosion breccia found along the west side of the inner crater, and is

consistent with explosion by distinct blasts directed to the WNW. Several lines of evidence could connect the explosion to either a dome or a plug at shallow levels: 1) LOI data indicates that upon explosion, the magma was not fully degassed, 2) glass in stony rhyolite thin sections indicate that devitrification was not complete upon explosion, also consistent with incomplete degassing, 3) non-resorbed quartz grains and large plagioclase grains when compared to material from earlier in the eruption suggests that the magma did not reside at shallow levels for long and/or that the flux of magma from deep in the chamber/conduit was rapid, 4) cemented crater fill ejected as breccia blocks, coated clasts in the final deposit of U3 (similar in character to those found in the three-stage deposits), and peperite blocks are all consistent with water circulating in the vent area under a pressure cap, which could result from either dome growth or a shallow plug, 5) the pink color observed in areas of this deposit indicate that explosion happened while the interior of the plug/dome was still hot, and 6) vesiculated breadcrust bombs indicate the magma was still degassing.

However, whether these deposits resulted from explosion of an extrusion above the surface or from a plug that resided below the level of crater fill is debatable. One of the more puzzling aspects of U3 is that if dome growth did occur, the subsequent explosions left no morphological record of its existence. Such complete destruction of a dome is considered unusual and largely depends on the original volume of the dome (i.e. a small dome may be completely destroyed easier than a large dome). An estimate of the volume of material erupted during deposition of U3 is $2.3 \times 10^6 \text{ m}^3$, or 15% of the total volume of the tuff ring. This amount of material would be the equivalent of a very small dome or a plug, but does not necessarily imply that it had a topographic expression within

the crater. Some of the morphological and textural features will be explored here in an attempt to resolve this issue.

Other lines of evidence strongly connect the deposits to dome growth rather than a sub-surface plug: 1) Componentry of U3 deposits reveals only rare lithic clasts in every deposit (0-2%), which is consistent with eruption above the level of crater fill. If a plug was erupting through overlying crater fill, it would be expected that more lithic grains would be incorporated into the deposits as recycled clasts from earlier eruptions, 2) componentry also reveals that U3 deposits are consistent with an ‘upside-down’ dome, as described by Manley and Fink (1987) and Fink and Manley (1987), 3) pumice float blocks have lithophysae textures with vapor phase crystallization, both consistent with formation inside a dome, and 4) group-3 breccia blocks, as described in chapter 4, are most consistent with carapace breccia as they are monolithologic with an ashy matrix and no lithic inclusions.

From the combination of this data, a small dome that extruded onto crater fill is the best explanation for U3 deposits. Explosions began at the surface of the dome and migrated retrogressively downward until the underlying breccias were ejected, leaving no evidence of the original structure, a process also described by Adams et al. (2006), where a similar pyroclastic series from a dacitic dome explosion during the 1912 eruption of Novarupta was documented. The final blocks associated with this eruption including flow-banded, pumiceous, and dense juvenile clasts, commonly with breadcrust textures, as well as fragmented breccia clasts presumed to be from the dome carapace. The mechanism(s) for explosion are not fully understood, and could involve a combination of magmatic, phreatomagmatic, and rainfall triggers. As the magma was poorly degassed

upon extrusion, high amounts of internal gas could have led to pressure build-up within the dome interior that may have triggered explosion. Poorly degassed magma could also result from a high magma flux, which is consistent with the non-resorbed quartz grains and large plagioclase crystals. Higher flux is associated with increased driving pressures and conduit diameter, which leads to more degassing at shallow levels and would have allowed little time for degassing prior to extrusion.

Adams et al. (2006) conclude that dome explosion at Novarupta was due to a combination of incomplete degassing and external water, perhaps rainwater seeping into the hot interior through cracks. External water may also have played a role in the final dome explosion at Tepexitl. Accretionary lapilli in the lowermost tuff beds of U3 are large and well-formed, very different in character from the smaller accretionary lapilli found in lower deposits. It is proposed here that these may reflect formation within storm clouds rather than moisture-rich surges. Elsworth et al. (2004) found that rainfall can cause additional gas pressurization of a dome, a process that has resulted in near-complete removal of lava domes at Montserrat. This process may have initiated explosions that removed the upper parts of the dome.

Phreatomagmatic activity from groundwater may also have played a potential role in the explosion, as surficially altered coated clasts in the final deposit coupled with peperitic textures and cemented crater fill present as float blocks imply that water was present beneath the dome during intrusion and/or at the end of the eruption. It is possible that weak phreatomagmatism (from rainwater and/or groundwater) caused initiation of dome explosion and/or caused the final explosions that removed the lower parts of the dome. Some of the breccias may potentially represent underlying diatreme material as

well, ejected from the final, deep explosions that removed the dome. Limestone blocks are found in drainages around the western side of the crater, although such blocks were not observed in crater wall deposits. They could indicate that the final phase of the eruption ejected material from the limestone basement, or that these blocks were rafted upward during dome extrusion and were erupted only at the end of the eruptive sequence.

c. Late-Stage Deposits

Late-stage deposits are seen in an arc from north to south along the eastern side of the inner crater, lapping onto the older debris-flow deposits (from syn- and/or post-L4). Late-stage deposits contain abundant deformational features, which indicate that they were wet upon deposition. As the tuff units of U2 and U3 are 'dry', the late-stage deposits most likely correlate with the transition from the lower sequence to the upper sequence, during deposition of L5 and/or U1.

D. Conclusions

a. Depositional Changes and Their Importance

Beginning with L5, the primary axis of deposition (PAD) changed from a single dominant depositional direction (to the southeast) to more than one dominant depositional direction, both with a strong western component (SW and NW). This trend is especially noticeable in Section 4 (eastern inner crater), which has abruptly fine-grained and laminated deposits from the end of L4 to the crater rim. Another indicator of low-energy deposition in the eastern half of the crater during eruptions of L5-U3 is the limited presence of late-stage deposits to that sector. The deposits of L5 and U1 are most poorly sorted in the SW (Section 2) and coarsest-grained in the NW (Section 2).

It appears that the transition from lower to upper sequence was marked by changes in depositional regime. Lower sequence eruptions likely resulted in directed, high-energy, wet surges to the southeast. In contrast, all upper-sequence deposits indicate that low-energy blasts were directed to the west. Additionally, L5 and U1 deposits show evidence for temporal overlap of eruptions from multiple sources. Upper sequence eruptive dynamics may have resulted from: 1) activity occurring from multiple vents (i.e. one vent with dome growth and another with pyroclastic activity); 2) peripheral phreatic eruptions occurring through saturated crater fill along the side of a growing dome, coupled with shallow-level magmatic eruptions; 3) multiple fragmentation and depositional systems operating within a single vent either simultaneously or alternating with each other on a short time scale (controlled by vent geometry, magma supply, and shallow controls on the eruptive system); and/or 4) a change in wind direction and weather patterns.

Dome growth during the upper sequence would have created an inner crater obstacle that affected both fragmentation and depositional processes, regardless of the number of active vents. At Tepexitl, dome growth likely occurred in limited areas of the western inner crater (possibly piling up along the base of the wall, as in Figure 54), effectively limiting surge-related deposition and build-up of crater walls to the eastern sections of the crater. Final, dome-destroying explosions were focused to the S and SW, causing crater expansion in those directions and resulting in the final, symmetrical tuff ring morphology. However, the lack of visible outcrop on the crater floor and western walls made it difficult to determine dome-growth dynamics. Extrusion could have

occurred: 1) from a single vent; 2) simultaneously from multiple vents; or 3) from distinct areas of the crater at different times.

Late-stage deposits in the eastern crater indicate that eruptive activity produced highly variable strike and dip patterns early during the dome-growth cycle. These deposits could result from: 1) low-energy phreatic/phreatomagmatic eruptions from one or more vents, while extrusion occurred elsewhere in the crater. Resulting surges would have been 'blocked' by the dome, limited circulation to within the eastern inner crater. The varied strikes and dips may represent reworking of these surges as they ramped off crater walls prior to final deposition. 2) Shallow phreatic/phreatomagmatic eruptions along the margins of a growing dome(s; Figure 54). Resulting surges would have been directed at varied angles, depending on dome geometry and crater characteristics.

In contrast, eruptions during deposition of U2 are most consistent with recycling of crater fill from eruptions with single PADs to the SW. Such deposits could result from either of these hypotheses (Figure 54). Final dome explosion (U3) was directed to the NNW (as in Figure 54). U3 deposits are most consistent with directed dome explosions. The 'thumb' in the SE sector of the inner crater is interpreted to be the location of 1-2 primary vents and is possibly the result of a late cryptodome that lifted crater fill material, or remanent debris from shallow, final dome explosions.

The variety of plausible theories for Tepexitl deposits implies that that fragmentation and depositional processes occurring over the course of a rhyolitic pyroclastic eruption are dynamic, changeable and are likely affected by many variables. Although phreatomagmatic behavior at the beginning of the eruption (lower sequence)

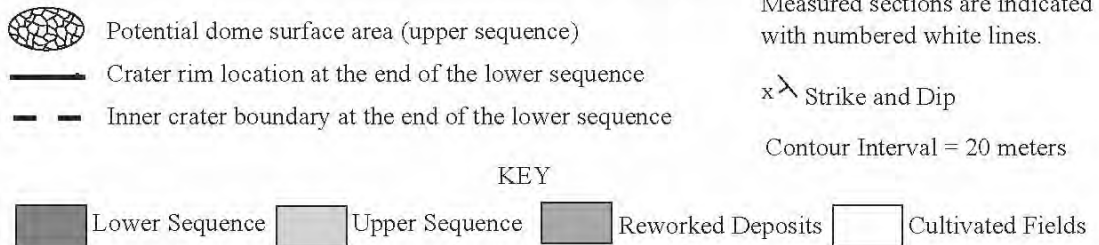
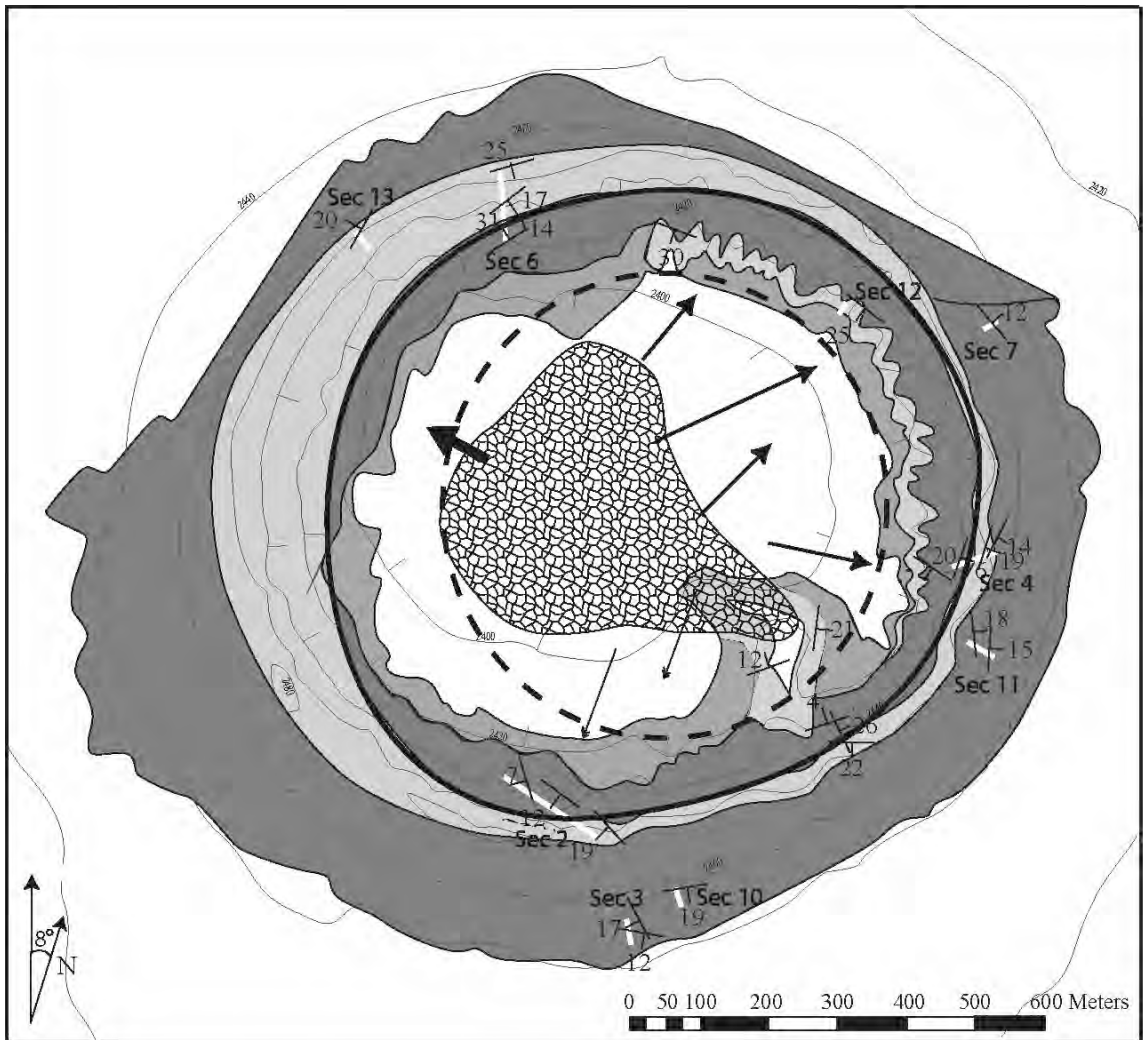


Figure 54: Potential final dome configuration within the inner crater. when crater rim and inner-crater boundary were likely centered around the NW-SE alignment of active vents. The boundary between lower and upper sequences was approximated by stitching photographs together and tracing beds around the inner crater, using stratigraphic sections as guides. This boundary is consistent with crater rim location when dome growth began. Marginal pyroclastic explosions to the east  occurred caused emplacement of the late-stage deposits. U2 deposits were directed to the SW  and could have originated from a southern vent, or from the margin of a dome. Final dome explosions  were directed to the west, widening the crater to its present-day shape, where the upper boundary of upper-sequence deposits is aligned with the current crater rim

graded into passive effusion at the end of the eruption (upper sequence), eruptive dynamics within these different phases of Tepexitl formation were complex. The resulting morphology of Tepexitl reflects these various eruptive regimes. Differences in slope angles of the exterior of the maar correlate with changing eruption patterns. The steepest apron slopes are in a clockwise arc from the ENE to the SW and correspond with an initial PAD to the SE, during deposition of the lower sequence when the deposits were wetter and more coherent. The shallower slopes to the SW correspond to deposition of L5-U3. The drier, coarser deposits of this phase were less cohesive and more susceptible to erosion. The shallowest slopes are to the NW and correlate with the poorly consolidated, easily eroded deposits from the final dome explosion.

b. Transition from Explosive to Effusive Behavior

The transition from explosive to effusive behavior at Tepexitl was accompanied by a change of dominant juvenile block composition from obsidian to stony rhyolite, which contain quartz grain textures that indicate a deeper source for the magma erupted during the upper sequence. Additionally, LOI data indicate that dome extrusion occurred at Tepexitl despite having high internal volatile contents. This combination of evidence suggests that the upper sequence eruption happened relatively quickly (rapid flux from depth), prior to complete degassing.

Heiken and Wohletz (1985) suggest that congealing of lava onto conduit walls (also consistent with an increase in flux) would block water access to the interior of the plug, thus limiting potential phreatomagmatic activity. Even if water did have access to the magma, the increase in internal degassing associated with lower pressures (shallower eruptive centers) would likely decrease the ability of a vapor film to effectively transfer

heat. The eruptive transition happened after deposition of L4, a particularly voluminous unit. It is possible erosive shearing occurred during eruption of L4, widening the conduit and causing both a decrease in phreatomagmatic behavior and an increase in the magma supply able to reach the surface.

c. Variables and Controls on Fragmentation

The intensity and style of fragmentation and eruption regimes during shallow rhyolitic intrusions through saturated sediments are shown to depend largely on shallow controls: depth of interaction, water: magma mass ratio, nature of the coolant, conduit geometry, flux rate and supply of the magma, degree of volatile exsolution, and structural features of basement rocks. The most efficient phreatomagmatic eruptions occurred early in the lower sequence, during deeper interactions and lower water:magma. However, if saturated sediments cannot be fluidized and intruded into fractures, phreatomagmatic eruption would likely be limited. Therefore, the nature of the coolant and the ability for heat transfer to occur play large roles in initiation of phreatomagmatic eruption. Conduit geometry controls both the volume of magma able to reach the surface as well as the volume of water able to gain access to the vent, variables affecting necessary surface area for efficient heat transfer. Dome growth following conduit widening appears to be related to an increased flux of magma from deeper levels and drier vent conditions.

Low amounts of vesiculation do not appear to be important to brittle fragmentation processes in Tepexitl rhyolites. However, phreatomagmatic fragmentation is limited to low-vesicularity magmas, so the degree of vesicularity could be a very important factor in determining the potential for phreatomagmatic eruption. From a hazards point of view, a volcanically active area with intra-basinal fine-grained saturated

sediments and a history of high-silica extrusions is at risk for future eruptions that begin with highly explosive phreatomagmatic eruptions and become less efficient and energetic with time. Especially at risk are areas along faults, as this situation seems to favor triggering phreatomagmatism with highly viscous melts.

d. Facies and Eruptive Processes

Six distinct facies represent all the deposits seen at Tepexitl, regardless of stratigraphic location. Grain-size distributions within facies remain comparable regardless of changes in fragmentation regimes with time (i.e. phreatomagmatic-triggered fine-ash beds of L1 have grain-size distributions similar to magmatically fragmented fine-ash beds of U1). This similar resulting granulometry of deposits could be accounted for by physical properties of the melt that produce characteristic grain sizes despite fragmentation mechanism (i.e. brittle failure to a melt with low tensile strength). Such parameters are difficult to evaluate post-eruption. Transportation processes may account for some degree of sorting within the deposits, but the granulometry of near-vent facies are more likely to be affected by vent processes. Based on the data, it appears that changes in componentry with time are more directly related to fragmentation processes than changes in grain-size distribution of a deposit.

e. Eruptive Summary and Universal Application

Early lower-sequence eruptions at Tepexitl were dominated by discrete, highly-efficient, phreatomagmatic blasts, which caused a progressive deepening of the eruptive center (Figure 54). Such downward penetration would have caused hydraulic pressures to lower the water table at the vent, resulting in directed eruption of progressively wetter surges. The powerful eruptions of L3 and corresponding large-scale magmatic response

deposits of L4 mark the end of diatreme development, as water supply diminished and explosion loci became shallower (Figure 55). The subsequent transition to dominantly magmatic behavior was defined by a combination of phreatomagmatic and magmatic explosions, likely with some degree of temporal overlap from multiple vents. Increased flux rates of fresh magma caused rapid dome growth, which was accompanied by marginal, low-energy, phreatic eruptions through crater fill. Subsequent complete retrogressive dome explosions, likely triggered by a combination of incomplete degassing and external water (storm water and/or groundwater), left no trace of the original dome morphology.

Phreatomagmatic deposits are fine-grained, planar to highly deformed, and are dominated by angular, non-vesicular ash particles. These result from deposition by variably wet to dry surges. Magmatic deposits are largely coarse-grained, thicker, and less coherent, primarily the result of fall-out and directed blasts. However, overall vesicularity of these deposits remains low (less than 40% vesicularity), and many grains have planar fracture faces consistent with brittle fragmentation.

Such a sequence is likely representative of many high-viscosity intrusions into shallow, unconsolidated, saturated sediments. Thus, it seems plausible that the conclusions drawn from Tepexitl can be applied to similar volcanically-active areas around the globe, to be used as a tool in understanding a likely eruptive progression and associated hazards (see Lorenz, 2007), particularly in 'at-risk' zones: areas with a high water table, high sediment flux, basement faulting, and a recent history of high-silica intrusions.

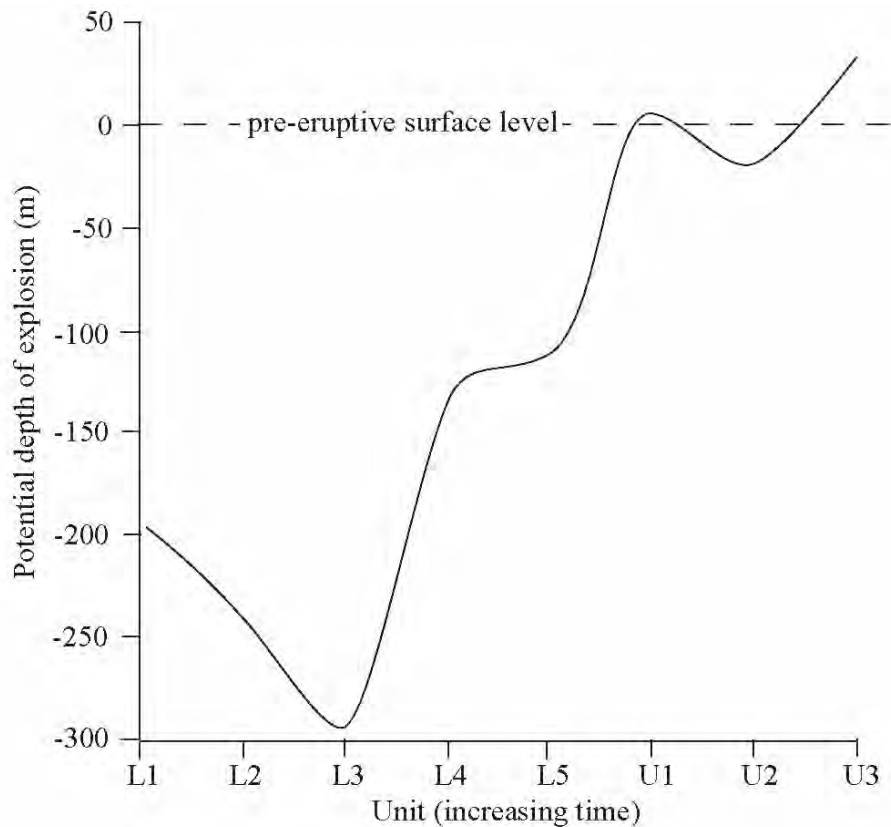


Figure 55: Fragmentation level varied as eruption progressed at Tepexitl, deepening into underlying Toba Cafe during early lower-sequence eruptions. The depth of explosions became progressively shallower following deposition of L3, migrating within the level of crater fill. Dome growth began during eruption of the upper sequence. Note that because Toba Cafe thickness remains unknown, these depths are based only on the interpretation that Tepexitl eruptions occurred at very shallow levels and do not represent any quantitative data.

The intensity and style of rhyolitic pyroclastic eruptions depends largely on the style of fragmentation, which has important consequences for hazards assessment.

Phreatomagmatic eruptions are associated with a distinct series of three deposits that are thinly bedded with sharp contacts, show rapid compositional changes, and are repeated throughout the lower sequence at Tepexitl. Evolution of these ‘three-stage deposits’ occurs as water:magma evolves and can be used to evaluate the efficiency and energy of phreatomagmatic explosions. The rapid onset of these powerful, high-energy explosions

would likely be preceded by earthquakes and other indications of impending activity, but nevertheless represents a significant potential hazard in populated areas.

It is interesting to note that a similar pattern of obsidian, pumice, and lithic-rich beds (similar to stage-2 deposits) were observed in Fryiplaka tuff ring, a series that also grades into coarser-grained stony rhyolite with time (Campo-Venuti and Rossi, 1996). This similar compositional sequence suggests that the three-stage process represents a more universal rhyolitic phreatmagmatic mixing process.

Final magmatic eruptions are associated with lower-energy pyroclastic explosions from degassing processes during dome growth, which are likely more sporadic with periods of quiescence (hours to weeks) making eruptions more unpredictable (and thus potentially more dangerous).

REFERENCES

- Austin, A., Zimanowski, B., Buettner, R., Dellino, P., Ort, M., in preparation. Phreatomagmatic explosions of rhyolite magma: experiments and field observations.
- Alidibirov, M., Dingwell, D., 1996. Magma fragmentation by rapid decompression. *Nature* 380: 146-149.
- Abrams, M.J., Siebe, C., 1994. Cerro Xalapaxco: an unusual tuff cone with multiple explosion craters in central Mexico (Puebla). *J. Volcanol. Geotherm. Res.* 63: 183-199.
- Adams, N.K., Houghton, B.F., Fagents, S.A., Hildreth, W., 2006. The transition from explosive to effusive eruptive regime; the example of the 1912 Novarupta eruption, Alaska. *Geol. Soc. Am. Bull.* 118 (5-6): 620-634.
- Aranda Gómez, J.J., Luhr, J.F., 1996. Origin of the Joya Honda maar, San Luis Potosi, Mexico. *J. Volcanol. Geotherm. Res.* 74: 1-18.
- Barberi, F., Cioni, R., Rosi, M., Santarocce, R., Sbrana, A., Vecci, R., 1989. Magmatic and phreatomagmatic phases in explosive eruptions of Vesuvius as deduced by grain-size and component analysis of the pyroclastic deposits. *J. Volcanol. Geotherm. Res.* 38: 287-307.
- Bonnichse, B., Kauffman, D.F., 1987. Physical features of rhyolite lava flows in the Snake River plain volcanic province, southwestern Idaho. *Geol. Soc. Am. Spec. Pap.* 212: 119-145.
- Branney, M.J., Kokelar, P., 2002. Pyroclastic density currents and the sedimentation of ignimbrites. *Memoir – Geol. Soc. Lond.* 27, London, 143 pp.

- Brooker, M. R., Houghton, B. F., Wilson, C. J. N., Gamble, J. A., 1993. Pyroclastic phases of a rhyolitic dome-building eruption; Puketarata tuff ring, Taupo volcanic zone, New Zealand. *Bull. Volcanol.* 55 (6): 395-406.
- Busby-Spera, C.J., White, J.D.L., 1987. Variation in peperite textures associated with differing host-sediment properties. *Bull. Volcanol.* 49 (6): 765-775.
- Büttner, R., Dellino, P., La Volpe, L., Lorenz, V., Zimanowski, B., 2002. Thermohydraulic explosions in phreatomagmatic eruptions as evidenced by the comparison between pyroclasts and products from Molten Fuel Coolant Interaction experiments. *J. Geophys. Res.* 107 (B11): 2277-2290.
- Büttner, R., Dellino, P., Zimanowski, B., 1999. Identifying modes of magma/water interaction from the surface features of ash particles. *Nature* 401: 688-690.
- Campos-Enriquez, J.O., Garduño-Monroy, V.H., 1987. The shallow structure of Los Humeros and Las Derrumbadas geothermal fields, Mexico. *Geothermics* 16 (5-6): 539-554.
- Campos Venuti, M., Rossi, P.L., 1996. Depositional facies in the Fyriplaka rhyolitic Tuff Ring, Milos Island (Cyclades, Greece). *Acta Vulcanol.* 8(2): 173-190.
- Carrasco- Núñez, G., Ort, M.H., Romero, C., 2007. Evolution and hydrologic conditions of a maar volcano (Atexcac crater, eastern Mexico). *J. Volcanol. Geotherm. Res.* 159: 179-197.
- Cas, R.A.F., Wright, J.V., 1987. Volcanic successions, modern and ancient; a geologic approach to processes, products and successions. Allen and Unwin, London, 528 pp.

Castro, J., Cashman, K.V., 1999. Constraints on rheology of obsidian lavas based on mesoscopic folds. *J. Struct. Geol.* 21 (7): 807-819.

Castro, J.M., Dingwell, D.B., Nichols, A.R.L., Gardner, J.E., 2005. New insights on the origin of flow bands in obsidian. *Geol. Soc. Am. Spec. Pap.* 396: 55-65.

Chough, S.K., Sohn, Y.K., 1990. Depositional mechanics and sequences of base surges, Songaksan tuff ring, Cheju Island, Korea. *Sedimentology*, 37 (6): 1115-1135.

Couch, S., Sparks, R.S.J., Carroll, M.R., 2001. Mineral disequilibrium in lavas explained by convective self-mixing in open magma chambers. *Nature* 411 (6841): 1037-1039.

Dadd, K.A., Van Wagoner, N.A., 2002. Magma composition and viscosity as controls on peperite texture: an example from Passamaquoddy Bay, southeastern Canada. *J. Volcanol. Geotherm. Res.* 114: 63-80.

Dellino, P., 2000. Phreatomagmatic deposits: fragmentation, transportation, and deposition mechanisms. *Terra Nostra*, 6: 99-105.

Dellino, P., Frazzetta, G., La Volpe, L., 1990. Wet surge deposits at La Fossa di Vulcano; depositional and eruptive mechanisms. *J. Volcanol. Geotherm. Res.* 43: 215-233.

Dellino, P., Isaia, R., La Volpe, L., Orsi, G., 2001. Statistical analysis of textural data from complex pyroclastic sequences: implications for fragmentation processes of the Agnano Monte Spina Tephra (4.1 ka), Phlegraean Fields, southern Italy. *Bull. Volcanol.* 63 (7): 443-461.

Dellino, P., Isaia, R., La Volpe, L., Orsi, G., 2004. Interaction between particles transported by fallout and surge in the deposits of Agnano-Monte Spina eruption (Campi Flegrei, southern Italy). *J. Volcanol. Geotherm. Res.* 133: 193-210.

Dellino, P., Kyriakopoulos, K., 2003. Phreatomagmatic ash from the ongoing eruption of Etna reaching the Greek island of Cefalonia. *J. Volcanol. Geotherm. Res.* 126: 341-345.

Dellino, P., La Volpe, L., 1995. Fragmentation versus transportation mechanisms in the pyroclastic sequence of Monte Pilato-Rocche Rosse (Lipari, Italy). *J. Volcanol. Geotherm. Res.* 64: 211-231.

Dellino, P., La Volpe, L., 1996. Image processing analysis in reconstructing fragmentation and transportation mechanisms of pyroclastic deposits; The case of Monte Pilato-Rocche eruptions, Lipari (Aeolian Island, Italy). *J. Volcanol. Geotherm. Res.* 71: 13-29.

Dellino, P., La Volpe, L., 2000. Structures and grain size distribution in surge deposits as a tool for modelling the dynamics of dilute pyroclastic density currents at La Fossa di Vulcano (Aeolian Islands, Italy). *J. Volcanol. Geotherm. Res.* 96: 57-78.

Dellino, P., Liotino, G., 2002. The fractal and multifractal dimension of volcanic ash particles contour: a test study on the utility and volcanological relevance. *J. Volcanol. Geotherm. Res.* 113: 1-18.

Dunbar, N.W., Kyle, P.R., 1992. Volatile contents in obsidian clasts in tephra from the Taupo volcanic zone, New Zealand; implications to eruptive processes. *J. Volcanol. Geotherm. Res.* 49: 127-145.

- Elsworth, D., Voight, B., Thompson, G., Young, S.R., 2004. Thermal-hydraulic mechanism for rainfall-triggered collapse of lava domes. *Geology* 32 (11): 969-972.
- Fink, J.H., Anderson, S.W., Manley, C.R., 1992. Textural constraints on effusive silicic volcanism; beyond the permeable foam model. *J. Geophys. Res.* 97 (B6): 9073-9083.
- Fink, J.H., Manley, C.R., 1987. Origin of pumiceous and glassy textures in rhyolite flows and domes. *Geol. Soc. Am. Spec. Pap.* 212: 77-78.
- Fisher, R.V., Schmincke, H., 1984. *Pyroclastic Rocks*. Springer-Verlag, Berlin, 472 pp.
- Folk, R.L. and Ward, W.C., 1957. Brazos River bar: a study in the significance of grain size parameters. *J. Sed. Petrol.* 27 (1): 3-26.
- Freda, C., Gaeta, M., Karner, D.B., Marra, F., Renne, P.R., Taddeucci, J., Scarlato, P., Christensen, J.N., Dallai, L., 2006. Eruptive history and petrologic evolution of the Albano maar (Alban Hills, Central Italy). *Bull. Volcanol.* 68: 567-591.
- Galerne C., Caroff, M., Rolet, J., Le Gall, B., 2006. Magma-sediment mingling in an Ordovician rift basin: The Plouézec-Plourivo half-graben, Armorican Massif, France, *J. Volcanol. Geotherm. Res.* 155: 164-178.
- Gevrek, A.I., Kazanci, N., 2000. A Pleistocene, pyroclastic-poor maar from central Anatolia, Turkey: influence of a local fault on a phreatomagmatic eruption. *J. Volcanol. Geotherm. Res.* 95: 309-317
- Gonnermann, H.M., Manga, M., 2005. Flow banding in obsidian; a record of evolving textural heterogeneity during magma deformation. *Earth. Plan. Sci. Lett.* 236 (1-2): 135-147.

Gourgaud, A., Thouret, J.C., Bourdier, J.L., 2000. Stratigraphy and textural characteristics of the 1982-83 tephra of Galunggung Volcano (Indonesia); implications for volcanic hazards. *J. Volcanol. Geotherm. Res.* 104: 169-186.

Gutmann, J.T., 2002. Strombolian and effusive activity as precursors to phreatomagmatism; eruptive sequence at maars of the Pinacate volcanic field, Sonora, Mexico. *J. Volcanol. Geotherm. Res.* 113 (1-2): 345-356.

Heiken, G., 1972, Morphology and Petrography of Volcanic Ashes. *Geol. Soc. Am.* 83 (7): 1961-1987.

Heiken, G., Wohletz, K., 1985. *Volcanic Ash*. University of California Press, Berkeley, 246 pp.

Heiken, G.H., Wohletz, K., 1987. Tephra deposits associated with silicic domes and lava flows. *Geol. Soc. Am. Spec. Pap.* 212: 55-76.

Heiken, G., Wohletz, K., Eichelberger, J., 1988. Fracture fillings and intrusive pyroclasts, Inyo Domes, California. *J. Geotherm. Res.* 93(B5): 4335-4350.

Houghton, B.F., Wilson, C.J., Pyle, D.M., 2000. Pyroclastic fall deposits. In: Sigurdsson, H (ed.), *Encyclopedia of Volcanoes*. Academic Press, San Diego, pp. 555-570.

Houghton, B.F., Smith, R.T., 1993. Recycling of magmatic clasts during explosive eruptions; estimating the true juvenile content of phreatomagmatic volcanic deposits. *Bull. Volcanol.* 55 (6): 414-420.

Houghton, B.F., Wilson, C.J.N., Smith, I.E.M., 1999. Shallow-seated controls on styles of explosive basaltic volcanism: a case study from New Zealand: *J. Volcanol. Geotherm. Res.* 91: 97-120.

Houghton, B.F., Wilson, C.J.N., Weaver, S.D., 1987. The Opo Bay tuff cone, Mayor Island; interaction between rising gas-poor pantelleritic magma and external water. *New Zealand Geol. Surv.* 18: 79-85.

Ichihara, M., Rittell, D., Sturtevant, B., 2002. Fragmentation of a porous viscoelastic material; implications to magma fragmentation. *J. Geophys. Res.* 107 (B10): 1-9.

Kokelaar, B., 1982. Fluidization of wet sediments during the emplacement and cooling of various igneous bodies. *J. Geol. Soc. Lond.* 139 (1): 21-33.

Kueppers, U., Bettina, S., Spieler, O., Dingwell, D., 2006. Fragmentation efficiency of explosive volcanic eruptions: A study of experimentally generated pyroclasts. *J. Volcanol. Geotherm. Res.* 153: 125-135.

Leat, P.T., Thompson, R.N., 1988. Miocene hydrovolcanism in NW Colorado, USA, fuelled by explosive mixing of basic magma and wet unconsolidated sediment. *Bull. Volcanol.* 50 (4): 229-243.

Lorenz, V., 1987. Phreatomagmatism and its relevance. *Chem. Geol.* 62 (1-2): 149-156.

Lorenz, V., 2000. Formation of maar-diatreme volcanoes. *Terra Nostra* 6: 284-291.

Lorenz, V., 2007. Syn- and posteruptive hazards of maar–diatreme volcanoes. *J. Volcanol. Geotherm. Res.* 159: 285-312.

Lorenz, V., Haneke, J., 2004. Relationship between diatremes, dykes, sills, laccoliths, intrusive-extrusive domes, lava flows, and tephra deposits with unconsolidated

water-saturated sediments in the late Variscan intermontane Saar-Nahe Basin, SW Germany. *Geol. Soc. Spec. Public.* 234: 75-124.

Lorenz, V., Kurszlaukis, S., 2007. Root zone processes in the phreatomagmatic pipe emplacement model and consequences for the evolution of maar–diatreme volcanoes. *J. Volcano. Geotherm. Res.* 159: 4-32.

Lorenz, V., Zimanowski, B., Büttner, R., 2002. On the formation of deep-seated subterranean peperite-like magma-sediment mixtures. *J. Volcanol. Geotherm. Res.* 114: 107-118.

Manley, C.R., Fink, J.H., 1987. Internal textures of rhyolite flows as revealed by research drilling. *Geology* 15 (6): 549-552.

Mastin, L., 1994. Explosive tephra emissions at Mount St. Helens, 1989-1991: The violent escape of magmatic gas following storms? *Geol. Soc. Am.* 106: 175-185.

Mastin, L., 2007. Generation of fine hydromagmatic ash by growth and disintegration of glassy rings. *J. Geophys. Res.* 112 (B02203): 1-17.

Maupomé, L., Alvarez, R., Keiffer, S.W., Dietz, R.S., 1975. On the Terrestrial Origin of Tepexitl Crater. *Meteoritics* 10 (3): 209-214.

McPhie, J., Doyle, M., Allen, R., 1993. *Volcanic textures: A guide to the interpretation of textures in volcanic rocks.* University of Tasmania, Launceston, 198 pp.

Morrissey, M., Zimanowski, B., Wohletz, K.H., Büttner, R., 2000. Phreatomagmatic Fragmentation. In: Sigurdsson, H (ed.), *Encyclopedia of Volcanoes.* Academic Press, San Diego, pp. 431-446.

Németh, K., White, J.D.L., 2003. Reconstructing eruption processes of a Miocene monogenetic volcanic field from vent remnants; Waipiata volcanic field, South Island, New Zealand. *J. Volcanol. Geotherm. Res.* 124: 1-21.

Ort, M.H., Carrasco-Núñez, G., 2004. Tecuitlapa - Evolution of fuel-coolant interactions at a young maar, Neogene-Quaternary continental margin volcanism. *Proceedings of GSA Penrose Conference. Metepec, Puebla, Mexico*, p. 58.

Ort, M.H., Wohletz, K., Hooten, J.A., Neal, C.A., McConnell, V.S., 2000. The Ukinrek maars eruption, Alaska, 1977: A natural laboratory for the study of phreatomagmatic processes at maars. *Terra Nostra* 6: 396-400.

Orth, K., McPhie, J., 2003. Textures formed during emplacement and cooling of a Paleoproterozoic, small volume rhyolitic sill. *J. Volcanol. Geotherm. Res.* 128: 341-362.

Riggs, N., Carrasco-Núñez, G., 2004. Evolution of a complex isolated dome system, Cerro Pizarro, central Mexico. *Bull. Volcanol.* 66: 322-335.

Roache, M.W., Allen, S.R., McPhie, J., 2000. Surface and subsurface facies architecture of a small hydroexplosive, rhyolitic centre in the Mesoproterozoic Gawler Range Volcanics, South Australia. *J. Volcanol. Geotherm. Res.* 104: 237-259.

Rodriguez, S.R., 2005. Geology of the Las Cumbres volcanic complex, Puebla and Veracruz states, Mexico. *Rev. Mex. Cienc. Geol.* 22 (2): 181-198.

Rodriguez, S.R., Siebe, C., Komorowski, J.C., Abrams, M., 2002. The Quetzlapa Pumice; a voluminous late Pleistocene rhyolite deposit in the eastern Trans-Mexican volcanic belt. *J. Volcanol. Geotherm. Res.* 113: 177-212.

Rust, A.C., Cashman, K.V., Wallace, P.J., 2004. Magma degassing buffered by vapor flow through brecciated conduit margins. *Geology* 32 (4): 349-352.

Scolamacchia, T., Macías, J.L., Sheridan, M.F., Hughes, S.R., 2005. Morphology of ash aggregates from wet pyroclastic surges of the 1982 eruption of El Chichón Volcano, Mexico. *Bull. Volcanol.* 68 (2): 171-200.

Self S., Kienle, J., Huot, J.P., 1980. Ukinrek Maars, Alaska; II, Deposits and formation of the 1977 craters. *J. Volcanol. Geotherm. Res.* 7: 39-65.

Sheridan, M.F., Barberi, 1983. *Explosive volcanism*. Elsevier, Amsterdam, 490 pp.

Sheridan, M.F., Updike, R.G., 1975. Sugarloaf Mountain Tephra; A Pleistocene rhyolitic deposit of base-surge origin in northern Arizona. *Geol. Soc. Am.* 86 (4): 571-581.

Sheridan, M.F., Wohltz, K.H., Dehn, J., 1987. Discrimination of grain-size subpopulations in pyroclastic deposits. *Geology* 15 (4): 367-370.

Siebe, C., 1986. On the possible use of cinder cones and maars as paleoclimate indicators in the closed basin of Serdán-Oriental, Puebla, Mexico. *J. Volcanol. Geotherm. Res.* 28: 397-400.

Siebe, C., Abrams, M., Sheridan, M.F., 1993. Major Holocene block-and-ash fan at the western slope of ice-capped Pico de Orizaba Volcano, Mexico; implications for future hazards. *J. Volcanol. Geotherm. Res.* 59: 1-33.

Siebe, C., Macías, J.L., Abrams, M., Rodríguez-Elizarrarás, S., Castro, R., Delgado, H., 1995. Quaternary explosive volcanism and pyroclastic deposits in east central Mexico: Implications for future hazards in Chacko. *Guidebook for the 1995 Annual Meeting of the Geological Society of America*. New Orleans, Louisiana, p. 1-47.

Siebe, C., Verma, S.P., 1988. Major element geochemistry and tectonic setting of Las Derrumbadas rhyolitic dome, Puebla, Mexico. *Chemie der Erde* 48 (3): 177-189.

Siebert, L., Carrasco- Núñez, G., 2002. Late-Pleistocene to precolumbian behind-the arc mafic volcanism in the eastern Mexican Volcanic Belt; implications for future hazards. *J. Volcanol. Geotherm. Res.* 115: 179-205.

Siehl, K., Bursik, M.I., 1986. Most recent eruption of the Mono Craters, eastern Central California. *J. Geophys. Res.* 91 (B12): 12,539-12,571.

Sohn, Y.K., 1996. Hydrovolcanic processes forming basaltic tuff rings and cones on Cheju Island, Korea. *Geol. Soc. Am.* 108 (10): 1199-1211.

Sohn, Y.K., Chough, S.K., 1989. Depositional processes of the Suwolbong tuff ring, Cheju Island (Korea). *Sedimentology* 36 (5): 837-855.

Sohn, Y.K., Chough, S.K., 1992. The Ilchulbong tuff cone, Cheju Island, South Korea: depositional processes and evolution of an emergent, Surtseyan-type tuff cone. *Sedimentology* 39 (4): 523-544.

Sohn, Y.K., Chough, S.K., 1993. The Udo tuff cone, Cheju Island, South Korea; transformation of pyroclastic fall into debris fall and grain flow on a steep volcanic cone slope. *Sedimentology* 40 (4): 769-786.

Spera, F.J., 2000. Physical properties of magmas. In: Sigurdsson, H (ed.), *Encyclopedia of Volcanoes*. Academic Press, San Diego, pp. 171-190.

Taylor, B.E., Eichelberger, J.C., Westrich, H.R., 1983. Hydrogen isotopic evidence of rhyolitic magma degassing during shallow intrusion and eruption. *Nature* 306 (5943): 541-545.

Tuffen, H., Dingwell, D.B., Pinkerton, H., 2003. Repeated fracture and healing of silicic magma generate flow banding and earthquakes? *Geology* 31 (12): 1089-1092.

Valentine, G.A., Fisher, R.V., 2000. Pyroclastic Surges and Blasts. In: Sigurdsson, H (ed.), *Encyclopedia of Volcanoes*. Academic Press, San Diego, pp. 571-580.

Valentine, G.A., Giannetti, B., 1995. Single pyroclastic beds deposited by simultaneous fallout and surge processes; Roccamonfina Volcano, Italy. *J. Volcanol. Geotherm. Res.* 64: 129-137.

Vazquez, J.A., Ort, M.H., 2006. Facies variation of eruption units produced by the passage of single pyroclastic surge currents, Hopi Buttes volcanic field, USA. *J. Volcanol. Geotherm. Res.* 154: 222-236.

Verma, S.P., 1999. Geochemistry of evolved magmas and their relationship to subduction-unrelated mafic volcanism at the volcanic front of the central Mexican volcanic belt. *J. Volcanol. Geotherm. Res.* 93: 151-171.

White, J.D.L., 1989. Basic elements of maar-crater deposits in the Hopi Buttes volcanic field, northeastern Arizona, USA. *Geology* 97 (1): 117-125.

White, J.D.L., 1991. Depositional architecture of a maar-pitted playa: sedimentation in the Hopi Buttes volcanic field, northeastern Arizona, USA. *Sed. Geol.* 67: 55-84.

White, J.D.L., 1996. Impure coolants and interaction dynamics of phreatomagmatic eruptions. *J. Volcanol. Geotherm. Res.* 74: 155-170.

Wilson, C.J.N., Hildreth, W.H., 1988. Hybrid fall deposits in the Bishop Tuff, California; a novel pyroclastic depositional mechanism. *Geology* 26 (1): 7-10.

Wilson, C.J.N., Houghton, B.F., 2000. Pyroclast transport and deposition. In: Sigurdsson, H (ed.), *Encyclopedia of Volcanoes*. Academic Press, San Diego, pp. 545-554.

Winter, John D., 2001. *An Introduction to Igneous and Metamorphic Petrology*. Prentice Hall, Boston, 699 pp.

Wohletz, K.H., 1983. Mechanisms of hydrovolcanic pyroclast formation; grain-size, scanning electron microscopy, and experimental studies. *J. Volcanol. Geotherm. Res.* 17: 31-63.

Wohletz, K., 1986. Explosive magma-water interactions; thermodynamics, explosion mechanisms, and field studies. *Bull. Volcanol.* 48: 245-264.

Wohletz, K.H., 2001. Pyroclastic surges and compressible two-phase flow. In: Freundt, A., Rosi, M. (eds.), *From Magma to Tephra*. El Sevier, Amsterdam, pp. 247-312.

Wohletz, K.H., Heiken, G., 1992. *Volcanology and Geothermal Energy*. University of California Press, Berkeley, 450 pp.

Wohletz, K.H., McQueen, R.G., 1984. Experimental studies of hydromagmatic volcanism. In: *Explosive volcanism; inception, evolution, and hazards: Studies in Geophysics*. National Academy Press, Washington D.C., pp. 158-169.

Wohletz, K.H., Sheridan, M.F., 1983. Hydrovolcanic explosions; II, Evolution of basaltic tuff rings and tuff cones. *Am. J. Sci.* 283 (5): 385-413.

Wohletz, K.H., Sheridan, M.F., Brown, W.K., 1989. Particle size distributions and the sequential fragmentation/transport theory applied to volcanic ash. *J. Geophys. Res.* 94: 15,703-15,721.

Wohletz, K., Orsi, G., de Vita, S., 1995. Eruptive mechanisms of the Neapolitan Yellow Tuff interpreted from stratigraphic, chemical, and granulometric data. *J. Volcanol. Geotherm. Res.* 67: 263-290.

Wohletz, K.H., Zimanowski, B., 2000. Eruption Physics. *Terra Nostra* 6, pp. 515-523; 535-543.

Zimanowski, B., 1998. Phreatomagmatic explosions. In: Freundt, A. and Rosi, M. (eds), *From magma to tephra: Developments in volcanology 4*. Elsevier, Amsterdam, pp. 25-54.

Zimanowski, B., Büttner, R., Lorenz, V., 1997. Premixing of magma and water in MFCI experiments. *Bull. Volcanol.* 58: 491-495.

Zimanowski, B., Büttner, R., Lorenz, V., Häfele, H.-G., 1997. Fragmentation of basaltic melt in the course of explosive volcanism. *J. Geophys. Res.* 102: 803-814.

Zimanowski, B., Fröhlich, G., Lorenz, V., 1991. Quantitative experiments on phreatomagmatic explosions. *Volcanol. Geotherm. Res.* 48: 341-358.

Zimanowski, B., Wohletz, K.H., Büttner, R., Dellino, P., 2003. The volcanic ash problem. *J. Volcanol. Geotherm. Res.* 122: 1-5.

Zimmer, B., 2007. Eruptive variations during the emplacement of Cerro Pinto Dome Complex. Masters Thesis, Northern Arizona University. Flagstaff, Arizona.

APPENDIX 1: Detailed Field Data (Chapter 2)

LITHIC MATERIAL PETROGRAPHY

Hand samples collected in the field were cut and described. Four thin sections of lithic clasts were also examined (one limestone, two andesite, and one basalt) and are incorporated into the description below. Andesite and basalt blocks are the most common lithic material throughout the stratigraphy of Tepexitl.

Basalt: The basalt is dark gray and plagioclase-olivine-phyric with 10% crystals up to 3 mm in diameter set in a palagonitic groundmass, which has variable amounts of alteration to smectite and chlorite.

Andesite: Andesite clasts occur with a variety of mineral assemblages and colors. The most common andesite is crystal-rich and pink – gray to dark pink – gray with oxyhornblende +/- plagioclase +/- olivine phenocrysts (all up to 3 mm in diameter). Phenocrysts average 40% by volume. The groundmass of these clasts varies from holocrystalline (plagioclase microlites) to dominantly palagonitized glass with minor amounts of felty microlites. Flow banding between pink and black zones is rare. The oxyhornblende is variably altered. All oxyhornblende crystals in holocrystalline samples have completely altered to a magnetite-rich alteration product, giving the surface a ‘rusty’ appearance. The plagioclase grains in this sample are also altered, with sericite rims around the crystals. Other observed clasts include white andesite with 30% mm-scale hornblende phenocrysts and pink finely crystalline hornblende-quartz-plagioclase – phyric andesite with small crystals (less than 1 mm in diameter).

Limestone: Limestone clasts include both white-gray to light-gray limestone blocks with a homogeneous matrix and one mottled sample, which has a variety of overlapping and

cross-cutting textures. A thin section of this clast reveals three distinct zones of: 1) white (fine-grained mosaic calcite with grains less than 0.5 mm in diameter), 2) gray (coarse-grained calcite veins with interlocking crystals between 0.2 and 1 mm), and 3) yellow (totally altered with no distinguishable grains).

MEASURED SECTIONS

Section 1

Section 1, located at the base of the main road into the crater, was later determined to be a slumped portion of Section 2 that stayed mostly intact. Therefore, this section was not examined in further detail.

Section 2

Section 2 is the type section. This composite section is located along the main road going into the crater from the south, and measures a total of 49.5 m. Since it was the first inner crater-wall section to be completed, it was also the blueprint for unit boundaries, which were based on changes seen in the bedding (such as dominant facies, sedimentary structures, and abundance of blocks in the outcrop).

Section 3

Apron deposits near the road show a confluence between three different events with strikingly different dips in the lower and upper deposits of the section. Section 3 consists of (from base to top): 1) 1.4 meters of deformed T1 with a strike and dip of 100° , 12° S. 2) Fines-poor B1 that thins dramatically away from the crater rim (from several meters thick to 70 cm thick over the course of 15 meters laterally). Abundant jig-saw clasts indicate primary deposition, 3) 1-m-thick deformed T1 with a much different

attitude: 150°, 17°SW. This primary sequence is overlain by massive, matrix-supported deposits, interpreted as secondary debris flow deposits and not described in detail.

Section 4

This complete inner-crater section was measured along the eastern wall with a total vertical height of 53.8 m. Section 4 begins 6.5 meters stratigraphically below the base of L1 at Section 2, and ends at the top of Section 7, as measured in Section 2.

Section 5

Section 5 was measured in a man-made pit excavated into the western apron. Stratigraphically, it appears to overlie everything on the crater walls and almost completely consists of reworked deposits, so is not an important section with regard to vent processes inside the Tepexitl crater. However, it is interesting for one reason – sandwiched between lower, cross-bedded fluvial deposits and upper, massive, matrix-supported, poorly-sorted lahar deposits is a 40-cm-thick deposit of obsidian breccia that is clast supported, fines poor, and monolithologic. The clast size ranges from 1 to 40 cm. This is a localized breccia, with no other indication of another crater. It is difficult to determine where it came from, what its mode of deposition was, and when it was deposited. It is assumed to be younger and not directly related to the formation of Tepexitl.

Section 6

Section 6 is the third complete inner-crater section and was measured in the north, along the drainage to the west of the large inner crater debris slump. It has visible deposits for 50.5 vertical meters. The top 10 m are particularly poorly consolidated and

the crater rim is covered with the same explosion debris found on the “thumb” and the western crater slopes.

Section 7

Section 7 is the first measurable apron outcrop clockwise from the north and is 3.1 meters thick.

Section 8

Distal primary bedding is only visible in one area, as deformed deposits of T1 facies lapping onto a limestone ridge 1.5 km to the SSW of the tuff ring. This total section height is 3.2 m and is predominantly planar, thinly-laminated fine-ash tuff with abundant well-preserved accretionary lapilli between 1 and 10 mm in diameter.

Section 9

Section 9 is the only other exposed distal section, measured 15 meters farther from the vent than Section 8. However, these deposits are predominantly re-worked, having been deposited after lapping onto and over the limestone crag. Therefore, this section is not considered in any further detail.

Section 10

Section 10 is a moderately well exposed southern apron deposit of 3.1 m height.

Section 11

Located in the southeast apron with 14 m of bedded tuff, Section 11 is the most well indurated and complete apron section of the whole tuff ring.

Section 12

Section 12 is a 3.3-m cross-section through a well-exposed northeastern section of “late-stage” deposits and is a good representation of all late-stage deposits.

Section 13

The single well-exposed, crater-wall section along the inner western wall is only measurable for the top 5 m because the rest of the slope is covered with debris.

UNIT DESCRIPTIONS:

LOWER SEQUENCE

Unit 1 (L1)

L1 is thickest at inner-crater Section 4 (12.5 m), thinner toward inner-crater Section 2 (5.8 m) and only exposed for the first 2.5 m of inner-crater Section 6 (Plate 1). No apron deposits are visible. The deposits are predominantly medium-bedded T1 facies, especially at the base, with planar, wispy, and discontinuous “dry” thin beds to laminae and 20-40 cm interbedded deposits of facies B1. Accretionary lapilli are scattered throughout the fine-grained beds. Scour channels are non-existent at the base but become more common up-section. In general, the deposits become richer in B1 facies in the middle and top, with laterally continuous beds and coarse grading (both normal and reverse). L1 in Section 4 has the thickest breccia deposit (1.8 m) around meter 10 as well as the only Fe-clasts found during this phase, in a 1.4-m-thick bed of B1 facies at meter 6 (these Fe-clasts are not found in other sections because this B1 bed is stratigraphically beneath the lowest exposed deposits of both Section 2 and 6). Beds of Bt facies are present only in L1 of Section 2. Disseminated blocks of both obsidian and river cobbles with maximum sizes of 20-40 cm cause sparse bomb sags, increasing in abundance up section (1-2% of total deposit). A distinct marker bed is a massive, fine-ash, highly-deformed deposit (up to 8 cm vertical displacement) in the middle of the phase, seen

around the tuff ring just below the point at which B1 facies deposits become dominant. These beds are interpreted as mud-rain deposits.

INTERPRETATION:

Section 4 has the thickest and most poorly-sorted L1 deposits, evidence that it was deposited prior to significant sorting of coarse and fine material by the transportation system. Facies Bt is only present in L1 of Section 2, in a breccia deposit richer in fine ash than the deposits of facies B1 found in L1 of Sections 4 and 6. L1 deposits in Section 6 are considerably finer grained than those of Sections 2 and 4, with dominantly undulatory T1 facies and only 20-cm-thick beds of facies B1. The combination of these observations suggests that Sections 2 and 4 lie closer to the dominant vent and/or to the primary axis of deposition, which means eruptive activity had a dominant southern and/or eastern component. Mud rain and accretionary lapilli are evidence of external water but do not clarify if the water was weather- or vent-related. However, scour channels and bomb sags increasing up-section indicate deposition of ash from wet surges that originated at the vent and are consistent with an increasingly higher water:magma. Atmospheric contribution, however, cannot be ruled out, especially with mud-rain deposits. Fe-clasts deposited in the middle of the sequence indicate heat transfer was occurring between the magma and the saturated sediments at that point in time, but the planar, continuous, non-deformed bedding associated with these deposits suggests that there was either very little water available or the eruption was efficient enough to transform most available water into vapor.

Unit 2 (L2)

L2 can be seen in inner-crater and apron deposits around the SE sector of the tuff ring. It is 4.4 m thick at Section 4, 5.5 m thick at Section 2, and 6 m thick at Section 6 (although three of these meters are obscured by vegetation). L2 is also seen in the eastern apron deposits as a 1.1-m-thick deposit at the base of Section 7 and a 2.2-m-thick bed at the base of Section 11, and in the distal deposits as a 1.1-m-thick stratum at the base of Section 8. Section 6 L2 deposits are the finest grained and most laminated, with thinner breccia beds that are mostly fines poor. Section 2 has the coarsest and most well-sorted overall L2 deposits.

Like L1, this sequence consists of alternating layers of facies T1 and B1/Bt with sharp contacts, but the layers are thinner (5-40 cm) and laminae are more common. The fine-grained layers are undulatory, discontinuous laminae with dune forms (1-2 cm height) and pods of coarser material. Both scour channels and scattered accretionary lapilli as discontinuous laminae and pods are common in all fine-grained deposits. The coarse beds are continuous, fines poor, and commonly crudely graded (both normal and reverse), with angular clasts that are commonly coated in fine adhering ash. Deposits of facies B1 become more dominant up-section, with abundant Fe-clasts toward the top of the phase in Sections 2, 4, 6, 7, and 8. The breccia deposits of L2 are distinct: thinly bedded; obsidian-rich; and commonly containing Fe-clasts. Blocks are found in slightly higher abundances in L2 of Section 2 (5-7% of the total deposit) than in L2 of Sections 4 and 6 (1-2%). The fine-grained beds commonly have up to 25-cm-deep deformation from ballistic blocks, much more pronounced than vertical deformation in the deposits of L1. These blocks are still dominated by river cobbles and obsidian but are larger than in L1

(20 cm to >1 m). Several obsidian bombs have jig-saw fractures. All deposits have a high number of lapilli and coarse-ash grains that are coated in fine ash.

INTERPRETATION

Apron deposits are concentrated on the eastern side of the maar but the coarsest-grained, Fe-clast rich breccia deposits are found in Section 2, to the south. A combination of these observations points to a primary depositional direction to the south and east. However, Section 6 to the north has the thickest and finest-grained L2 deposits, which could either relate to offset obscured by slumping and vegetation or that more than one depositional mechanism was operating at one time.

Unit 3 (L3)

A distinct marker sequence, L3 consists of a medium- to thickly-bedded Fe-clast- and obsidian-rich breccia (B1) followed by a thick sequence of dominantly fine-grained deposits of T1. In the inner crater deposits, the entire sequence is 2.9 m in Section 2, 3.6 m in Section 4, and 2.8 m at Section 6. In the apron deposits, it is visible for the basal 1.4 m in Section 3, as well as 0.2 m in Section 7 and 3.1 m in Section 11. It is also present as a 1-m deposit in distal Section 8. The breccia in this deposit is continuous laterally and reversely graded. The fine-grained tuff is composed of planar to undulatory laminae with intermittent coarser ash to small lapilli laminae. Accretionary lapilli are common as non-continuous, very thin beds. The coarser beds in these deposits are no more than 5 cm thick, but cause scouring of underlying fine ash. Although blocks are rare (<1%, 10-30 cm in diameter), lapilli sags are abundant, causing up to 20 cm vertical deformation of underlying ash. Like underlying units, blocks are still dominantly river cobbles and

obsidian blocks. Some of the sagged tuff is sheared at the top from overlying beds, indicating that there was a strong lateral component to deposition.

INTERPRETATION:

Deposits of L3 are thickest and most poorly sorted in inner-crater Section 4 (to the east), but apron Section 11 to the southeast has a much thicker L3 sequence than Section 7 to the northeast. This evidence, coupled with the thick sequence of L3 observed in distal Section 8, points to deposition that had a primary axis of deposition with strong southern and eastern components

The basal breccia of L3 is extensive, seen as an outcrop in inner-crater, apron, and distal sections. It is the thickest Fe-clast-containing deposit of B1 facies of the entire stratigraphy, making it a good marker bed. This breccia is followed by a very thick sequence of fine-grained, deformed tuff, which could either be related to phreatic eruptions through crater fill or to highly efficient eruptions with high fragmentation energies. The wide distribution of deposits and lack of blocks and bombs are consistent with high depositional energies, which are mostly associated with efficient eruptions. This sequence of deposits follows a similar pattern as the three-stage deposits seen in L2.

Unit 4 (L4)

L4 is the coarsest grained and most voluminous sequence of the entire tuff ring. It is thickest in the inner-crater Section 2 (12.6 m), thinning toward Section 4 (11.5 m) and Section 6 (9.6 m). Around the apron, it is 1.5 m thick in Section 7, 8.2 m thick in Section 11, 3 m thick in Section 10, and 70 cm thick in Section 3. It is 15 cm thick in distal Section 8. Section 2 has the thickest L4, with the most poorly-sorted deposits, and L4 in Section 6 is the thinnest sequence with the finest-grained beds. Section 11 deposits are

well sorted and moderately thick, with sparse Fe-clasts observed at the top of the sequence. L4 thins considerably laterally toward Sections 7, 3 and 10. At Section 3, L4 thins from several meters thick to only 70-cm thick over the course of 15 meters laterally. At distal Section 8, L4 is only visible as a 15-cm deposit of B1 facies, a very small percentage of the amount of L4 material observed closer to the crater. L4 is dominantly thinly- to thickly-bedded B1 with thinly-interbedded tuff, becoming more breccia-rich up section. Breccia layers are continuous, fines poor, and commonly graded – both normal and reverse.

The basal breccia bed (between 0.6 and 1.4 m thick) is a good marker for the beginning of the L4 sequence, as it contains 30-40% disseminated blocks and bombs. These blocks, still dominantly obsidian and river cobbles between 5 and 50 cm in diameter, become rarer mid-unit (1-2%) and increase again toward the top (10-15%). These blocks cause 4-10-cm-deep deformation of underlying tuff. A second good marker for L4 is the presence of massive tuff with highly deformed upper contacts, interpreted as mud-rain deposits. All sections of adequate thickness have such a deposit in the middle of the unit, immediately below the final, thick-breccia sequence. Sections 2, 4, and 6 all have another such deposit toward the base of the unit (Section 4 has two separate earlier deposits), and Section 11 has a very undulatory, fine-grained deposit toward the top of the unit. With these noted exceptions, the fine layers are mostly planar, with occasional scour channels. Many have pods of coarser material that pinch and swell laterally. Intermittent accretionary lapilli layers increase up-section.

INTERPRETATION

The larger median grain size when compared to stratigraphically lower deposits, coupled with the sheer volume of juvenile material deposited (and a clear dominance by stony rhyolite) mark a change in eruptive style during deposition of L4. Less vertical deformation from bomb sags indicates that L4 tuff had less excess water in the depositional system when compared to the highly deformed and “soupy” tuff of the underlying units. Mud-rain deposits could be from water in the atmosphere and thus cannot be assumed to come from water in the vent area. Isolated Fe-clasts in Section 11 are evidence for fuel-coolant heat transfer, but it is unclear why this feature is not observed in other sections and may indicate a localized, secondary eruptive process. The high degree of lateral thinning when compared to units below, coupled with coarse nature of the deposits, suggest that the transport process during this stage of the eruption was poorly efficient. The thickness of the breccia deposits that dominate this unit is consistent with deposition by fall, with the majority of the material being deposited near the vent. Such a phenomenon may be called a ‘maelstrom’ – a blast that ejects unsorted material from fine ash to large blocks, but turbulence leads to a rapid loss of energy and results in chaotic near-vent deposition. The large percentage of blocks early and late in the eruption may correspond to poorly efficient and/or poorly energetic fragmentation mechanisms during those periods of time. The stratigraphic evidence indicates that the eruptive style still had a strong primary axis of deposition/vent location to the southeast during deposition of L4.

Unit 5 (L5)

L5 is much finer grained than L4, and has an approximately equal thickness around the inner crater: 5.6 m in Section 4, 5.2 m in Section 2, and 4.8 m in Section 6. L5 is the uppermost deposit found outside of the crater rim – as 1.1 m in apron Section 3, 10 cm at the top of section 11, and 0.6 m at distal Section 8. L5 in Section 4 is finer grained and better sorted than in both Sections 2 and 6, which have laminated to thinly-bedded deposits. Section 2 has the most poorly sorted L5 deposits and Section 6 has the coarsest L5 breccias. L5 deposits are dominantly planar to slightly undulatory deposits of T1 and Tlap facies with abundant facies AC interbeds (up to 30% of fine-grained deposits) and rare duneforms up to 4 cm high. Scour channels of 1-6 cm depth are common. Occasional blocks (1-2% of the deposit) are composed primarily of river cobbles (10-50 cm in size), with some obsidian and flow-banded juvenile clasts (10-20 cm in diameter), and cause 1-30-cm-deep deformation in the underlying tuff. The minor coarse-grained beds are mostly reversely-graded deposits of B1 facies (between 2 cm and 15 cm thick) and commonly have ash coatings on the grains. Fe-clasts and abundant obsidian lapilli are present in coarse-grained deposits in the middle of L5 in both Sections 2 and 4.

INTERPRETATION:

L5 in Section 4 is finer grained and better sorted than in other sections, which indicates it is farther away from the primary axis of deposition/ vent location. The paucity of L5 deposits in Sections 7 and 11 confirms this observation. The poor sorting and coarse-grained deposits characteristic of L5 in Sections 2 and 6, respectively, indicate that the primary axis of deposition must have had a strong western component, rather than the southeasterly depositional direction seen in older deposits. The difference in L5

between Sections 2 and 6 (degree of sorting vs. coarseness of deposits) may be related to their relative distance from the active vent(s) and/or to multiple depositional mechanisms occurring simultaneously. Excess water throughout L5 is indicated by abundant AC, ash coatings on the grains, bomb sags, and scour channels. Fe-clasts indicate both heat and water played a role in the eruptive system. Figure 11 in chapter 2 shows a coarse-grained bed of L5 shearing the top of underlying cohesive tuff beds, suggesting it was deposited with a strong lateral component.

UPPER SEQUENCE

Unit 1 (U1)

U1 deposits are of comparable thickness around the inner crater: 8 m thick in Section 4, 8.2 m in Section 2, and 8.1 m in Section 6. Section 2 has the coarsest-grained U1 deposits, Section 6 the most poorly-sorted U1 deposits, and Section 4 the most fine-grained and laminated U1 deposits. Thin- to medium-bedded, coarse-grained Bt is the primary facies, with interbedded laminae to thin layers of tuff. The coarse-grained breccias are laterally continuous with both normal and reverse crude grading. Intermittent fine-grained tuff is planar to undulatory with thin beds of facies AC throughout and rare scour channels, particularly in the lower tuff units. Large blocks are dominantly stony rhyolite (10-60 cm in size), instead of the lithic and obsidian blocks that occur lower in the section, and cause downward deformation between 2 and 15 cm into the underlying tuff. Blocks also increase in abundance from L5, to 20-30%.

INTERPRETATION:

The change from dominantly obsidian and river cobble blocks to stony rhyolite blocks, the higher concentration of blocks, and the dominantly coarse-grained beds indicate that U1 is the result of some change(s) in eruptive dynamics. Bomb sags and scour channels are consistent with wet ash resulting from water in the eruptive system, although the overall coarser deposits make it difficult to estimate if the water:magma ratio changed from below. The stratigraphic changes point to a primary axis of deposition/primary vent location with a strong western direction. As with L5, the difference between Section 2 (coarsest-grained deposits) and Section 6 (most poorly-sorted deposits) could be related to their relative distances from the vent and/or from more than one depositional mechanism operating at the same time. The lack of U1 deposits in apron sections either means the deposits were not preserved due to reworking or they were deposited by poorly-energetic surges that did not make it over the crater rim.

Unit 2 (U2)

Similar to U1, U2 outcrops occur only in inner-crater sections and not around the apron. Its thickness in Section 2 is 9.2 m, Section 6 is 11.5 m and Section 4 is 8.1 m. Section 2 has the most poorly-sorted and the coarsest-grained U2 deposits. Facies Bt dominates at the base and facies Tlap/Tl and B/Bl are interbedded at the top. Section 6 U2 deposits are still quite coarse grained, but are better sorted than unit 2 deposits in Section 2, where the coarse and fine material alternate on a laminae- to thinly-bedded scale. Section 4 U2 deposits are mostly fine grained and laminated with better sorting and only sporadic 10-20-cm-thick beds of Bl facies. U2 is also similar to U1 in that stony rhyolite blocks are abundant (20-30% of the deposit and up to 80 cm in diameter).

However, fine-grained laminated deposits are more abundant. These deposits are planar and non-deformed with no scour channels or bomb sags. They do contain thin interbeds of facies AC, which increase toward the top and are 2-6 cm thick. The coarse beds are fines poor, continuous and planar with crude grading (both normal and reverse).

INTERPRETATION:

Stratigraphic relations indicate the primary axis of deposition/primary vent location had a dominant western component, based on the consistently coarser and more poorly-sorted U2 deposits of Section 2 to the south, and the thicker sequence of deposits preserved in Section 6 to the north. The decrease in ash deformation (no scour channels or bomb sags) suggests that U2 was the result of dry surges from a lower water:magma ratio in the vent area. Again, the lack of apron deposits of Unit 2 could be related to reworking or to low-energy surges unable to make it out of the crater.

Unit 3 (U3)

U3 was measured at the top of the western crater rim in Section 13 and is drastically different from all previously described deposits. It is a 5-m-thick sequence dominated by coarse-grained, clast-supported, fines-poor deposits of B facies with angular, juvenile clasts. Interbedded between each breccia deposit is 5-10 cm of facies T1 or AC. The basal breccia is 45 cm thick with approximately 50% vitrophyre and flow-banded material and an average clast size of 2 cm. The second breccia bed is 20 cm thick and dominated by stony rhyolite clasts with an average size of 3-4 cm. On top of this breccia is a 20-cm-thick deposit of facies AC with unusually large, well-indurated accretionary lapilli (cm-scale), unlike the smaller accretionary lapilli seen previously. The third breccia is the thickest (3 m) and the coarsest grained (average clast size of 5 cm). It

is dominantly stony rhyolite with 5-10% flow-banded clasts and less than 1% obsidian and lithic grains. Much of the rhyolite material is pumiceous with breadcrust exteriors and finely-vesicular interiors, similar to those found as loose debris on the western slopes. At least 10% of clasts in this deposit are greater than 10 cm in diameter. On top of this thick deposit are three smaller breccias, each only 15 cm thick. The first two are similar in character, with approximately 40% of the clasts composed of obsidian and flow-banded juvenile material and an average clast size of 3 cm. The uppermost deposit (and the youngest one seen in the tuff ring stratigraphy) is pumice- and obsidian-rich with yellow-coated clasts, fragmented juvenile-breccia clasts, and an average clast size of 1 cm. On one isolated high point along the western rim, the U3 deposits are capped with a thin veneer of tuff (less than 5-cm thick). U3 was also observed in Section 6 as a 4-m-thick, fines-poor B/BI-dominated sequence with 20-40 cm of facies AC interbedded between each breccia.

INTERPRETATION:

The coarse-grained, fines-poor, texturally-diverse, angular deposits with a paucity of lithic clasts in U3 are consistent with dome explosion. As U3 is only observed along the western half of the crater and was deposited with the coarsest clasts to the WNW, that is also the presumed primary axis of deposition.

WESTERN CRATER DEPOSITS

Unconformable contact between tuff and explosion breccia:

At the location depicted in figure 21 (chapter 2), the explosion breccia is approximately 2 m thick. Approximately 90% of the clasts in this deposit are dense to

slightly vesicular, angular stony rhyolite. The remaining 10% are of flow-banded or obsidian material, with very rare lithic clasts. Some blocks within the deposit have distinct breadcrust texture and jigsaw fractures – similar to the clasts found in the 3-m-thick middle breccia deposit of U3. Clast size ranges from 5 mm to greater than 1 m, with an average size of 10 cm.

Pumice

A variety of pumice textures are observed, but breadcrust textures with slight – moderate interior vesicularities are the most common. The following samples can be seen in figure 23 in chapter 2. P1 is a breadcrust bomb with a dark-gray, distinct, glassy external rind and a light-gray, moderately-vesicular interior. It is slightly friable, which has kept these fragile textures relatively well preserved. P4, however, is a highly friable breadcrust bomb, with an inconsistent, thin glassy rind and a highly fractured and broken outer surface. The interior is mostly dense with mm-scale spherical lithophysal cavities and parallel sub-mm cracks extending in concentrated zones through the matrix, perpendicular to flow banding. Both of these pumice fragments have faint mm-scale flow banding, defined by light and dark gray streaks. P2 has a dense, well-preserved, black breadcrust exterior and a dark-gray to black, dense lithophysal (up to 2.5 mm in diameter) interior. Crystallization of quartz and sanidine occurs along the outer margins of the vugs, but does not fill them. P5 is the only non-breadcrust pumice sampled, a minority in the field. The whole-pumice and close-up images in figure 23 show the moderate-high vesicularity, dominated by tube pumices with thin walls. This clast has surficial orange alteration that does not extend into the interior of the sample.

INTERPRETATION:

The range of pumice textures described are all consistent with explosion from a still-cooling dome. In general, vesicularity is low, particularly in the breadcrust bombs. In order to expand upon quenching yet not be highly vesiculated, these clasts must have been hot and poorly degassed at the time of explosion. The cracks seen in P4 are consistent with vertical joints that form in the outer surfaces of a dome during cooling (Manley and Fink, 1987). The lithophysae in this sample are consistent with the middle rhyolite portion of a dome (Manley and Fink, 1987). P2 is the only observed sample in the entire Tepexitl stratigraphy in which an obsidian clast had either lithophysae or breadcrust texture. This unusual sample is consistent with vitrophyre from the middle or lower obsidian zone of a dome, areas commonly with associated lithophysae. The crystals inside the vugs of P2 are interpreted as resulting from vapor-phase crystallization, which may explain clast expansion without significant vesiculation. P5 is consistent with the frothy dome exterior that characterizes the finely vesicular zone of a dome (Manley and Fink, 1987).

Fragmented Breccia

Breccia blocks are confined to drainages and are only present in smaller grain sizes in the final deposit of U3. These breccias are all matrix-supported with dominantly juvenile clasts, fragmented after cementation. They can be subdivided into three groups of similar textures, which can be seen in figure 23 of chapter 2: 1. poly lithic, poorly-sorted clasts in a yellow matrix; 2. obsidian clasts set in an oxidized pink matrix; 3. gray stony rhyolite clasts in a gray matrix. Samples B1 and B5 fall in group 1. The clasts in B1 are poorly sorted, poly lithic, and sub-rounded with no flow alignment. They include gray

stony rhyolite, dense flow-banded rhyolite, and black vesiculated obsidian that resembles the breadcrust bomb P2. Lithic fine-lapilli to coarse-ash clasts are scattered throughout. Sample B5 is very similar to B1 except that it does not have vesiculated obsidian clasts, but stony rhyolite clasts with quenched margins instead. The clasts in this sample are also dominantly angular to sub-angular. The matrix of these breccias is very fine ash that has been altered yellow and envelops each individual clast. The alteration is limited to the matrix and does not extend into the clasts.

Group 2 breccias include samples B2, B3, and B6. B2 is a highly unusual breccia block, with two contrasting clasts cemented together along an unconformable linear boundary. The upper part (figure 23) is composed of laminated, alternating layers of poly lithic coarse and fine ash (juveniles and lithic grains) with subtle bedding structures. This is welded onto an obsidian breccia that is composed of rounded to wispy, dense obsidian clasts that show faint alignment and jig-saw textures. The pink matrix is glassy and slightly vesiculated. B3 is composed of dominantly intact but fractured, blocky obsidian clasts. The pink matrix invades fractures in the obsidian and is vesiculated with a brecciated, disorganized appearance and disseminated lithic clasts. B6 is similar to B3 but shows wispy fragments of obsidian clasts with jig-saw textures and edges that grade into the vesiculated, pink matrix

Group 3 breccias are represented by sample B4, composed of poorly-sorted, sub-rounded to sub-angular, stony rhyolite clasts held in a vesiculated matrix of fine, white-gray ash. Clasts are moderately vesicular and show no alignment, although some have flow-banding textures. They are monolithologic and have no evidence of lithic clasts.

INTERPRETATION

Group 1 breccia clasts are visually most consistent with cemented crater fill that was fractured and ejected at the end of the dome/plug explosion. The cementation and alteration of the fine ash may be related to hydrothermal fluids percolating through underlying wet crater fill during dome/plug growth. The quenched margins indicate that at least some of the clasts were hot upon fall-back into the crater, where the exteriors became quenched upon rapid cooling during exposure to external water. The friable, vesiculated obsidian clasts of sample B1 may be related to pyroclasts from dome/plug explosion during the upper sequence, as their unusual texture is not observed elsewhere in the stratigraphic sequence. The implication of group 1 breccias is that crater fill was still saturated upon passive extrusion and became cemented during dome/plug growth.

The pink matrix of group 2 is consistent with deposition during heating. These clasts have characteristics of monolithologic internal breccias and carapace breccias (as described in chapter 3). The presence of lithic grains in B3 argues for formation along conduit walls or the base of a dome, where the fractured juvenile material would have access to sediment. The wispy to blocky to globular shapes of obsidian are consistent with peperitic textures, which represent a viable process both along the base/edges of a dome/plug that is intruding into wet, fluidized sediments and/or the edges of an intrusion within a phreatomagmatic diatreme. A vesiculated matrix is consistent with heat and water. B2 is most likely a preservation of cemented crater fill and group-2 obsidian breccia that is possibly shear-related, as they are poorly cemented along an unconformable linear boundary. Group 3 breccias are consistent with the outer carapace breccia of a dome (Manley and Fink, 1987).

APPENDIX 2: Detailed Methodology (Chapter 3)

GRANULOMETRY

Samples were sieved dry from -5 phi to 4.5 phi on a half phi interval. The large amount of sieves required three intervals of sieving. The entire sample was first sieved from -3 phi to 0.5 phi, using the Roto-tap (only rotation, no tapping) for 5-7 minutes, depending on the amount of fine material (finer-grained samples required longer rotation times). The pan fraction of the first set of 8 sieves was then sieved from 1 to 4.5 phi for 8-10 minutes on the Roto-tap (only rotation, no tapping). Any material coarser than -3 phi was sieved by hand, as were sieve sizes 1 to 4.5 for the samples with abundant sticky fine material (limited to some accretionary lapilli samples). For each sample, the material from each sieve was weighed and placed in an individual sample bag. Each sieve was cleaned between each sample. The weight percent of each size interval was normalized to 100 for each sample. In the coarse-sample grain-size-distribution graphs, the final peak at 5 phi is a false peak, representing the amount of material in the pan fraction after sieving. Samples with greater than 8 wt% fines in this final pan fraction were further analyzed using a Coulter LS 230 Version 2.11a. This arbitrary cutoff was a conservative estimate of an important fine component to the overall deposit subpopulation distribution, based on comparative peak sizes for 5 phi. A study done by Eshel et al. (2004) concluded that laser diffraction is a valid method for determining grain-size distributions.

The Fraunhofer optical model with a pump speed of 60 was used on the Coulter LS. Four runs of each sample were conducted, so that any anomalous distributions could be identified. To minimize the clumping tendencies of fine ash, a dispersant of 8 mL 50 g/L Na Hexametaphosphate solution was added to 0.03 grams of well-mixed ash

(determined as the optimal weight percent of solids for accurate results through trial and error). The data are presented as volume percent measured within channels of defined diameter. The total volume percent per phi size could be determined by counting how many volume bins composed a single phi category, calculated using the formula:

$$\text{Phi} = -\log_2 d, \text{ where}$$

d is particle diameter

Using the assumption that the density differences between fine-grained glassy particles are negligible (Dellino and La Volpe, 1995), volume percent was converted to normalized mass percent with the following formula:

$$\text{Mass}_x = (\text{Vol}_x / (\text{Vol}_T)) * \text{Mass}_T, \text{ where}$$

Mass_x is the mass % of x phi size

Vol_x is the volume % of x phi size

Mass_T is the total normalized mass of the final pan fraction

Vol_T is the total volume of the final pan fraction

Grain-size data were entered into the SFT program for determination of subpopulation distributions (as discussed in chapter 3). Because many samples had more than 6 subpopulations (the amount allowed to be entered and optimized at one time by the program), multiple runs were conducted for these samples using the coarse and fine weight percent removal feature. Mode, dispersion, and fraction were adjusted manually

until the optimization of the entered peaks had the lowest possible residuals, indicating the best possible fit. Dispersion (γ) is a quantification of the width of the peak, with a narrower width corresponding to a lower dispersion and a higher degree of sorting (Figure A).

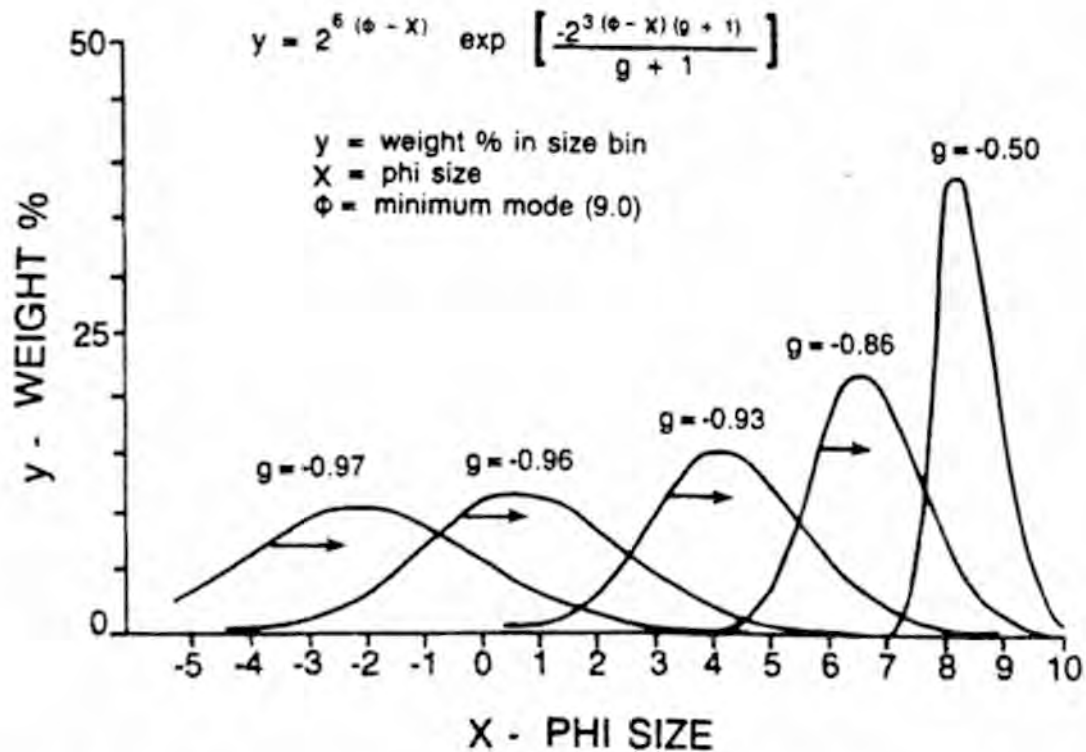


Figure A: This diagram illustrates the progressive changes in subpopulation distribution with decreasing dispersion (g), as well as the formula used for calculating dispersion in the SFT program. This figure is taken from Wohletz et al., 1989.

All displayed statistics were recorded for each subpopulation within a sample in an Excel worksheet. For 88% of the samples, the sum of the weight percent represented by each subpopulation within a sample was equal to 100% within error of 0.05. The remaining 12% were within error of 0.13, always weight percent unaccounted for rather than too much. These 12% of samples are all fine-grained, with a very fine tail that was not

accounted for in dominant subpopulation peaks, as it appears to be unimportant for primary fragmentation mechanisms, likely the result of saltation and traction – a transport mechanism rather than a fragmentation mechanism (as discussed in chapters 2 and 3).

R value was calculated from SFT data (mode, dispersion, and weight percent of subpopulations). Because the dispersion of peaks found in the 2-4 phi range may be the result of magmatic, phreatomagmatic, or original sedimentary lithic signatures, R value cannot be reliably used in this study to calculate the water:magma percent. Instead, the goal was to provide a visual reference of changes in fine grained subpopulation peak width and distribution. The formulas used for this calculation were taken from Wohletz and McQueen (1984):

$$R = 1.373*(D_{Total}) , \text{ where}$$

D stands for SFT ratio discriminator for each subpopulation, which is calculated with the formula:

$$D = [(Mode+5)*(Gamma+1)]-1$$

D_{Total} is a weighted average of all D values for each sample.

COMPONENTRY

An optical microscope was used for grain identification of all samples. All samples were washed in an ultrasonication bath after identifying the percentage of accretionary lapilli, if any, as they quickly disintegrated during sonication. Sonication was necessary to remove any adhering fine ash (vitric, white to yellow, micron scale), common on most samples. Dellino et al. (1990) also documents the need for sonication when describing

ash grains. For Tepexitl samples, a simple test was conducted on two samples – one with abundant fine ash and one with very little. A Petri dish was divided into 4 quarters – 2 with non-sonicated sample and 2 with the sonicated version. For both samples, the grains were much clearer in the sonicated versions, which made counting easier and more accurate. However, especially with the finer grains, care had to be taken not to oversonicate and introduce erroneous surface features such as pitting and chipping from abrasion. All samples were sonicated on timed intervals then rinsed with clean water. The process was repeated until the water remained clear after a sonication cycle. The -2-phi grains were sonicated on a one minute interval, the 0 phi grains for 30 seconds, and the 2-phi material for 10 seconds.

200 individual grains were counted for each phi size and the data normalized. For the -2-and 0-phi sizes, components were counted dry and separated into respective categories for later lab use. The 2-phi size was too small for effective and accurate separation. These grains were counted wet (in ethanol) to minimize the tendency of such small ash grains to ‘leap’ out of the Petri dish. Using the optical microscope beyond the 2-phi size is not possible, as the grains are too small. In order to confirm category distinctions between the dry and wet samples, one sample of 2-phi grain size was counted twice: once dry and once wet. The percentages were equal within error. Additionally, when component categories in this sample were separated dry and carefully made wet, the distinctions remained the same. Thus, the results between all phi sizes are comparable.

In chapter 3, data were plotted both by sample and stratigraphically. For the stratigraphic profiles, data was adjusted to include only juvenile and lithic populations,

the dominant components and the most telling of vent process. Each sample was normalized to the sum of these components. Samples whose sum of these components was less than 80% of the total normalized componentry were eliminated from the graphs to minimize error. The $-2\text{-}\phi$ data were limited to most of the coarse-grained deposits and were not of much use in analyzing fragmentation processes.